

# Optical Properties of Nanostructured Silicon-rich Silicon Dioxide

by  
Michael Anthony Stolfi

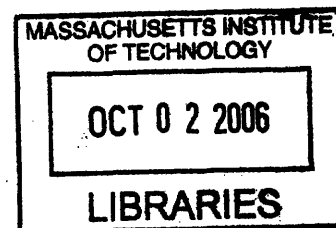
B.S. Materials Science and Engineering, with University Honors  
Carnegie Mellon University, 2000

SUBMITTED TO THE DEPARTMENT OF MATERIALS SCIENCE AND ENGINEERING  
IN PARTIAL FULFILLMENT OF THE REQUIREMENTS FOR THE DEGREE OF

DOCTOR OF PHILOSOPHY IN MATERIALS SCIENCE AND ENGINEERING  
AT THE  
MASSACHUSETTS INSTITUTE OF TECHNOLOGY

September 2006

Copyright ©2006 Massachusetts Institute of Technology.



Signature of Author: \_\_\_\_\_

*Michael A. Stolfi*  
Michael A. Stolfi  
Department of Materials Science and Engineering  
July 21, 2006

Certified by: \_\_\_\_\_

*Lionel C. Kimerling*  
Lionel C. Kimerling  
Thomas Lord Professor of Materials Science and Engineering  
Thesis Advisor

Certified by: \_\_\_\_\_

*John R. Haavisto*  
John R. Haavisto  
Principal Member of the Technical Staff, Charles Stark Draper Laboratory  
Thesis Supervisor

Accepted by: \_\_\_\_\_

*Samuel M. Allen*  
Samuel M. Allen  
POSCO Professor of Physical Metallurgy  
Chair, Departmental Committee on Graduate Students

**ARCHIVES**

# Optical Properties of Nanostructured Silicon-rich Silicon Dioxide

by  
Michael Anthony Stolfi

Submitted to the Department of Materials Science and Engineering in partial fulfillment of the requirements for the degree of Doctor of Philosophy in Materials Science and Engineering at the Massachusetts Institute of Technology

## Abstract

We have conducted a study of the optical properties of sputtered silicon-rich silicon dioxide (SRO) thin films with specific application for the fabrication of erbium-doped waveguide amplifiers and lasers, polarization sensitive devices and devices to modify the polarization state of light. The SRO thin films were prepared through a reactive RF magnetron sputtering from a Si target in an O<sub>2</sub>/Ar gas mixture. The film stoichiometry was controlled by varying the power applied to the Si target or changing the percentage of O<sub>2</sub> in the gas mixture. A deposition model is presented which incorporates the physical and chemical aspects of the sputtering process to predict the film stoichiometry and deposition rate for variable deposition conditions.

The as-deposited films are optically anisotropic with a positive birefringence ( $n_{TM} > n_{TE}$ ) that increases with increasing silicon content for as-deposited films. The dependence of the birefringence on annealing temperature is also influenced by the silicon content. After annealing, samples with high silicon content (>45 at%) showed birefringence enhancement while samples with low silicon content (<45 at%) showed birefringence reduction. A birefringence of more than 3% can be generated in films with high silicon content (50 at% Si) annealed at 1100°C. We attribute the birefringence to the columnar film morphology achieved through our sputtering conditions.

Er was incorporated through reactive co-sputtering from Er and Si targets in the same O<sub>2</sub>/Ar atmosphere in order to investigate the energy-transfer process between SRO and Er for low annealing temperatures. By studying the photoluminescence (PL) intensity of Er:SRO samples annealed in a wide range of temperatures, we demonstrated that the Er sensitization efficiency is maximized between 600°C and 700°C. Temperature-resolved PL spectroscopy on SRO and Er:SRO samples has demonstrated the presence of two different emission sensitizers for samples annealed at 600°C and 1100°C. This comparative study of temperature-resolved PL spectroscopy along with energy Filtered Transmission Electron Microscopy (EFTEM) has confirmed that the more efficient emission sensitization for samples annealed at 600°C occurs through localized centers within the SRO matrix without the nucleation of Si nanocrystals. Er-doped SRO slab waveguides were fabricated to investigate optical gain and loss for samples annealed at low temperatures. Variable stripe length gain measurements show pump dependent waveguide loss saturation due to stimulated emission with a maximum modal gain of  $3 \pm 1.4 \text{ cm}^{-1}$  without the



observation of carrier induced losses. Pump and probe measurements on ridge waveguides also confirms the presence of SRO sensitized signal enhancement for samples annealed at 600°C. Transmission loss measurements demonstrate a significant loss reduction of  $1.5 \text{ cm}^{-1}$  for samples annealed at 600°C compared to those annealed at 1000°C. These results suggest a possible route for the fabrication of compact, high-gain planar light sources and amplifiers with a low thermal budget for integration with standard Si CMOS processes.

**Thesis Advisor: Professor Lionel C. Kimerling**

**Title: Thomas Lord Professor of Materials Science and Engineering**

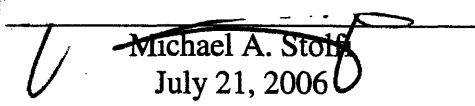
**Thesis Supervisor: Dr. John R. Haavisto**

**Title: Principal Member of the Technical Staff, Charles Stark Draper Laboratory**

# ACKNOWLEDGEMENTS

This thesis was prepared at The Charles Stark Draper Laboratory, Inc., under Internal Research and Development Project # 18052 Flame Hydrolysis Deposition Process Development.

Publication of this thesis does not constitute approval by Draper or the sponsoring agency of the findings or conclusions contained herein. It is published for the exchange and stimulation of ideas.

  
Michael A. Stoff  
July 21, 2006

Throughout my education I have been blessed by the kind support of so many people who, in their own way, have made this work possible.

To Professor Lionel Kimerling for being an excellent mentor. He has also been a terrific role model and has shown me so much respect, kindness and encouragement through my time at MIT. It has been an honor and a privilege to be a member of his research group.

To Dr. Jack Haavisto who has been a great resource in experimental techniques and the theory of photonic devices. I am very thankful that he shared his insight and enthusiasm with me throughout my thesis.

To Dr. Luca Dal Negro whose ideas have stimulated several of the studies in this work. His passion and enthusiasm for science along with his work ethic are so intense they are contagious and have left a permanent mark on me for which I am very grateful.

To John LeBlanc for sharing his hands-on, methodical approach to solving engineering problems. Also many thanks for sacrificing his lunches to help with the photolithography of the waveguides used in this study.

To the members of Electronic Materials Group, both past and present, for many stimulating discussions about the materials science of microphotonics. I am also thankful for their help and enthusiasm in solving experimental and theoretical problems encountered in this thesis. Special thanks to Dr. Jurgen Michel, Dr. Dan Sparacin, Jae-Hyung Yi, Rong Sun, Juejun Hu, Dr. Chingyin Hong, Dr. Anat Eshed, Dr. Sajan Saini, Dr. Jessica Sandland and Jifeng Liu as well as my fellow students and friends Josh Hertz, Dr. Joe Bullard, Ryan Williams and Scott Litzelman for their words of encouragement and support. Many thanks to Mindy Baughman, Ellen Weene and Kathy Farrell for their support, which often goes unnoticed but is always appreciated.

To Dr. Xiaoman Duan for her help in performing the TEM studies in this thesis and for facilitating my collaboration with the failure analysis researchers at National Semiconductor. To Bruce Billings for providing access to the failure analysis labs at National Semiconductor. To Larry Mayes for sharing his Sundays with me, for his excellent training in TEM sample preparation and for teaching me the patience to do the job right every time. To Dr. Tony Garratt-Reed, Mike Frongillo and Yong Zhang at MIT for their assistance and training in performing the TEM and SEM studies in this thesis.

To the many technical staff members at Draper Laboratory who have shared their time to deepen my thesis experience. To Dr. George Schmidt and Loretta Mitrano in the Draper education office for facilitating my interactions with Draper technical staff through the Draper Fellow program. To Dr. Bill Kelleher, Dr. Neil Barbour, Dr. John Dowdle, Rich Russell and Neil Adams for their interest in this thesis work and their support of the Draper internal research and development projects and university research and development projects that have funded this work. To all of the members of the Fiber-/Electro-Optics group especially Dr. Charles Tapalian, Jason Langseth, Jesse Tawney, Farhad Hakimi, Fran Rogomentich, Paul Jones, Dr. Paul Lane, Phil Burke, Dr. Rick Stoner and Dr. J.P. Laine for sharing their insights, talents, experience and most importantly, their time. Special thanks to Jesse Tawney for taking me under his wing and introducing me to photonics device analysis in my first few months at Draper. To Dan Pulver for providing access to the fabrication facilities at Draper.

To John Chervinsky of Harvard University and Dr. Nilanjan Chatterjee at MIT for their help in the chemical analysis of the SRO films. Also to Kurt Broderick at MIT for helping with the development of the etching process to fabricate ridge waveguides.

To Professor Caroline Ross and Professor Samuel Allen for sharing their insight in very helpful discussions.

To the people who inspired me to pursue a career in the sciences. To Mrs. Ding my high school chemistry and physics teacher for sparking my interest in science and for encouraging me to study the sciences in college. To Professor Prashant Kumta at Carnegie Mellon University, my undergraduate research advisor, who first introduced me to Materials Science research and who encouraged me to pursue a career in research. To Professor Robert Doremus at Rensselaer Polytechnic Institute for hosting me in his research group as a summer research associate the summer after my junior year and for deepening my interest in pursuing a career in research.

I owe so much to my parents and my sister for their constant words of support and encouragement. Finally to my wife Michelle who has supported me and sacrificed so much through this thesis that she practically deserves to be awarded the degree. I am dedicating this work to her and to my son Jacob.



# Table of Contents

Chapter 1 Introduction .....	20
1.1. Motivation.....	20
1.2. Background and Previous Work .....	23
Fabrication of Si-rich SiO <sub>2</sub> and Si Nanostructures .....	23
Optical Anisotropy .....	24
Light Emission from Nanostructured Si .....	25
Light Emitting Properties of Undoped Si Nanocrystals .....	25
The Energy-transfer Process to Er Ions .....	26
Optical Gain in Er-doped Si-rich SiO <sub>2</sub> .....	28
1.3. Organization of this Thesis .....	29
Chapter 2 Deposition of Si-rich SiO <sub>2</sub> and Er-doped Si-rich SiO <sub>2</sub> through Reactive Sputtering ..	31
2.1. Description of the Sputtering Process.....	31
2.2. Modeling the Reactive Sputter Deposition Process.....	33
2.2.1. Description of the Apparatus .....	33
2.2.2. General Model of the Reactive Sputtering Process .....	34
2.3. Application of the Sputtering Model to SRO Deposition.....	36
2.3.1. Measuring the Si Content versus Deposition Parameters .....	36
Rutherford Backscattering Spectroscopy.....	36
Wavelength Dispersion Spectroscopy .....	38
2.3.2. Comparison of the Deposition Model with SRO Film Properties .....	39
SRO Deposition – The Low %O <sub>2</sub> Regime.....	39
Target Oxidation in the High %O <sub>2</sub> Regime .....	41
2.4. Incorporating Erbium.....	43
Chapter 3 Si-rich SiO <sub>2</sub> Phase Transformations.....	47
3. 1. Formation of Si Nanocrystals .....	48
3.1.1. Homogeneous vs. Heterogeneous Nucleation .....	48
3.1.2.1. Micro-Raman Spectroscopy.....	54
3.1.2.2. Transmission Electron Microscopy .....	56
3.2. Low Temperature Phenomena .....	57
Chapter 4 Optical Anisotropy and Dispersion in Si-rich SiO <sub>2</sub> Films.....	62
4.1. Measuring the Refractive Index through Prism Coupling .....	62
4.2. Birefringence.....	66
4.2.1. Effect of Waveguide Structure.....	69
4.2.2. Effect of Film Stress .....	70
4.2.3. Effect of Film Structure .....	72
4.3. Dispersion .....	81
Chapter 5 Photoluminescence Characterization of SRO, Er:SiO <sub>2</sub> and Er:SRO Films .....	85
5.1. Description of the Experimental Setup.....	85
5.2. Photoluminescence Characterization of Undoped SRO Films .....	87
5.2.1. Photoluminescence Spectroscopy .....	87
5.2.2. Time Resolved Photoluminescence .....	90
5.2.3. Non-radiative Auger Recombination in SRO .....	93

5.3. Photoluminescence Characterization of Er-doped SiO <sub>2</sub> .....	95
5.3.1. Photoluminescence Spectroscopy .....	95
5.3.2. Time Resolved Photoluminescence .....	97
5.3.3. Non-radiative Recombination through Upconversion .....	98
5.4. Photoluminescence Characterization of Er-doped SRO .....	100
5.4.1. Photoluminescence Spectroscopy .....	100
5.4.2. Time Resolved Photoluminescence .....	105
5.4.3. Non-radiative Recombination through Upconversion .....	107
5.5. Low Temperature Photoluminescence Spectroscopy of SRO and Er-doped SRO.....	108
5.6. Gamma Irradiation Effects on SRO and Er Light Emission.....	112
Chapter 6 Slab Waveguide Devices.....	114
6.1. Optical Modes in Asymmetric Slab Waveguides .....	114
6.2. Optical Amplification – The Variable Stripe Length Technique.....	121
6.2.1. Description of the Technique and Apparatus.....	121
6.2.2. Measurement of Er:SRO Samples Annealed at 600°C.....	124
6.3. Rate Equation Modeling of the Er – SRO System.....	127
6.4. Transmission Loss through Prism Coupling Measurements .....	131
6.4.1. Description of the Technique and Apparatus.....	131
6.4.2. Measurement of Er:SRO and Er,Ge SiO <sub>2</sub> Absorption Spectra.....	133
6.4.3. Measurement of the Er Absorption Cross Section for Er:SRO and Er,Ge:SiO <sub>2</sub> .....	136
6.4.4. SRO Matrix Transmission Loss.....	138
Scattering from Si Nanoclusters .....	138
Scattering from the Columnar SRO Medium .....	140
Effect of Multiple Scattering and the Coherent Potential Approximation .....	142
Discussion of the Scattering Calculation Results .....	147
Chapter 7 Er-doped SRO Ridge Waveguide Devices.....	149
7.1. Design and Fabrication of SRO Ridge Waveguides.....	149
7.2. Transmission Loss – The Cutback Loss Technique .....	153
7.2.1. Description of the technique and apparatus .....	153
7.2.2. Er-doped SRO Ridge Waveguide Losses and Comparison to Prism Coupling.....	154
7.3. Optical amplification – The Pump and Probe Technique.....	155
7.3.1. Description of the technique and apparatus .....	155
7.3.2. Measurement of Er:SRO Samples .....	157
Thermal Effects in Waveguides Deposited on Clad Silicon Wafers .....	157
Signal Enhancement in Waveguides Deposited on Fused Silica Wafers .....	159
Chapter 8 Conclusions and Future Work.....	162
Appendix A Computing the Effective Index, Confinement Factor and E-field Profile for Optical Modes in a Slab Waveguide .....	166
Appendix B Program for Rate Equation Modeling of the Er-Sensitizer Coupling.....	173
Appendix C Program for Calculating the Scattering Cross Section, Scattering Efficiency and Loss Coefficient for Spherical Scatterers .....	177
Appendix D Program for Calculating the Scattering Cross Section, Scattering Efficiency and Loss Coefficient for Cylindrical Scatterers .....	184
References .....	190

# List of Figures

Figure 2.1 (a) Photograph of the Kurt J. Lesker Co. CMS 18 sputtering system. (b) Schematic diagram of the same system..... 33

Figure 2.2 RBS Spectrum of a sputtered SRO sample. The black line is the experimental spectrum collected using 2MeV He+ ions and a total integrated charge of 5 $\mu$ C. The red line is a simulation using RUMP [104,105] software with the Si stopping powers from [106] and yielding a Si content of 37.8 at%, an O content of 62.0 at% and an Ar content of 0.2 at%..... 37

Figure 2.3 (a) Si content and (b) deposition rate versus Si cathode power for samples prepared in 10% O<sub>2</sub> in Ar (open squares) and 12.5% O<sub>2</sub> in Ar (open circles). The solid lines are calculations using equations 2.4 and 2.6 with  $A_S = 81.07 \text{ cm}^2$ ,  $A_T = 31.77 \text{ cm}^2$ ,  $\xi_{Si} = 6.15 \times 10^{12} \text{ atoms/cm}^2\text{sW}$ ,  $\alpha_S = 1.19 \times 10^{-2}$  and  $\phi_{O,loss} = 1.32 \times 10^{17} \text{ atoms/s}$ . .... 40

Figure 2.4 (a) Experimental results of atomic fraction of Si (solid circles) and deposition rate (solid triangles) for SRO samples deposited with 350W applied to the Si cathode at several % O<sub>2</sub> in Ar. (b) Results of a calculation of the fraction of the Si target covered with oxide from the data in panel (a) according to equation 2.12..... 42

Figure 2.5 Er concentration measured through RBS versus Er cathode power for 20% O<sub>2</sub> in Ar (open squares) and 10% O<sub>2</sub> in Ar (solid circles) with a fixed Si cathode power of 300 W..... 44

Figure 2.6 Percentage change in Er concentration relative to the Er concentration at a Si/O ratio of 0.6 for samples prepared by varying the Si cathode power at a constant Er cathode power (solid circles) and changing the percentage of O<sub>2</sub> in Ar at a constant Si cathode power and Er cathode power (open squares)..... 45

Figure 2.7 Percentage increase in Er concentration relative to the Er concentration at a Si/O ratio of 0.6 for samples prepared by changing the percentage of O<sub>2</sub> in Ar at a constant Si cathode power and Er cathode power (open squares). We also show the percentage increase in Er concentration for samples prepared by changing the percentage of O<sub>2</sub> in Ar at a constant Si cathode power with a variable Er cathode power (open circles). .... 45

Figure 3.1 Si-O phase diagram at low pressure. (from Binary Alloy Phase Diagrams [114]) ..... 47

Figure 3.2 Calculated Gibbs free energy of formation normalized by kT versus Si content for several temperatures with  $\gamma_{CM} = 0.3 \text{ J/m}^2$ ,  $V_M = 12.1 \text{ cm}^3/\text{mol}$  and  $X_{Si}^{eq} = 0.33$  ..... 50

Figure 3.3 Calculated diffusivity of Si in SRO from Iacona *et al.*  $D = 5 \times 10^{-13} e^{-\frac{1.2\text{eV}}{kT}} \text{ cm}^2\text{s}^{-1}$  [54] in SRO from Tsoukalas *et al.*  $D = 1.378 e^{-\frac{4.74\text{eV}}{kT}} \text{ cm}^2\text{s}^{-1}$  [118] and in SiO<sub>2</sub> from Jaoul *et al.*  $D = 106.1 e^{-\frac{7.6\text{eV}}{kT}} \text{ cm}^2\text{s}^{-1}$  [119]. .... 51

Figure 3.4 (a) Elastic strain energy per nanocluster calculated for spheroid nanoclusters of different radii. (b) Shape function for different precipitates (from Nabarro [120])..... 52

Figure 3.5 Micro-Raman spectra for an SRO sample deposited on SiO<sub>2</sub> with 40 at% Si as-deposited (dash line) and annealed at 1100°C for 1 hour (solid line). The spectrum for a reference Si wafer is shown for comparison (dot line). All spectra are normalized to the intensity of the first order TO phonon peak..... 54

Fig. 3.6 Micro-Raman spectra for SRO samples on SiO<sub>2</sub> substrates with the following compositions (a) 35.9 at% Si (b) 40.5 at% Si (c) 41.8 at% Si, (d) 45.8 at% Si, (e) 47.0 at% Si and



(f) 50.0 at% Si. For all panels the dash line is the as-deposited spectrum and the solid line is the sample spectrum after annealing at 1100°C for 1 hour. In each panel the Micro-Raman spectrum of a reference crystalline Si wafer is shown for comparison (dash-dot line).....	56
Figure 3.7 Plan view TEM image of an SRO sample deposited on a Si substrate with 38 at% Si annealed at 1100°C for 1 hour. (inset) Electron diffraction pattern for the same sample acquired from the same region as the image. ....	57
Figure 3.8 Electron energy-loss spectra for Si and SiO <sub>2</sub> (from Iacona <i>et al.</i> [54]). ....	59
Figure 3.9 Plan view scanning transmission electron microscope images from an SRO sample with 55 at% Si annealed at 1100°C for 1 hour under (a) bright-field conditions, (b) energy filtered conditions at the Si electron energy-loss peak of 17 eV and (c) energy filtered conditions at the SiO <sub>2</sub> electron energy-loss peak. ....	60
Figure 3.10 Plan view scanning transmission electron microscope images from an SRO sample with 38 at% Si annealed at 600°C for 1 hour under (a) bright-field conditions, (b) energy filtered conditions at the Si electron energy-loss peak of 17 eV and (c) energy filtered conditions at the SiO <sub>2</sub> electron energy-loss peak. (d) A higher resolution image of the same sample at the Si electron energy-loss peak.....	61
Figure 4.1 Schematic of the prism coupling apparatus in the Metricon 2010 system. ....	63
Figure 4.2 Ray optics diagram of the film/prism system during prism coupling where $\theta_{\text{ext}}$ is the angle of incidence of the laser beam with respect to the prism normal, $\theta_p$ is the prism angle, $\theta_{\text{int}}$ is the internal angle of the beam that strikes the prism base in contact with the film, $\theta_f$ is the angle of the beam propagating in the film and $\beta$ is the propagation constant of the propagating mode in the film. ....	63
Figure 4.3 Metricon measurement of a SRO thin film, with three film modes, on a silica substrate at $\lambda = 1550$ nm. ....	64
Figure 4.4 (a) Film birefringence, $B = (n_{\text{TM}} - n_{\text{TE}})/n_{\text{TE}}$ , versus TE index of refraction for a Ge-doped SiO <sub>2</sub> sample (open triangle) and SRO samples (open circles). The solid line is a linear fit to the data. ....	67
Figure 4.5 (a) Birefringence change, $\Delta B = B_{\text{Annealed}} - B_{\text{Unannealed}}$ , after annealing for SRO films with 40 at% Si (squares) and 50 at% Si (circles). All samples were annealed for a fixed time of 1 hour. (b) Birefringence change after annealing at 1100°C for 1 hour for several SRO samples with variable Si content. ....	68
Figure 4.6 (a) Transmitted intensity versus effective index obtained through prism coupling for a sample with 40 at% Si as-deposited. (b) Transmitted intensity versus effective index obtained through prism coupling for a sample with 50 at% Si as-deposited. The dot lines represent the calculated effective indices for the TE and TM modes as well as the effective index for the TM mode assuming an isotropic index of refraction. ....	69
Figure 4.7 (a) Wafer radius of curvature for 1cm x 1 cm squares of SRO samples deposited on SiO <sub>2</sub> substrates. (b) Film stress calculated from the measurements of wafer radius of curvature using Stoney's equation. ....	71
Figure 4.8 Structure zone model indicating the expected film microstructure versus deposition pressure and substrate temperature (from Thornton [134]). ....	73
Figure 4.9 AFM images of a 1 $\mu\text{m}$ by 1 $\mu\text{m}$ area of the surface of the following SRO samples deposited on SiO <sub>2</sub> substrates (a) an as-deposited SRO sample with 40 at% Si with an RMS roughness of 5.2 nm (b) an SRO sample with 40 at% Si annealed at 1100°C for 1 hour with an RMS roughness of 4.2 nm. (c) an as-deposited SRO sample with 50 at% Si with an RMS	

roughness was 8.9 nm and (d) an SRO sample with 50 at% Si annealed at 1100°C for 1 hour with an RMS roughness of 4.6 nm.....	74
Figure 4.10 Cross section SEM images of as-deposited SRO samples on SiO <sub>2</sub> substrates with (a) 40 at% Si at 10kX, (b) 50 at% Si at 10kX and (c) 50 at% Si at 90kX.....	75
Figure 4.11 Cross section SEM image of an as-deposited SRO sample on a SiO <sub>2</sub> substrate with 40 at% Si at 4kX. The white arrow indicates the location of the film – substrate interface.....	76
Figure 4.12 Schematic of the slab waveguide structure with the direction of the light polarization indicated. Schematic of the column-boundary microstructure relative to the x, y and z directions defined in the schematic of the waveguide structure. ....	77
Figure 4.13 (a) Calculated index of refraction for the column and boundary region for as-deposited samples based on the effective-medium model for the following conditions: (i) low boundary index (diamonds) and high column index (squares) and (ii) high boundary index (circles) and low column index (triangles). The solid and dotted lines are a guide for the eyes. (b) Calculated index of refraction for the column and boundary region for samples annealed at 1100°C for 1 hour based on the effective-medium model for the following conditions: (i) low boundary index (diamonds) and high column index (squares) and (ii) high boundary index (circles) and low column index (triangles). The solid and dotted lines are a guide for the eyes..	79
Figure 4.14 Measured birefringence for an SRO sample with 50 at% Si annealed at 1100°C for various time (triangles). Calculated index of refraction of the boundary (circles) and the column (squares) based on the measured birefringence. ....	81
Figure 4.15 Material dispersion at 1535nm for SRO samples with different Si content calculated using equation 4.15 from the data listed in Table 4.1.....	83
Figure 5.1 Schematic of the photoluminescence setup used for this study. ....	86
Figure 5.2 Normalized spectral response of the photoluminescence setup. ....	86
Figure 5.3 (a) Photoluminescence spectra for SRO films annealed at 1100°C for 1 hour with Si contents of 34 at%, 35 at%, 38 at% and 43 at%. The spectra were collected using an Ando Optical Spectrum Analyzer. (b) Integrated photoluminescence intensity for several SRO films with different Si content (open circles). The solid line is a Gaussian fit to the experimental data. ....	87
Figure 5.4 (a) Photoluminescence spectra for SRO films with 40 at% Si annealed at 300 °C (dotted line), 600 °C (solid line) and 1100 °C (dashed line). (b) Integrated photoluminescence intensity for SRO films with 40 at% Si versus annealing temperature. The photoluminescence was integrated between 652 – 1500 nm. (c) Photoluminescence spectra for SRO films with 50 at% Si annealed at 300 °C (dotted line), 600 °C (solid line) and 1100 °C (dashed line). (d) Integrated photoluminescence intensity for SRO films with 50 at% Si versus annealing temperature. The photoluminescence was integrated between 652 – 1500 nm.....	88
Figure 5.5 (a) Integrated PL intensity for samples with 38 at% Si annealed at 1100°C. (b) Integrated PL intensity for samples with 50 at% Si annealed at 1100°C. ....	89
Figure 5.6 Schematic of the energy level diagram for the Si nanocrystal. ....	91
Figure 5.7 Inverse rise time versus pump-photon flux for a sample with 38 at% Si annealed at 1100°C for 1 hour with the detection wavelength set at 930 nm (open circles). The solid line is a linear fit to the data yielding an excitation cross section of $1 \times 10^{-17} \text{ cm}^2$ and an emission lifetime of 80 $\mu\text{s}$ . ....	92

Figure 5.8 Photoluminescence decay for a SRO sample with 38 at% Si annealed at 1100°C for 1 hour measured with the detection wavelength set at 800 nm and a pump power of 10 mW (open circles). The line is an exponential decay fit to the data yielding an emission lifetime of 80  $\mu$ s. 92

Figure 5.9 Schematic representation of the inter-site upconversion process between two coupled SRO sensitizers (or Si nanocrystals)..... 93

Figure 5.10 Steady-state photoluminescence for an SRO sample annealed at 600°C for 1 hour (open circles). The solid line is a simulation of the data with  $n_T = 6 \times 10^{18} \text{ cm}^{-3}$ ,  $\sigma_{ab} = 1.6 \times 10^{-17} \text{ cm}^2$  and  $C_A = 1 \times 10^{-13} \text{ cm}^3 \text{ s}^{-1}$ . The emission lifetime for this simulation was set to 1  $\mu$ s which is the resolution of our measurement system. .... 94

Figure 5.11 (a) Photoluminescence spectrum from an Er:SiO<sub>2</sub> sample with  $8.7 \times 10^{19} \text{ ions/cm}^3$  annealed at 1000°C for 1 hour. (b) Peak Er photoluminescence intensity for Er:SiO<sub>2</sub> samples with  $8.7 \times 10^{19} \text{ ions/cm}^3$  annealed for 1 hour at various temperatures. .... 95

Figure 5.12 Er emission for samples annealed at 1000°C for 1 hour with variable Er concentration..... 96

Figure 5.13 Er emission intensity at 1535nm for samples with an Er concentration of  $1 \times 10^{20} \text{ ions/cm}^3$  annealed at 1000°C for various times. .... 96

Figure 5.14 Inverse rise time versus pump-photon flux for a sample with an Er concentration of  $8.7 \times 10^{19} \text{ Er ions/cm}^3$  annealed at 1100°C for 1 hour with the detection wavelength set at 1535 nm (open circles). The solid line is a linear fit to the data yielding an excitation cross section of  $1 \times 10^{-19} \text{ cm}^2$  and an emission lifetime of 9.9 ms..... 97

Figure 5.15 Photoluminescence decay for an Er:SiO<sub>2</sub> sample with an Er concentration of  $8.7 \times 10^{19} \text{ ions/cm}^3$  annealed at 1100°C for 1 hour measured with the detection wavelength set at 1535 nm and a pump power of 7.6 mW (open circles). The solid line is an exponential decay fit to the data yielding an emission lifetime of  $9.7 \pm 0.6 \text{ ms}$ . .... 98

Figure 5.16 Schematic of the upconversion process between two excited Er<sup>3+</sup> ions. .... 99

Figure 5.17 Er emission intensity at 1535nm versus 488 nm pump-photon flux from a reference Er in SiO<sub>2</sub> sample with an Er concentration of  $8.7 \times 10^{19} \text{ ions/cm}^3$  annealed at 1100°C (open circles). The dot line is a linear fit of the data. .... 100

Figure 5.18 Room temperature photoluminescence versus wavelength for a Si-nc in SiO<sub>2</sub> sample with 38 at% Si annealed at 1100 °C (dot line), for an Er in SRO sample with 38 at% Si and Er concentration of  $8.2 \times 10^{19} \text{ cm}^{-3}$  annealed at 1100 °C (dash line) for an Er in SRO sample with 38 at% Si and Er concentration of  $8.2 \times 10^{19} \text{ cm}^{-3}$  annealed at 600 °C (dash - dot line) and an Er in SiO<sub>2</sub> sample with an Er concentration of  $8.7 \times 10^{19} \text{ cm}^{-3}$  annealed at 1100 °C (solid line)..... 101

Figure 5.19 (a) RT Er emission versus annealing temperature for Er:SRO samples with thickness  $\sim 1.85 \mu\text{m}$ , 38 at % Si and Er concentration of  $8.2 \times 10^{19} \text{ cm}^{-3}$  (circles) and reference Er in SiO<sub>2</sub> samples with thickness  $\sim 1.24 \mu\text{m}$  and an Er concentration of  $8.7 \times 10^{19} \text{ cm}^{-3}$  (squares, magnified by 10). The PL intensity has been scaled to account for the difference in sample thickness. (b) Emission enhancement (where the enhancement is equal to the ratio of the Er:SRO 1.54  $\mu\text{m}$  PL intensity to the PL intensity of the reference Er in SiO<sub>2</sub> samples) versus annealing temperature (triangles). .... 102

Figure 5.20 Photoluminescence spectra under resonant (488 nm, dash-dot line) and non-resonant (457 nm, solid line) pumping conditions for an Er:SRO sample with 38 at% Si and an Er concentration of  $8.2 \times 10^{19} \text{ ions/cm}^3$  and an Er:SiO<sub>2</sub> sample with an Er concentration of  $8.7 \times$

$10^{19}$  ions/cm<sup>3</sup> magnified by 50. The intensities have been scaled to account for different sample thicknesses. .... 103  
 Figure 5.21 (a) Room temperature photoluminescence versus wavelength for an Er in SiO<sub>2</sub> sample with an Er concentration of  $8.7 \times 10^{19}$  ions/cm<sup>3</sup> annealed at 900 °C (dash line), Er in SRO sample with 38 at% Si and Er concentration of  $8.2 \times 10^{19}$  ions/cm<sup>3</sup> annealed at 900 °C (solid line) and Er in SRO sample with 38 at% Si and Er concentration of  $8.2 \times 10^{19}$  ions/cm<sup>3</sup> annealed at 600 °C (dot line). (b) Er emission full width half maximum for Er in SRO samples with an Er concentration of  $8.2 \times 10^{19}$  ions/cm<sup>3</sup> (solid circles) and Er in SiO<sub>2</sub> samples with an Er concentration of  $8.7 \times 10^{19}$  ions/cm<sup>3</sup> (solid squares). .... 104  
 Figure 5.22 Normalized Er emission intensity at 1535nm from Er:SRO samples annealed for 1 hour at various temperatures with the following Er and Si contents: 33 at% Si and an Er concentration of  $8.2 \times 10^{20}$  ions/cm<sup>3</sup> (squares), 35 at% Si and an Er concentration of  $6.2 \times 10^{20}$  ions/cm<sup>3</sup> (stars), 38 at% Si and an Er concentration of  $7.9 \times 10^{19}$  ions/cm<sup>3</sup> (circles), 41 at% Si and an Er concentration of  $7.7 \times 10^{20}$  ions/cm<sup>3</sup> (diamonds) and 53 at% Si and an Er concentration of  $1.1 \times 10^{21}$  ions/cm<sup>3</sup> (triangles). .... 104  
 Figure 5.23 (a) Er emission inverse rise time versus pumping photon flux at 488 nm for the Er:SRO sample annealed at 600°C with 38 at% Si and an Er concentration of  $8.2 \times 10^{19}$  ions/cm<sup>3</sup>. The solid line is a linear fit yielding an excitation cross section of  $\sigma_{exc} = 9.05 \times 10^{-17}$  cm<sup>2</sup>. (b) Er emission inverse rise time versus pumping photon flux at 488 nm for the Er:SRO sample annealed at 1100°C with 38 at% Si and an Er concentration of  $8.2 \times 10^{19}$  ions/cm<sup>3</sup>. The solid line is a linear fit yielding an excitation cross section of  $\sigma_{exc} = 5.30 \times 10^{-17}$  cm<sup>2</sup>. .... 105  
 Figure 5.24 Room temperature Er photoluminescence lifetime for an Er:SRO sample with 38at% Si and an Er concentration of  $8.2 \times 10^{19}$  ions/cm<sup>3</sup> annealed at various temperatures for 1 hour. 107  
 Figure 5.25 Er emission intensity at 1535nm versus 488nm pump-photon flux from a reference Er in SiO<sub>2</sub> sample with an Er concentration of  $8.7 \times 10^{19}$  ions/cm<sup>3</sup> annealed at 1100°C for 1 hour (open squares) and an Er in SRO sample with 38 at% Si and an Er concentration of  $8.2 \times 10^{19}$  ions/cm<sup>3</sup> annealed at 600°C for 1 hour (open circles). The dot line is a linear fit of the data for the reference Er in SiO<sub>2</sub> sample which has been superimposed on the low photon flux data for the Er in SRO sample for comparison. .... 108  
 Figure 5.26 (a) PL emission for the high temperature annealed (1100 °C) sample at 10 K (solid line), 125 K (dash line) and 295 K (dot line) pumping with 488 nm light at a pump power of 58 mW. (b) PL emission for the low temperature annealed (600 °C) sample at 10 K (solid line), 125 K (dash line) and 295 K (dot line) pumping with 488 nm light at a pump power of 98 mW. (c) Integrated PL intensity for a SRO sample with 38 at% Si annealed at 1100 °C (solid squares) and an SRO sample with 38 at% Si annealed at 600 °C (solid circles) versus temperature. The PL for the sample annealed at 1100 °C was integrated from 652 – 1000 nm while the PL for the sample annealed at 600 °C was integrated from 652 – 1600 nm. (d) Integrated PL intensity for an Er in SRO sample with 38 at% Si and an Er concentration of  $1.08 \times 10^{20}$  cm<sup>-3</sup> annealed at 1100 °C (solid squares) and an Er in SRO sample with 38 at% Si and an Er concentration of  $1.08 \times 10^{20}$  cm<sup>-3</sup> annealed at 600 °C (solid circles) versus temperature. The PL for both samples was integrated from 1400 – 1600 nm. .... 110

Figure 5.27 Integrated Er emission intensity for the following gamma irradiated samples (a) Er-doped SiO<sub>2</sub> with  $1 \times 10^{20}$  Er atoms/cm<sup>3</sup> annealed at 1000°C for 1 hour, (b) Er-doped SRO with 38at% Si and  $1 \times 10^{20}$  Er atoms/cm<sup>3</sup>, unannealed, (c) Er-doped SRO with 38at% Si and  $1 \times 10^{20}$  Er atoms/cm<sup>3</sup> annealed at 600°C for 1 hour and (d) Er-doped SRO with 38at% Si and  $1 \times 10^{20}$  Er atoms/cm<sup>3</sup> annealed at 1100°C for 1 hour. The intensity for each sample was integrated between 1400 nm and 1700 nm..... 113

Figure 6.1 Schematic of an asymmetric slab waveguide..... 115

Figure 6.2 Refractive index and E-field profile for an Er-doped SRO slab waveguide with an index of refraction of 1.5465 and thickness of 1.3μm. The power confinement factor was calculated to be 0.8474. .... 121

Figure 6.3 Side view schematic of the variable stripe length optical gain measurement setup.. 122

Figure 6.4 Pump beam profile measured in the longitudinal direction at the beginning of the gain measurement (squares) and at the end of the gain measurement (circles). The solid lines are Gaussian fits of the data with a center position and width of 0.3300 cm and 1.838mm measured for the beam at the beginning of the measurement and a center position and width of 0.3316 cm and 1.896 mm measured for the beam at the end of the measurement. The dash line indicates the position of the sample edge relative to the beam profile during the gain measurements. .... 123

Figure 6.5 Measured intensity versus excitation stripe length for an Er-doped SRO sample with 36.5at% Si and  $1.2 \times 10^{20}$  Er ions/cm<sup>3</sup> annealed at 600°C for 1 hour (circles) collected at pump-power densities of (a) 26.5 W/cm<sup>2</sup>, (b) 133 W/cm<sup>2</sup> and (c) 2654 W/cm<sup>2</sup>. The solid lines are fits to the data using the one-dimensional amplifier model equation 7.25 yielding modal gain values of (a)  $-11.6 \text{ cm}^{-1}$  (b)  $-8.74 \text{ cm}^{-1}$  and (c)  $-5.3 \text{ cm}^{-1}$ ..... 125

Figure 6.6 Modal gain versus pump-power density determined from fits of emission intensity versus excitation stripe length data for various pump-power densities for an Er-doped SRO sample with 36.5 at% Si and  $1.2 \times 10^{20}$  Er ions/cm<sup>3</sup> annealed at 600°C for 1 hour. The horizontal dotted lines are guides to the eyes to indicate the saturation regions at low and high pump-power densities as well as the transparency threshold at  $-8.68 \text{ cm}^{-1}$  which separates the absorption bleaching and stimulated emission regimes..... 126

Figure 6.7 Schematic of a coupled two level system for the SRO sensitizer – Er interaction with phenomenological parameters describing the transitions between levels as described in the text. .... 127

Figure 6.8 Simulations of (a) gain and (b) Er excited-state population using the rate equations in equation 6.27 and 6.28 to demonstrate the effect of changing sensitizer density,  $n_{\text{tot}}$ . The other simulation parameters were held constant at values of  $N_{\text{tot}} = 1.1 \times 10^{20} \text{ cm}^{-3}$ ,  $\gamma_{\text{ac}} = 150 \times 10^{-15} \text{ cm}^3 \text{ s}^{-1}$ ,  $\sigma = 1 \times 10^{-19} \text{ cm}^2$ ,  $\tau = 3 \times 10^{-3} \text{ s}$ ,  $\sigma_{\text{ab}} = 9 \times 10^{-17} \text{ cm}^2$ ,  $\tau_{\text{ba}} = 1 \times 10^{-6} \text{ s}$ ,  $C_{\text{A}} = 1 \times 10^{-13} \text{ cm}^3 \text{ s}^{-1}$ ,  $C_{\text{up}} = 2.5 \times 10^{-17} \text{ cm}^3 \text{ s}^{-1}$  and  $\sigma_{\text{emis}} = 3 \times 10^{-20} \text{ cm}^2$ ..... 129

Figure 6.9 Simulations of (a) gain and (b) Er excited-state population using the rate equations in equation 6.27 and 6.28 to demonstrate the effect of changing the coupling coefficient between the sensitizer and Er,  $\gamma_{\text{ac}}$ . The other simulation parameters were held constant at values of  $N_{\text{tot}} = 1.1 \times 10^{20} \text{ cm}^{-3}$ ,  $n_{\text{tot}} = 3 \times 10^{18} \text{ cm}^{-3}$ ,  $\sigma = 1 \times 10^{-19} \text{ cm}^2$ ,  $\tau = 3 \times 10^{-3} \text{ s}$ ,  $\sigma_{\text{ab}} = 9 \times 10^{-17} \text{ cm}^2$ ,  $\tau_{\text{ba}} = 1 \times 10^{-6} \text{ s}$ ,  $C_{\text{A}} = 1 \times 10^{-13} \text{ cm}^3 \text{ s}^{-1}$ ,  $C_{\text{up}} = 2.5 \times 10^{-17} \text{ cm}^3 \text{ s}^{-1}$  and  $\sigma_{\text{emis}} = 3 \times 10^{-20} \text{ cm}^2$ ..... 129

Figure 6.10 Simulations of gain using the rate equations in equation 6.27 and 6.28 to demonstrate the effect of changing the emission cross section of Er. The other simulation parameters were held constant at values of  $N_{\text{tot}} = 1.1 \times 10^{20} \text{ cm}^{-3}$ ,  $n_{\text{tot}} = 3 \times 10^{18} \text{ cm}^{-3}$ ,  $\gamma_{\text{ac}} = 3 \times 10^{-15} \text{ cm}^3 \text{ s}^{-1}$ ,  $\sigma = 1 \times 10^{-19} \text{ cm}^2$ ,  $\tau = 3 \times 10^{-3} \text{ s}$ ,  $\sigma_{\text{ab}} = 9 \times 10^{-17} \text{ cm}^2$ ,  $\tau_{\text{ba}} = 1 \times 10^{-6} \text{ s}$ ,  $C_{\text{A}} = 1 \times 10^{-13} \text{ cm}^3 \text{ s}^{-1}$  and  $C_{\text{up}} = 2.5 \times 10^{-17} \text{ cm}^3 \text{ s}^{-1}$ .130

Figure 6.11 (a) Measured optical gain versus pump-power density for the Er-doped SRO gain sample with 36.5 at% Si and  $1.2 \times 10^{20}$  Er ions/cm<sup>3</sup> annealed at 600°C for 1 hour (open circles). (b) Measured steady-state Er emission at 1535nm for the same gain sample (open circles). The solid lines is a linear fit using the rate equation model for the Er – SRO interaction with the following parameters  $n_{\text{tot}} = 6 \times 10^{18}$  sensitizers/cm<sup>3</sup>,  $\gamma_C = 150 \times 10^{-15}$  cm<sup>3</sup>s<sup>-1</sup>,  $\sigma = 1 \times 10^{-19}$  cm<sup>2</sup>,  $\tau = 4.2$  ms,  $\sigma_{\text{ab}} = 1.6 \times 10^{-17}$  cm<sup>2</sup>,  $\tau = 1$   $\mu$ s,  $C_{A1} = 1 \times 10^{-13}$  cm<sup>3</sup>s<sup>-1</sup>,  $C_{UP} = 3 \times 10^{-18}$  cm<sup>3</sup>s<sup>-1</sup>,  $\sigma_{\text{emis}} = 3.5 \times 10^{-20}$  cm<sup>2</sup> and  $\alpha = 9.2$  cm<sup>-1</sup>. ..... 130

Figure 6.12 Schematic of the prism coupling loss setup for measuring propagation losses in slab waveguides..... 132

Figure 6.13 Experimental data of transmitted intensity versus prism spacing for Er,Ge-doped SiO<sub>2</sub> samples (a) annealed at 600°C at 1470nm (diamonds)  $\alpha = -0.193$  cm<sup>-1</sup>, 1534nm (circles)  $\alpha = -0.794$  cm<sup>-1</sup>, 1550nm (squares)  $\alpha = -0.371$  cm<sup>-1</sup> and 1620nm (triangles)  $\alpha = -0.043$  cm<sup>-1</sup> and (b) 1000°C at 1525nm (diamonds)  $\alpha = -0.503$  cm<sup>-1</sup>, 1532nm (circles)  $\alpha = -0.720$  cm<sup>-1</sup>, 1550nm (squares)  $\alpha = -0.401$  cm<sup>-1</sup> and 1620nm (triangles)  $\alpha = -0.056$  cm<sup>-1</sup>. The solid lines are linear fits of the experimental data yielding the loss coefficients stated above. .... 134

Figure 6.14 Experimental data of transmitted intensity versus prism spacing for Er,Ge-doped SiO<sub>2</sub> samples (a) annealed at 600°C at 1470nm (diamonds)  $\alpha = -0.124$  cm<sup>-1</sup>, 1535nm (circles)  $\alpha = -1.686$  cm<sup>-1</sup>, 1550nm (squares)  $\alpha = -1.250$  cm<sup>-1</sup> and 1620nm (triangles)  $\alpha = -0.840$  cm<sup>-1</sup> (b) 800°C at 1525nm (diamonds)  $\alpha = -2.066$  cm<sup>-1</sup>, 1534nm (circles)  $\alpha = -2.399$  cm<sup>-1</sup>, 1550nm (squares)  $\alpha = -1.948$  cm<sup>-1</sup> and 1620nm (triangles)  $\alpha = -1.477$  cm<sup>-1</sup> and (c) 1000°C at 1525nm (diamonds)  $\alpha = -2.830$  cm<sup>-1</sup>, 1536nm (circles)  $\alpha = -2.757$  cm<sup>-1</sup>, 1540nm (squares)  $\alpha = -2.719$  cm<sup>-1</sup> and 1620nm (triangles)  $\alpha = -2.288$  cm<sup>-1</sup>. The solid lines are linear fits of the experimental data yielding the loss coefficients stated above. .... 135

Figure 6.15 Transmission loss spectra for (a) Er-doped SRO and (b) Er,Ge-doped SiO<sub>2</sub>..... 136

Figure 6.16 (a) Log-log plot of the extinction coefficient for Er,Ge-doped SiO<sub>2</sub> annealed at 600°C for 1 hour (solid squares) and Er-doped SRO annealed at 600°C for 1 hour (solid circles). The dotted lines represent the linear subtraction that was performed to remove the background losses. (b) Plot of the Er absorption spectrum obtained after the background subtraction in panel (a) for an Er,Ge-doped SiO<sub>2</sub> sample annealed at 600°C for 1 hour (solid squares) and an Er-doped SRO sample annealed at 600°C for 1 hour (solid circles). .... 137

Figure 6.17 Transmission loss spectrum for an Er-doped SRO sample with 36.5 at% Si and an Er concentration of  $1.22 \times 10^{20}$  cm<sup>-3</sup> annealed at 1000°C (open squares). The solid line is a calculation of the attenuation coefficient assuming  $1.2 \times 10^{17}$  nanocrystals/cm<sup>3</sup> with a 1.5 nm radius. .... 140

Figure 6.18 Transmission loss spectrum for an Er-doped SRO sample with 36.5 at% Si and an Er concentration of  $1.22 \times 10^{20}$  cm<sup>-3</sup> annealed at 600°C (open squares). The solid line is a calculation of the attenuation coefficient assuming columns of 170 nm radius and a volume fraction of 0.83. .... 141

Figure 6.19 Transmission loss spectrum for an Er-doped SRO sample with 36.5 at% Si and an Er concentration of  $1.22 \times 10^{20}$  cm<sup>-3</sup> annealed at 600°C (open squares). The solid line is a calculation of the attenuation coefficient according to multiple scattering theory with a volume fraction of 0.82 and a scatterer radius of 150 nm. .... 143

Figure 6.20 Measurement of the (a) real and (b) imaginary index of refraction of an Er-doped SRO sample with a thickness of 1.885  $\mu$ m, 38 at% Si and an Er concentration of  $8.2 \times 10^{19}$  cm<sup>-3</sup>. .... 145

Figure 6.21 Cross section STEM image of an SRO sample with 50 at% Si after annealing at 1100°C for 1 hour. ....	146
Figure 6.22 (a) Energy dispersive x-ray spectra of (a) the embedded cluster, (b) the SiO <sub>2</sub> substrate and (c) the SRO film. The inset in each spectrum indicates the region of the sample where the x-ray signal was collected. ....	147
Figure 7.1. Schematic of a ridge waveguide. ....	149
Figure 7.2 Power confined in the region defined by w and t in Figure 7.1 versus etch depth for three waveguide samples considered in this study that had the following characteristics: w = 9 μm, t = 1.38 μm and n = 1.49 (solid circles), w = 3 μm, t = 1.34 μm and n = 1.56 (solid squares) and w = 3 μm, t = 1.81 μm and n = 1.62 (solid triangles). The wavelength used for the calculation was 1.551 μm with n = 1.444 for the 10 μm thick SiO <sub>2</sub> undercladding and n = 3.48 for the Si wafer. The waveguide overcladding is air. ....	150
Figure 7.3 Fabrication process for forming ridge waveguides. A description of each step is given in the text. ....	151
Figure 7.4 Etch surface of SRO films after being exposed to the AZ422 developer for 0, 1 and 5 minutes. After being removed from the developer the samples were rinsed in DI water for 1 minute. The etch parameters used for all samples were 20 sccm CHF <sub>3</sub> at 300 W RF power and a pressure of 20 mTorr for 22 minutes. All images were taken at 100x using circularly polarized differential interference contrast. ....	152
Figure 7.5 (a) Er-SRO ridge waveguides on a silica substrate. The etch parameters used were 20 sccm CHF <sub>3</sub> at 300 W RF power and a pressure of 20 mTorr for 23.25 minutes. The etch depth was ~0.4 μm. The image was taken at 10x using circularly polarized differential interference contrast. (b) Scanning electron microscope image of the ~9 μm wide waveguide at the input facet indicated by the black box in panel (a). ....	152
Figure 7.6 Insertion loss versus waveguide length for a 3μm wide Er-doped SRO waveguide with 0.5μm etch depth, 38 at% Si, an Er concentration of 1 x 10 <sup>20</sup> cm <sup>-3</sup> annealed at 600°C for 1 hour. ....	153
Figure 7.7 (a) Comparison of the transmission loss for Er:SRO ridge waveguides with 3μm width and 0.5 μm etch depth, an Er concentration of 1x10 <sup>20</sup> cm <sup>-3</sup> and 38 at% Si annealed for 1 hour at 600°C (solid line) and 1100°C (dash-dot line). (b) Normalized transmission loss for the Er:SRO ridge waveguide from panel (a) (solid line) and the Er:SRO slab waveguide analyzed in Chapter 6 (open circles). Both waveguides were annealed at 600°C for 1 hour. ....	154
Figure 7.8 Schematic of the pump and probe measurement setup. ....	156
Figure 7.9 Ratio of the probe signal with the pump on to the probe signal with the pump off versus pump-power density for an Er-doped SRO ridge waveguide sample with 36.5 at% Si annealed at 600°C for 1 hour. The waveguide width was 3 μm, the probe wavelength was 1.535 μm, the probe power was 200 μW and the probe frequency was 10 kHz. ....	157
Figure 7.10 (a) Decay and (b) recovery of the probe intensity at a pump-power density of 55 W/cm <sup>2</sup> for an Er:SRO ridge waveguide sample with 36.5 at% Si and 1x10 <sup>20</sup> ions/cm <sup>3</sup> annealed at 600°C for 1 hour. (c) Decay and (d) recovery of the probe intensity at a pump-power density of 788 W/cm <sup>2</sup> for the same waveguide. The probe wavelength was 1310 nm. The measurement was triggered to the 488 nm pump chopping frequency of 10 Hz. The solid lines are exponential decay and rise fits to the data with decay and recovery times as indicated on the figure. ....	158
Figure 7.11 Ratio of the probe signal with the pump on to the probe signal with the pump off versus pump-power density for an Er-doped SRO ridge waveguide sample with 35.75 at% Si and an Er concentration of 8.3x10 <sup>19</sup> ions/cm <sup>3</sup> annealed at 600°C for 1 hour. The waveguide width	

was 9  $\mu\text{m}$ , the probe wavelength was 1.535  $\mu\text{m}$ , the probe power was 100  $\mu\text{W}$  and the probe frequency was 10 kHz..... 159

Figure 7.12 (a) Optical mode profile for the Er-doped SRO waveguide on a  $\text{SiO}_2$  substrate considered in this experiment. The mode profile was calculated using the Apollo Photonics, Inc. APSS software. (b) Calculate signal enhancement coefficient from the signal enhancement data reported in Figure 7.10 using equation 7.1. For the calculation we used a waveguide confinement factor of 0.55 and a pumping length of 0.09 cm..... 160

Figure 8.1 Schematic of the size scale of the nanostructure considered in this thesis..... 162

Figure C1 (a) Calculated extinction efficiency of water spheres in air using our computer program. (b) Calculated extinction efficiency of water spheres in air from Bohren and Huffman [101]..... 180



# List of Tables

Table 2.1. Film composition and deposition parameters for samples analyzed through RBS.	38
Table 2.2 Experimental results for the deposition rate from Si and SiO <sub>2</sub> targets with 300 W applied to the cathode in pure Ar at a pressure of 3 mTorr.	43
Table 4.1 Results of a Cauchy's equation fit of the wavelength dependence of the index of refraction for several SRO samples.	83
Table 6.1 Sample characteristics for the Er,Ge-doped SiO <sub>2</sub> and Er-doped SRO slab waveguides considered in this study.	133
Table 7.1 Guided photoluminescence intensity and signal enhancement coefficient for the Er-doped SRO waveguide with 35.75 at% Si and an Er concentration of $8.3 \times 10^{19}$ ions/cm <sup>3</sup> annealed at 600°C for 1 hour at a pump-photon flux of $2.3 \times 10^{20}$ photons/cm <sup>2</sup> s for both pumping wavelengths.	161

# Chapter 1 | Introduction

## 1.1. Motivation

Silicon has impacted our way of life more significantly than any other material over the past several decades. The development of the microprocessor and its use in the personal computer have allowed humankind to achieve unprecedented levels of information manipulation, storage and transfer. Microprocessor technology has met the demands for improved computational performance at low cost through size scaling of transistors and interconnects. This scaling, embodied in Moore's Law, has the number of on-chip transistors doubling every six months. However, the trend of improving microprocessor performance through size scaling has several challenges that threaten the microelectronics industry's ability to follow Moore's law. Large resistance-capacitance (RC) time delays and the heat dissipation produced by closely spaced, small cross section metal interconnects have replaced transistor gate delays as the primary limiting factor in improving performance, stimulating the development of novel approaches for device interconnection.

Si microphotronics, the monolithic integration of Si-based optics and electronics, is one approach to device interconnection that offers significantly improved communication bandwidth with negligible heat dissipation and cross-talk. This technology would achieve high clock speed, low latency interconnection between microprocessors operating in parallel. Optical interconnection, when applied to the telecommunications industry, led to improvements of several orders of magnitude in information transmission capacity. The goal is to achieve all of the passive functionality of planar lightwave circuits while adding active functionality for electrical-optical and optical-electrical signal conversion within a small footprint at low cost. Attaining this goal requires the development of four elements:

- (1) a laser as an optical power source
- (2) an optical modulator for electrical to optical signal conversion
- (3) high-index contrast optical waveguides for signal routing and passive waveguide devices for optical add/drop, multiplexing/demultiplexing and switching

#### (4) a photodetector for optical to electrical signal conversion

Planar lightwave circuit technology has demonstrated that packaging of hybrid optical systems is costly due to the tight alignment tolerances required for optical components. Reducing the overall cost of the system will drive the development of all components in one process flow using Si or CMOS compatible materials and standard CMOS processing techniques. This has already been achieved for several of the required elements including low loss, high-index contrast optical waveguides in Si [1,2], Si<sub>3</sub>N<sub>4</sub> [3,4] and SiON [5], splitters [6], directional couplers [7] and ring resonators [8,9], arrayed waveguide gratings for multiplexing/demultiplexing for > 40 channels [10,11], high speed optical modulation [12], optical switching [13], optical isolators [14] and high speed photodetectors [15,16].

Missing from these elements is an efficient Si-based light emitter. It is well known that Si is an indirect bandgap material where photon emission originates from low-probability, phonon-mediated transitions that compete unfavorably with fast, non-radiative de-excitation paths, such as Auger recombination and free-carrier absorption [17]. As a result, the only reports of lasing in Si are based on stimulated Raman scattering which suffers from a high threshold and low wall-plug efficiency [18,19]. To overcome the limitations for light emission in Si, several strategies have been recently developed to engineer Si into a more efficient light emitting material. These include passivation and purification of bulk Si [20,21], quantum confinement in Si nanostructures embedded in SiO<sub>2</sub> [22,23,24,25] and the use of extrinsic light emitting sources such as Si A-centers [26] or rare-earth dopants in silica-based glasses [27,28,29], bulk Si [30,31,32,33,34,35] or Si nanostructures [36,37,38,39,40,41]. The approach of quantum confinement has led to a dramatic improvement of the light generation efficiency in Si nanostructures resulting in reported emission efficiencies of up to 23 % under optical excitation in porous Si after high-pressure water-vapor annealing [25]. The integration of a porous Si light emitting diode and bipolar transistor [42] and sizeable optical gain recently demonstrated in Si nanocrystals embedded in SiO<sub>2</sub> matrices [43,44,45,46,47,48] have opened the race towards the fabrication of an integrated, fully Si-based laser [23]. An attractive application of Si nanocrystals is as emission sensitizers for rare-earth ions, particularly Er ions, to achieve efficient infrared light emission. The Er emission at 1.54  $\mu\text{m}$ , which is below the band gap of Si, is ideal for integration with Si waveguides and microelectronics. As an emission sensitizer the nanocrystals absorb light

from a pumping source and transfer the excitation to the Er with two performance benefits over traditional Er-doped glass devices:

- (1) Broadband pumping – Si nanocrystals are characterized by a wide absorption band located in the visible spectrum. In comparison, Er ions absorb light within narrow wavelength ranges corresponding to transitions between excitation states. Since the excitation is occurring through the nanocrystals, any pump wavelength within the nanocrystal absorption band can be used to efficiently excite the Er ions [49] allowing for optical pumping via white light or LED sources [49,50]. This offers low-cost alternatives for pumping sources compared to the narrow wavelength lasers sources traditionally used to excite Er ions.
- (2) Enhancement of the excitation cross section – The excitation cross section of Si nanocrystals is  $10^{-17} - 10^{-16} \text{ cm}^2$  [51] which is 1000x larger than Er ions. Due to the high efficiency of the energy-transfer process Er ions are effectively excited at the same high excitation efficiency as Si nanocrystals [40] leading to the possibility of fabricating devices with a lower turn on threshold compared to traditional Er doped glasses.

Electrical excitation of Er emission has also been demonstrated [52,53].

Initially it was thought that efficient energy-transfer required the formation of Si nanocrystals with strong light emission. This presented a major drawback for using Si nanocrystals as emission sensitizers since generating efficient Si nanocrystal emission requires high temperature annealing [54] which is not compatible with Si CMOS. However, recent experimental observations have demonstrated that strong Er emission enhancement is exhibited by samples annealed at low temperatures ( $< 800^\circ\text{C}$ ) [55,56] which show a relatively weak Si nanocrystal light emission. This observation calls into question the nature of the energy-transfer process while suggesting a possible route to fabricating a CMOS compatible process through an optimization of the energy-transfer properties of the donor Si-rich  $\text{SiO}_2$  (SRO).

Pump and probe experiments performed on Er and Si nanocrystal doped waveguides have demonstrated that minimization of carrier induced losses is critical in achieving optical gain [57, 58]. There have also been reports that the Er emission cross section is strongly enhanced in the

presence of Si nanocrystals [57, 59,60]. Although the detailed nature of the emission cross section enhancement is not understood and there is a disagreement in the magnitude of this enhancement, it has major ramifications for the fabrication of ultra-compact devices or devices for high-power operation since the total gain is proportional to the emission cross section. Transmission loss measurements revealed that Si nanocrystals within the SRO matrix led to scattering which dominates the overall transmission losses of the system [58, 61].

Despite these exciting and stimulating results the energy-transfer process is not precisely known especially for samples annealed at low temperatures. There are also no studies of optical gain and transmission loss for samples annealed at the low annealing temperatures which are most relevant for integration with CMOS technologies. Finally there are no detailed studies of nanocrystal nucleation in structurally heterogeneous films, such as sputtered films with columnar morphologies, and their application to fabricate novel devices. It is with these points in mind that we have conducted this thesis study.

## **1.2. Background and Previous Work**

### **Fabrication of Si-rich SiO<sub>2</sub> and Si Nanostructures**

We have focused on the fabrication of Si nanocrystal devices through annealing of SRO films [62,63,64,65,66,67]. SRO can be fabricated through a variety of techniques such as ion implantation into stoichiometric SiO<sub>2</sub> [63,64], chemical vapor deposition [62,65], sputtering [68] and thermal evaporation of SiO [67]. After deposition the films are annealed to induce a precipitation transformation where the metastable Si-rich dielectric film decomposes into two stable phases: Si clusters and a matrix which is closer in composition to the equilibrium (stoichiometric) composition. Several studies have been devoted to monitoring the nucleation process through the use of transmission electron microscopy [54], Fourier Transform Infrared Spectroscopy [69] and micro-Raman spectroscopy. [70]

Alternative techniques for fabricating Si nanocrystals include electrochemical etching [71,72], laser assisted processing [73,74], solution synthesis [75] and annealing of Si/SiO<sub>2</sub> [76] or SiO/SiO<sub>2</sub> superlattices [77]. Among these the use of Si/SiO<sub>2</sub> and SiO/SiO<sub>2</sub> superlattices has been demonstrated to yield nanocrystals with a narrow size distribution with the average size and density determined by the thickness of the Si (or SiO) and SiO<sub>2</sub> layers, respectively. This technique also allows for the spatial control of the nanocrystal formation since the nanocrystals are confined to the Si and SiO layers.

## Optical Anisotropy

In optical crystals with specific non-centrosymmetric structures light propagates with two different phase velocities corresponding to two different polarization states. At the interface between the crystal and air (or any optically isotropic material) light will exit at two angles corresponding to the two phase velocities, a property known as double refraction or birefringence. The term birefringence is also associated with a measurement of the relative difference between these refractive indices or the optical anisotropy of the matrix.

Si and SiO<sub>2</sub> are both optically isotropic. As a result optical anisotropy must be engineered into these materials through structural modifications (form birefringence) or stress. Birefringence in nanostructured Si has been reported in porous Si [78] and Si nanocrystal films prepared through annealing of Si and SiO<sub>2</sub> superlattices [79]. Porous Si is formed through electrochemical etching of bulk (110) Si wafers resulting in pores along the [100] and [010] crystallographic directions. The Si layers of Si/SiO<sub>2</sub> superlattices are unstable at high temperatures and decompose to form sheets of closely spaced Si nanocrystals. The structure of these films is highly anisotropic with the observed birefringence is attributed to differences in dielectric screening for the two polarizations of light within the film structure.

High birefringence has also been demonstrated for so-called sculptured thin films where SiO<sub>2</sub> is sputter deposited at an oblique angle to obtain a highly porous columnar structure [80]. Due to their high porosity these films suffer from a high sensitivity to environmental conditions. An

intriguing possibility would be to obtain high birefringence through the same self-assembled processes in films with higher density which are more robust. We have investigated this approach through the use of sputtered films with columnar morphologies. We have demonstrated a strong birefringence enhancement after annealing for samples with high Si content. Through an investigation of several samples we showed that the magnitude of the birefringence can be tuned from near zero to values approaching several bulk anisotropic crystals through the appropriate selection of annealing temperature and Si content. This birefringence enhancement is absent from nanocrystals formed through annealing of SRO prepared by other techniques [79].

## **Light Emission from Nanostructured Si**

### **Light Emitting Properties of Undoped Si Nanocrystals**

Si nanocrystals possess several intriguing optical properties with application toward the fabrication of optoelectronic devices. Among these is a broad, near infrared emission spectrum, located above the band edge of bulk Si, with a peak emission wavelength that can be tuned over a few hundred nanometers by varying processing parameters [73,81,82]. Several studies have been conducted to understand the origin of this strong emission. Time-resolved photoluminescence experiments have revealed a stretched exponential decay of the nanocrystal emission with a decay time in the range of 10-100  $\mu\text{s}$  [83]. The stretched exponential decay is caused by energy migration from small Si nanocrystals to large Si nanocrystals with the degree to which the exponential is stretched decreasing with increasing excitation wavelength (selectively exciting progressively larger nanocrystals) [51]. Emission experiments performed on single Si nanocrystals have revealed a homogeneous linewidth of 100-150 meV at room temperature; the typical spectral width, which can be as large as 500 meV, is therefore dominated by inhomogeneous broadening due to the broad size and shape distributions that exist in typical Si nanocrystal ensembles [84]. Despite the strong luminescence from Si nanocrystals it has been shown through spectral hole burning experiments that the indirect bandgap properties of bulk Si are still retained in Si nanocrystals [85]. The effect of quantum confinement of excitons within the Si nanocrystal is to increase the energy gap leading to a decrease in the

emission wavelength and enhance the probability of no-phonon radiative recombination. In general, the trend of emission energy versus nanocrystal size follows a model consistent with quantum confinement for large nanocrystals. For small nanocrystals it has been observed that the emission energy does not increase beyond 2 eV although the nanocrystal size is decreased. Wolkin *et al.* attributed this pinning of the bandgap to exciton recombination via Si=O bonds located at the nanocrystal/oxide interface [86]. The sensitivity of the optical properties to the nanocrystal surface chemistry was further examined by Pudzer *et al.* revealing the complex interplay between size and surface effects [87].

## **The Energy-Transfer Process to Er Ions**

Several studies have been devoted to understanding and optimizing the energy-transfer process from Si nanocrystals to Er ions. There are several common features that have been observed for all samples independent of preparation conditions. When Er is doped into a film containing Si nanocrystals the nanocrystal emission spectrum is uniformly reduced but not completely quenched and the Er emission is enhanced relative to Er in stoichiometric SiO<sub>2</sub> [37,40]. The degree to which the Si nanocrystal emission is quenched increases as the concentration of Er increases [40,88]. The energy-transfer process to Er ions is a non-radiative decay path which competes with the radiative recombination in the nanocrystal. In this regard it is expected that the presence of Er would reduce the nanocrystal lifetime. This is not observed experimentally since the lifetime is slightly reduced [89] or unchanged [90] with the addition of Er ions.

These experimental observations are explained using a strongly-coupled energy-transfer model first proposed by Kik *et al.* [39]. In this model energy-transfer occurs through a subset of the nanocrystals that are located spatially close to Er ions. These nanocrystals become completely dark. The observed nanocrystal emission is only due to those nanocrystals not coupled to Er ions and is therefore not influenced by the presence of Er. For the coupled nanocrystals to become completely dark the energy-transfer time was expected to be very short compared to the nanocrystal recombination lifetime. Recent measurements have confirmed this fact with the energy-transfer time expected to be on the order of 100 ns, 1000x faster than the typical recombination lifetime for



Si nanocrystals [91]. Spectral hole burning experiments have shown that the energy-transfer process is a combination of resonant and non-resonant processes [92]. In the resonant process only nanocrystals with an energy that matches an atomic level of Er transfer their energy. In the non-resonant processes the energy difference between the nanocrystal and Er energy levels is satisfied through the emission of various combinations of optical and acoustical phonons. The overall energy-transfer process is predominantly non-resonant; only 1% of the energy-transfer is estimated to be resonant based on photoluminescence measurements performed at 5K.

The most technologically significant result for the fabrication of devices with improved CMOS compatibility is the demonstration of an enhanced energy-transfer process for samples annealed at low temperatures [55,56]. The enhanced energy-transfer has been associated with the formation of a large density of small amorphous clusters where the enhancement is due to an increase in the number of nanocrystals interacting with the Er ions. The use of sputtering techniques to simultaneously introduce Er into the SRO films allow for the determination of the minimum annealing temperature at which strong energy-transfer is still achieved since ion implantation processes introduce defects in the SRO matrix which can only be removed using annealing temperatures  $>800^{\circ}\text{C}$  [93]. We have demonstrated that strong Er excitation can be achieved for annealing temperatures as low as  $600^{\circ}\text{C}$  in agreement with other authors. We have also demonstrated a 2x enhancement of the excitation cross section for Er relative to samples annealed at high temperatures and a 50x enhanced coupling coefficient for the SRO – Er energy-transfer based rate equation modeling [94]. These observations suggest that the strong Er excitation for low annealing temperatures is a combination of an increase in the density of energy-transfer centers and a stronger energy-transfer process. Temperature-resolved photoluminescence experiments we performed on undoped SRO films annealed at low and high temperatures have revealed the possibility of two different emission sensitizers with two different transfer rates for the Er emission: (1) Si nanocrystals at high annealing temperatures and (2) localized centers in the SRO matrix for samples annealed at low temperatures. The possibility of two energy-transfer processes was previously proposed by Fujii *et al.* based on time-resolved photoluminescence of Er-doped Si nanocrystal samples [95]. In that work they identified fast and slow components in the photoluminescence rise time where the fast component was associated with excitation of the first excited-state through a mechanism similar to Er excitation in bulk Si and the slow component was

related to transfer to higher excited-states of the Er ion from Si nanocrystals. The Er excitation mechanism in bulk Si has been attributed to recombination at a deep level introduced by the Er into the Si band gap [96,97]. A possible analog for SRO could be a localized center in the SiO<sub>2</sub> bandgap or surface states located on small Si clusters embedded in the matrix since the surface properties are expected to dominate clusters with a radius less than 2 nm [86,87].

## Optical Gain in Er-doped Si-rich SiO<sub>2</sub>

Demonstration of optical gain in Er-doped SRO requires the reduction of free carrier losses within the matrix [57,58]. Kik *et al.* proposed that charge carriers which are physically separated in the matrix and have a significantly enhanced lifetime with respect to quantum confined carriers are responsible for the observed induced losses in pump and probe transmission experiments [98]. This observation has been independently confirmed by Daldosso *et al.* who showed that, in the presence of free carriers, optical gain was only possible through direct photoexcitation of Er ions at high pumping fluxes [58]. The possible mechanisms suggested for the spatial separation of carriers were trapping in nanocrystal surface states or tunneling into adjacent nanocrystals [98]. It is expected that this carrier separation process would increase with increasing density of nanocrystals placing a cap on the maximum Si content at which sensitized gain could be observed. As a result sensitized optical gain has only been demonstrated for samples where a low Si content (~34 at%) and short annealing time (5 minutes) limited the nanocrystal density [59,60]. We have demonstrated, through variable stripe length techniques and rate equation modeling, sensitized optical gain for slab waveguide samples with ~36.5 at% Si annealed at 600°C. Since the studies of Kik *et al.* and Pavesi *et al.* were performed on samples with ~40at% Si we can consider 40at% Si as an approximate value for the threshold for free carrier induced losses.

An intensely debated topic in the field of sensitized gain is the presence or absence of an enhanced emission cross section at 1.54 μm for Er ions in SRO. Early measurements performed by Shin *et al.* [59,60] and Kik *et al.* [57] yielded enhancements of the emission cross section of 30x ( $2.0 \times 10^{-19}$  cm<sup>2</sup>) and 10x ( $8.0 \times 10^{-20}$  cm<sup>2</sup>), respectively. Other measurements of the absorption cross section at 1.54 μm showed no enhancement [58, 99] and the argument was made that the emission cross

section is also not enhanced due to the equivalence of the absorption and emission cross section between two non-degenerate states [100]. We have observed a difference between the absorption and emission cross section measured on the same Er-doped SRO sample annealed at 600°C with the emission cross section enhanced by ~ 5x compared to Er-doped SiO<sub>2</sub> while the absorption cross section for the same sample was unchanged compared to a reference Er,Ge-doped SiO<sub>2</sub>.

Achieving net optical gain requires reducing background transmission losses below the total gain. Studies of transmission losses waveguides have shown that scattering due to the presence of Si nanocrystals is the dominant loss mechanism with loss values of ~ 2 dB/cm reported near 1.54 μm [61]. We have demonstrated that the background transmission loss of the matrix is reduced for annealing temperatures of 600°C compared to samples annealed at high temperatures. It is expected that the loss reduction is due to the small size of Si nanoclusters that are present in the matrix at these annealing temperatures relative to the wavelength which yields a lower scattering cross section [101].

### **1.3. Organization of this Thesis**

In this thesis we present a systematic study of the optical properties of SRO with application towards the fabrication of polarization sensitive and light emitting devices. The organization of this thesis follows the same logical flow we have adopted for this study.

Chapter 2 discusses the deposition of SRO through a reactive sputtering process. The control of film stoichiometry and deposition rate with deposition conditions is described through a model which takes into consideration the physical and chemical aspects of the reactive sputtering process. Er incorporation through co-sputtering is also discussed.

Chapter 3 discusses phase transformations that occur in SRO upon annealing. An analysis of the nucleation of Si nanocrystals reveals that the process is exclusively heterogeneous. We also offer evidence that the heterogeneous nucleation sites are incorporated during the film deposition.

Chapter 4 discusses the optical anisotropy and dispersion in SRO films. We demonstrate that the anisotropy and dispersion are directly correlated with the amount of Si which is incorporated into the film at deposition.

Chapter 5 discusses the photoluminescence characterization of undoped SRO, Er-doped SiO<sub>2</sub> and Er-doped SRO. Measurements of the excitation cross section, emission lifetime and non-radiative decay paths are reported for all systems. The origin of the enhanced energy-transfer from SRO to Er for samples annealed at 600°C is discussed with reference to temperature-resolved photoluminescence characterization of the samples.

Chapter 6 discusses the performance of slab waveguide devices fabricated from Er-doped SRO films. Demonstrations of optical gain and transmission loss reduction for samples annealed at 600°C through the use of variable stripe length and prism coupling techniques, respectively, are presented. A rate equation model using several of the values reported in Chapter 5 is applied to describe the optical gain results.

Chapter 7 discusses the design, fabrication and performance of Er-doped SRO ridge waveguides where light is confined in two dimensions. The demonstration of sensitized signal enhancement for ridge waveguides fabricated on silica substrates is presented.

# Chapter 2 | Deposition of Si-rich SiO<sub>2</sub> and Er-doped Si-rich SiO<sub>2</sub> through Reactive Sputtering

## 2.1. Description of the Sputtering Process

Sputtering is a physical vapor deposition process where the source atoms are removed from a solid target through the impact of an ionized inert gas (plasma) which is accelerated towards the target surface. The ejected source atom diffuses through the plasma and arrives at the substrate where it attaches to the substrate and is incorporated into the growing film. There are several variations on this process depending on the film being deposited, the source material and the configuration of the target holder. The simplest variation of the process is DC sputtering where the target is held at a fixed negative voltage with respect to the substrate and deposition chamber which are grounded. In this case the plasma is generated through impact ionization of high energy electrons with the inert gas, typically Ar. The ionization reaction is



Secondary electrons are generated through the ionization process and the plasma is considered self-sustaining when there are enough secondary electrons generated to replace the primary electrons. The positively charged Ar ions are accelerated towards the negatively charged target and eject target atoms through a series of collisions. DC sputtering is only appropriate for deposition of conductive materials. For insulators the accumulation of the positively charged Ar ions would reduce the negative charge of the target, lower the potential in the chamber, reduce the kinetic energy of the electrons, reduce the number of ionization events and eventually extinguish the plasma. To deposit insulating materials pulsed DC and RF techniques were developed. During RF sputtering the applied voltage is cycled positive and negative at a

frequency of 13.56 MHz to prevent the buildup of positive charges at the target. Since electrons are more mobile than ions they can follow the changing voltage and impact the surfaces within the chamber leading to a plasma potential which is positive with respect to both the substrate and the target. Although sputtering occurs at both the target and the substrate the system can be configured such that significantly more sputtering occurs at the target. This is achieved by making the target area small with respect to the substrate area which is electrically connected to the entire chamber. In order to draw the same current on both cycles the potential adjacent to the target must be larger than the potential adjacent to the substrate to compensate for the difference in area. It has been demonstrated that the ratio of the potential adjacent to target and substrate is approximately equal to the inverse of the area ratio to the fourth power. Several contemporary sputtering systems use magnetron sources where a permanent magnet is placed behind the target and the Lorentz forces confine the electrons to a small region near the surface of the target. By enhancing the concentration of electrons near the target surface and confining the ionization process near the target surface the efficiency of the sputtering process is enhanced. This allows for fast deposition rates for a wide variety of materials at the expense of target material underutilization.

There are two approaches to achieve compound deposition. The first is to sputter from a compound target. Unlike evaporation, sputtering can yield thin films with the same composition as the source material. There are two reasons for this: 1) there is no bulk diffusion in the water cooled target and 2) if there is a difference in the sputtering yields of the atoms in the compound target the yields will adjust in order to maintain the equilibrium concentration of the target at the surface. The second approach towards compound deposition is reactive sputtering where one or more components of the film are introduced into the chamber in the gas phase. The chemical reaction to form the film occurs at the substrate surface. For diatomic molecules such as  $O_2$  and  $N_2$  the molecules must dissociate before being incorporated into the growing film. Although reactive sputtering can be more difficult to control it has the advantage of yielding the deposition of non-equilibrium, metastable thin films. We have used this approach to deposit silicon-rich  $SiO_2$  (SRO) films of varying Si content from stoichiometric  $SiO_2$  (33 at% Si) to  $SiO$  (50 at% Si) which we have identified as the Si composition range of interest for forming optical devices in SRO.

## 2.2. Modeling the Reactive Sputter Deposition Process

### 2.2.1. Description of the Apparatus

The deposition was carried out in a Kurt J. Lesker Co. CMS 18 system. A photograph of the system is shown in Figure 2.1 (a) with a schematic in Figure 2.1 (b).

The system was equipped with three cathodes in which we used undoped Si, Ge and Er targets. The Si and Er targets were connected to RF power supplies while the Ge was connected to a pulsed DC power supply. We also performed depositions with a SiO<sub>2</sub> target connected to a RF power supply to compare the Si and SiO<sub>2</sub> deposition rates under identical conditions. A cryo pump was used to achieve chamber base pressures of  $1 \times 10^{-7} - 1 \times 10^{-8}$  Torr. A capacitance manometer was used to fix the chamber pressure at 3 mTorr during deposition. Ar was introduced near the target surfaces while oxygen was introduced through a gas distribution ring located between the targets and the substrate. The flow rates of O<sub>2</sub> and Ar were adjusted at the input to maintain the deposition pressure while achieving O<sub>2</sub> percentages of 8 – 20% in the gas

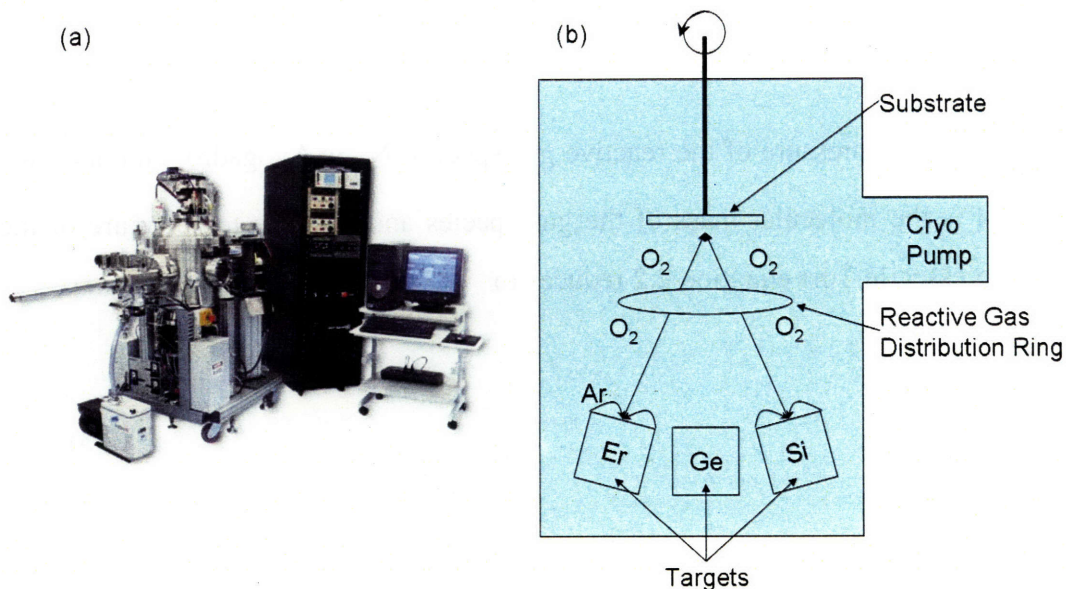


Figure 2.1 (a) Photograph of the Kurt J. Lesker Co. CMS 18 sputtering system. (b) Schematic diagram of the same system.

mixture. The substrate was attached to a shaft which allowed it to be rotated at ~ 15 – 20 rpm. The substrate was not heated during the deposition.

## 2.2.2. General Model of the Reactive Sputtering Process

We want to extend a phenomenological model that incorporates the physical and chemical aspects of the reactive sputter process in order to obtain estimates of important coefficients that determine how the deposition parameters affect the film properties. The model we will apply is a variation of models first developed by Berg *et al.* [102] and Sandland [103] to simulate the sputter deposition process under reactive sputtering conditions. For oxygen the growth kinetics are dependent on the flux of oxygen to the substrate surface relative to the flux of Si incorporated into the film. The gas impingement flux, the number of gas molecules (or atoms) that strike a surface per unit area per unit time. For O atoms the impingement flux is given by

$$F_{O_{2},total} = \frac{2P_{O_2} N_A}{\sqrt{2\pi RMT}} \quad (2.2)$$

where  $P_{O_2}$  is the partial pressure of the reactive gas species,  $N_A$  is Avogadro's number,  $R$  is the gas constant,  $M$  is the molecular mass of the gas species and  $T$  is the temperature of the gas. When  $P_{O_2}$  is expressed in Torr equation 2.2 reduces to

$$F_{O_{2},tot} = \frac{2(3.513 \times 10^{22})P_{O_2}}{\sqrt{MT}} \quad (2.3)$$

For Si, the flux of Si atoms incorporated into the film is always controlled by the arrival rate of Si atoms. We assume that the arrival rate at the substrate, in units of atoms per time, is equal to



the sputtering rate which is controlled by the power applied to the Si cathode according to the expression

$$\phi_{Si} = \xi_{Si} P_{cathode, Si} A_T \quad (2.4)$$

where  $P_{cathode, Si}$  is the power applied to the Si cathode in Watts, the coefficient  $\xi_{Si}$  is the rate at which Si atoms are removed from the target per Watt applied to the Si cathode and  $A_T$  is the area of the target. Since we will be comparing the model to the properties of the deposited film we note that the coefficient  $\xi_{Si}$  is a combination of the number of Si atoms sputtered per Watt applied to the Si cathode, the sticking coefficient of Si on the substrate and geometrical factors including the target – substrate distance.

Since O will not stick to a surface covered with  $SiO_2$  the incorporation of O will be influenced by the arrival rate of elemental Si. When the arrival of O is significantly higher than the arrival rate of elemental Si only  $SiO_2$  will be formed. Since two O atoms must attach to form  $SiO_2$  the attachment rate of O is limited to twice the arrival of Si

$$\phi_O = 2\phi_{Si} \quad (2.5)$$

In the opposite extreme, when the impingement rate of O is less than twice the arrival rate of Si the attachment rate of O is given by the expression

$$\phi_O = \alpha_S F_{O, total} A_S \quad (2.6)$$

where  $\alpha_S$  is the sticking coefficient of O to Si and  $A_S$  is the substrate area. From these simple arguments we notice that there is a cross-over arrival rate equal to  $2\phi_{Si}$  where the attachment kinetics of the O switches from a regime limited by gas-phase mass transport (high Si arrival rates) to a regime limited by the surface reaction to for  $SiO_2$  (low Si arrival rates). We will evaluate the model on the basis of its ability to accurately determine this cross-over arrival rate and from a comparison of the film Si content and deposition rate predicted by the model with the

values measured experimentally for various processing conditions. By comparing the predictions of the model against the Si content and deposition rate simultaneously we can test the ability of the model to predict the ratio and total number of atoms incorporated into the film.

## **2.3. Application of the Sputtering Model to SRO**

### **Deposition**

#### **2.3.1. Measuring the Si Content versus Deposition**

##### **Parameters**

Before applying the model described above to relate the Si content of the films to the deposition parameters we will first describe the methods used to measure the Si content. We have applied two methods: 1) Rutherford Backscattering and 2) Wavelength Dispersion Spectroscopy.

### **Rutherford Backscattering Spectroscopy**

In Rutherford Backscattering Spectroscopy (RBS) the sample is bombarded with high energy  $\text{He}^+$  ions. When the  $\text{He}^+$  ions strike the sample they undergo direct collisions with the atomic nuclei of the sample, are scattered backwards and are collected by a detector at a fixed angle away from the incoming beam. A very simple theory exists to correlate the energy of the backscattered  $\text{He}^+$  ions to the atomic mass of the sample atoms. As a result the sample composition can be determined through the relative counts of backscattered  $\text{He}^+$  ions versus their energy. RBS can also yield composition versus depth information because several of the incoming  $\text{He}^+$  ions will penetrate into the sample, continuously losing energy through electronic excitation of sample atoms or ionization of sample atoms before undergoing a nuclear collision. As a result these  $\text{He}^+$  ions experience a linear loss of energy in their path in and out of the sample. For thick samples, there will be a range of energies associated with each atom in the sample with

the low energy yield generated near the film/substrate interface and the high energy yield associated with the film surface. Figure 2.2. shows a typical RBS spectrum of a sputtered SRO film on a Si substrate with the backscattered yield for the components of the film Si, O and Ar as well as the Si substrate identified.

During our experiments an As-implanted Si wafer with a thin surface layer of Au was used as a reference sample. The Au peak and Si edge were used to calibrate the absolute energy and energy per channel. The As implant, a standard for aerial density, was used to calibrate the detector solid angle. The composition of the film was determined through a simulation of the RBS spectrum using the RUMP software package [104,105]. After the calibration the simulation composition parameters and layer thickness were adjusted to obtain the best agreement between the simulation and experimental spectrum over the Si, O and Ar ranges. Table 2.1. lists the film

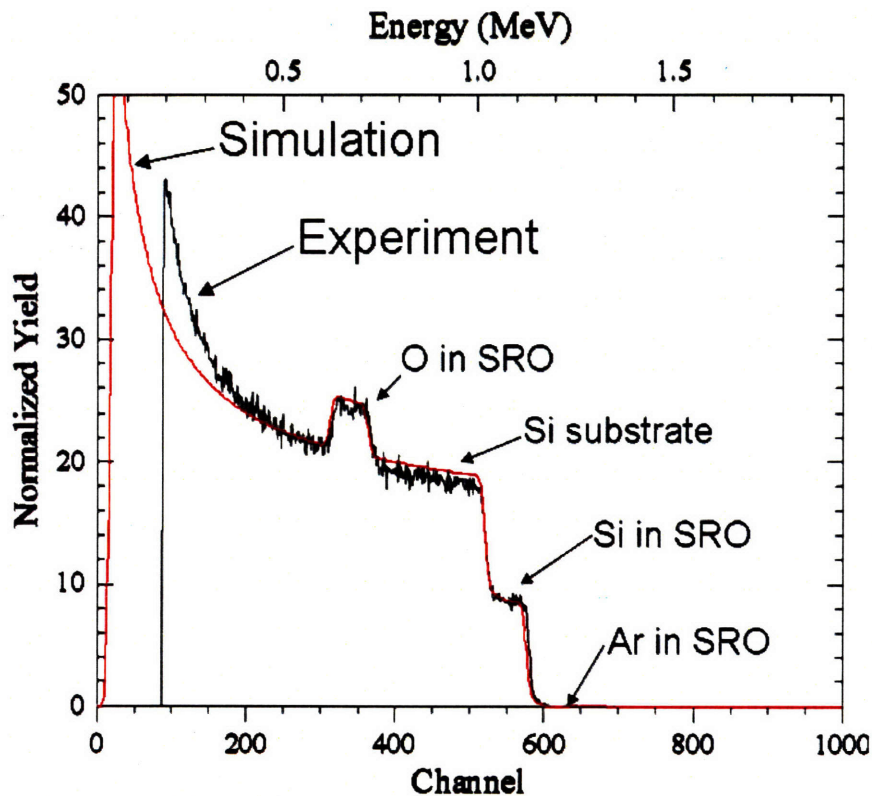


Figure 2.2 RBS Spectrum of a sputtered SRO sample. The black line is the experimental spectrum collected using 2MeV He<sup>+</sup> ions and a total integrated charge of 5 $\mu$ C. The red line is a simulation using RUMP [104,105] software with the Si stopping powers from [106] and yielding a Si content of 37.8 at%, an O content of 62.0 at% and an Ar content of 0.2 at%.

Table 2.1. Film composition and deposition parameters for samples analyzed through RBS.

Sample ID	Si Content (at%)	O Content (at%)	Ar Content (at%)	Si Cathode Power (W)	% O <sub>2</sub> in Ar
SRO18	35.58	64.28	0.14	415	12.5
SRO26	35.43	64.42	0.15	444	12.5
SRO28	39.53	60.26	0.21	450	12.5
SRO31	44.27	55.52	0.21	330	10

composition determined through RBS and deposition parameters for the samples analyzed.

As expected increasing the power to the Si cathode for a fixed percentage of O<sub>2</sub> in the gas mixture leads to an increase in the Si content of the film. Also, decreasing the percentage of O<sub>2</sub> in the gas mixture leads to an increase in the Si content of the thin film even for lower Si powers applied to the Si cathode. It is also important to note that a measurable amount of Ar was detected in all samples which roughly increases as the Si content increases.

Finally we note that recent round-robin experimental studies have estimated the accuracy of RBS techniques to be within 2 – 6 % for H [107].

## Wavelength Dispersion Spectroscopy

We have also performed chemical analysis through the use of wavelength dispersion spectroscopy using a JEOL JXA-733 superprobe. The technique uses electrons focused onto a 1 μm x 1 μm area of the sample to excite x-ray emission from the atomic species within the film. This x-ray emission impinges on a crystal which selectively diffracts the wavelength of the particular atomic emission onto a detector allowing each emission to be detected independently through the proper selection of the diffracting crystal and distance between the sample and the crystal. The intensity is integrated over a fixed time and compared to the emission of a standard material to determine the atomic fraction in the film. For our analysis we used a quartz reference for Si and O and an ErPO<sub>4</sub> reference for Er. We have demonstrated agreement between RBS and

WDS for samples with a thickness greater than 1  $\mu\text{m}$ , roughly the penetration depth of the electrons in the WDS experiment. For samples thinner than 1  $\mu\text{m}$  there is a significant contribution to the WDS signal from the substrate which influences the measured values for the film composition. Although the penetration depth for the  $\text{He}^+$  beam in the RBS experiment is similar, the simulation of the RBS spectra allows the user to clearly separate the contributions from the film and substrate and acquire accurate measurements of the film composition.

## 2.3.2. Comparison of the Deposition Model with SRO Film Properties

### SRO Deposition for Low % $\text{O}_2$ in Ar

During our process the percentage of  $\text{O}_2$  in the gas mixture is controlled at the input by varying the flow of  $\text{O}_2$  relative to Ar in order to maintain a constant pressure of the gas species. To accurately determine the partial pressure of O during the deposition for the constant pressure process we must include the differential pumping speed of the reactive gas ( $\text{O}_2$ ) relative to the inert gas (Ar). We incorporated this effect in the model by introducing a factor  $P_{\text{O}_2,\text{loss}}$  which represents the decrease in the partial pressure of the reactive gas in the chamber relative to the partial pressure of the reactive gas at the input due to the differential pumping speeds. The impingement flux,  $F_{\text{O,tot}}$  in 2.6 is then replaced by  $F_{\text{O,eff}}$  where

$$F_{\text{O,eff}} = \frac{2(3.513 \times 10^{22})(P_{\text{O}_2,\text{input}} - P_{\text{O}_2,\text{loss}})}{\sqrt{MT}} \quad (2.7)$$

Figure 2.3 shows a comparison of the film Si content and deposition rate predicted by the model and measured experimentally for two different % $\text{O}_2$  in Ar. We calculated the Si content and deposition rate from equations 2.4 and 2.6 using

$$X_{Si} = \frac{\phi_{Si}}{\phi_{Si} + \phi_{O}} \quad (2.8)$$

for the Si content and

$$R_{dep} = \frac{1}{\rho_{film} A_S} (\phi_{Si} + \phi_{O}) \quad (2.9)$$

where  $\rho_{film}$  is the density of the film which we assume to be equal to the density of  $SiO_2$   $6.6 \times 10^{22}$  atoms/cm<sup>3</sup>.

By considering  $P_{O_2,loss} = 5.6 \times 10^{-5}$  Torr, a sticking coefficient of  $1.19 \times 10^{-2}$  and a sputtering rate of  $\xi_{Si} = 6.15 \times 10^{12}$  atoms/cm<sup>2</sup>sW we achieved the best agreement between the calculated and experimental Si content and deposition rate for both percentages of O<sub>2</sub> in Ar.

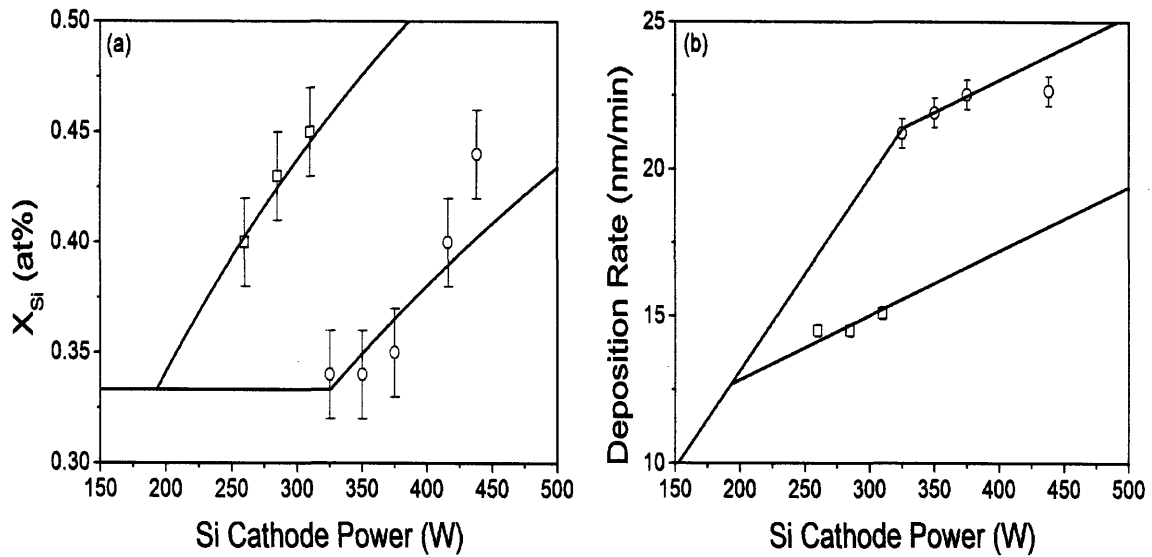


Figure 2.3 (a) Si content and (b) deposition rate versus Si cathode power for samples prepared in 10% O<sub>2</sub> in Ar (open squares) and 12.5% O<sub>2</sub> in Ar (open circles). The solid lines are calculations using equations 2.4 and 2.6 with  $A_S = 81.07$  cm<sup>2</sup>,  $A_T = 31.77$  cm<sup>2</sup>,  $\xi_{Si} = 6.15 \times 10^{12}$  atoms/cm<sup>2</sup>sW,  $\alpha_S = 1.19 \times 10^{-2}$  and  $\phi_{O,loss} = 1.32 \times 10^{17}$  atoms/s.

We compared the value for  $P_{O_2,loss}$  with a value calculated from the differential pumping speed for our pump. The pumping speed of Ar for our cryo pump quoted by the manufacturer was 1200 L/s [108]. The manufacturer also suggested that we calculate the pumping speed of O<sub>2</sub> from the pumping speed of Ar using the equation [109]

$$S_{O_2} = S_{Ar} \sqrt{\frac{M_{Ar}}{M_{O_2}}} \quad (2.10)$$

where S is the pumping speed of the gas. This yields a pumping speed for O<sub>2</sub> of 1342 L/s. We calculated the factor  $P_{O_2,loss}$  from the fraction of O<sub>2</sub> at the input using the expression

$$P_{O_2,loss} = \theta_{O_2} P_{tot, chamber} - P_{tot, chamber} \left[ \frac{S_{Ar} \theta_{O_2}}{S_{Ar} \theta_{O_2} - S_{O_2} \theta_{O_2} + S_{O_2}} \right] \quad (2.11)$$

where  $\theta_{O_2}$  is the fraction of O<sub>2</sub> at the input and  $P_{tot, chamber}$  is the total pressure in the chamber ( $3 \times 10^{-3}$  Torr). For  $\theta_{O_2} = 0.1$  and  $0.125$  we calculated values of  $3.81 \times 10^{-5}$  Torr and  $4.65 \times 10^{-5}$  mTorr, respectively, which are in good agreement with the loss pressure considered in our model.

## Target Oxidation in the High %O<sub>2</sub> Regime

The best agreement between the model we presented in the previous section and the experimental results for 10 and 12.5% O<sub>2</sub> in Ar considered the sputtering rate to be equal to the elemental sputtering rate. When the % O<sub>2</sub> in the gas mixture is increased such that the flux of O to the substrate is significantly greater than  $\phi_{Si}$  the incorporation of O into the film is limited by the arrival of Si and a significant amount of O remains in the gas phase. This increases the probability that the residual O in the gas phase will attach to the target surface leading to compound formation at the target surface. In addition to the surface attachment mechanism [110] of compound formation it has been shown that ion implantation also plays a role [111,112]. Ion beam analysis of the target surface has demonstrated that the compound formation is

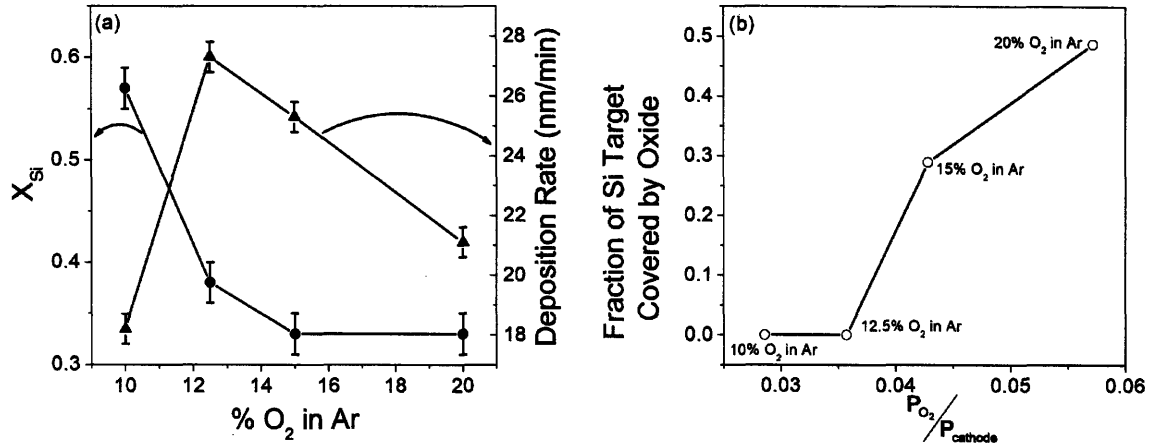


Figure 2.4 (a) Experimental results of atomic fraction of Si (solid circles) and deposition rate (solid triangles) for SRO samples deposited with 350W applied to the Si cathode at several % O<sub>2</sub> in Ar. (b) Results of a calculation of the fraction of the Si target covered with oxide from the data in panel (a) according to equation 2.12.

predominantly occurring at the center and edge of the target and not in the race-track created during target erosion [113].

Figure 2.4 shows a plot of the atomic fraction of Si and deposition rate for various %O<sub>2</sub> at a fixed target power. The onset of compound formation occurs between 12.5 and 15 % O<sub>2</sub> in Ar as indicated by the drop in deposition rates. Just prior to this series of depositions, we performed depositions from Si and SiO<sub>2</sub> targets in Ar to determine the relative deposition rates at an RF power of 300W. The results of this comparative study are shown in Table 2.2.

We can determine the fraction of the Si target,  $\theta_C$ , covered by SiO<sub>2</sub> from the measured flux of Si into the film in Figure 2.4 (a) and the values for  $\xi_{Si}$  and  $\xi_{SiO_2}$  in Table 2.2 using the equation

$$\phi_{Si} = P_{cathode, Si} [(1 - \theta_C) \xi_{Si} + \theta_C \xi_{SiO_2}] \quad (2.12)$$

where  $\theta_C$  is the fraction of the target covered by SiO<sub>2</sub> and  $\xi_{SiO_2}$  is the rate at which SiO<sub>2</sub> molecules are removed from the target per Watt applied to the Si cathode. The results of this calculation, shown in Figure 2.4 (b), indicate that as much as 50% of the Si target can be covered with SiO<sub>2</sub> for a process using 20% O<sub>2</sub> in Ar and 350 W applied to the Si cathode.



Table 2.2 Experimental results for the deposition rate from Si and SiO<sub>2</sub> targets with 300 W applied to the cathode in pure Ar at a pressure of 3 mTorr.

Target Material	Film Deposition Rate (nm/min.)	Si Density in the Film (atoms/cm <sup>3</sup> )	$\xi_{Si}$ atoms/Wcm <sup>2</sup> s
Si	10.58	5x10 <sup>22</sup>	3.26x10 <sup>12</sup>
SiO <sub>2</sub>	9.21	2.178x10 <sup>22</sup>	1.06x10 <sup>12</sup>

## 2.4. Incorporating Erbium

To add Er to our films we used a co-sputtering process from an Er target in the same O<sub>2</sub>/Ar atmosphere. In this process the Er content of the film could be controlled independently through the Er target power. Figure 2.5 shows the variation of Er content with Er target power for processes at 10% O<sub>2</sub> in Ar and 20% O<sub>2</sub> in Ar.

The typical Er concentration used for light emitting devices is 10<sup>20</sup> Er atoms/cm<sup>3</sup> which is slightly below the threshold for concentration quenching of the Er photoluminescence which we will discuss in Chapter 5. With our process we can achieve Er concentrations near this concentration of interest with 16 W applied to the Er target.

We can incorporate Er into the model by defining the flux of Er incorporated into the film as

$$\phi_{Er} = \xi_{Er} P_{cathode,Er} A_T \quad (2.13)$$

where  $P_{cathode,Er}$  is the power applied to the Er cathode in Watts and the coefficient  $\xi_{Er}$  is the flux of Er atoms into the film per Watt applied to the Er cathode which is a combination of the sticking coefficient of Er and the number of Er atoms sputtered per Watt applied to the Er cathode.

While preparing Er doped SRO samples with varying Si content we noticed that the Er concentration, for a constant power applied to the Er target, increased with an increase in the

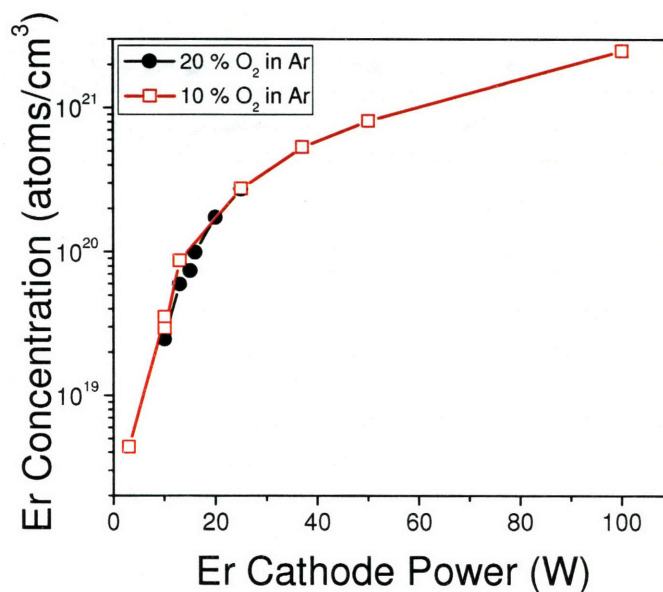


Figure 2.5 Er concentration measured through RBS versus Er cathode power for 20% O<sub>2</sub> in Ar (open squares) and 10% O<sub>2</sub> in Ar (solid circles) with a fixed Si cathode power of 300 W.

Si/O ratio in the film. This effect is shown in Figure 2.6 for samples prepared by varying the power applied to the Si target and changing the percentage of O<sub>2</sub> in Ar. As we see from Figure 2.6 varying the Si/O ratio by 10% leads to a nearly 100% increase (doubling) of the Er concentration in the film. There are two possible causes of this effect:

1. Compound formation on the Er target which lowers the sputtering yield
2. Reduced sticking coefficient of Er on “oxygen rich” surfaces

Given the low power applied to the Er cathode (16W) we expect that it would be more susceptible to compound formation compared to the Si target which is operated at a much higher power (~300 W). We interpret the increase in Er concentration in the film as a decrease in the fraction of compound on the target surface with increasing Si/O ration in the film since under the O mass transport limited regime a greater amount of O from the gas phase will be incorporated into the film as the Si/O ratio increases. Berg *et al.* [102] have also discussed this effect with respect to their model noting that when two targets are placed in the same chamber and exposed to the same supply of reactive gas they are no longer independent because the conditions of one target will influence the amount of reactive gas seen by the other target.

We have shown that the variation of Er concentration with changing Si concentration in the film can be reduced by adjusting the power applied to the Er cathode. Through this approach the

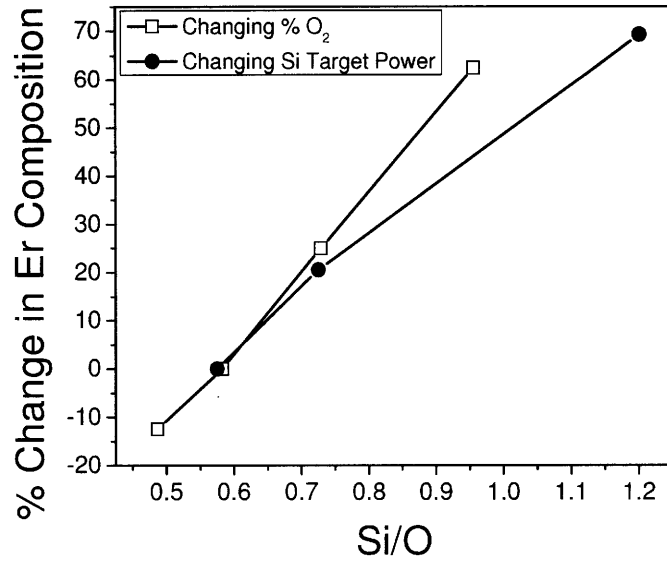


Figure 2.6 Percentage change in Er concentration relative to the Er concentration at a Si/O ratio of 0.6 for samples prepared by varying the Si cathode power at a constant Er cathode power (solid circles) and changing the percentage of O<sub>2</sub> in Ar at a constant Si cathode power and Er cathode power (open squares).

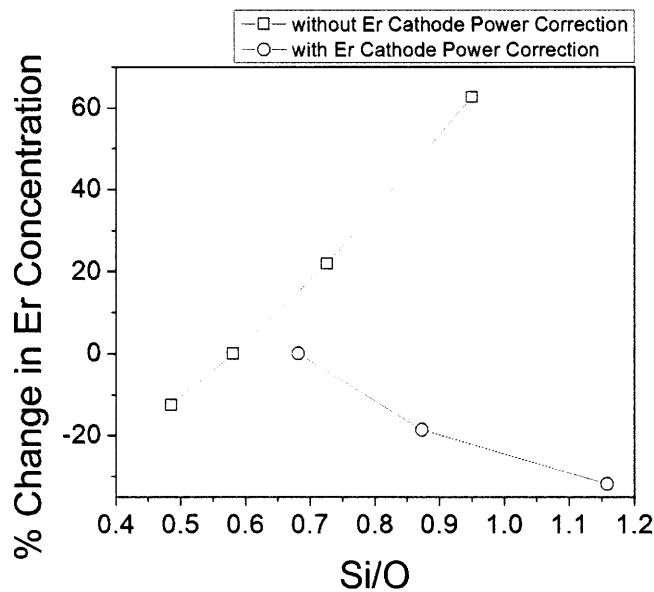


Figure 2.7 Percentage increase in Er concentration relative to the Er concentration at a Si/O ratio of 0.6 for samples prepared by changing the percentage of O<sub>2</sub> in Ar at a constant Si cathode power and Er cathode power (open squares). We also show the percentage increase in Er concentration for samples prepared by changing the percentage of O<sub>2</sub> in Ar at a constant Si cathode power with a variable Er cathode power (open circles).

variation in Er concentration was reduced to 30% (Figure 2.7, open circles) which is roughly half of the variation measured for samples without the Er cathode power correction (Figure 2.6 and 2.7, open squares). However our experiments demonstrate the difficulty of using this approach to carefully control the Er concentration due to the high sensitivity of Er deposition rate on Er cathode power.

# Chapter 3 | Si-rich SiO<sub>2</sub> Phase Transformations

Figure 3.1 is the Si – O phase diagram. There are several polymorphic phase transformations of silica as the temperature is increased but no intermediate phases between pure Si and SiO<sub>2</sub>.

For SRO the most intensely investigated phase transformation is the precipitation reaction where the metastable Si-rich dielectric film decomposes into two stable phases: Si clusters and a matrix which is closer in composition to the equilibrium (stoichiometric) composition. Measurements performed on annealed SRO and Er:SRO films have identified two important temperature ranges: 1) high annealing temperature greater than 1000°C where Si nanocrystal formation occurs and 2) intermediate annealing temperatures ~600 – 700°C which are lower than the threshold temperatures for forming observable Si clusters but where significant changes in the energy-transfer process to Er occurs.

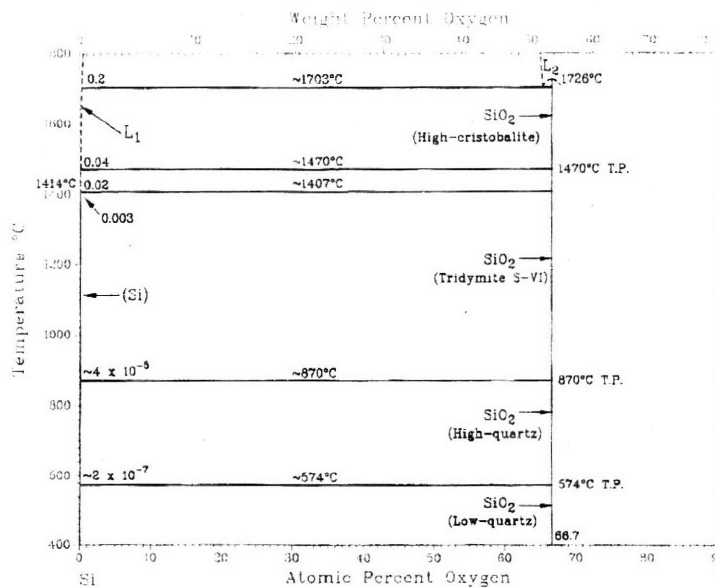


Figure 3.1 Si-O phase diagram at low pressure. (from Binary Alloy Phase Diagrams [114])

## 3. 1. Formation of Si Nanocrystals

### 3.1.1. Homogeneous vs. Heterogeneous Nucleation

In this section we will review the fundamentals of nucleation theory with specific emphasis on the nucleation of Si nanoclusters from SRO in reference to the discussions of several authors [115,116,117]. According to classical nucleation theory the driving force for the precipitation transformation is a volume free energy reduction  $\Delta G_v(X_{Si}, T_A)$  which increases as the Si content is increased above the stoichiometric level (given by the mole fraction of Si,  $X_{Si}$ ) and the annealing temperature,  $T_A$ , is increased. Opposing the volume free energy reduction is the energy required to create the interface between the Si cluster and the matrix,  $A\gamma_{CM}$ , where  $A$  is the surface area and  $\gamma_{CM}$  is the cluster-matrix interfacial energy. Combining these two contributions the total free energy change for the precipitation reaction, for spherical clusters, is

$$\Delta G_{\text{hom}} = -\frac{4\pi r^3}{3} \Delta G_v + 4\pi r^2 \gamma_{CM} \quad (3.1)$$

The total free energy passes through a maximum as a function of cluster radius where the maximum is associated with the free energy to form a critical nucleus which is given by the expression

$$\Delta G^* = \frac{16\pi\gamma_{CM}^3}{3\Delta G_v^2} \quad (3.2)$$

for with a critical cluster radius of

$$r^* = \frac{2\gamma_{CM}}{\Delta G_v} \quad (3.3)$$

Assuming a dilute or ideal solution the chemical driving force for precipitation is given by

$$\Delta G_v = \frac{RT}{V_M} \ln \left( \frac{X_{Si}^{SRO}}{X_{Si}^{eq}} \right) \quad (3.4)$$

where R is the gas constant,  $V_M$  is the molar volume of the precipitate phase,  $X_{Si}^{SRO}$  is the mole fraction of Si in SRO and  $X_{Si}^{eq}$  is the mole fraction of Si in the equilibrium phase which in this case is SiO<sub>2</sub>. At any moment there are several embryos with a size smaller than the critically sized nucleus that exist within the matrix. These embryos are unstable and will decay back into the SRO matrix unless enough Si diffuses through the matrix and attaches to the embryo to form a critically sized nucleus. Therefore the homogeneous nucleation rate is dependent on the chemical driving force as well as the energy of migration of Si atoms through the matrix

$$N_{hom} = \omega C_0 e^{\frac{-\Delta G_M}{kT}} e^{\frac{-\Delta G_{hom}^*}{kT}} \quad (3.5)$$

where  $\Delta G_M$  is the free energy associated with migration of atoms through the matrix,  $\Delta G_{hom}$  is the free energy for homogeneous nucleation (equation 3.1),  $\omega$  depends on the atomic jump frequency and the area of the critical nucleus and  $C_0$  is the concentration of nucleation sites which, for homogeneous nucleation, is the number of atoms per unit volume. To determine if the nucleation process is chemical driving force or migration limited we can calculate each term individually. The chemical driving force term is calculated in equation 3.2, as shown in Figure 3.2, as a function of Si content in the film at several temperatures.

As observed in Figure 3.2, the energy of formation for a critically sized nucleus is very large with respect to kT corresponding to a chemical free energy term,  $e^{\frac{-\Delta G_{hom}^*}{kT}}$ , of  $10^{-200} - 10^{-50}$ .

For the migration term we can calculate the diffusivity of Si in the matrix which is of the form

$$D = D_0 e^{\frac{-E_A}{kT}} \quad (3.6)$$

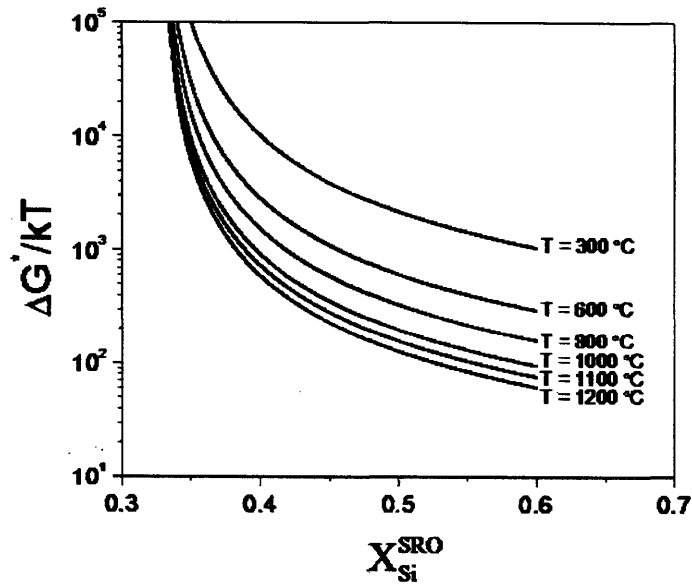


Figure 3.2 Calculated Gibbs free energy of formation normalized by  $kT$  versus Si content for several temperatures with  $\gamma_{CM} = 0.3 \text{ J/m}^2$ ,  $V_M = 12.1 \text{ cm}^3/\text{mol}$  and  $X_{Si}^{eq} = 0.33$ .

where  $D_0$  is the temperature independent prefactor and  $E_A$  is the activation enthalpy for the atomic diffusion. Several studies have been performed to measure the diffusivity of Si in stoichiometric Si and SRO [54,118,119]. The corresponding diffusivity values are plotted in Figure 3.3.

The diffusivity of Si in  $\text{SiO}_2$  as measured from the  $\text{Si}^{30}$  diffusion profile by Jaoul *et al.* [119], is lower than the values of the diffusivity of Si in SRO. The difference in the measured diffusivity in SRO by Iacona *et al.* [54] and Tsoukalas *et al.* [118] most likely results from the techniques used in the measurement. In Iacona *et al.* [54] the diffusivity was calculated by fitting the average size of Si nanocrystals measured through TEM with a diffusion controlled coarsening model while in Tsoukalas *et al.* [118] the diffusivity was calculated from the measured diffusion profiles of  $\text{Si}^{28}$  and  $\text{Si}^{30}$ .

From a comparison of the calculations shown in Figures 3.2 and 3.3 we see that the homogeneous nucleation reaction is chemical driving force limited since the chemical term is several orders of magnitude lower than the migration term. The product of these two terms



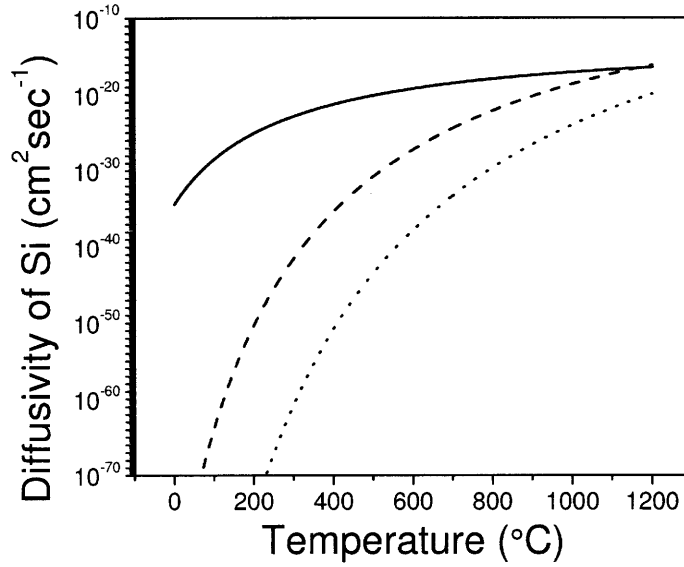


Figure 3.3 Calculated diffusivity of Si in SRO from Iacona *et al.*  $D=5 \times 10^{-13} e^{-\frac{1.2\text{eV}}{kT}} \text{ cm}^2\text{s}^{-1}$  [54] in SRO from Tsoukalas *et al.*  $D=1.378 e^{-\frac{4.74\text{eV}}{kT}} \text{ cm}^2\text{s}^{-1}$  [118] and in SiO<sub>2</sub> from Jaoul *et al.*  $D=106.1 e^{-\frac{7.6\text{eV}}{kT}} \text{ cm}^2\text{s}^{-1}$  [119].

indicates that the homogeneous nucleation rate is negligible. The transformation therefore must occur through heterogeneous nucleation. Unlike homogeneous nucleation, where all of the energy required to form the cluster-matrix interface is supplied by the chemical driving force, heterogeneous nucleation occurs at pre-existing defect sites where the threshold for nucleation is reduced by the energy released through the annihilation of the defect,  $\Delta G_{\text{defects}}$ . For these conditions equation 3.1 is modified to

$$\Delta G_{\text{het}} = \frac{-4\pi r^3}{3} \Delta G_v + 4\pi r^2 \gamma_{CM} - \Delta G_{\text{defects}} \quad (3.7)$$

with a heterogeneous nucleation rate of

$$N_{\text{het}} = \omega C_1 e^{-\frac{-\Delta G_M}{kT}} e^{-\frac{-\Delta G_{\text{het}}^*}{kT}} \quad (3.8)$$

where  $C_1$  is the concentration of heterogeneous nucleation sites.

The interface between the nanocluster and  $\text{SiO}_2$  matrix is incoherent (no lattice misfit as for crystalline precipitates in a crystalline matrix), therefore the strain is generated through the large volume mismatch between Si and  $\text{SiO}_2$  which is given by the expression

$$\Delta = \frac{V_m^{\text{SiO}_2} - V_m^{\text{Si}}}{V_m^{\text{SiO}_2}} \quad (3.9)$$

where  $V_m^{\text{SiO}_2}$  is the molar volume of  $\text{SiO}_2$ ,  $22.6 \text{ cm}^3/\text{mol}$ , and  $V_m^{\text{Si}}$  is the molar volume of Si,  $12.1 \text{ cm}^3/\text{mol}$ . The elastic strain generate by this volume misfit is given by the expression of Nabarro for an incompressible precipitate [120]

$$\Delta G_s = \frac{2}{3} \mu \Delta^2 V f \left( \frac{c}{a} \right) \quad (3.10)$$

where  $\mu$  is the shear modulus of  $\text{SiO}_2$ ,  $f$  is a function which depends on the shape of the

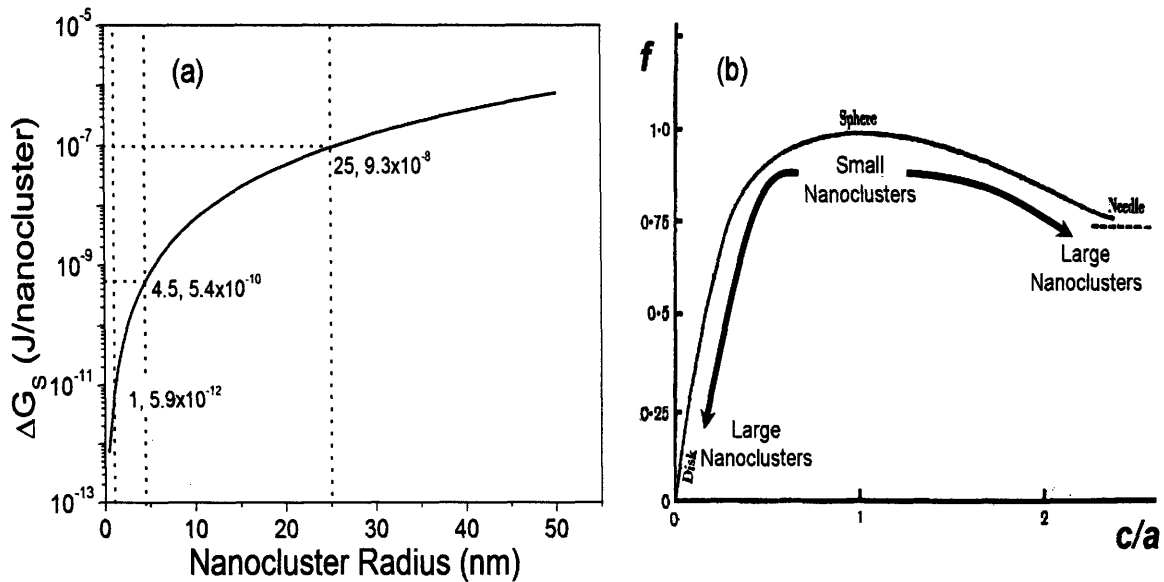


Figure 3.4 (a) Elastic strain energy per nanocluster calculated for spheroid nanoclusters of different radii. (b) Shape function for different precipitates (from Nabarro [120]).

precipitate which is defined by the axes  $c$  and  $a$  of the precipitate and  $V$  is the volume of the precipitate.

In Figure 3.4 (a) we plot the strain energy versus Si nanocluster radius assuming spherical clusters  $\left(f\left(\frac{c}{a}\right)=1\right)$ .

We observe that the elastic strain energy increases by a factor of 100 as the radius of the cluster increases from 1 to 4.5 nm. Large spheroidal nanocrystals, approaching 25 to 50 nm in radius, generate such a large elastic strain energy that we would expect them to form as a disk or needle which lowers the strain energy through the shape term  $f$  (Figure 3.4 (b)) in equation 3.10.

Once an equilibrium distribution of particles has formed the size and shape distributions are determined through a process known as coarsening. The driving force for coarsening is a reduction in surface through the Gibbs-Thompson effect which relates the local concentration near a cluster  $X_r$  to the cluster radius

$$X_r = X_\infty e^{\frac{2\gamma_{CM}V_m^{Si}}{RT r}} \quad (3.11)$$

where  $X_\infty$  is the matrix composition far from the cluster. The Gibbs-Thompson effect leads to the enhancement of the local concentration near small clusters which generates an effective concentration gradient in the sample and favors the growth of large clusters. Since the process is diffusion controlled, the growth of large clusters is parabolic in time.

In the following sections we will consider the possible formation mechanism of nanoclusters by considering micro-Raman spectroscopy and transmission electron microscopy.

### 3.1.2 Micro-Raman Spectroscopy

We used Raman spectroscopy to examine the evolution of the Si-rich dielectric matrix with annealing conditions. Amorphous Si, crystalline Si and SRO have unique Raman signatures [70]. By using a confocal microprobe we limit the measured area to a small region near the film surface to optimize the collection of signal from the thin film and minimizing the collection of signal from the substrate. In Figure 3.5 we show typical first-order Raman spectra for as-deposited and annealed SRO. The Raman spectrum for a reference Si wafer is shown for comparison.

For the reference Si wafer (Figure 3.5, dot line) the spectrum is sharp and symmetric at  $521\text{ cm}^{-1}$  corresponding to the transverse-optical (TO) phonon mode in Si. For as-deposited SRO (Figure 3.5 dash line) we observe a broad Raman band near  $475 - 480\text{ cm}^{-1}$  due to the amorphous Si network. After annealing, an additional band near  $517\text{ cm}^{-1}$  is observed, due to the presence of nanosized Si clusters (crystalline or amorphous) within the SRO matrix. This band is broader, more asymmetric and shifted compared to the reference Si wafer due to phonon confinement in the nanosized Si

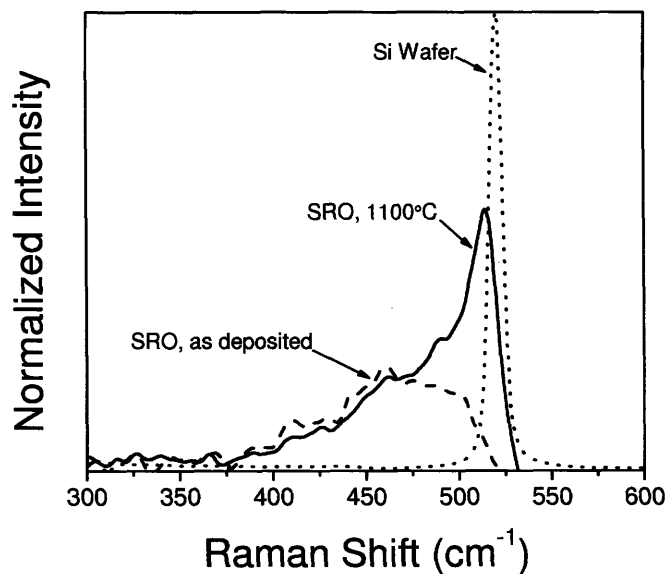


Figure 3.5 Micro-Raman spectra for an SRO sample deposited on SiO<sub>2</sub> with 40 at% Si as-deposited (dash line) and annealed at 1100°C for 1 hour (solid line). The spectrum for a reference Si wafer is shown for comparison (dot line). All spectra are normalized to the intensity of the first order TO phonon peak.

clusters, which increases the uncertainty in the phonon momentum allowing contributions to the Raman spectrum from phonons with a momentum  $q \neq 0$  [121]. The shape of the first-order Raman peak for nanosized Si can be modeled according to the phonon confinement [122] calculated using the integral transform [123]:

$$I(\omega) = \int_0^1 \frac{e^{-qL^2/4a^2}}{[\omega - \omega(q)]^2 + (\Gamma_0/2)^2} d^3q \quad (3.12)$$

with  $q$  expressed in units of  $2\pi/a$  where  $L$  is the average Si nanocluster radius,  $\Gamma_0$  is the linewidth of the bulk Si LO phonon  $\sim 4\text{cm}^{-1}$  and  $a$  is the Si lattice constant =  $5.430 \text{ \AA}$ . The LO phonon dispersion of the bulk material is given by the relation  $\omega^2(q) = A + B \cos(\pi q/2)$  with  $A = 1.714 \times 10^5 \text{ cm}^{-2}$  and  $B = 1.000 \times 10^5 \text{ cm}^{-2}$  [121,123]. This approach can be used to determine the average nanocluster radius from the measured lineshape of the first-order Raman peak.

A comparison of the micro-Raman spectra for samples with several different Si contents (shown in Figure 3.6) offers a possible explanation of the heterogeneous nucleation sites for forming Si nanoclusters.

For samples with less than 45 at% Si the Raman spectra for the as-deposited films are broad and featureless. The asymmetric peak associated with nanocrystal formation is observed only after annealing which demonstrates that activation energy must be supplied to induce the formation of Si nanocrystals for these concentrations. However, for samples with more than 45 at% Si the broad and asymmetric band characteristic of nanoclusters can be observed even in the as-deposited film. The shift of this nanocluster band with respect to the Si band decreases and the lineshape becomes narrower and more symmetric as the Si content is increased indicating that the material response is approaching the Si bulk due to an increase in the cluster size. These results suggest that there is a threshold of approximately 45 at% Si for clustering in the as-deposited film. We can interpret the trend of increased Si clustering by considering the probability of forming Si – Si bonds in the SRO matrix. For low Si contents the number of

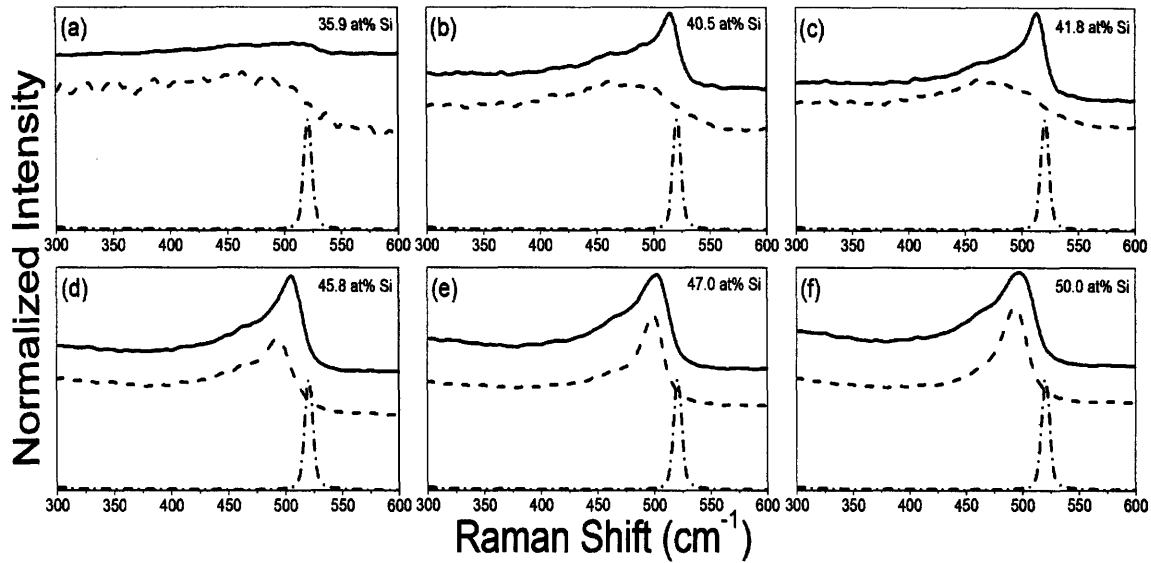


Fig. 3.6 Micro-Raman spectra for SRO samples on SiO<sub>2</sub> substrates with the following compositions (a) 35.9 at% Si (b) 40.5 at% Si (c) 41.8 at% Si, (d) 45.8 at% Si, (e) 47.0 at% Si and (f) 50.0 at% Si. For all panels the dash line is the as-deposited spectrum and the solid line is the sample spectrum after annealing at 1100°C for 1 hour. In each panel the Micro-Raman spectrum of a reference crystalline Si wafer is shown for comparison (dash-dot line).

excess Si atoms is small and the number of Si – Si bonds low. The basic structural unit in this case could be a Si = Si bond with each Si also bonded to two O atoms. As the Si content is increased the number of Si – Si bonds increases to the point where the basic structural unit is a small Si cluster which gives an observable spectral feature in the micro-Raman experiment. From the point of view of nucleation we propose that it is these structural units that act as nucleation sites for amorphous and crystalline Si nanoclusters when the film is annealed.

### 3.1.3. Transmission Electron Microscopy

Transmission electron microscopy yields structural information of thin samples by electron scattering. As the electron beam passes through the sample several electrons are diffracted through inelastic scattering due to interaction with defects within the matrix. A bright-field image is obtained from the primary beam passing through the sample with all diffracted beams rejected. Since Si nanocrystals diffract the electron beam they appear as dark spots in the bright-field image. By obtaining plan view and cross section images the nanocrystal size,

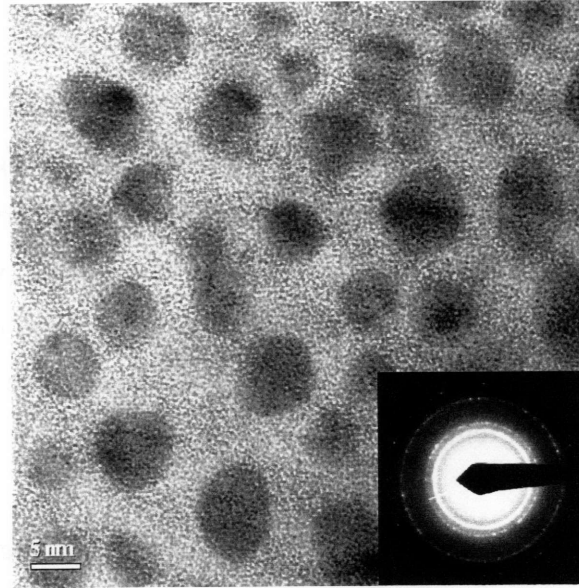


Figure 3.7 Plan view TEM image of an SRO sample deposited on a Si substrate with 38 at% Si annealed at 1100°C for 1 hour. (inset) Electron diffraction pattern for the same sample acquired from the same region as the image.

morphology, density and location within the film can be determined. Figure 3.7 shows a plan view bright-field image of a SRO sample with 38 at% Si annealed at 1100°C.

The nanocrystals are roughly spherical with an average radius of 3 nm. The inset electron diffraction pattern from the same region of the sample which shows diffraction lines for several crystallographic orientations, suggesting that the nanocrystals form with random orientations within the SRO matrix. Our microscopy studies also suggest that the nanocrystal formation occurs randomly throughout the matrix since we have observed no clear evidence of clustered growth, oriented growth or the formation of anisotropic clusters. This supports our hypothesis from the micro-Raman spectra that the heterogeneous nucleation site or embryo is a small Si cluster which is incorporated during the deposition since we expect these sites to be randomly distributed throughout the SRO matrix.

## 3.2. Low Temperature Phenomena

In Chapters 5 and 6 we will discuss the optical properties of Er-doped SRO with particular emphasis on the transfer of optical pump energy from SRO to Er ions. Through those

experiments we have identified a second annealing temperature range from 600 – 700°C which is below the threshold annealing temperature for forming crystalline Si nanoclusters but where strong energy-transfer to Er ions has been observed. Modeling of optical gain experiments, presented in Chapter 6, suggest that the density of energy-transfer centers is  $\sim 6 \times 10^{18} \text{ cm}^{-3}$  which is one order of magnitude larger than the density of Si nanocrystals we observed for similar samples annealed at 1100°C. This increased density is expected from our analysis of classical nucleation theory which predicts a high density of small Si clusters due to limited diffusion and coarsening that occurs during low temperature annealing treatments.

Amorphous clusters are not observable in the bright-field image due to the low  $Z$  contrast between Si and SiO<sub>2</sub>. To enhance the contrast between the amorphous Si clusters and the amorphous SiO<sub>2</sub> network energy-loss spectroscopy and energy filtered TEM have been applied [54]. As nominally implied, during energy filtered TEM the energy of the electrons transmitted through the sample is measured and the image is generated by only those electrons which have lost a characteristic energy due to interactions with the atomic or molecular species of interest. These characteristic energies are determined through energy-loss spectroscopy which measures the electron count versus energy lost as shown in Figure 3.8 for Si and SiO<sub>2</sub> which have loss peaks at 17 eV and 22 eV, respectively.

We have acquired images under bright-field conditions as well as through energy-loss at 17 eV and 22 eV loss peaks to observe the formation of nanoclusters as well as to assess the amorphous to crystalline quality of the nanoclusters. The results are shown in Figure 3.9 for samples annealed at 1100°C and Figure 3.10 for samples annealed at 600°C.

For the sample annealed at 1100°C we notice the presence of several nanocrystals in the bright-field image (Figure 3.9 (a)). The number of observable clusters is enhanced under energy filtered conditions at the Si electron energy-loss peak (Figure 3.9 (b)) due to the contribution of amorphous clusters and crystalline clusters that were not diffracting under the conditions for which the bright-field image was obtained. As expected there is no evidence of clustering in the SiO<sub>2</sub> electron energy-loss image.



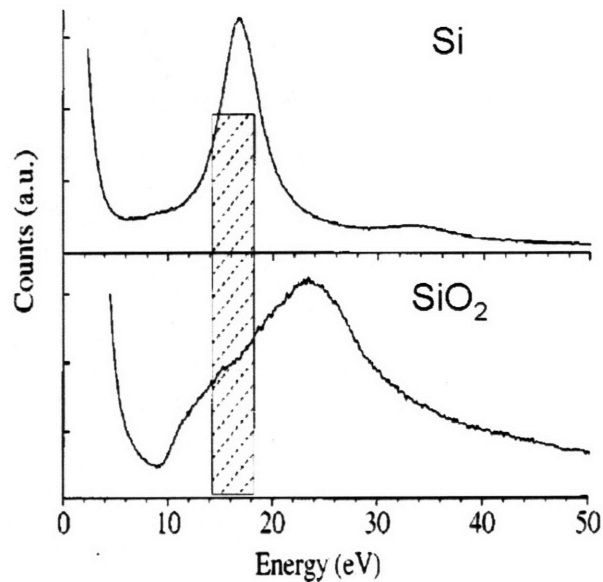


Figure 3.8 Electron energy-loss spectra for Si and SiO<sub>2</sub> (from Iacona *et al.* [54]).

In comparison the sample annealed at 600°C shows no evidence of Si clustering under bright-field (Figure 3.10 (a)) or energy filtered conditions at the Si loss peak (Figure 3.10 (b) or (d)).

From the estimated density ( $6 \times 10^{18} \text{ cm}^{-3}$ ) obtained from optical gain analysis and the total number of excess Si atoms in the matrix ( $2.2 \times 10^{21} \text{ cm}^{-3}$ ) we calculate a sensitizer radius of  $\sim 1 \text{ nm}$ . This is considered an upper limit for the size since the calculation assumes that all of the excess Si in the matrix has been transformed into Si clusters. Moreover, we have also attempted energy filtered TEM experiments on low temperature annealed samples at a higher resolution where we have also not observed any evidence of Si clustering (Figure 3.13 (d)). The lack of observable Si clusters in the energy filtered STEM image suggests that the sensitizers for the enhanced Er emission occurring in the range of 600 - 700°C are smaller than 1nm in radius. In this size range the optical properties of Si clusters are strongly dependent on the structural character of their surfaces [86,87]. The calculated short diffusion length for Si atoms at 600°C (Figure 3.3) suggests that only short-range structural modifications leading to changes in the surface structure of small amorphous clusters within the SRO matrix or the formation of localized centers such as Si=Si bonds are possible. All of these sites could be responsible for the optical properties observed from Er-doped SRO films annealed within this temperature range and are consistent

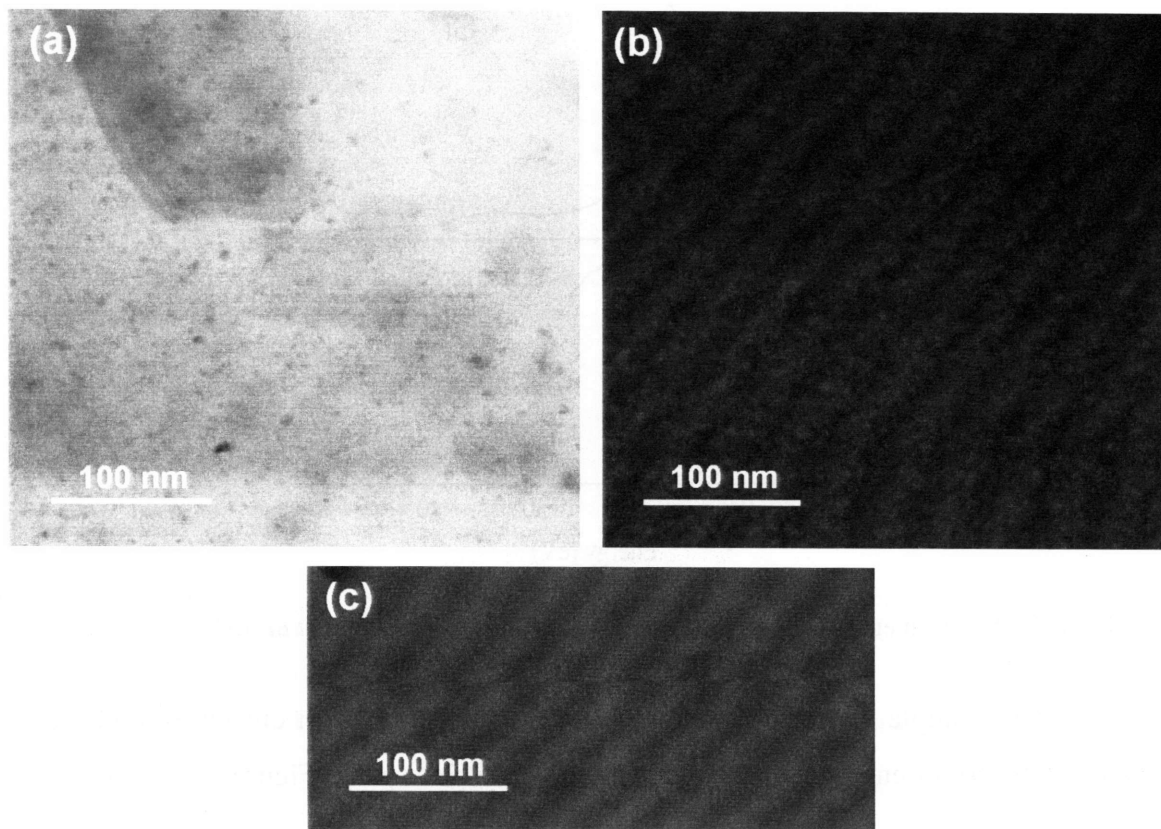


Figure 3.9 Plan view scanning transmission electron microscope images from an SRO sample with 55 at% Si annealed at 1100°C for 1 hour under (a) bright-field conditions, (b) energy filtered conditions at the Si electron energy-loss peak of 17 eV and (c) energy filtered conditions at the SiO<sub>2</sub> electron energy-loss peak.

with our EFTEM observations and our measurements of the temperature dependent photoluminescence of SRO presented in Chapter 5.

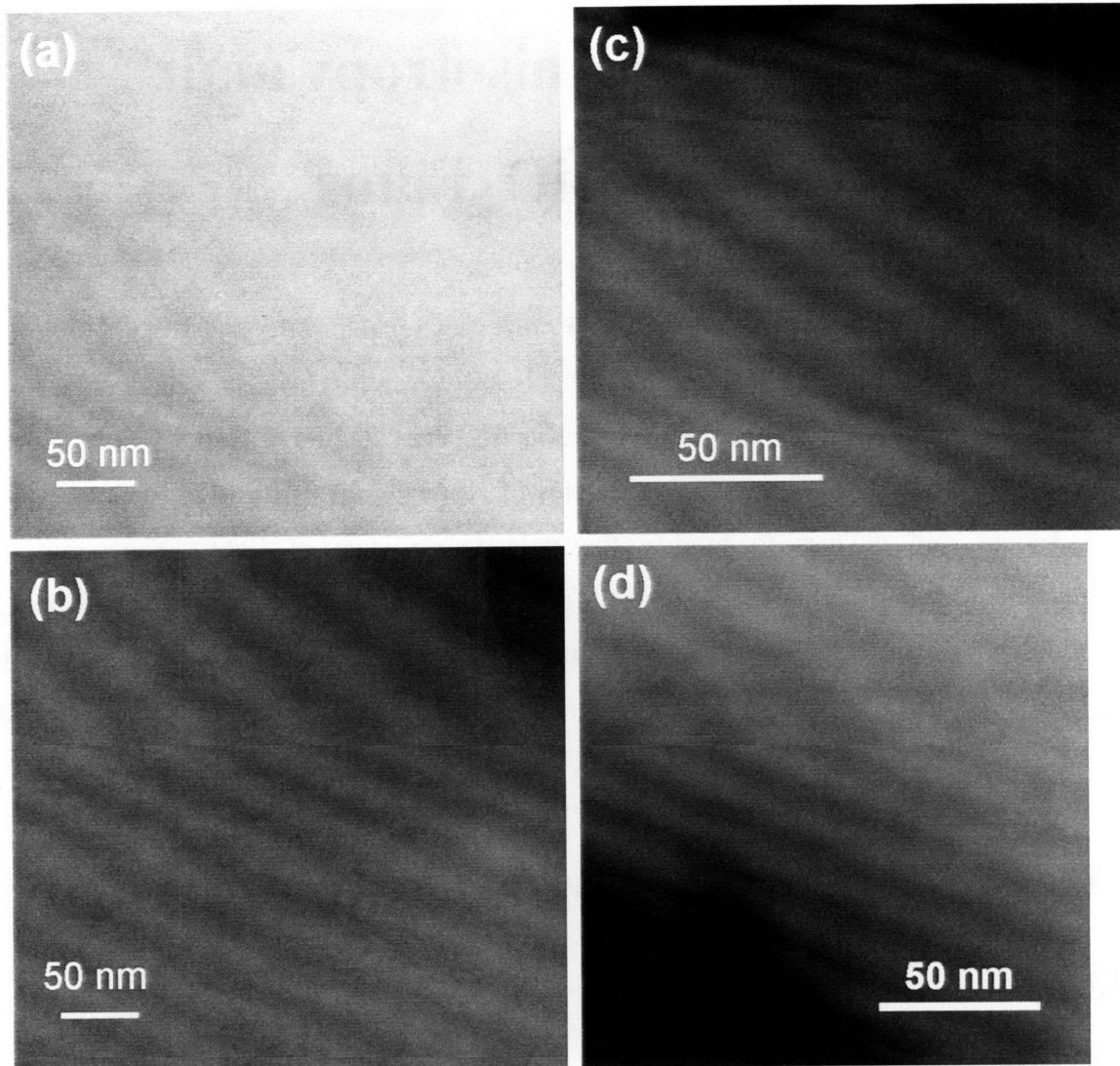


Figure 3.10 Plan view scanning transmission electron microscope images from an SRO sample with 38 at% Si annealed at 600°C for 1 hour under (a) bright-field conditions, (b) energy filtered conditions at the Si electron energy-loss peak of 17 eV and (c) energy filtered conditions at the SiO<sub>2</sub> electron energy-loss peak. (d) A higher resolution image of the same sample at the Si electron energy-loss peak.

# Chapter 4 | Optical Anisotropy and Dispersion in Si-rich SiO<sub>2</sub> Films

In this chapter we will discuss two optical properties related to the index of refraction of SRO films before and after annealing: optical anisotropy, or birefringence, and dispersion. Birefringence, the difference in the index of refraction for TE and TM polarized light, is important for determining the polarizing properties of SRO for the fabrication of polarization sensitive devices and devices to modify the polarization state of light. Dispersion, the wavelength dependence of the index of refraction, is important from the perspective of optical data communications and optical pulse propagation in SRO waveguides. First we will discuss the prism coupling technique used to measure the index of refraction as a function of polarization and wavelength.

## 4.1. Measuring the Refractive Index through Prism Coupling

We performed prism coupling experiments using a Metricon 2010 prism coupler [124]. Here I will describe the principle of operation of the prism coupling system for measuring the film index of refraction and thickness [125,126].

A schematic of the prism coupling apparatus is shown in Figure 4.1.

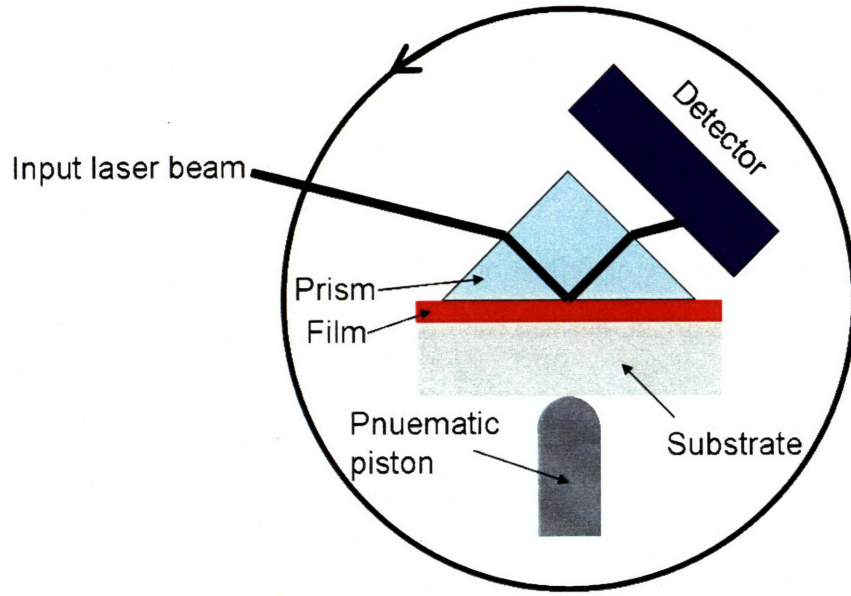


Figure 4.1 Schematic of the prism coupling apparatus in the Metricon 2010 system.

During the experiment a laser beam is shined on the face of a prism, with a higher index of refraction relative to the film being measured, that is held against the film through the use of a pneumatic piston. The prism and film are rotated with respect to the laser beam, changing the

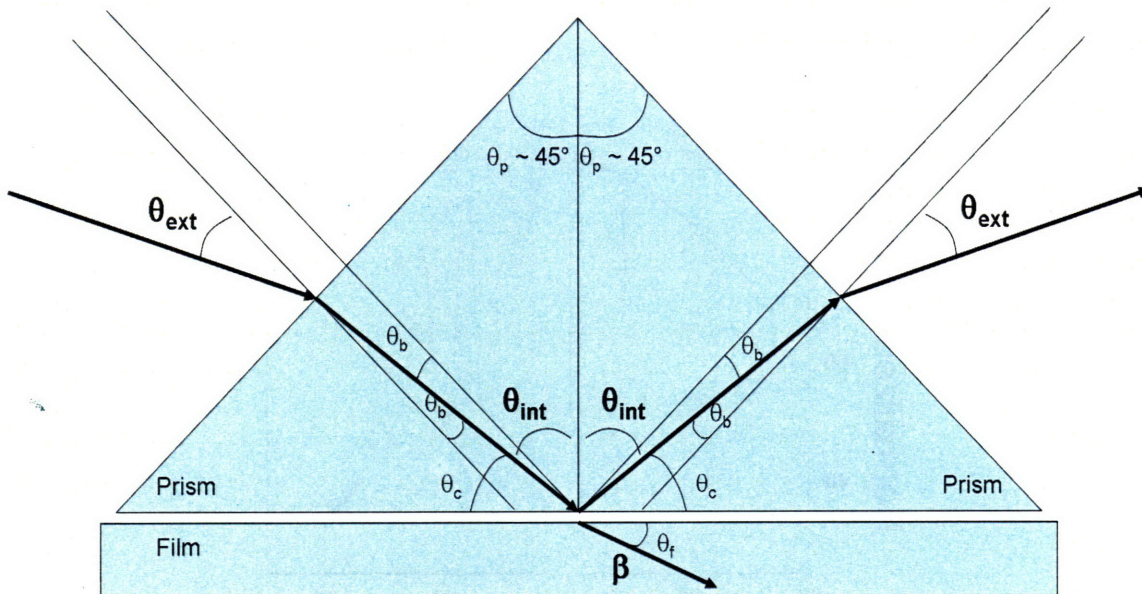


Figure 4.2 Ray optics diagram of the film/prism system during prism coupling where  $\theta_{ext}$  is the angle of incidence of the laser beam with respect to the prism normal,  $\theta_p$  is the prism angle,  $\theta_{int}$  is the internal angle of the beam that strikes the prism base in contact with the film,  $\theta_f$  is the angle of the beam propagating in the film and  $\beta$  is the propagation constant of the propagating mode in the film.

angle of incidence of the beam on the prism face and, through Snell's law, the angle at which the beam strikes the surface of the prism in contact with the film. A ray optics model of the film – prism system is shown in Figure 4.2.

If the prism has a higher index of refraction than the film there are certain angles where the propagation constant in the prism, defined as  $n_p \sin(\theta_{\text{int}})$  is equal to the propagation constant of the film,  $\beta = kn_{\text{eff}}$ , where  $k = \frac{2\pi}{\lambda}$  and  $n_{\text{eff}}$  is the effective refractive index of the propagating mode. At these angles the light is coupled from the prism into a propagating mode in the film. For all other angles the light is simply reflected at the base of the prism and exits the prism at the opposite face. During the measurement the light intensity exiting the prism is measured by a detector as the prism and film are rotated. Figure 4.2 shows the intensity versus external angle for a typical Metricon measurement of an SRO film on an  $\text{SiO}_2$  substrate.

As shown in Figure 4.3, when a propagating mode is excited in the film the measured intensity will drop and the effective index of the mode can be calculated through trigonometry knowing the external angle, the prism angle and the prism index of refraction. Each effective index is a

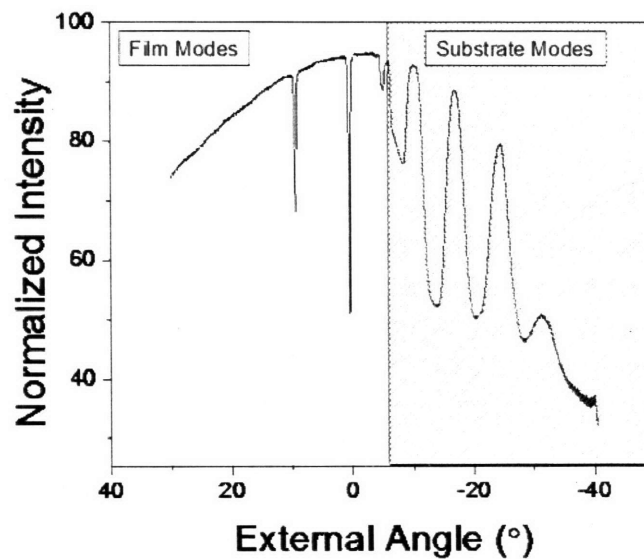


Figure 4.3 Metricon measurement of a SRO thin film, with three film modes, on a silica substrate at  $\lambda = 1550$  nm.

function of both the index of refraction and thickness of the film. In Chapter 6, where we discuss the slab waveguide devices, we derive the transcendental equations relating the effective index to the properties of the film for both TE and TM polarizations. Here we record the transcendental equations for the asymmetric condition (substrate and cover index of refraction are not equal) which is relevant to the Metricon measurement:

$$2V\sqrt{1-b} = m\pi + \tan^{-1} \sqrt{\frac{b}{1-b}} + \tan^{-1} \sqrt{\frac{b+\gamma}{1-b}} \quad \text{for TE polarizations} \quad (4.1)$$

$$2V\sqrt{1-b} = m\pi + \tan^{-1} \left( \frac{n_{film}^2}{n_{film}^2} \sqrt{\frac{b}{1-b}} \right) + \tan^{-1} \left( \frac{n_{film}^2}{n_{air}^2} \sqrt{\frac{b+\gamma}{1-b}} \right) \quad \text{for TM polarizations} \quad (4.2)$$

$$\text{with } b = \frac{n_{neff}^2 - n_{substrate}^2}{n_{film}^2 - n_{substrate}^2}, \quad \gamma = \frac{n_{substrate}^2 - n_{air}^2}{n_{film}^2 - n_{substrate}^2} \quad \text{and } V = \sqrt{k^2 d^2 (n_{film}^2 - n_{substrate}^2)}.$$

In equations 4.1 and 4.2  $m$  is the mode order ( $m = 0, 1, 2$ , etc. corresponding to the first, second, third, etc. guided modes in the film) and  $d$  is the film thickness. For a film that can support more than one mode, the transcendental equations can be solved for the two unknowns: the index of refraction and film thickness.

The index of refraction and thickness can also be determined for so-called leaky waveguides consisting of a low-index film on a high-index substrate. In this case the guided modes exponentially decay in the film according to [127]

$$R_{film-air} R_{film-substrate} e^{2ik_x d} = 1 \quad (4.3)$$

where  $R$  is the reflection coefficient for each interface and  $k_x$  is the wavevector of the leaky mode given by the expression

$$k_x = \frac{2\pi}{\lambda} (n_{film}^2 - n_{eff}^2)^{\frac{1}{2}} \quad (4.4)$$



In the next sections we will discuss how the index of refraction for different polarizations of light and wavelengths of light is influenced by the Si content of the film.

## 4.2. Birefringence

Birefringence is typically associated with propagation in anisotropic crystals where the beam propagates in two modes with different phase velocities corresponding to orthogonal polarization states. There are three ways that birefringence can be induced in materials that are nominally optically isotropic: 1) stress, 2) film structure and 3) waveguide structure. Birefringence in nanostructured Si has been reported in porous Si [128] and Si nanocrystal films prepared through annealing of Si and SiO<sub>2</sub> superlattices [129]. These waveguide films are anisotropic due to the fabrication process with a structure that constrains the formation of Si nanocrystals to specific regions resulting in birefringence. In comparison previous measurements on thin films of Si nanocrystals embedded in SiO<sub>2</sub> exhibited only form birefringence due to the planar waveguide structure with no material birefringence due to the uniform distribution of nanocrystals in the matrix [129].

We deposited SRO films on silica substrates to investigate the birefringence as a function of the sample preparation conditions. Silica substrates were chosen to facilitate the measurement of birefringence through prism coupling. Since the prism coupling technique requires rotating the sample to match the propagation constant of the light coupled from the prism into the film, TM polarized optical modes for films deposited on high-index substrates will be suppressed for a certain range of angles near the Brewster's angle for the film/substrate interface. This suppression of the mode pattern can lead to errors in the measurement of the TM index of refraction and the birefringence. Figure 4.4 shows the birefringence, defined as  $B=(n_{TM} - n_{TE})/n_{TE}$ , for as-deposited films.

For SRO films, the birefringence is positive ( $n_{TM}>n_{TE}$ ) and increases with increasing Si content. In comparison, the birefringence of sputtered Ge-doped stoichiometric SiO<sub>2</sub> is negligible which



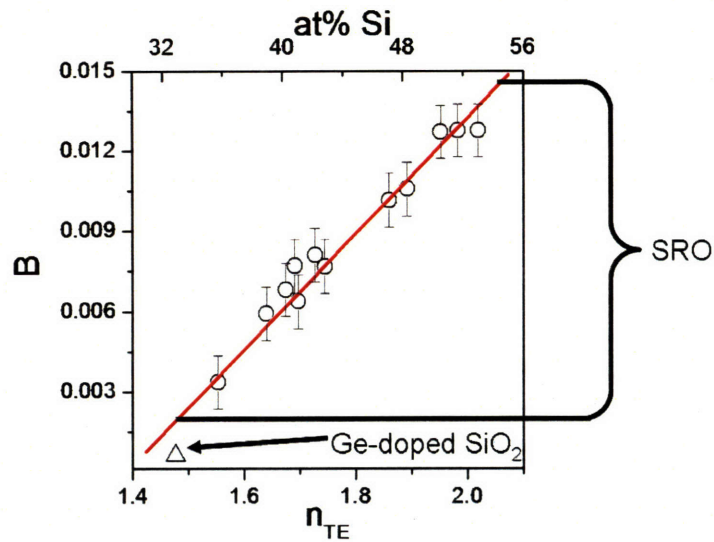


Figure 4.4 (a) Film birefringence,  $B = (n_{TM} - n_{TE})/n_{TE}$ , versus TE index of refraction for a Ge-doped  $\text{SiO}_2$  sample (open triangle) and SRO samples (open circles). The solid line is a linear fit to the data.

demonstrates that the resolution of the prism coupling measurement is on the order of  $10^{-4}$  which is one order of magnitude smaller than the smallest birefringence measured in SRO.

More interesting than the birefringence observed for as-deposited films is the annealing temperature dependence of the birefringence for SRO films, which is also influenced by the Si content of the film. As shown in Figure 4.5 (a) films with moderate Si content (40 at% Si, squares) exhibit birefringence reduction for all annealing temperatures. On the other hand, the birefringence of films containing a high Si content (50 at% Si, circles) initially remains constant, or slightly decreases, for annealing temperatures up to  $600^\circ\text{C}$  and then increases for higher annealing temperatures. We note that the temperature range of  $\sim 700 - 800^\circ\text{C}$ , coinciding with the onset of the birefringence enhancement, is the range of temperatures for the appearance of observable Si nanocluster formation [130]. A comparison of the birefringence before and after annealing at  $1100^\circ\text{C}$  for 1 hour for samples with variable Si content (Figure 4.5 (b)) shows that there is a threshold Si content for birefringence enhancement of  $\sim 45$  at% Si. The maximum birefringence increase of 0.027, observed in a sample with 50 at% Si annealed at  $1100^\circ\text{C}$ , is equivalent to an absolute birefringence of 0.039 which is comparable in magnitude to the values

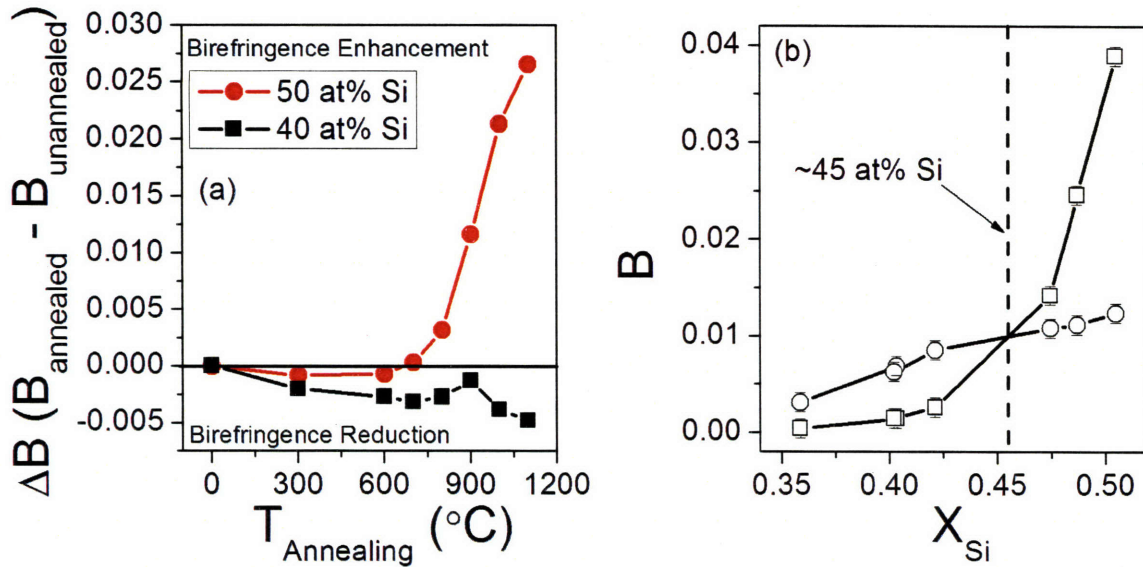


Figure 4.5 (a) Birefringence change,  $\Delta B = B_{\text{Annealed}} - B_{\text{Unannealed}}$ , after annealing for SRO films with 40 at% Si (squares) and 50 at% Si (circles). All samples were annealed for a fixed time of 1 hour. (b) Birefringence change after annealing at 1100°C for 1 hour for several SRO samples with variable Si content.

measured for several bulk anisotropic crystals such as  $\text{LiNbO}_3$  (-0.039),  $\text{BaTiO}_3$  (-0.03) and KDP (-0.028) [131].

We also attempted an experiment to determine if the birefringence was electrically tunable as in the case of electro-optic crystals. For the experiment we fabricated a slab waveguide on a Si substrate with a 10  $\mu\text{m}$  undercladding and used the prism coupling setup that will be discussed in Section 6.4 to couple light from a 1550 nm laser into the film. For this experiment the setup shown in Figure 6.12 was modified by placing Glan-Thompson prism at the input and output of the waveguide. The polarizers were 90° out of phase to transform any phase modulation into amplitude modulation. A 1  $\text{cm}^2$  area in the center of the sample was coated with a thick ( $\sim 6 \mu\text{m}$ )  $\text{SiO}_2$  overcladding before having an aluminum electrode deposited on the overcladding. The backside of the wafer was mechanically polished to remove the thermal oxide and attached to the aluminum sample holder using silver paint. Electrical contact was made to the top electrode and the sample holder and a DC voltage was applied across the sample. We did not observe any measurable change in the transmitted power, and thus no electrically tunable birefringence, even for 5 kV applied.

As discussed in the opening of this section the possible origins of birefringence in nominally isotropic materials is stress, structure and waveguide form. We will now consider each of these effects independently in the next sections.

### 4.2.1. Effect of Waveguide Structure

The samples used to measure the birefringence are asymmetric optical slab waveguides where light is confined within the high-index SRO film layer through total internal reflection at the air/film and film/substrate interfaces. The optical modes within this structure propagate with a velocity that is dependent on the effective index of refraction of the mode which can be calculated based on the material index of refraction and film thickness. More about slab waveguides will be discussed in Chapter 6 including the method for calculating the effective index of the waveguide for TE and TM polarizations. At this point it is important to know that the optical modes for any slab waveguide are dependent on polarization with their difference equal to the modal or form birefringence. Figure 4.6 shows the transmitted intensity versus

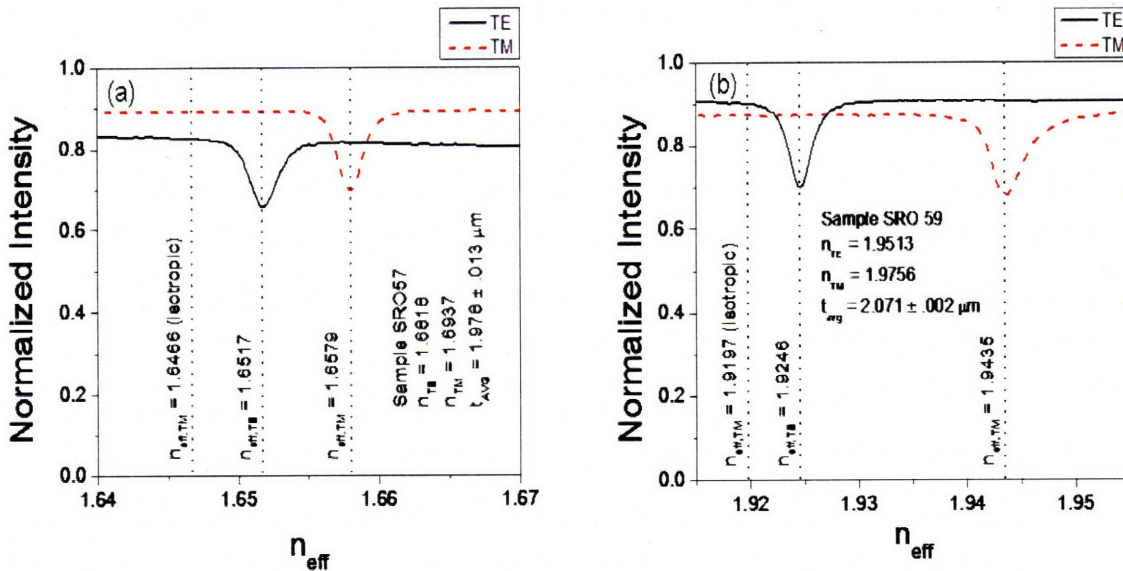


Figure 4.6 (a) Transmitted intensity versus effective index obtained through prism coupling for a sample with 40 at% Si as-deposited. (b) Transmitted intensity versus effective index obtained through prism coupling for a sample with 50 at% Si as-deposited. The dot lines represent the calculated effective indices for the TE and TM modes as well as the effective index for the TM mode assuming an isotropic index of refraction.

effective index for the first mode of samples with 40 at% Si and 50 at% Si, respectively, along with the calculated effective index for the TE and TM modes using the approach outlined in Chapter 6. Also included in the figure is the effective index for the TM mode calculated assuming an isotropic index of refraction equal to the TE index of refraction. We notice that for both samples the calculations of the effective index for the TE and TM modes based on the material index for anisotropic conditions give very good agreement with the dips in the transmission corresponding to the optical modes within the waveguide structure. On the other hand, the modal birefringence calculated under isotropic conditions is the opposite sign of the observed birefringence. Therefore the modal birefringence cannot explain the positive birefringence we have measured for our samples.

## 4.2.2. Effect of Film Stress

For birefringence due to film stress the index of refraction change is related to the stress through the stress-optic coefficients. The index of refraction change due to a triaxial stress state in cylindrical coordinates is given by the following equations [132]

$$\Delta n_r = n_r - n = -C_2 \sigma_r - C_1 (\sigma_\theta + \sigma_z) \quad (4.5)$$

$$\Delta n_\theta = n_\theta - n = -C_2 \sigma_\theta - C_1 (\sigma_r + \sigma_z) \quad (4.6)$$

$$\Delta n_z = n_z - n = -C_2 \sigma_z - C_1 (\sigma_r + \sigma_\theta) \quad (4.7)$$

where  $\sigma$  is the stress  $z$  is the direction normal to the substrate,  $\theta$  is the circumferential or hoop direction,  $r$  is the radial direction and  $C_1$  and  $C_2$  are the stress-optic coefficients of the material. The film and wafer are in a state of plane stress

$$\begin{aligned} \sigma_z &= 0 \\ \sigma_r &= \sigma_\theta = \sigma_{film} \end{aligned} \quad (4.8)$$

Under plane stress conditions the birefringence due to stress is given by the equation



$$B = \frac{\Delta n_z - \Delta n_r}{\Delta n_r - n} = \frac{(C_2 - C_1)\sigma_{film}}{-(C_2 + C_1)\sigma_{film} - n} \quad (4.9)$$

For silica the stress-optic coefficients are  $C_1 = 4.2 \times 10^{-6} \text{ MPa}^{-1}$  and  $C_2 = 6.5 \times 10^{-7} \text{ MPa}^{-1}$  [132]. A compressively stressed film would therefore lead to a positive birefringence. We calculated the film stress through measurements of wafer curvature using a Tencor FLX 2320 using Stoney's formula [133]

$$\sigma_{film} = \frac{Ed_{substrate}^2}{6R(1-\nu)d_{film}} \quad (4.10)$$

where E is Young's modulus (85 GPa for silica),  $\nu$  is Poisson's ratio (0.17 for silica), R is the radius of curvature,  $d_{substrate}$  is the substrate thickness (0.5 mm) and  $d_{film}$  is the film thickness. For all films we measured a compressive stress (Figure 4.7) which increases as the Si content of the film increases, consistent with the observation of a positive birefringence. If the birefringence

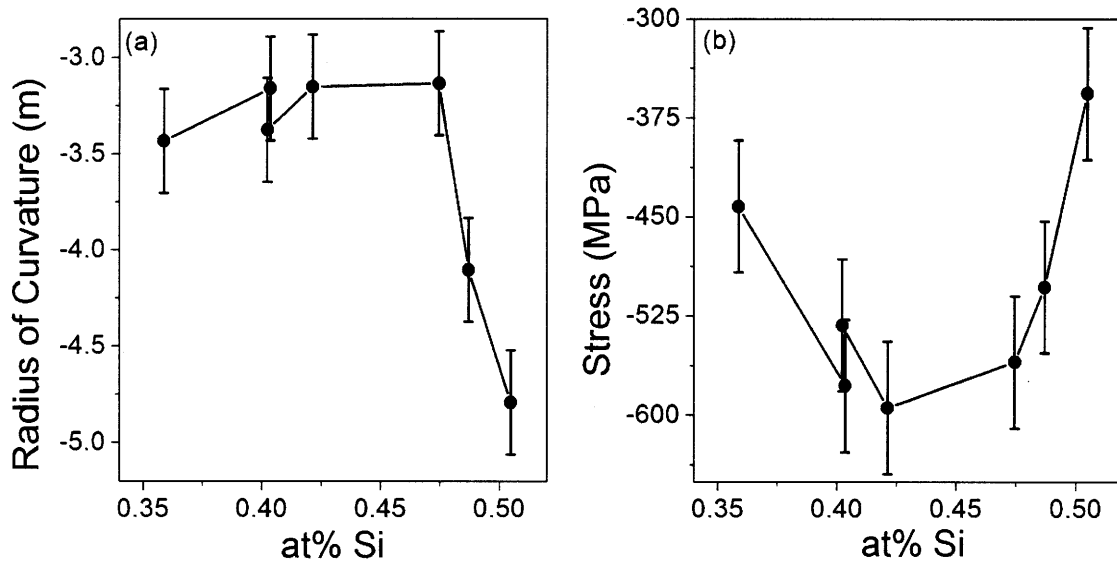


Figure 4.7 (a) Wafer radius of curvature for 1cm x 1 cm squares of SRO samples deposited on  $\text{SiO}_2$  substrates. (b) Film stress calculated from the measurements of wafer radius of curvature using Stoney's equation.

were only due to the stress we would expect to see the same linear dependence on Si content that we observed for the birefringence in Figure 4.4; we do not observe that here. We have also measured the film stress before and after annealing at 1100°C for all samples considered in the experiment of Figure 4.5 (b). The results show that for an annealing temperature of 1100°C the film stress changes from compressive to tensile consistent with the observation of film thickness reduction upon annealing. The tensile stress is expected after annealing due to the higher thermal expansion coefficient for SRO and film densification. Again, if the birefringence were only due to stress, the change in sign of the stress after annealing would result in a change in stress of the birefringence which is also not observed. The fact that the birefringence is positive for all deposition and annealing conditions confirms the marginal role of film stress in the birefringence.

### **4.2.3. Effect of Film Structure**

Our analysis of film stress before and after annealing of SRO suggests that there is another contribution to the birefringence that allows the sign of the birefringence to remain invariant while the sign of the stress changes; this contribution to the birefringence is from film structure. Figure 4.8 shows the structure zone model for sputter deposition processes that was developed by Thornton [134]. The film structure is determined by shadowing, attachment, surface diffusion and desorption which are controlled through the process parameters of deposition pressure and homologous substrate temperature (normalized to the melting point of the film).

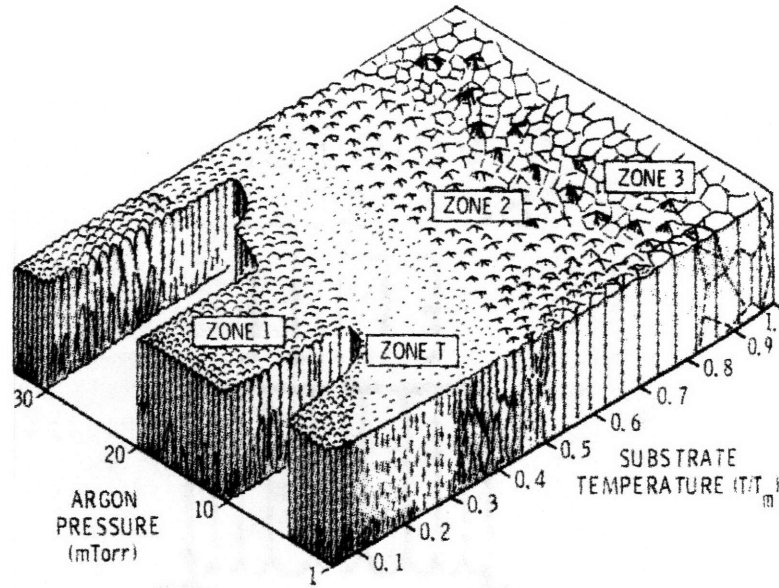


Figure 4.8 Structure zone model indicating the expected film microstructure versus deposition pressure and substrate temperature (from Thornton [134]).

The diagram shown in Figure 4.8 was developed by observing the structure of refractory metal thin films. Messier *et al.* [135] published a revised structure zone model based on examining the morphology of amorphous Ge and Si films prepared through ion-assisted deposition. For a homologous temperature of  $T/T_M = 0.27$  they observed a columnar film structure where the size scale of the structure was dependent on the film thickness. Using microscopy techniques they observed column sizes of 1 – 3 nm, 5 – 20 nm, 20 – 40 nm, 50 – 200 nm and 200 – 400 nm with the smaller sizes for thinner films (~15 nm in thickness) and the larger sizes for thicker films (~10  $\mu\text{m}$  in thickness). More recently Burmeister *et al.* have demonstrated column sizes of 100 – 500 nm in TiAlN and TiO<sub>2</sub> deposited through RF sputtering [136]. For our sputter deposition conditions of 3 mTorr Ar pressure and a normalized substrate temperature of ~0.1 the structure zone model of Thornton predicts films with a moderately dense columnar structure. In Figure 3.6 we show atomic force micrographs of SRO surfaces for two Si contents: 40 at% Si and 50 at% Si, as-deposited and after annealing at 1100°C for 1 hour.

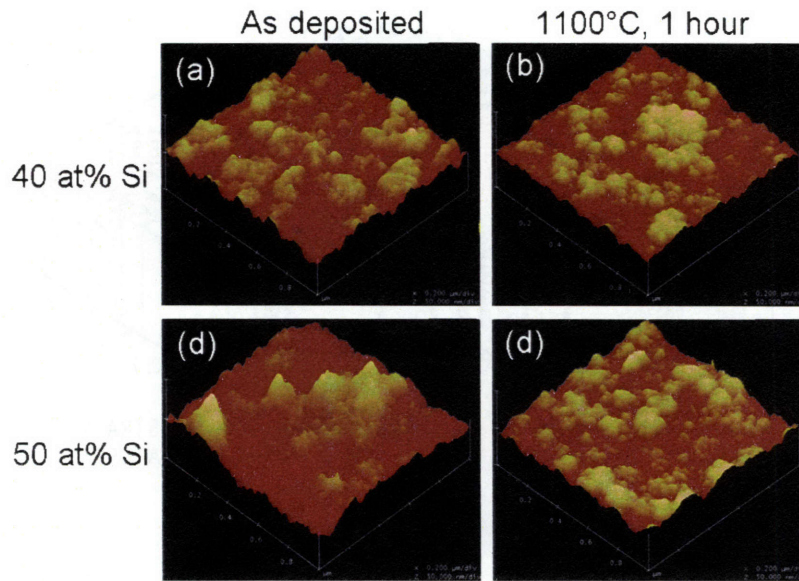


Figure 4.9 AFM images of a 1  $\mu\text{m}$  by 1  $\mu\text{m}$  area of the surface of the following SRO samples deposited on  $\text{SiO}_2$  substrates (a) an as-deposited SRO sample with 40 at% Si with an RMS roughness of 5.2 nm (b) an SRO sample with 40 at% Si annealed at 1100°C for 1 hour with an RMS roughness of 4.2 nm. (c) an as-deposited SRO sample with 50 at% Si with an RMS roughness was 8.9 nm and (d) an SRO sample with 50 at% Si annealed at 1100°C for 1 hour with an RMS roughness of 4.6 nm.

For all samples the film surface is rough with an RMS roughness of 4 – 8 nm which is characteristic of a columnar microstructure. We have additionally performed cross sectional scanning electron microscopy (SEM) of as-deposited films to determine if the columnar structure extends through the thickness of the film. The cross section samples were prepared by scoring the backside of the silica wafer and dipping the sample in liquid nitrogen for 1 – 2 minutes to improve the quality of the cleave. Figure 3.7 shows SEM images for samples with 40 and 50 at% Si shown in Figure 3.7 (a) and (b), respectively.



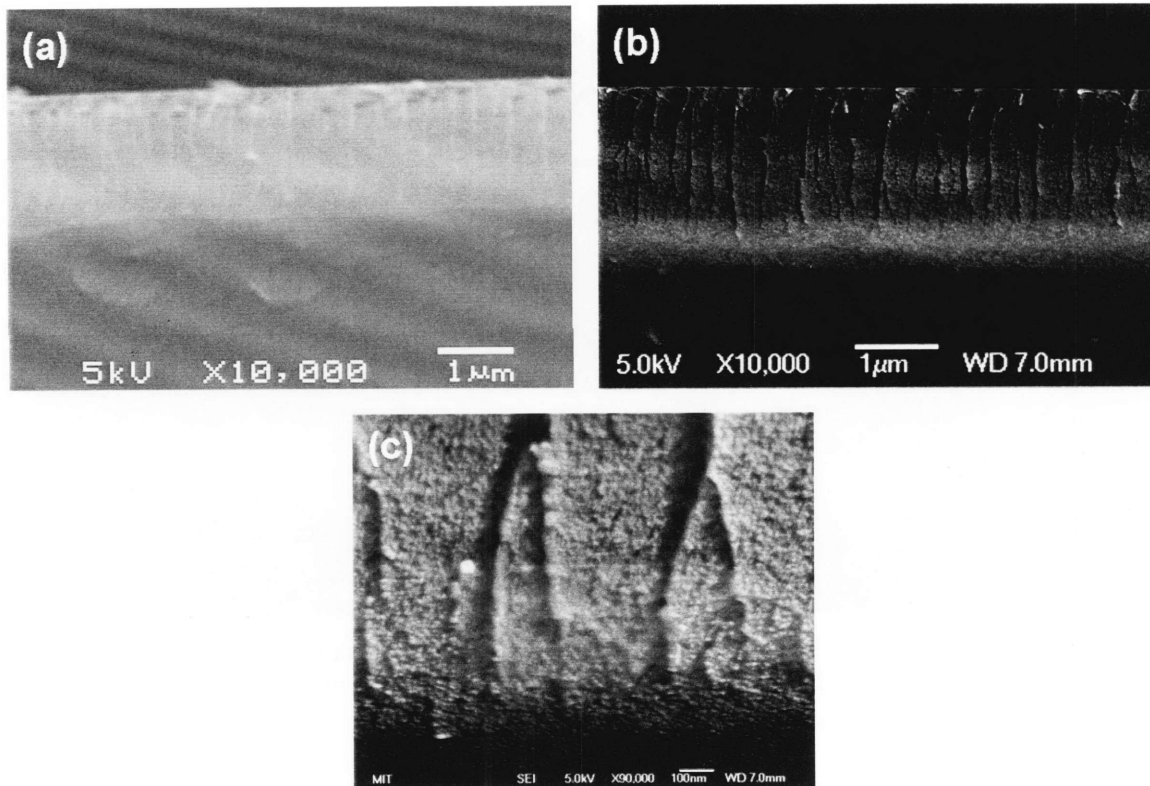


Figure 4.10 Cross section SEM images of as-deposited SRO samples on  $\text{SiO}_2$  substrates with (a) 40 at% Si at 10kX, (b) 50 at% Si at 10kX and (c) 50 at% Si at 90kX.

The cross section SEM images clearly show that the films, with different Si content, have a columnar morphology. In Figure 3.7 (c) we show a high magnification image of the region near the film/substrate interface. We notice that in this region there is a higher density of interfaces (boundaries between columnar regions) in the film due to the impingement of isolated islands in the early stages of the deposition process. The simultaneous observation of  $\sim 10$  nm structure in the AFM and  $>100$  nm structure in the SEM is also consistent with the observations of Messier *et al.* [135].

We would like to comment on the difference between the film structure and false structure induced by the fracture. Since SRO is an amorphous material, the boundaries that exist between columns are not discrete (as in the case of a polycrystal). The contrast observed in the image occurs when the film fractures along the low density intercolumnar regions. In Figure 4.11 we show a cross section SEM image of what we refer to as a bad cleave of an unannealed SRO film with 40 at% Si.

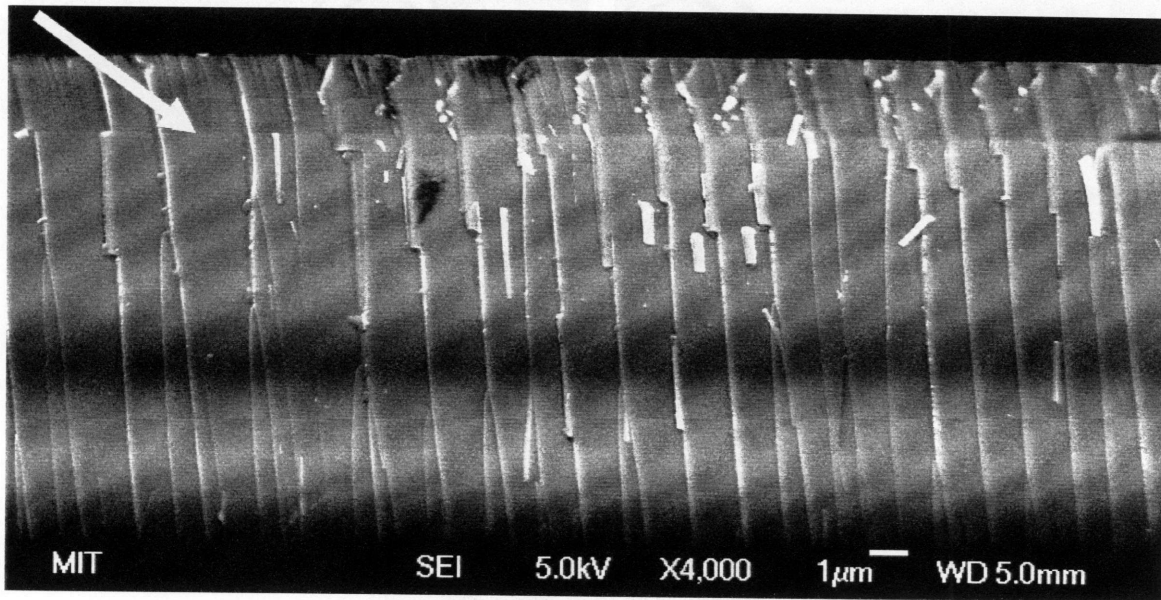


Figure 4.11 Cross section SEM image of an as-deposited SRO sample on a SiO<sub>2</sub> substrate with 40 at% Si at 4kX. The white arrow indicates the location of the film – substrate interface.

In the case of the bad cleave the features are not located only in the film thickness but extend into the substrate below. It has been after observing several cross sections that we interpreted the features in Figure 4.10 as a columnar microstructure obtained using our sputtering conditions. We have not observed the columnar morphology after annealing at 1100°C for 1 hour, but it is not clear if this observation is the result of consolidation of the film during the anneal or a poor quality of the cleaved surface. The columnar structure was also not observed for as-deposited or annealed films in cross-sectional TEM.

An exact description of this materials system and its optical properties is almost impossible given its microscopic complexity. However, in this section we apply a simple model that, in the end, proves to be very powerful in linking the microscopic details of the material to the macroscopic optical properties. Figure 4.12 shows the approximate material structure as a series of columns and boundaries with its symmetry in relation to the polarization of light in the slab waveguide structure.

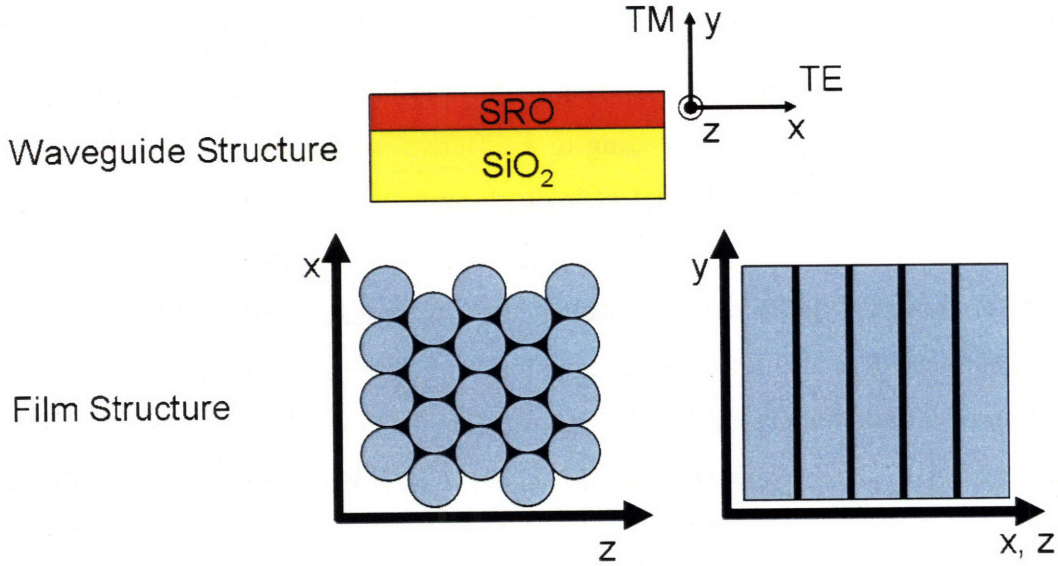


Figure 4.12 Schematic of the slab waveguide structure with the direction of the light polarization indicated. Schematic of the column-boundary microstructure relative to the x, y and z directions defined in the schematic of the waveguide structure.

If we assume that the boundary and column are composed of materials with different composition (i.e. possessing two different densities [137] or two different amounts of excess Si in  $\text{SiO}_2$ ) we can estimate the index of refraction of the medium in the TE and TM directions through an effective-medium approximation where the response of the material to the two polarizations will be different due to differences in dielectric screening. The following expressions have been developed for this configuration [138].

$$n_x = n_z = n_{TE} = \frac{f_{\text{boundary}}}{n_{\text{boundary}}^2} + \frac{f_{\text{column}}}{n_{\text{column}}^2} = n_o \quad (4.11)$$

$$n_y = n_{TM} = f_{\text{boundary}} n_{\text{boundary}}^2 + f_{\text{column}} n_{\text{column}}^2 = n_e \quad (4.12)$$

where  $f_{\text{boundary}}$  is the volume fraction of the boundary,  $f_{\text{column}}$  is the volume fraction of the column,  $n_{\text{boundary}}$  is the refractive index of the boundary and  $n_{\text{column}}$  is the refractive index of the column. A column/boundary interface oriented parallel to the polarization of light (TM) feels a uniform electric field giving an index of refraction that is a simple volume weighted average of the refractive index of each region. For a column/boundary interface oriented perpendicular to the polarization of light (TE) a polarization charge develops at the interface which reduces the

contribution to the average index of refraction from the higher index of refraction region. In this case the dielectric displacement in each region is constant with the electric field strength modified by the polarization charge leading to a different weighting of the index of refraction from each region. If we consider the dielectric displacement as a proxy for the charge deposited on a capacitor and the electric field as a proxy for the applied voltage, equations 4.11 and 4.12 are identical to those for the effective capacitance of two capacitors operating in series and in parallel, respectively. It is also important to note that similar expressions have been derived from the dispersion of a photonic crystal in the long-wavelength limit (scatterer size and period very small with respect to the wavelength of light) [139]. Comparing the results above with those derived from the long-wavelength dispersion analysis of photonic crystals, the expression for refractive index of the TM polarization is identical while the refractive index of the TE polarization, in the photonic crystal case, is given by the Maxwell-Garnett expression [139].

$$n_{TE}^2 = n_{boundary}^2 \left( 1 + \frac{2f \left( \frac{n_{column}^2 - n_{boundary}^2}{n_{column}^2 + n_{boundary}^2} \right)}{1 - f \left( \frac{n_{column}^2 - n_{boundary}^2}{n_{column}^2 + n_{boundary}^2} \right)} \right) \quad (4.13)$$

As a result of the material symmetry the index of refraction is equivalent in the x and z directions, in agreement with our measurements. Therefore the index of refraction for the TE polarization corresponds to the ordinary index of refraction while the index of refraction in the y direction or TM polarization corresponds to the extraordinary index of refraction. Both the effective-medium approximation and the long-wavelength dispersion of a photonic crystal predict an extraordinary index which is greater in magnitude than the ordinary index of refraction. Therefore the column-boundary microstructure has polarizing properties equivalent to a positive uniaxial material which is consistent with the sign and symmetry of the birefringence we measured in our films. Within this approximate system the fraction of columns and boundaries is determined by their respective thicknesses. For given column and boundary thicknesses we can solve equations 4.11 and 4.12 to determine the index of refraction of the column and boundary materials. Since the magnitude of the birefringence is related to the index contrast between the boundary and column there are two possible solutions for  $n_e$  and  $n_o$  corresponding to boundaries with lower and higher

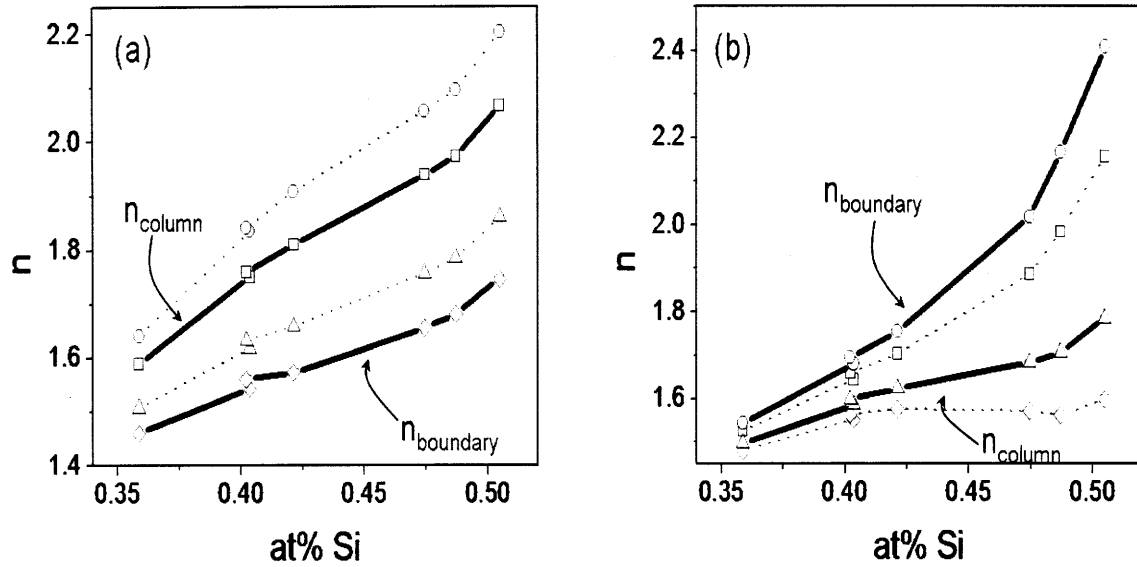


Figure 4.13 (a) Calculated index of refraction for the column and boundary region for as-deposited samples based on the effective-medium model for the following conditions: (i) low boundary index (diamonds) and high column index (squares) and (ii) high boundary index (circles) and low column index (triangles). The solid and dotted lines are a guide for the eyes. (b) Calculated index of refraction for the column and boundary region for samples annealed at 1100°C for 1 hour based on the effective-medium model for the following conditions: (i) low boundary index (diamonds) and high column index (squares) and (ii) high boundary index (circles) and low column index (triangles). The solid and dotted lines are a guide for the eyes.

indices of refraction with respect to the column. From the cross sectional SEM images in Figure 4.10 we can estimate the column and boundary volume fractions to be 0.83 and 0.17, respectively and calculate the column and boundary index of refraction for as-deposited and annealed samples with variable Si content from the  $n_e$  and  $n_o$  measured for samples shown in Figure 4.5 (b). In Figure 4.13 we show the results of the calculations.

Based on the SEM observations above we can suggest which variation of the column and boundary index most closely resembles what is physically occurring in the samples. For the as-deposited case we expect the boundary index to be lower than the column index since the boundary region has a lower density [137]. This situation is represented by the solid guide lines in Figure 4.13 (a) for the column and boundary index of refraction.

After annealing, if we assume the same volume fraction of boundary and column regions as in the as-deposited case, the calculations predict two possible microstructure modifications:

1. the boundary index is decreased with respect to the column index
2. the boundary index is increased with respect to the column index

The latter situation is represented by the solid guide lines in Figure 4.13 (b). For low Si content samples the sintering process coupled with random Si nanocrystal nucleation throughout the matrix leads to a more homogeneous index of refraction and a near zero birefringence. In the case of samples with a high Si content we notice from Figure 4.5 that the birefringence enhancement begins at an annealing temperature of 700°C. Since the diffusion is limited at this annealing temperature we suggest that the sintering process involves the flow of Si rich material which has a lower viscosity compared to SiO<sub>2</sub>. This is consistent with several studies on the viscous flow of silicate melts which has been attributed to the motion of line defects composed of SiO molecules [140]. In silicate melts the temperature dependence of the activation energy and viscosity are explained through the temperature dependence of the fraction of SiO molecules in the line defects [140]. We interpret the increase in the enhancement of the birefringence for samples with high Si content to an increase in the fraction of SiO molecules diffusing into the boundary region during the sintering process. Finally we measured the birefringence for the sample with 50 at% Si annealed at 1100°C for various annealing times, Figure 4.14.

We notice that the birefringence increases rapidly for an annealing time of just 1 – 5 minutes and then slowly saturates for annealing times greater than 1 hour. The calculated index of refraction for the boundary and column reveals that the sharp increase in the birefringence for short annealing times is due to a sharp increase in the index of refraction of the boundary region while the slow saturation is a combination of a decrease in the index of refraction in the column and an increase in the index of refraction of the boundary. We associate the sharp increase in the boundary index of refraction with the densification of the boundary region through the sintering process described above. The slow decrease of the index of refraction of the column and increase of the index of refraction of the boundary is associated with nanocrystal coarsening through atomic diffusion from the column which is proportional to  $\sqrt{t}$ .

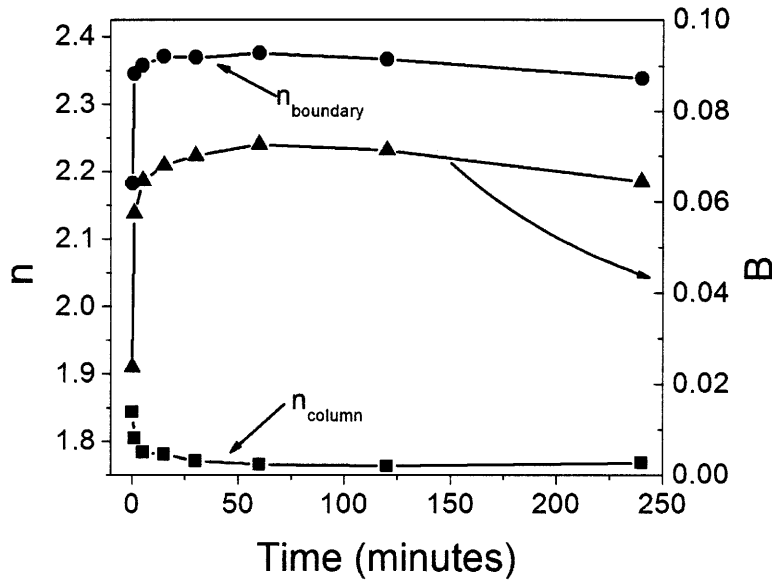


Figure 4.14 Measured birefringence for an SRO sample with 50 at% Si annealed at 1100°C for various time (triangles). Calculated index of refraction of the boundary (circles) and the column (squares) based on the measured birefringence.

Our interpretation of the sintering process leading to the formation of a high-index of refraction boundary region would also predict a higher density of Si nanocrystals in this region due to the large concentration of excess Si. We attempted to obtain evidence of Si accumulation or clustered nanocrystal growth in the boundary regions of birefringent thin films annealed at 1100°C through bright-field and energy-filtered TEM to support our proposed mechanism of birefringence enhancement. However, we did not observe either effect. Another limitation of our interpretation of the birefringence enhancement is the fact that we assume the same volume fraction of boundaries and columns after annealing as the as-deposited case which might not be the case after the sintering process is complete. Further high resolution microscopy studies will be required to clearly identify the mechanism of birefringence enhancement.

### 4.3. Dispersion

Dispersion or wavelength dependence of the refractive index is an important property which influences the propagation of light pulses in waveguide materials within an optical communication system. Since the index of refraction determines the speed of propagation within the medium an optical pulse, possessing a specific spectral width, will become broadened due to

the fact that the individual photons within the pulse will travel at different speeds. This will lead to an enhanced bit error rate or probability of error per bit with a bit rate – distance product given by [141]

$$LB_0 = \frac{1}{4|D_\lambda|\sigma_\lambda} \quad (4.14)$$

where  $D_\lambda$  is the dispersion coefficient of the medium at a specific wavelength  $\lambda$ ,  $\sigma_\lambda$  is the source linewidth,  $L$  is the distance of propagation and  $B_0$  is the bit rate. The dispersion coefficient (in units of  $s/m \cdot nm$ ) is given by the expression

$$D_\lambda = -\frac{\lambda_0}{c} \frac{d^2n}{d\lambda_0^2} \quad (4.15)$$

The wavelength dependence of the index of refraction for optical fibers has been studied extensively and is given by the Sellmeier equation.

$$n^2(\lambda) = 1 + \frac{B_1\lambda^2}{\lambda^2 - C_1} + \frac{B_2\lambda^2}{\lambda^2 - C_2} + \frac{B_3\lambda^2}{\lambda^2 - C_3} \quad (4.16)$$

where the coefficients  $B_{1,2,3}$  and  $C_{1,2,3}$  are specific to each material.

Si has a stronger wavelength dependence for the index of refraction compared to silica due to the presence of optical absorption in the near infrared at the band-edge (1.1 eV). The absorption (imaginary part of the index of refraction) influences the real part of the index of refraction through the Kramers-Kronig relations.

As a dispersive medium SRO is expected to have a performance which is intermediate between silica and Si. We have measured the index of refraction for several SRO samples at four wavelengths 632 nm, 1064 nm, 1307 nm and 1551 nm to determine the effect of Si content on the dispersion. We have fit the data in the range 1064 – 1551 nm using Cauchy's equation



Table 4.1 Results of a Cauchy's equation fit of the wavelength dependence of the index of refraction for several SRO samples.

Sample	X <sub>Si</sub>	n (1064 nm)	n (1307 nm)	n (1551 nm)	A	B x10 <sup>4</sup>	C x10 <sup>9</sup>
OX39	33	1.4476	1.4492	1.4427	1.4395	1.2972	-2.6880
OX44	34	1.5147	1.5116	1.5080	1.5012	1.8664	-3.5039
SRO17	34.4	1.5764	1.5727	1.5671	1.5583	2.4747	-4.0788
SRO25	35.4	1.6295	1.6256	1.6191	1.6096	2.6866	-3.9843
SRO27	38.4	1.6693	1.6630	1.6576	1.6463	2.9447	-3.5707
OX46	43	1.7584	1.7481	1.7466	1.7349	2.5592	0.18957
OX38	50	2.1522	2.1303	2.1124	2.0519	17.393	-68.372

$$n(\lambda) = A + \frac{B}{\lambda^2} + \frac{C}{\lambda^4} \quad (4.17)$$

to determine the coefficients A, B and C as a function of Si content. Table 4.1 summarizes the results of the data fitting.

The Cauchy equation for each sample allows us to calculate the material dispersion at 1535 nm which corresponds to the emission peak for Er in SRO and SiO<sub>2</sub>, an important wavelength for Si microphotonic systems. The results are shown in Figure 4.15.

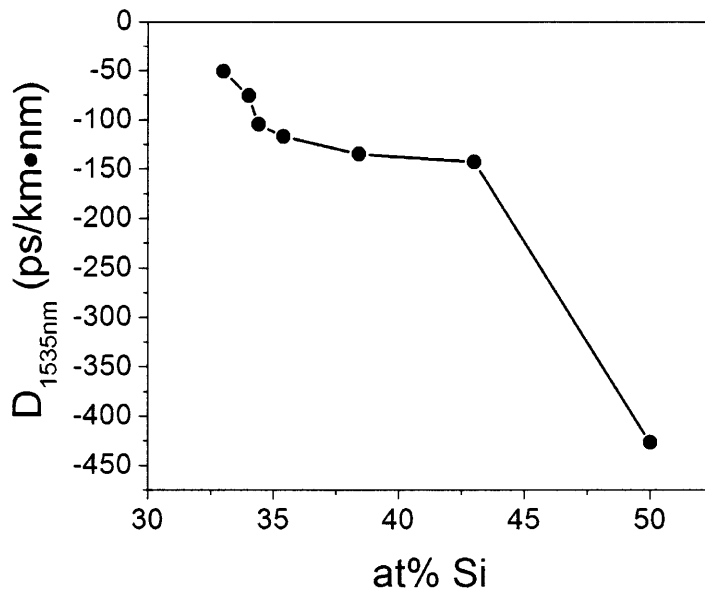


Figure 4.15 Material dispersion at 1535nm for SRO samples with different Si content calculated using equation 4.15 from the data listed in Table 4.1.

Based on the calculated dispersion at 1535 nm a pulse with a 1nm linewidth transmitted at 10 Gb/sec could propagate through an SRO waveguide with 38 at% for a length of 12 cm without distortion. Since the most likely application of SRO is for active devices which will have a length of approximately 1cm the material dispersion effect will be minimal. However, as the data rates are increased to > 100 Gb/sec these measurements will guide systems engineers as they design dispersion compensating structures for error-free data transmission.

# Chapter 5 | Photoluminescence

## Characterization of SRO, Er:SiO<sub>2</sub> and Er:SRO Films

In this chapter we will present our results on the photoluminescence characterization of thin films of SRO, Er:SiO<sub>2</sub> and Er:SRO. There are two goals of this chapter. The first is to discuss the emission sensitization process in Er:SRO films annealed at low temperatures in comparison to those annealed at high temperatures. The second is to measure several key parameters that will be used to model the SRO – Er energy-transfer process in Chapter 6.

### 5.1. Description of the Experimental Setup

Figure 5.1 shows a schematic diagram of the photoluminescence setup used for our characterization. Pump light from an Ar-ion laser was mechanically chopped and focused onto the sample. The photoluminescence from the sample is collected, collimated and focused onto a liquid nitrogen cooled Hamamatsu InGaAs photomultiplier tube through a monochromator. The signal from the photomultiplier tube was input into a lock-in amplifier, referenced to the chopper frequency, to measure the signal. Chopping frequencies between 10 and 40 Hz were used. To correct for the spectral response of the optics, grating in the monochromator and the detector the setup was calibrated using an Ando fiber-coupled white light source whose spectrum was measured by an Ando Optical Spectrum Analyzer. The normalized system response is shown in Figure 5.2. By dividing the measured spectra by the spectral response we could accurately characterize the spectral features of the photoluminescence of our samples. For brightly emitting samples spectra were also measured using the Ando Optical Spectrum Analyzer by coupling the emitted light into a fiber using a microscope objective and coupling the fiber to the spectrum analyzer. To perform time-resolved measurements the signal from the photomultiplier tube was input into an oscilloscope.

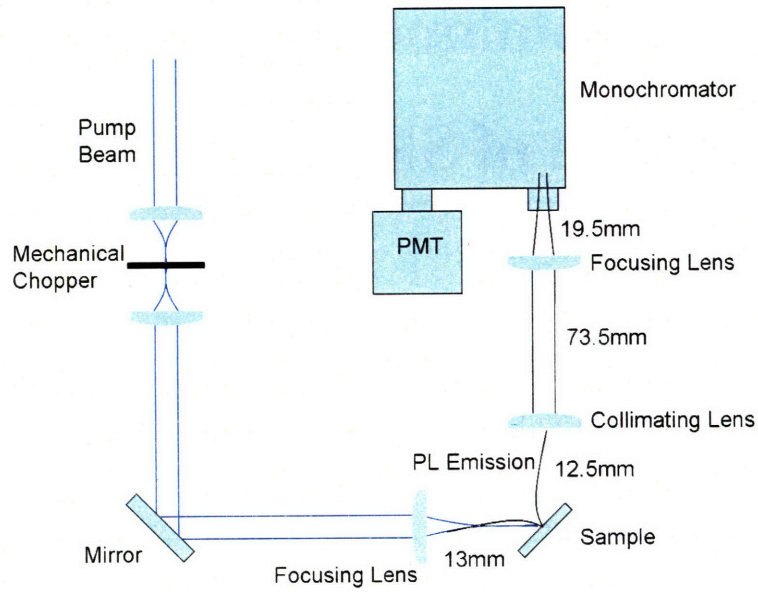


Figure 5.1 Schematic of the photoluminescence setup used for this study.

Low temperature photoluminescence measurements were performed between 10K and 295K using a continuous-flow liquid He cryostat with built-in heater.

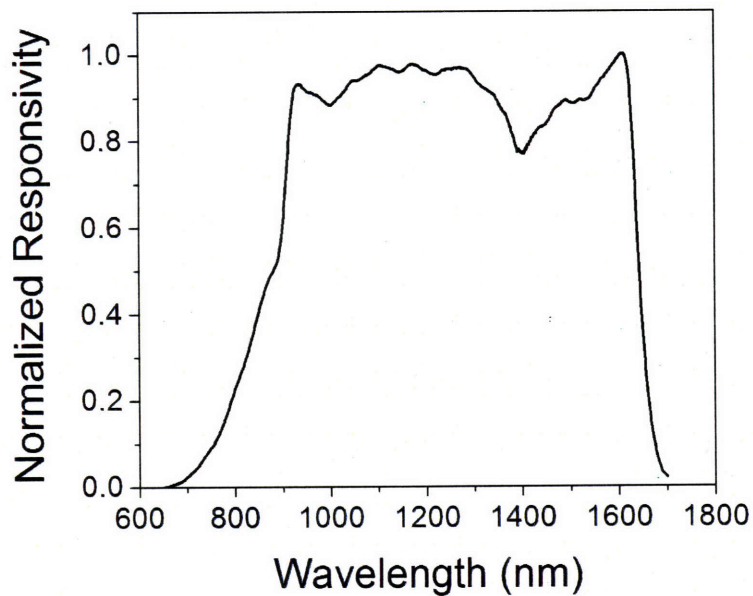


Figure 5.2 Normalized spectral response of the photoluminescence setup.

## 5.2. Photoluminescence Characterization of Undoped SRO Films

### 5.2.1. Photoluminescence Spectroscopy

Figure 5.3 shows the photoluminescence spectra for several SRO films with variable Si content annealed at 1100°C for 1 hour. The photoluminescence spectra appear in the visible resulting from the combined effect of quantum confinement and surface state mediated recombination, as proposed by several authors [86,87], due to the formation of nanometer sized Si crystals during the annealing process. The spectra are broad with a linewidth of approximately 135 nm. This broad spectrum, due to a combination of homogeneous broadening and inhomogeneous broadening from the size and shape distribution of typical nanocrystal ensembles, is in agreement with the literature [84]. The peak intensity and integrated intensity increases up to a Si content of 38 at% before decreasing for higher Si contents. Additionally the peak

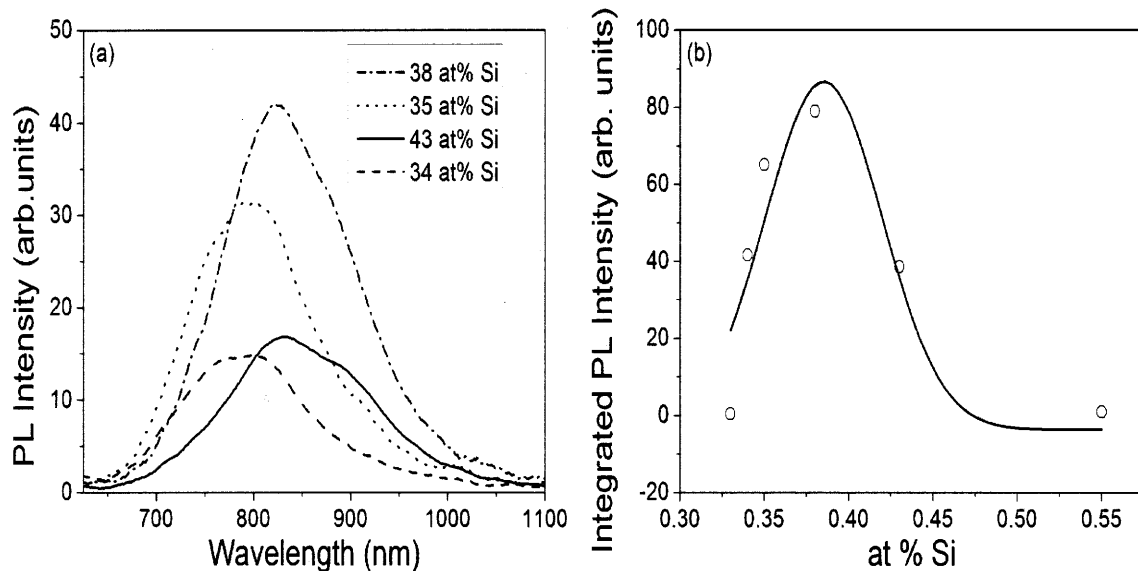


Figure 5.3 (a) Photoluminescence spectra for SRO films annealed at 1100°C for 1 hour with Si contents of 34 at%, 35 at%, 38 at% and 43 at%. The spectra were collected using an Ando Optical Spectrum Analyzer. (b) Integrated photoluminescence intensity for several SRO films with different Si content (open circles). The solid line is a Gaussian fit to the experimental data.

emission wavelength increases continuously with increasing Si content. The observed dependence of emission intensity and peak emission wavelength on the Si content of the film is attributed to the size of the Si nanocrystals formed for this fixed annealing condition. As the amount of Si is increased the Si nanocrystal size increases which leads to a red shift of the emission spectrum. Also, the quantum confinement is weaker for large sized Si nanocrystals which reduces their radiative efficiency and the photoluminescence intensity. The maximum emission observed for the sample with 38 at% is due to an optimization of the size and density of Si nanocrystals for this particular annealing condition.

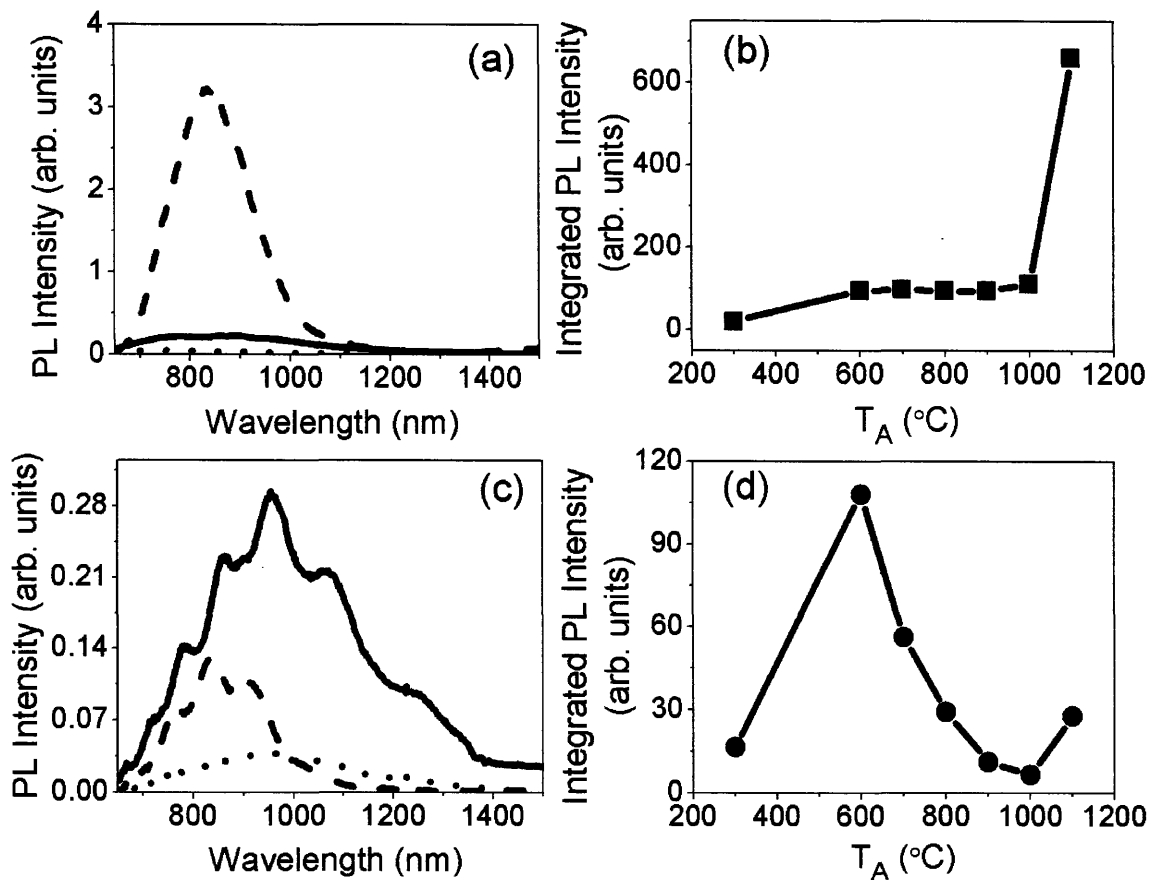


Figure 5.4 (a) Photoluminescence spectra for SRO films with 40 at% Si annealed at 300 °C (dotted line), 600 °C (solid line) and 1100 °C (dashed line). (b) Integrated photoluminescence intensity for SRO films with 40 at% Si versus annealing temperature. The photoluminescence was integrated between 652 – 1500 nm. (c) Photoluminescence spectra for SRO films with 50 at% Si annealed at 300 °C (dotted line), 600 °C (solid line) and 1100 °C (dashed line). (d) Integrated photoluminescence intensity for SRO films with 50 at% Si versus annealing temperature. The photoluminescence was integrated between 652 – 1500 nm.

We selected the Si content which yielded the maximum emission, 38 – 40 at% Si, and a much higher Si content sample of 50 at% Si and performed anneals for a fixed time of 1 hour and variable temperature and a fixed temperature of 1100°C for variable time to understand the influence of the annealing conditions on the photoluminescence intensity. The results for the annealing temperature dependent measurements are shown in Figure 5.4.

The PL spectra for both samples (Figure 5.4 (a) and (c)) is very broad at low annealing temperatures and becomes narrower as the annealing temperature is increased to 1100°C. For the sample with 40 at% Si the maximum integrated photoluminescence intensity is for the sample annealed at 1100°C which is consistent with the activation energy required to form Si nanocrystals [142]. For the sample with 50 at% Si there are two maxima in the integrated photoluminescence intensity versus annealing temperature, one at 600°C and one at 1100°C. The peak at 1100°C is attributed to the formation of nanocrystals and the enhancement of the radiative efficiency. The peak at 600°C is most likely due to structural rearrangements in the SRO matrix since we have determined that the expected diffusion length at that annealing temperature is negligible (see Figure 3.3). We also notice the relationship between the photoluminescence intensity and the birefringence discussed in Chapter 4. Comparing the evolution of the photoluminescence intensity with the birefringence we notice that the samples

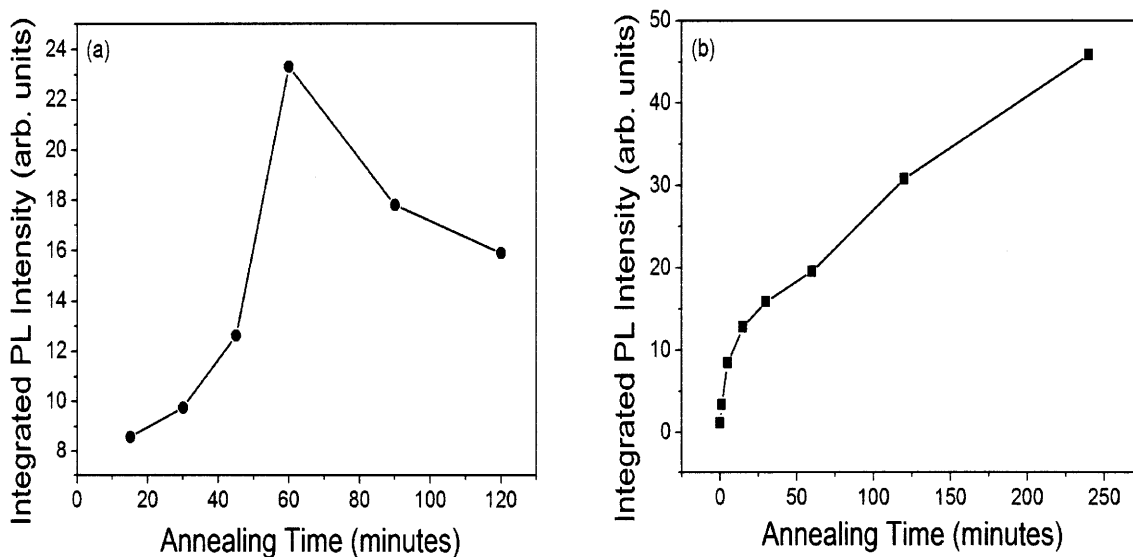


Figure 5.5 (a) Integrated PL intensity for samples with 38 at% Si annealed at 1100°C. (b) Integrated PL intensity for samples with 50 at% Si annealed at 1100°C.

with the highest photoluminescence intensity have the lowest birefringence and exhibit birefringence reduction upon annealing.

Figure 5.5 shows the integrated intensity versus annealing time at a fixed temperature of 1100°C. For the sample with 40 at% Si the integrated intensity increases to an annealing time of 1 hour before decreasing for longer annealing times. The increase in integrated intensity is due to an increase in the density of nanocrystals (number of nanocrystals per unit volume) while the decrease is most likely due to nanocrystal coarsening which increases the average size of the nanocrystals (decreases their radiative efficiency) and decreases the density of nanocrystals. In comparison the sample with 50 at% Si showed a nearly continuous increase in the integrated intensity as the annealing time increased which is not consistent with nanocrystal coarsening and is possibly due to a reduction in the number of non-radiative defects within the sample.

## 5.2.2. Time Resolved Photoluminescence

Next we performed time resolved photoluminescence to understand the dynamics of the emission process through an analysis of the emission lifetime and the excitation cross section. The excitation cross section is a measurement of the probability that a photon will be absorbed leading to the excitation of an electron from the ground-state to the excited-state and subsequent relaxation to the ground-state leading to the emission of a photon. In this analysis we consider the energy level diagram of the Si nanocrystal in Figure 5.6 where the transitions between electronic states in the nanocrystal are represented by the excitation cross section,  $\sigma_{ab}$  and the emission lifetime,  $\tau_{ba}$ , which is a combination of the radiative and non-radiative lifetimes.

At low pump powers several non-radiative paths leading to a saturation of the emission can be neglected. Under these conditions the nanocrystals are in the linear excitation regime. In this regime the rise time of the photoluminescence is related to the excitation cross section and emission lifetime according to the expression



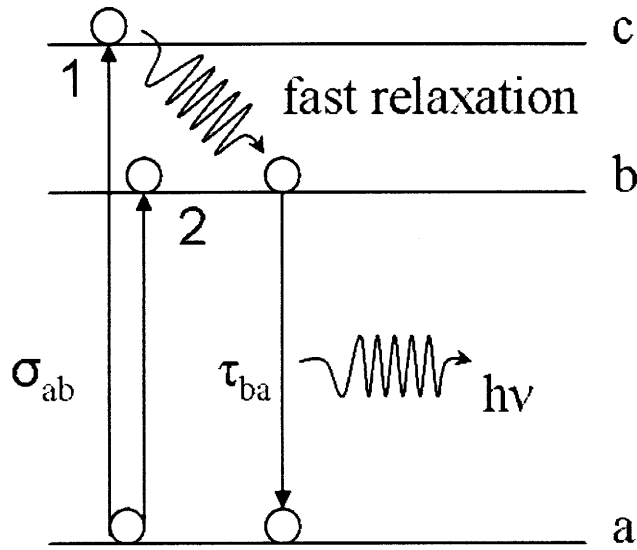


Figure 5.6 Schematic of the energy level diagram for the Si nanocrystal.

$$\frac{1}{\tau_{on}} = \sigma_{ab}\phi_p + \frac{1}{\tau_{ba}} \quad (5.1)$$

where  $\tau_{on}$  is the rise time of the photoluminescence and  $\phi_p$  is the pump-photon flux in units of photons/cm<sup>2</sup>s.

We measured the rise time for several pump-photon fluxes. The excitation cross section is measured from the slope of the inverse rise time versus pump-photon flux data while the inverse emission lifetime is measured from the intercept according to equation 5.1 as shown in Figure 5.7. Here the excitation cross section was measured to be  $1 \times 10^{-17}$  cm<sup>2</sup> and the lifetime was measured to be 80  $\mu$ s, both values consistent with measurements quoted in the literature for Si nanocrystal samples [83]. We also measured the lifetime of the same sample at a low pump power from the decaying edge of the photoluminescence as shown in Figure 5.8. The direct measurement of the photoluminescence decay yielded a value of  $70 \pm 10$   $\mu$ s for the in excellent agreement with the value obtained from the fit of the inverse rise time versus pump-photon flux data.

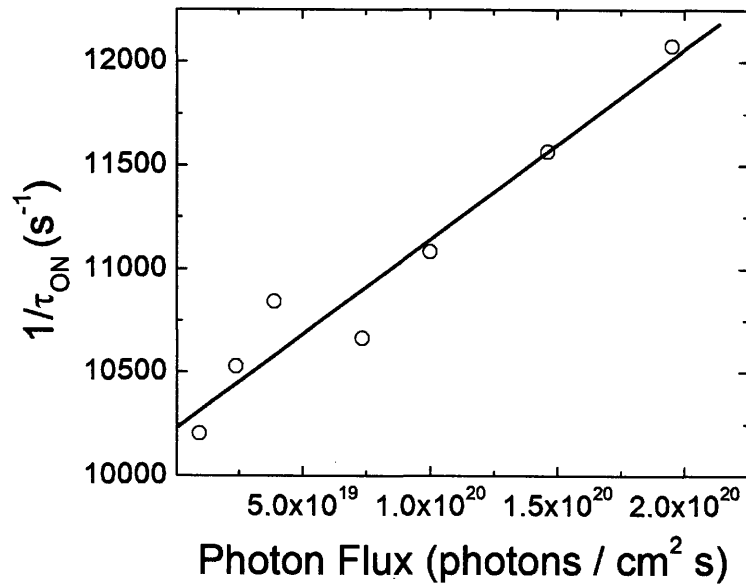


Figure 5.7 Inverse rise time versus pump-photon flux for a sample with 38 at% Si annealed at 1100°C for 1 hour with the detection wavelength set at 930 nm (open circles). The solid line is a linear fit to the data yielding an excitation cross section of  $1 \times 10^{-17} \text{ cm}^2$  and an emission lifetime of 80  $\mu\text{s}$ .

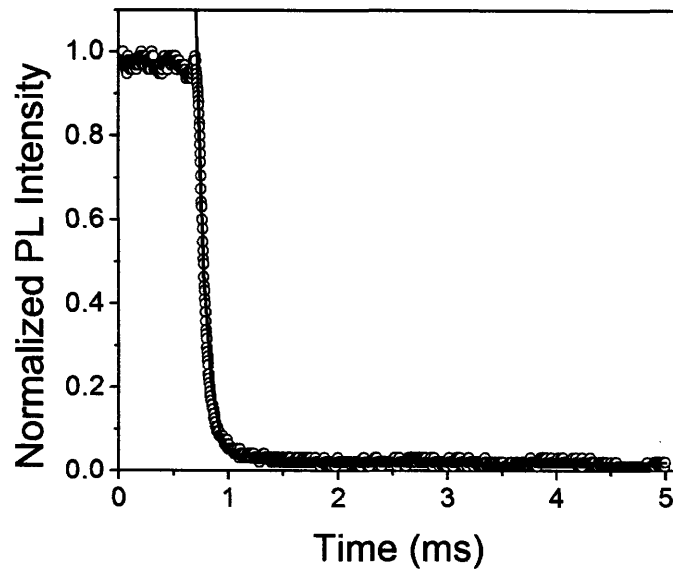


Figure 5.8 Photoluminescence decay for a SRO sample with 38 at% Si annealed at 1100°C for 1 hour measured with the detection wavelength set at 800 nm and a pump power of 10 mW (open circles). The line is an exponential decay fit to the data yielding an emission lifetime of 80  $\mu\text{s}$ .

### 5.2.3. Non-radiative Inter-site Upconversion in SRO

We have observed a non-radiative recombination process in SRO which causes the emitted intensity to saturate according to the square of the excited-state population of the SRO sensitizers. A schematic of this process is shown in Figure 5.9.

During the recombination process an electron in an excited sensitizer transfers its energy to an electron located in a nearby excited sensitizer. The electron in the second sensitizer is promoted to a higher state while the electron in the first sensitizer falls down to the ground-state. We will refer to this process as an inter-site upconversion process due to the similarity of this process with the well-known upconversion process in Er-doped glasses. Since this process involves two electrons it will depend on the square of the excited-state sensitizer population. We can write the time dependent excited-state population of the sensitizer by taking into account the excitation, decay and inter-site upconversion processes according the following expression

$$\frac{dn_b}{dt} = \sigma_{ab}n_a\phi_p - \tau_{ba}n_b - C_A n_b^2 \quad (5.2)$$

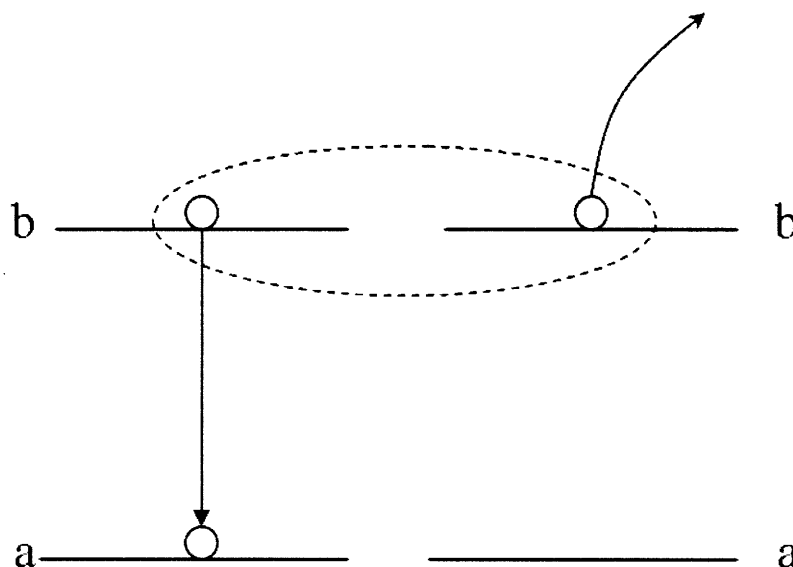


Figure 5.9 Schematic representation of the inter-site upconversion process between two coupled SRO sensitizers (or Si nanocrystals).

where  $n_a$  is the ground-state population and  $n_b$  is the excited-state population and  $C_A$  is the inter-site upconversion coefficient in units of  $\text{cm}^3\text{s}^{-1}$ . We can solve this differential equation in the steady-state  $\frac{dn_b}{dt} = 0$  with  $n_{\text{tot}} = n_a + n_b$  where  $n_{\text{tot}}$  is the total density of sensitizers. To determine the inter-site upconversion coefficient the steady-state photoluminescence was measured for various pump-photon fluxes and the data was simulated using equation 5.2. The results are shown in Figure 5.10 for a sample annealed at  $600^\circ\text{C}$ . As expected the data saturates quadratically due to the inter-site upconversion process with an inter-site upconversion coefficient of  $1 \times 10^{-13} \text{ cm}^3\text{s}^{-1}$ .

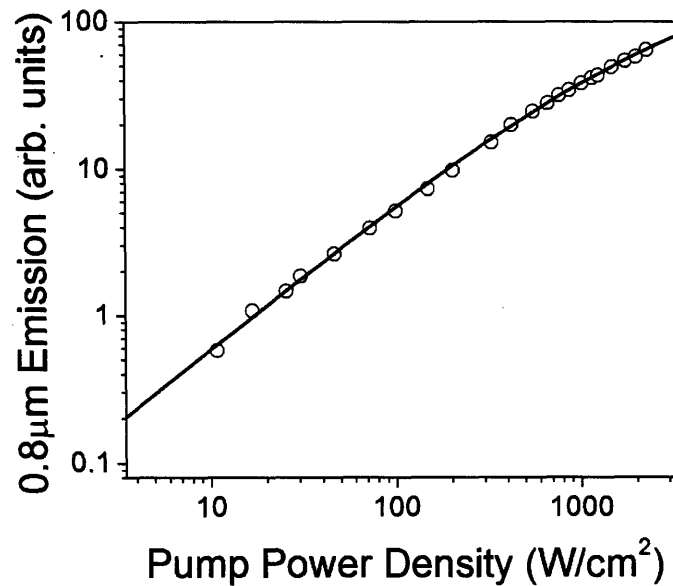


Figure 5.10 Steady-state photoluminescence for an SRO sample annealed at  $600^\circ\text{C}$  for 1 hour (open circles). The solid line is a simulation of the data with  $n_T = 6 \times 10^{18} \text{ cm}^{-3}$ ,  $\sigma_{\text{ab}} = 1.6 \times 10^{-17} \text{ cm}^2$  and  $C_A = 1 \times 10^{-13} \text{ cm}^3\text{s}^{-1}$ . The emission lifetime for this simulation was set to  $1 \mu\text{s}$  which is the resolution of our measurement system.

## 5.3. Photoluminescence Characterization of Er-doped SiO<sub>2</sub>

### 5.3.1. Photoluminescence Spectroscopy

Figure 5.11 (a) shows the typical PL spectrum of Er in SiO<sub>2</sub> with a primary maximum at 1535 nm and a secondary maximum at 1550 nm. We have investigated the Er emission as a function of the annealing temperature and the concentration of Er ions in SiO<sub>2</sub>. Figure 5.11 (b) shows the variation of Er peak emission intensity versus annealing temperature for samples with  $8.7 \times 10^{19}$  ions/cm<sup>3</sup>.

No emission was observed for annealing temperatures below 600°C with the maximum intensity achieved for annealing temperatures between 900°C and 1000°C. We also measured the Er emission for samples with variable Er content for a fixed annealing condition of 1000°C for 1 hour (Figure 5.12).

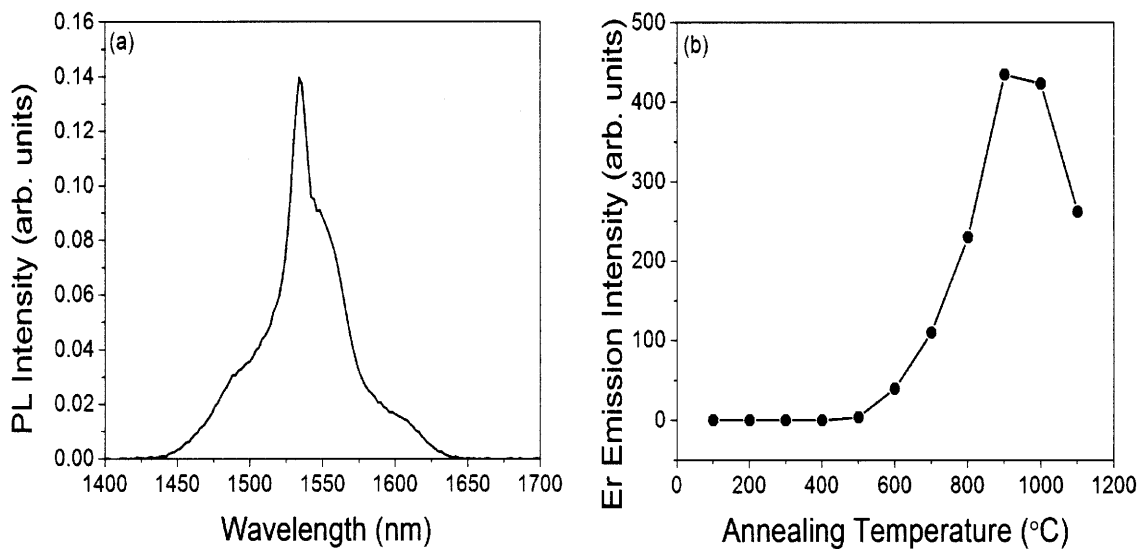


Figure 5.11 (a) Photoluminescence spectrum from an Er:SiO<sub>2</sub> sample with  $8.7 \times 10^{19}$  ions/cm<sup>3</sup> annealed at 1000°C for 1 hour. (b) Peak Er photoluminescence intensity for Er:SiO<sub>2</sub> samples with  $8.7 \times 10^{19}$  ions/cm<sup>3</sup> annealed for 1 hour at various temperatures.

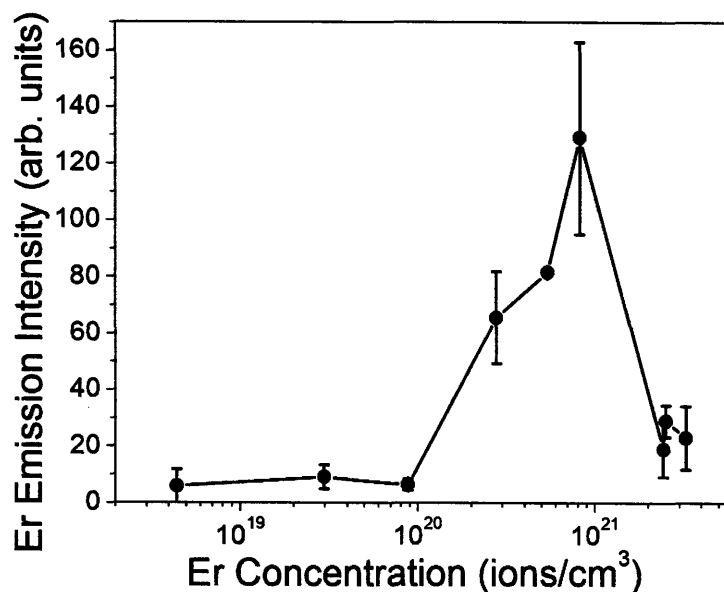


Figure 5.12 Er emission for samples annealed at 1000°C for 1 hour with variable Er concentration.

The emission intensity increases to a concentration of  $9 \times 10^{20} \text{ cm}^{-3}$  before decreasing for higher Er concentrations. For high concentrations the Er ions are closely spaced within the  $\text{SiO}_2$  matrix; excited Er ions can transfer their energy to nearby Er ions in the ground-state through dipole-dipole coupling. This energy migration process increases the chance of non-radiative

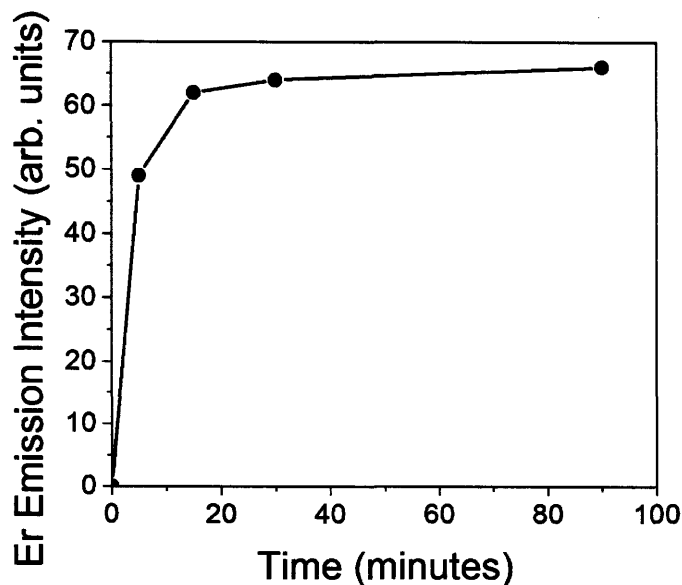


Figure 5.13 Er emission intensity at 1535nm for samples with an Er concentration of  $1 \times 10^{20} \text{ ions/cm}^3$  annealed at 1000°C for various times.

recombination by increasing the probability of coupling the excitation to an Er ion located near a defect site within the matrix. Since the dipole-dipole coupling decreases as the distance between the Er ions to the sixth power this process, called concentration quenching, is only active for high Er concentrations and is responsible for the decrease in the Er emission intensity [143]. We have chosen an Er concentration of  $1 \times 10^{20} \text{ cm}^{-3}$  for our experiments which is below this threshold for concentration quenching. Figure 5.13 shows the Er emission intensity for variable annealing times at a fixed annealing temperature of  $1000^\circ\text{C}$ . The results, shown in Figure 5.13, show that the emission saturates for annealing times greater than 30 minutes.

### 5.3.2. Time Resolved Photoluminescence

Similar to the analysis for annealed SRO samples we have measured the excitation cross section and emission lifetime for samples of Er in  $\text{SiO}_2$ .

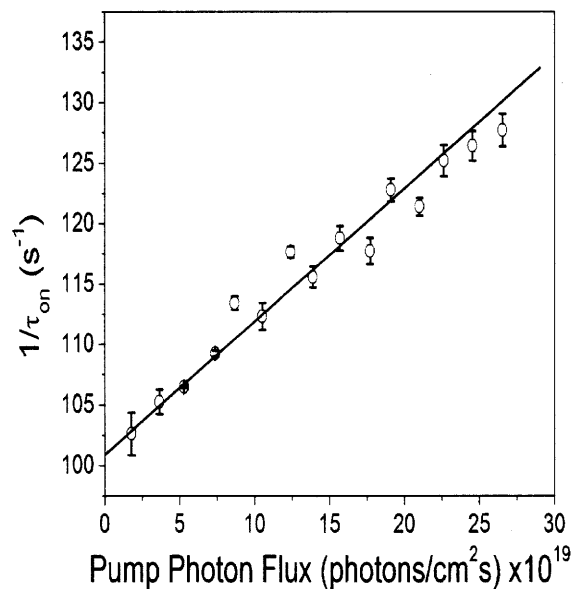


Figure 5.14 Inverse rise time versus pump-photon flux for a sample with an Er concentration of  $8.7 \times 10^{19} \text{ Er ions/cm}^{-3}$  annealed at  $1100^\circ\text{C}$  for 1 hour with the detection wavelength set at  $1535 \text{ nm}$  (open circles). The solid line is a linear fit to the data yielding an excitation cross section of  $1 \times 10^{19} \text{ cm}^2$  and an emission lifetime of  $9.9 \text{ ms}$ .

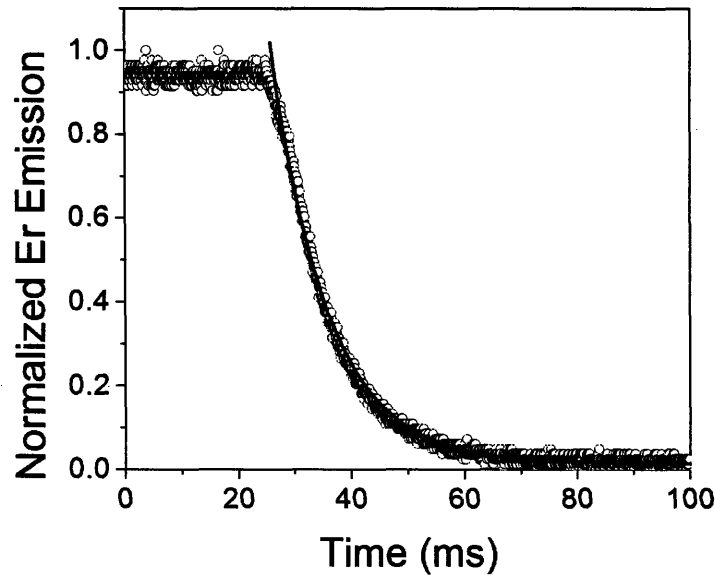


Figure 5.15 Photoluminescence decay for an Er:SiO<sub>2</sub> sample with an Er concentration of  $8.7 \times 10^{19}$  ions/cm<sup>3</sup> annealed at 1100°C for 1 hour measured with the detection wavelength set at 1535 nm and a pump power of 7.6 mW (open circles). The solid line is an exponential decay fit to the data yielding an emission lifetime of  $9.7 \pm 0.6$  ms.

We measured an excitation cross section for Er in SiO<sub>2</sub> of  $1 \times 10^{-19}$  cm<sup>2</sup> (Figure 5.14) which is consistent with measurements reported in the literature [51] and >100 times smaller than the cross section of SRO. Also, the analysis yielded an emission lifetime of 9.9 ms which is consistent with the lifetime of Er in several glass hosts [100]. This emission lifetime is also in excellent agreement with a direct measurement performed on the same sample which yielded a value of  $9.7 \pm 0.6$  ms (Figure 5.15).

### 5.3.3. Non-radiative Recombination through Upconversion

The dominant mechanism of non-radiative recombination which occurs in Er-doped devices is upconversion which is schematically depicted in Figure 5.16.

When two excited Er<sup>3+</sup> ions are located in close proximity one Er ion will transfer its energy to the other promoting the latter to an excited energy level and lowering the first Er ion to the



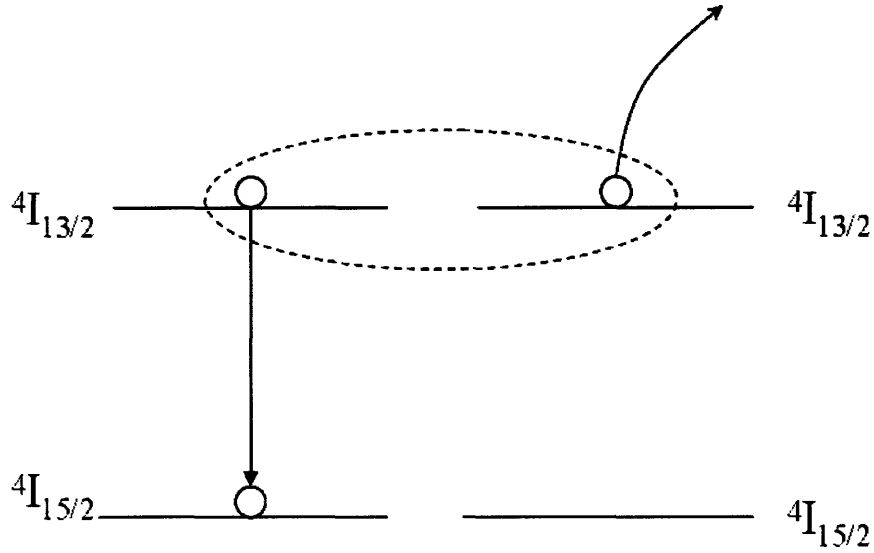


Figure 5.16 Schematic of the upconversion process between two excited  $\text{Er}^{3+}$  ions.

ground-state. The excited Er ion will typically emit from the  ${}^4\text{I}_{11/2}$  level leading to 980 nm light emission. If two or more excited Er ions simultaneously transfer their energy to another excited Er the process is known as cooperative upconversion with an emission in the visible.

The upconversion depends on the square of the excited-state Er population. We can write the time dependent excited-state population of the Er taking into account the excitation, radiative decay and upconversion processes according the following expression

$$\frac{dN_2}{dt} = \sigma N_2 \phi_p - \alpha N_2 - C_{UP} N_2^2 \quad (5.3)$$

where  $N_1$  is the ground-state population and  $N_2$  is the excited-state population and  $C_{UP}$  is the Upconversion coefficient in units of  $\text{cm}^3\text{s}^{-1}$ . We can solve this differential equation in the steady-state  $\frac{dN_2}{dt} = 0$  with  $N_T = N_1 + N_2$  and  $N_T$  equal to the total concentration of Er ions. To determine the upconversion coefficient the steady-state photoluminescence was measured for various pump-photon fluxes and the data was simulated using equation 5.3. The results are shown in Figure 5.17 for a sample annealed at 1100°C.

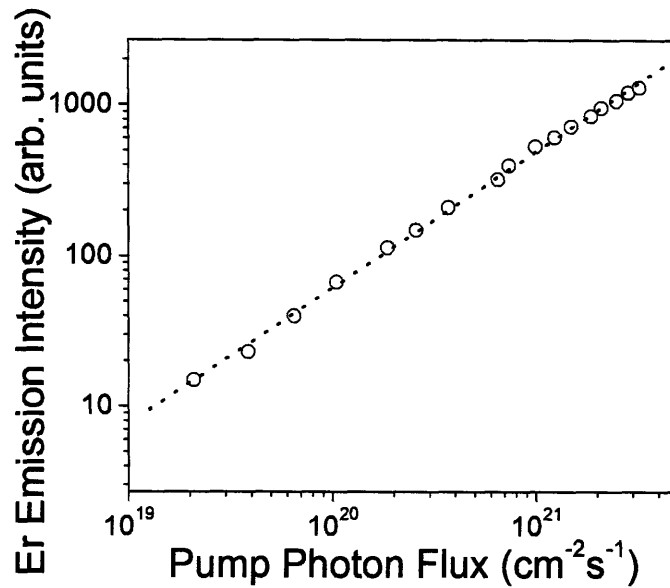


Figure 5.17 Er emission intensity at 1535nm versus 488 nm pump-photon flux from a reference Er in SiO<sub>2</sub> sample with an Er concentration of  $8.7 \times 10^{19}$  ions/cm<sup>3</sup> annealed at 1100°C (open circles). The dot line is a linear fit of the data.

We notice in Figure 5.17 that the data increases linearly with no evidence of quadratic saturation within the powers considered for this experiment and no evidence of upconversion.

## 5.4. Photoluminescence Characterization of Er-doped SRO

### 5.4.1. Photoluminescence Spectroscopy

Having investigated the emission properties of SRO and Er independently we now consider how the light emitting properties of each are influenced by combining the two approaches. In Figure 5.18 we show the emission spectra for SRO and Er:SiO<sub>2</sub> annealed at 1100°C and an Er:SRO sample annealed at 600°C and 1100°C.

We notice from Figure 5.18 that when Er is added to SRO annealed at 1100°C the Er emission is enhanced while the Si nanocrystal emission is decreased due to the energy-transfer process.

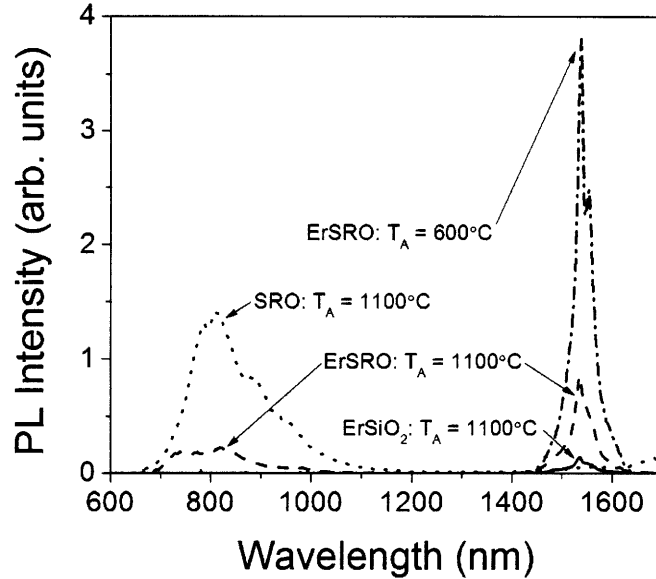


Figure 5.18 Room temperature photoluminescence versus wavelength for a Si-nc in SiO<sub>2</sub> sample with 38 at% Si annealed at 1100 °C (dot line), for an Er in SRO sample with 38 at% Si and Er concentration of  $8.2 \times 10^{19} \text{ cm}^{-3}$  annealed at 1100 °C (dash line) for an Er in SRO sample with 38 at% Si and Er concentration of  $8.2 \times 10^{19} \text{ cm}^{-3}$  annealed at 600 °C (dash - dot line) and an Er in SiO<sub>2</sub> sample with an Er concentration of  $8.7 \times 10^{19} \text{ cm}^{-3}$  annealed at 1100 °C (solid line).

Since the energy-transfer time is faster than the emission lifetime of the nanocrystal (~100ns compared to the emission lifetime of 100μs) the energy-transfer process is the preferred decay path for an excited nanocrystal. Another consequence of the fast energy-transfer time compared to the short emission lifetime of Er is the possibility of exciting more than one Er ion via energy-transfer from a single nanocrystal within a single Er ion decay time. When the Er:SRO sample is annealed at 600°C we notice that the Er emission is strongly enhanced while the nanocluster emission is completely quenched. We have compared the emission intensity for Er:SRO and Er:SiO<sub>2</sub> samples annealed at various temperatures to determine the optimum annealing temperature for both matrixes (Figure 5.19).

From the comparison of the Er:SRO emission peak intensity (Figure 5.19 (a), circles) and the emission of the reference Er:SiO<sub>2</sub> sample (Fig. 5.19 (a), squares) over a wide range of annealing temperatures we notice that the strongest sensitized Er emission occurred for an annealing temperature of 700°C which is 300°C lower than the optimized annealing temperature for the reference Er:SiO<sub>2</sub> sample and 400°C lower than the optimum annealing temperature for Si nanocrystal emission. The plot of emission enhancement (ratio of Er:SRO to Er:SiO<sub>2</sub> emission,

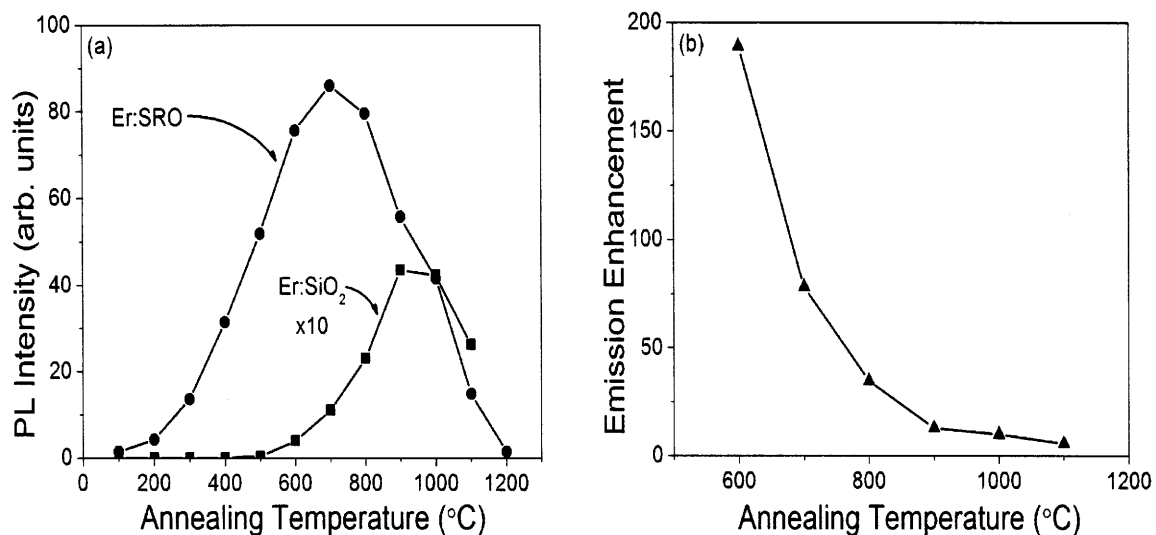


Figure 5.19 (a) RT Er emission versus annealing temperature for Er:SRO samples with thickness  $\sim 1.85 \mu\text{m}$ , 38 at % Si and Er concentration of  $8.2 \times 10^{19} \text{cm}^{-3}$  (circles) and reference Er in  $\text{SiO}_2$  samples with thickness  $\sim 1.24 \mu\text{m}$  and an Er concentration of  $8.7 \times 10^{19} \text{cm}^{-3}$  (squares, magnified by 10). The PL intensity has been scaled to account for the difference in sample thickness. (b) Emission enhancement (where the enhancement is equal to the ratio of the Er:SRO  $1.54 \mu\text{m}$  PL intensity to the PL intensity of the reference Er in  $\text{SiO}_2$  samples) versus annealing temperature (triangles).

Figure 5.19 (b)) shows that an enhancement of up to 200x can be achieved for an annealing temperature of  $600^\circ\text{C}$  as opposed to a 6x enhancement for the higher annealing temperature of  $1100^\circ\text{C}$ . We emphasize that the optimized Er:SRO emission intensity observed in the temperature range  $600 - 700^\circ\text{C}$  is not correlated with the formation of Si nanocrystals in the SRO matrix, as no evidence of observable cluster formation was found by energy filtered TEM analysis (Figure 3.10 (b) and (d)). This enhancement of the Er:SRO emission for annealing temperatures below the temperature for Si nanocrystal formation has been demonstrated by other authors [41,55,56] and has significant implications for understanding the energy-transfer process. To determine if the Er ions are still being excited through energy-transfer from the SRO matrix in the absence of Si nanocrystals we have performed photoluminescence spectroscopy under resonant and non-resonant conditions using pump wavelengths of 488 nm (resonant with the  $^4\text{F}_{7/2}$  energy level of Er) and 457 nm (not resonant with any Er energy levels but within the SRO absorption band). In Figure 5.20 we show the results of this experiment for an Er:SRO sample annealed at  $600^\circ\text{C}$  and a reference Er:SiO<sub>2</sub> sample annealed at  $600^\circ\text{C}$ . We have chosen the annealing temperature of  $600^\circ\text{C}$  for our detailed analysis for two reasons: (1) compatibility with

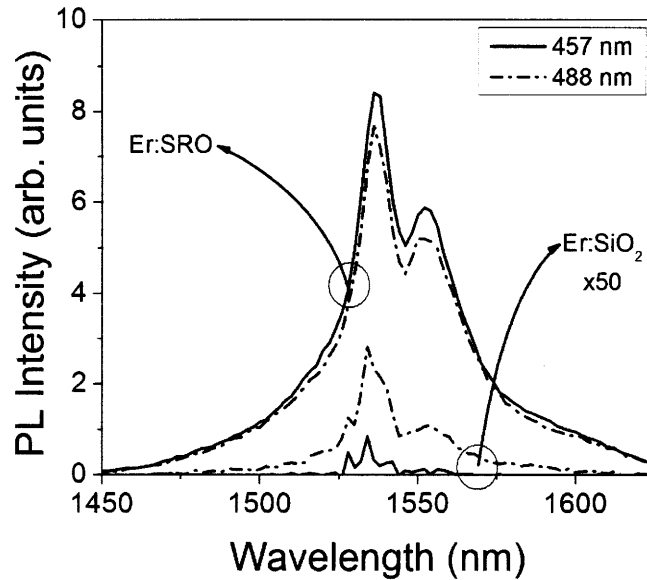


Figure 5.20 Photoluminescence spectra under resonant (488 nm, dash-dot line) and non-resonant (457 nm, solid line) pumping conditions for an Er:SRO sample with 38 at% Si and an Er concentration of  $8.2 \times 10^{19}$  ions/cm<sup>3</sup> and an Er:SiO<sub>2</sub> sample with an Er concentration of  $8.7 \times 10^{19}$  ions/cm<sup>3</sup> magnified by 50. The intensities have been scaled to account for different sample thicknesses.

CMOS processing limits the thermal budget for processing making the lowest annealing temperatures the most attractive for integration and (2) the negligible emission of Er:SiO<sub>2</sub> samples for annealing temperatures lower than 600°C prevents a direct comparison between the emission properties.

From Figure 5.20 we see that the Er is efficiently excited in SRO under both resonant and non-resonant excitation with the slight difference in emission intensity due to the increase of the SRO absorption coefficient between 457 nm and 488 nm. On the other hand, the Er in SiO<sub>2</sub> is only excited under resonant conditions with negligible emission measured under non-resonant conditions. This is direct evidence that the Er excitation is mediated by the SRO matrix for annealing temperatures as low as 600°C.

The annealing temperatures influences the Er:SRO lineshape as shown in Figure 5.21 (a). The variation in the width of the Er emission peak is determined by inhomogeneous broadening which accounts for the variation in the local environment surrounding each Er ion in the SRO matrix. We have shown that Er:SRO samples annealed at 600°C have a narrower linewidth

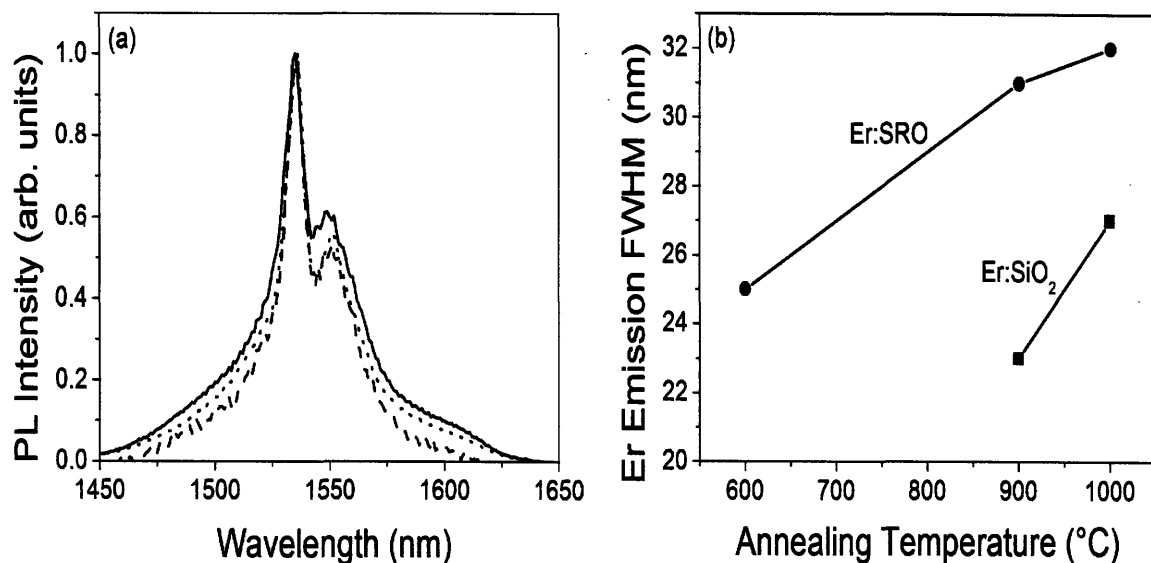


Figure 5.21 (a) Room temperature photoluminescence versus wavelength for an Er in SiO<sub>2</sub> sample with an Er concentration of  $8.7 \times 10^{19}$  ions/cm<sup>3</sup> annealed at 900 °C (dash line), Er in SRO sample with 38 at% Si and Er concentration of  $8.2 \times 10^{19}$  ions/cm<sup>3</sup> annealed at 900 °C (solid line) and Er in SRO sample with 38 at% Si and Er concentration of  $8.2 \times 10^{19}$  ions/cm<sup>3</sup> annealed at 600 °C (dot line). (b) Er emission full width half maximum for Er in SRO samples with an Er concentration of  $8.2 \times 10^{19}$  ions/cm<sup>3</sup> (solid circles) and Er in SiO<sub>2</sub> samples with an Er concentration of  $8.7 \times 10^{19}$  ions/cm<sup>3</sup> (solid squares).

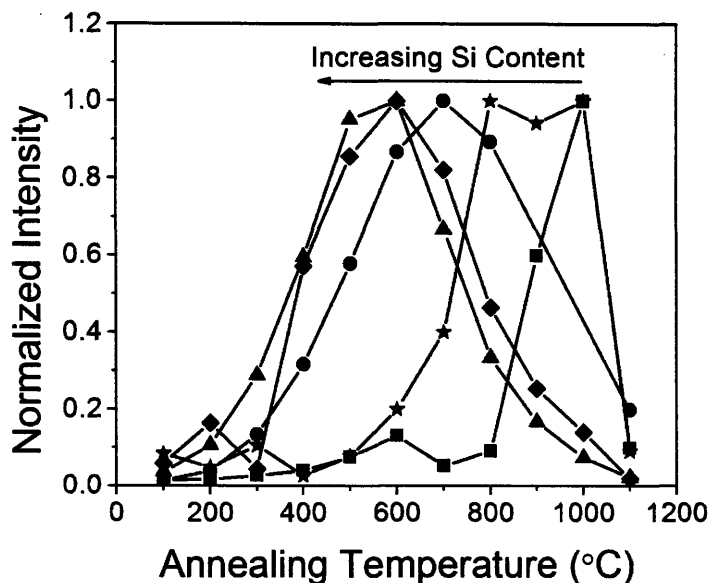


Figure 5.22 Normalized Er emission intensity at 1535nm from Er:SRO samples annealed for 1 hour at various temperatures with the following Er and Si contents: 33 at% Si and an Er concentration of  $8.2 \times 10^{20}$  ions/cm<sup>3</sup> (squares), 35 at% Si and an Er concentration of  $6.2 \times 10^{20}$  ions/cm<sup>3</sup> (stars), 38 at% Si and an Er concentration of  $7.9 \times 10^{19}$  ions/cm<sup>3</sup> (circles), 41 at% Si and an Er concentration of  $7.7 \times 10^{20}$  ions/cm<sup>3</sup> (diamonds) and 53 at% Si and an Er concentration of  $1.1 \times 10^{21}$  ions/cm<sup>3</sup> (triangles).

indicating a more uniform and more favorable local environment of Er which is comparable to Er in SiO<sub>2</sub> annealed at higher temperatures (Figure 5.21 (b)).

Finally we have performed measurements of the Er emission versus annealing temperature for SRO samples with variable Si content. The normalized emission intensities from this experiment are shown in Figure 5.22. We notice that the annealing temperature which maximizes the Er emission intensity decreases as the Si content of the film increases before becoming fixed at 600°C for Si contents greater than 40 at% Si.

## 5.4.2. Time Resolved Photoluminescence

In order to quantify the efficiency of the energy-transfer process from SRO to Er we have performed excitation cross section measurements for annealing temperatures of 600°C and

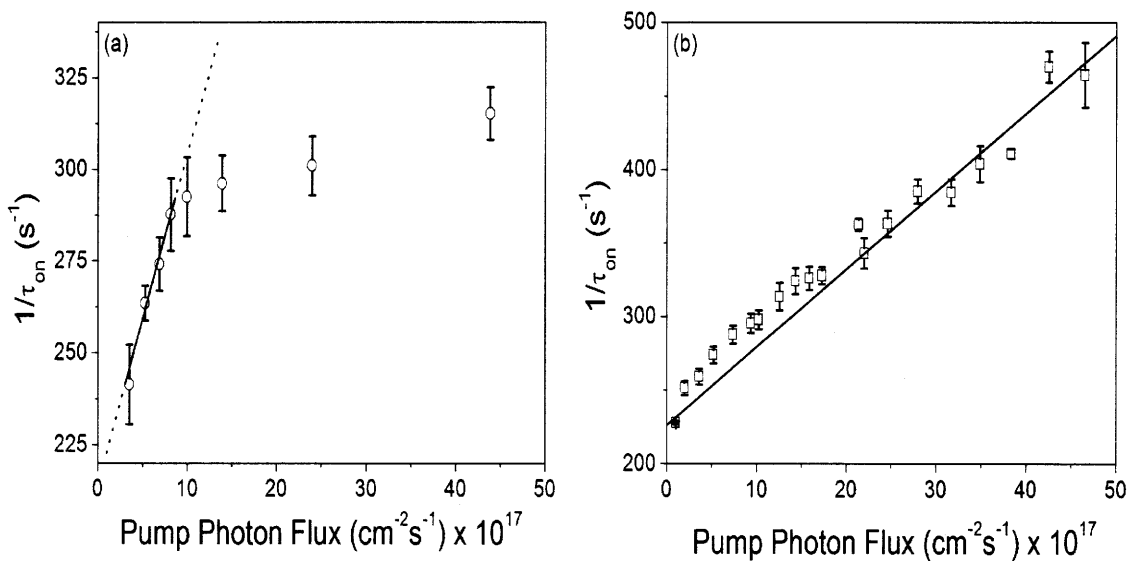


Figure 5.23 (a) Er emission inverse rise time versus pumping photon flux at 488 nm for the Er:SRO sample annealed at 600°C with 38 at% Si and an Er concentration of  $8.2 \times 10^{19}$  ions/cm<sup>3</sup>. The solid line is a linear fit yielding an excitation cross section of  $\sigma_{exc} = 9.05 \times 10^{-17}$  cm<sup>2</sup>. (b) Er emission inverse rise time versus pumping photon flux at 488 nm for the Er:SRO sample annealed at 1100°C with 38 at% Si and an Er concentration of  $8.2 \times 10^{19}$  ions/cm<sup>3</sup>. The solid line is a linear fit yielding an excitation cross section of  $\sigma_{exc} = 5.30 \times 10^{-17}$  cm<sup>2</sup>.

1100°C for comparison with the results shown in the previous sections.

Our analysis of the inverse rise time versus pump-photon flux data resulted in the measured excitation cross section of  $9.05 \times 10^{-17} \text{ cm}^2$  and  $5.3 \times 10^{-17} \text{ cm}^2$  for 600°C and 1100°C annealing respectively. For both annealing temperatures the Er:SRO excitation cross section is comparable to that measured for Si nanocrystal emission and  $\sim 1000\times$  stronger than the excitation cross section for Er:SiO<sub>2</sub>. A factor of 2 enhancement of the excitation cross section was observed for the sample annealed at 600°C compared to the sample annealed at 1100°C. This slightly stronger excitation efficiency for the sample annealed at 600°C triggers a stronger upconversion for high pump-photon fluxes which limits the linear excitation regime to fluxes  $< 10^{17} \text{ cm}^{-2}\text{s}^{-1}$ , as shown in Fig. 5.23 (a) by the saturation of the PL rise-rate versus photon flux. In the same pumping regime, a linear response is observed for the sample annealed at 1100°C (Fig. 5.23 (b)). The analysis of the excitation cross section also yields measurements of the emission lifetime of Er in these two samples of 4.67 ms and 4.42 ms for annealing temperatures of 600°C and 1100°C respectively. The nearly constant Er emission lifetime with annealing temperature has been confirmed through direct measurements as shown in Figure 5.24.

Our results demonstrate that the Er emission lifetime in the annealing temperature range 600 – 1100°C (Fig. 5.24) is almost constant (3 – 4 ms), even though the sensitized Er emission is maximized for annealing temperatures around 600 – 700°C, as shown in Fig. 5.19 (a). This behavior indicates that the maximum PL intensity of Er:SRO samples annealed at 600 – 700°C results from a more efficient SRO-mediated energy-transfer rate, as opposed to an improved emission efficiency of the Er ions.



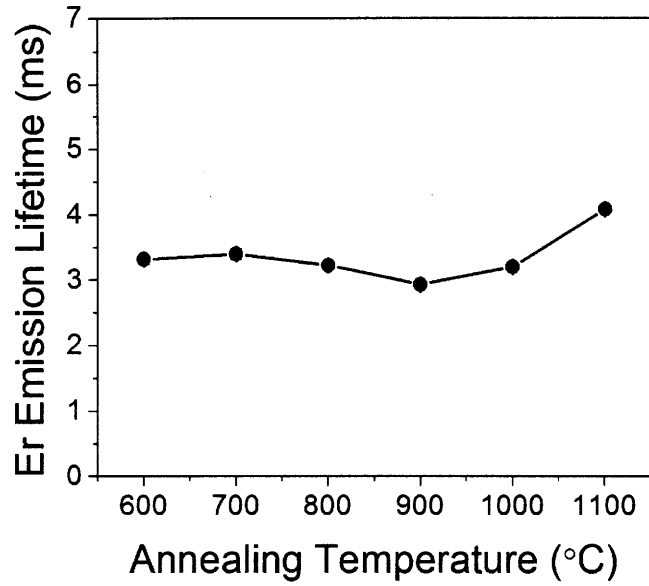


Figure 5.24 Room temperature Er photoluminescence lifetime for an Er:SRO sample with 38at% Si and an Er concentration of  $8.2 \times 10^{19}$  ions/cm<sup>3</sup> annealed at various temperatures for 1 hour.

### 5.4.3. Non-radiative Recombination through Upconversion

We have also analyzed the upconversion process in Er-doped SRO where we expect the enhanced excitation efficiency over Er-doped SiO<sub>2</sub> to play a role in the onset of the upconversion. Figure 5.25 shows a measurement of the steady-state Er emission versus pump-photon flux.

While the emission from the Er:SiO<sub>2</sub> sample is linear within the range of pump-photon fluxes considered in the experiment the emission from the Er:SRO sample saturates quadratically at high pump powers consistent with SRO mediated upconversion process. The role of SRO in the upconversion process is to enhance the excitation efficiency leading to a larger excited-state population of Er which leads to upconversion in agreement with the measurements shown in Figure 5.25.

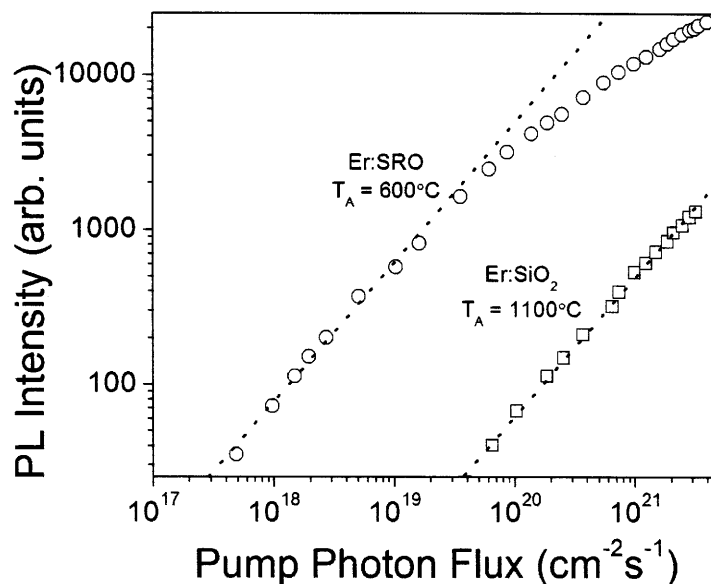


Figure 5.25 Er emission intensity at 1535nm versus 488nm pump-photon flux from a reference Er in SiO<sub>2</sub> sample with an Er concentration of  $8.7 \times 10^{19}$  ions/cm<sup>3</sup> annealed at 1100°C for 1 hour (open squares) and an Er in SRO sample with 38 at% Si and an Er concentration of  $8.2 \times 10^{19}$  ions/cm<sup>3</sup> annealed at 600°C for 1 hour (open circles). The dot line is a linear fit of the data for the reference Er in SiO<sub>2</sub> sample which has been superimposed on the low photon flux data for the Er in SRO sample for comparison.

## 5.5. Low Temperature Photoluminescence Spectroscopy of SRO and Er-doped SRO

In order to clarify the origin of the enhanced energy-transfer mechanism in the Er:SRO films annealed at low temperatures we have studied the temperature dependence of the PL emission of SRO and Er:SRO samples annealed at 600°C and 1100°C deposited under identical conditions. The results of the study are summarized in Figure 5.26.

Fig. 5.26 (a) shows the PL spectra for an SRO sample annealed at 1100 °C for three different measurement temperatures (10 K solid line, 125 K dash line, and 295 K dot line). The PL spectrum obtained at room temperature is identical to those shown in Section 5.3 (a) with a broad Si nanocrystal emission band located in the near infrared. For the sample annealed at high temperatures we also observed an additional, broad band near 1.3 μm at cryogenic temperatures

that we attribute to localized centers in the oxide matrix (144,145,146). This additional band is absent in the sample annealed at low temperature.

The integrated SRO PL intensity for the sample annealed at 1100°C (Figure 3 (c), without considering the localized-center related band) increases for temperatures above 10K, peaks at 125K and decreases for temperatures up to room temperature. This particular temperature dependence is attributed to the singlet/triplet exciton splitting within the Si nanocrystal and the relative populations of singlet and triplet states versus annealing temperatures which was first proposed by Calcott [147,148,149] and experimentally verified by Brongersma *et al.* [150]. For the SRO sample annealed at 600°C we observe a broad and featureless band for all temperatures which is lower in magnitude than the emission from the sample at 1100°C despite the fact that the pump-photon flux is almost 2x larger for the 600°C sample. It should be noted that these featureless and broad spectra are inconsistent with the spectral features typically attributed to Si nanocrystals, which, along with their weak intensity, is evidence that the emission for samples annealed at 600°C is not associated with radiative recombination of Si nanocrystals. The measured PL temperature dependence also shows a typical defect ionization trend for low temperature annealed samples (Fig. 3 (c), circles). This observed temperature dependence suggests, that the weak and broad emission of the low temperature annealed SRO samples originates from localized centers in the SRO matrix. In Fig. 5.26 (d) we show the Er:SRO emission at 1535 nm for samples annealed at 1100°C (squares) and at 600°C (circles). The temperature trends of the PL data follow exactly the behavior shown in Fig. 5.26 (c) for SRO samples without Er which is additional confirmation that Er is sensitized through the SRO matrix. The different temperature dependence of the SRO emission demonstrates that the different energy-transfer efficiencies measured through the excitation cross section and enhancement of the Er emission intensity for samples at low annealing temperatures result from two different emission sensitizers depending on the presence or absence of Si nanocrystals. For samples annealed at high temperatures, despite the presence of the band at 1.3  $\mu\text{m}$ , the temperature dependence of the Er emission follows the Si nanocrystal emission temperature dependence suggesting that the energy-transfer is related to dipole coupling from Si nanocrystals to Er ions. The energy-transfer process for low temperature annealed samples is more efficient and also differs from the Si nanocrystal transfer process since its efficiency is not proportional to the

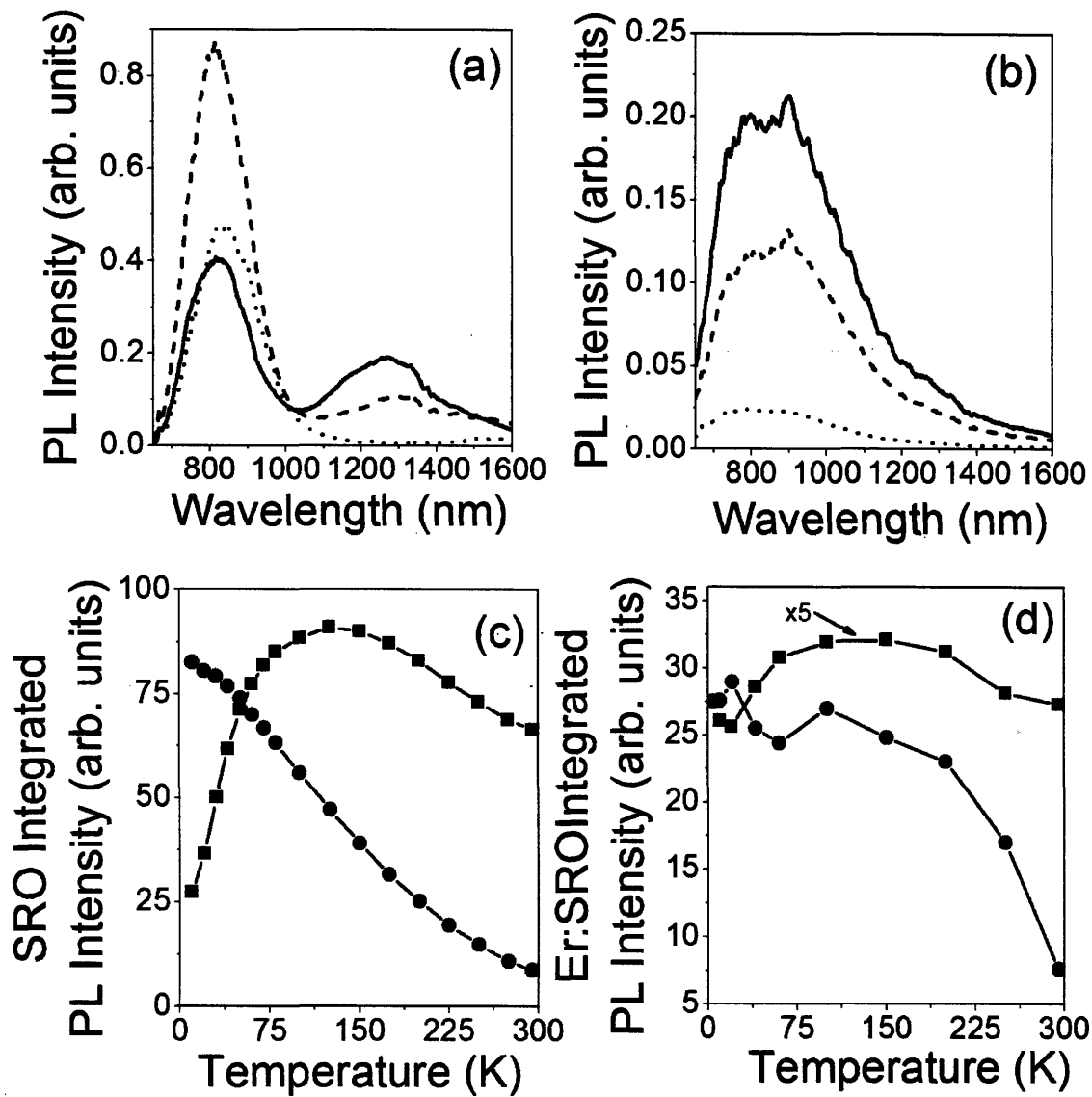


Figure 5.26 (a) PL emission for the high temperature annealed (1100 °C) sample at 10 K (solid line), 125 K (dash line) and 295 K (dot line) pumping with 488 nm light at a pump power of 58 mW. (b) PL emission for the low temperature annealed (600 °C) sample at 10 K (solid line), 125 K (dash line) and 295 K (dot line) pumping with 488 nm light at a pump power of 98 mW. (c) Integrated PL intensity for a SRO sample with 38 at% Si annealed at 1100 °C (solid squares) and an SRO sample with 38 at% Si annealed at 600 °C (solid circles) versus temperature. The PL for the sample annealed at 1100 °C was integrated from 652 – 1000 nm while the PL for the sample annealed at 600 °C was integrated from 652 – 1600 nm. (d) Integrated PL intensity for an Er in SRO sample with 38 at% Si and an Er concentration of  $1.08 \times 10^{20} \text{ cm}^{-3}$  annealed at 1100 °C (solid squares) and an Er in SRO sample with 38 at% Si and an Er concentration of  $1.08 \times 10^{20} \text{ cm}^{-3}$  annealed at 600 °C (solid circles) versus temperature. The PL for both samples was integrated from 1400 – 1600 nm.

radiative efficiency of the donor (SRO). Although the exact nature of this energy-transfer process is unknown we suggest that localized centers in the SRO matrix can act as efficient sensitizers for the emission of Er:SRO samples annealed at 600°C. Further studies will need to be performed to determine the detailed nature of the sensitization process and develop a microscopic structural model of the sensitizing center.

## 5.6. Gamma Irradiation Effects on SRO and Er Light Emission

We have also studied the response of Er-doped SiO<sub>2</sub> and Er-doped SRO after gamma irradiation to determine the applicability of Er-doped SRO based devices for applications that require radiation hardness. It has been demonstrated that the effects of gamma irradiation are comparable to the effects of energetic protons found in outer space [151]. The typical degradation of the performance of erbium-doped fiber amplifiers has been attributed to the generation of defects which absorb in the range of the 980 nm pump signal. The effect of irradiation with ionizing species on the optical properties of vitreous silica has been studied extensively [152,153]. It has been shown that the effect of gamma radiation is closely tied to the type and density of defect precursors that exist in the silica matrix prior to irradiation [152]. ESR measurements performed on SRO samples have revealed the presence of several paramagnetic defects within the SRO matrix [144] which could lead to enhanced radiation induced effects influencing the energy-transfer process to Er ions. We have performed a study of the effect of gamma radiation on the emission of Er from SiO<sub>2</sub> and SRO annealed at various temperatures. Gamma irradiation was performed in a Co<sup>60</sup> cell at doses of 0.5, 1, 5 and 10 Mrads. A control for each group of samples was not exposed to gamma radiation. Figure 5.27 shows the integrated Er emission intensity for samples considered in this study.

We notice for all the samples the Er emission intensity decreases with increasing dose saturating for doses greater than 5 Mrads. We fit the experimental data with an exponentially decaying function in the dose in order to obtain an estimate of the decay rate for each sample. The fitting results demonstrate that the Er:SiO<sub>2</sub> sample annealed at 1000°C and the Er:SRO unannealed sample have the highest decay rate. It is interesting to note that the Er:SRO sample annealed at 600°C has an approximately 10 times lower decay rate than all other samples. Although further studies will be needed to confirm the repeatability of the gamma radiation induced reduction of the Er emission intensity and identify the origin of the degradation in Er emission this result suggests a route to achieving more radiation hard Er-doped light sources based on low temperature annealed Er-doped SRO.

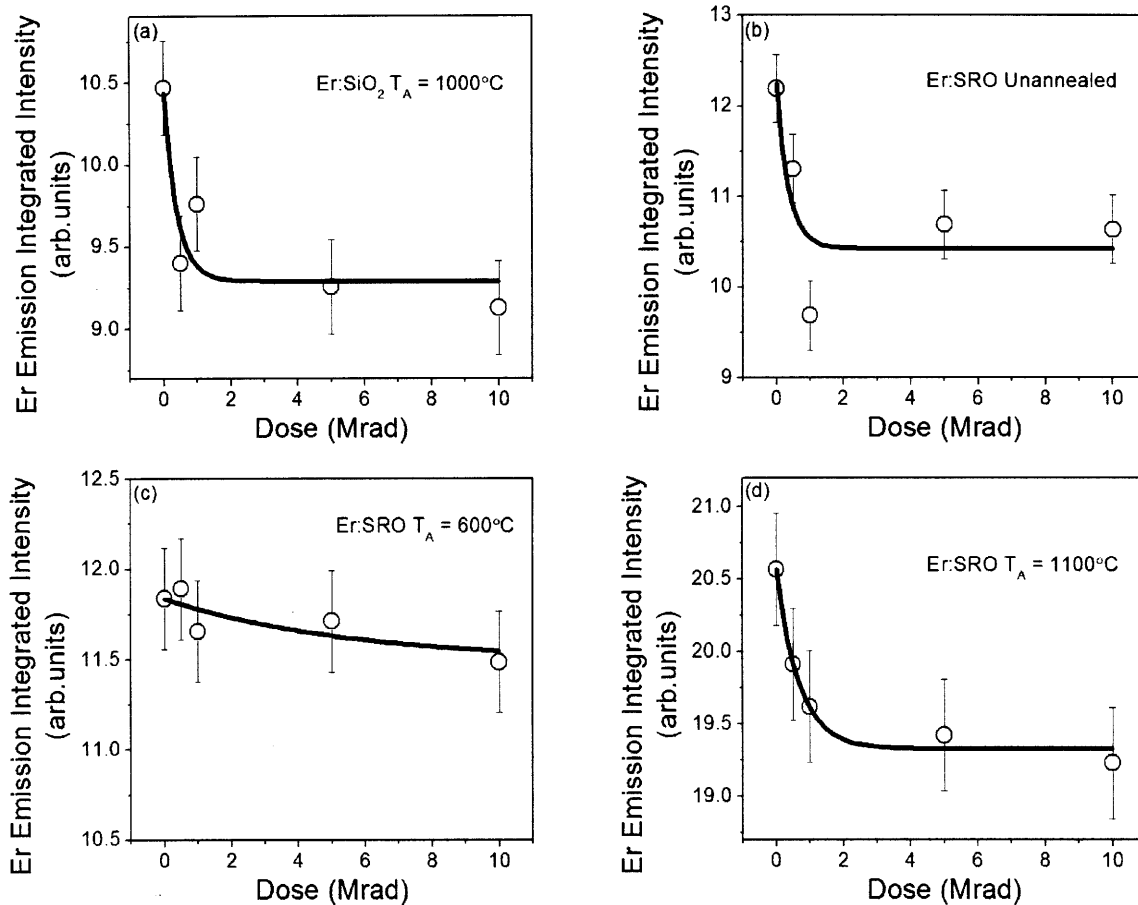


Figure 5.27 Integrated Er emission intensity for the following gamma irradiated samples (a) Er-doped SiO<sub>2</sub> with  $1 \times 10^{20}$  Er atoms/cm<sup>3</sup> annealed at 1000°C for 1 hour, (b) Er-doped SRO with 38at% Si and  $1 \times 10^{20}$  Er atoms/cm<sup>3</sup>, unannealed, (c) Er-doped SRO with 38at% Si and  $1 \times 10^{20}$  Er atoms/cm<sup>3</sup> annealed at 600°C for 1 hour and (d) Er-doped SRO with 38at% Si and  $1 \times 10^{20}$  Er atoms/cm<sup>3</sup> annealed at 1100°C for 1 hour. The intensity for each sample was integrated between 1400 nm and 1700 nm.

# Chapter 6 | Slab Waveguide Devices

In Chapter 5 we provided a detailed study of the light emitting properties of undoped SRO and Er-doped SRO to highlight the similarities and differences between Er emission in SiO<sub>2</sub> and SRO. As we discussed in the motivation for this thesis the goal of the study of light emission in this system is the realization of a Si based light source or amplifier that can be integrated with Si microelectronics. In order to reduce to practice the concepts presented in Chapter 5 to fabricate a working device we need to evaluate the material in terms of device parameters of gain and loss and determine if net gain (gain greater than loss) is possible. The simplest structure for optical confinement and edge emitting devices is a planar optical waveguide which consists of a high-index waveguide layer on a low-index undercladding layer. Light is confined in one dimension within the waveguide layer through total internal reflection from the air/waveguide and undercladding/waveguide interfaces. In this chapter we will analyze the performance of Er-doped SRO slab waveguides.

## 6.1. Optical Modes in Asymmetric Slab Waveguides

Asymmetric slab waveguides are formed by surrounding a thin film core layer with layers of different index of refraction on top and bottom such that  $n_{\text{core}} > n_{\text{overcladding}}, n_{\text{undercladding}}$ . Light is confined in one dimension through total internal reflection from the overcladding/core and core/undercladding interfaces. The slab waveguide samples we will consider in this chapter are SRO, Er-doped SRO and Er,Ge-doped SiO<sub>2</sub> deposited on a 10 $\mu\text{m}$  thick stoichiometric SiO<sub>2</sub> layer on Si with air as the top cladding (Figure 6.1).

We can analytically solve the wave equation for this device geometry to obtain the effective index of the guided mode, E-field profile and the power confinement factor which are all important parameters for the analysis of amplification and propagation losses in our devices. Similar derivations can be found in Haus [154], Chuang [155], Okamoto [156] and Hunsperger [157].



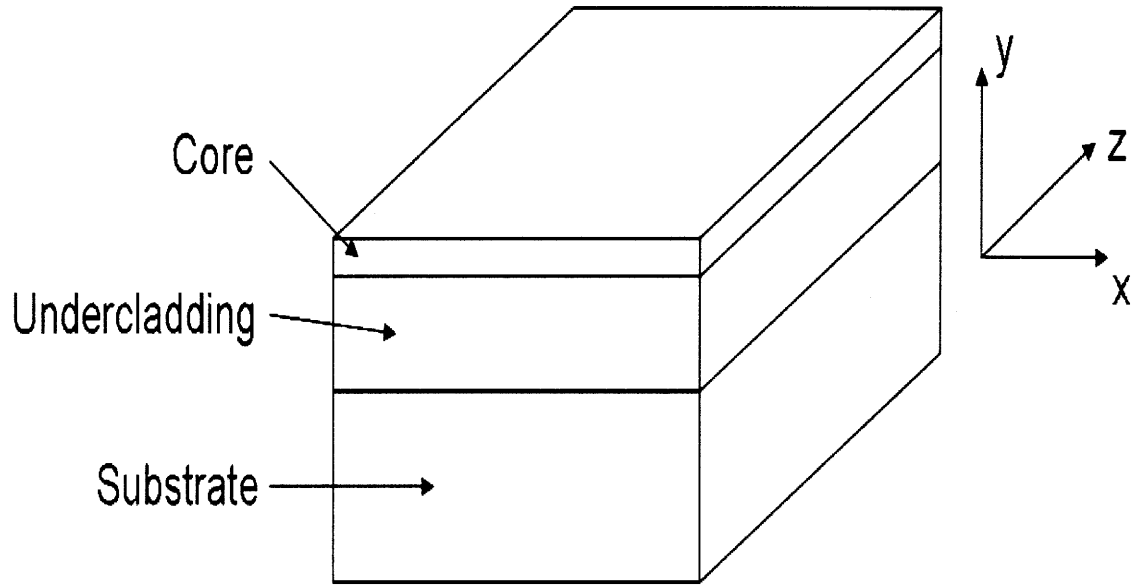


Figure 6.1 Schematic of an asymmetric slab waveguide.

The wave equation is

$$(\nabla^2 + \omega^2 \mu \epsilon)E = 0 \quad (6.1)$$

If we apply the electric field in the x direction, TE case, and define z as the propagation direction with an electric field in the propagation direction of the form  $e^{ik_z z}$  the form of the solution for the electric field in the y direction (confinement direction) is given by the following expressions

$$E_y = e^{ik_z z} \begin{cases} B_c e^{-\alpha_c y} & y \geq 0 \\ A \cos(k_y y + \phi) & -d \leq y \leq 0 \\ B_s e^{\alpha_s (y+d)} & y \leq -d \end{cases} \quad (6.2)$$

First we write the coefficients  $B_s$  and  $B_c$  in terms of A by forcing the electric field solution to be continuous at  $y = 0$  and  $y = -d$ . This modifies equations 6.2 to the form

$$E_y = e^{ik_x z} \begin{cases} A \cos(\phi) e^{-\alpha_c y} & y \geq 0 \\ A \cos(k_y y + \phi) & -d \leq y \leq 0 \\ A \cos(-k_y d + \phi) e^{\alpha_s (y+d)} & y \leq -d \end{cases} \quad (6.3)$$

Next we define the magnetic field from the electric field through Faraday's Law

$$H_x = \frac{i}{\omega \mu} \frac{d}{dy} E_y \quad (6.4)$$

which gives the solution for the magnetic field of the form

$$H_x = \frac{i}{\omega \mu} e^{ik_x z} \begin{cases} -\alpha_c A \cos(\phi) e^{-\alpha_c y} & y \geq 0 \\ -k_y A \sin(k_y y + \phi) & -d \leq y \leq 0 \\ \alpha_s A \cos(-k_y d + \phi) e^{\alpha_s (y+d)} & y \leq -d \end{cases} \quad (6.5)$$

By forcing the  $H_x/E_y$  ratio to be continuous (both electric field and its derivative are continuous) at the  $y = 0$  boundary we obtain the condition

$$\frac{\alpha_c}{k_y} = \tan(\phi) \quad (6.6)$$

Similarly for the  $y = -d$  boundary we obtain

$$\frac{\alpha_s}{k_y} = \tan(k_y d - \phi) \quad (6.7)$$

Combining 6.6 and 6.7 to eliminate  $\phi$  we obtain an expression for the guidance condition

$$k_y d = m\pi + \tan^{-1}\left(\frac{\alpha_c}{k_y}\right) + \tan^{-1}\left(\frac{\alpha_s}{k_y}\right) \quad (6.8)$$

From the wave equation, 6.1, we obtain the expressions for  $k_y$ ,  $\alpha_c$  and  $\alpha_s$  in terms of the waveguide parameters and the effective index of the guided mode

$$\begin{aligned}\alpha_c^2 &= \beta^2 - \omega^2 \mu_c \epsilon_c \\ k_y^2 &= \omega^2 \mu \epsilon_f - \beta^2 \\ \alpha_s^2 &= \beta^2 - \omega^2 \mu_s \epsilon_s\end{aligned}\tag{6.9}$$

where  $\beta$  is the propagation constant with  $\beta = kn_{eff}$  and  $k = \frac{2\pi}{\lambda}$ . We can substitute equations 6.9 into 6.8 with  $\mu = \mu_c = \mu_s$  to obtain

$$kd\sqrt{n_f^2 - n_{eff}^2} - m\pi = \tan^{-1}\left(\frac{\sqrt{n_{eff}^2 - n_c^2}}{\sqrt{n_f^2 - n_{eff}^2}}\right) + \tan^{-1}\left(\frac{\sqrt{n_{eff}^2 - n_s^2}}{\sqrt{n_f^2 - n_{eff}^2}}\right)\tag{6.10}$$

Rearranging equation 6.10 using the identity

$$\tan(x + y) = \frac{\tan x + \tan y}{1 - \tan x \tan y}\tag{6.11}$$

we obtain an alternative expression of the guidance condition

$$\tan\left(kd\sqrt{n_f^2 - n_{eff}^2} - m\pi\right) = \frac{\left(\frac{\sqrt{n_{eff}^2 - n_c^2}}{\sqrt{n_f^2 - n_{eff}^2}}\right) + \left(\frac{\sqrt{n_{eff}^2 - n_s^2}}{\sqrt{n_f^2 - n_{eff}^2}}\right)}{1 - \left(\frac{\sqrt{n_{eff}^2 - n_c^2} \sqrt{n_{eff}^2 - n_s^2}}{n_f^2 - n_{eff}^2}\right)}\tag{6.12}$$

Typically the guidance condition for arbitrary slab waveguides is expressed in terms of a normalized frequency,  $V$ , normalized propagation parameter,  $b$ , and asymmetry parameter,  $a$ . They are

$$\begin{aligned}
V &= kd\sqrt{(n_f^2 - n_s^2)} \\
b &= \frac{n_{eff}^2 - n_s^2}{n_f^2 - n_s^2} \\
a &= \frac{n_s^2 - n_c^2}{n_f^2 - n_s^2}
\end{aligned} \tag{6.13}$$

Substituting equation 6.13 into equation 6.12 we get

$$\tan(V\sqrt{1-b} - m\pi) = \frac{\sqrt{\frac{b+a}{1-b}} + \sqrt{\frac{b}{1-b}}}{1 - \frac{\sqrt{b(b+a)}}{1-b}} \tag{6.14}$$

Similarly we can define the guiding condition for TM polarized light by starting from the solution for  $H_y$  which is similar in form to equation 6.5

$$H_y = e^{ik_z z} \begin{cases} A \cos(\phi) e^{-\alpha_y y} & y \geq 0 \\ A \cos(k_y y + \phi) & -d \leq y \leq 0 \\ A \cos(-k_y d + \phi) e^{\alpha_y (y+d)} & y \leq -d \end{cases} \tag{6.15}$$

Next we define the electric field from the magnetic field through Ampere's Law

$$E_x = \frac{1}{\omega\mu\epsilon} \frac{d}{dx} H_y \tag{6.16}$$

which gives the solution for the electric field in the form of

$$E_x = \frac{1}{i\omega\mu} e^{ik_z z} \begin{cases} -\frac{\alpha_c}{\epsilon_c} A \cos(\phi) e^{-\alpha_c y} & y \geq 0 \\ -\frac{k_y}{\epsilon_f} A \sin(k_y y + \phi) & -d \leq y \leq 0 \\ \frac{\alpha_s}{\epsilon_s} A \cos(-k_y d + \phi) e^{\alpha_s (y+d)} & y \leq -d \end{cases} \quad (6.17)$$

By requiring that  $E_x/H_y$  is continuous at  $y = 0$  and  $y = -d$  we obtain the guiding condition for the TM mode

$$k_y d = m\pi + \tan^{-1}\left(\frac{\epsilon_f \alpha_s}{\epsilon_s k_y}\right) + \tan^{-1}\left(\frac{\epsilon_f \alpha_c}{\epsilon_c k_y}\right) \quad (6.18)$$

which in terms of the normalized frequency, normalized propagation parameter and asymmetry parameter is

$$\tan(V\sqrt{1-b} - m\pi) = \frac{\left(\frac{n_f^2}{n_c^2}\right)\sqrt{b+a} + \left(\frac{n_f^2}{n_s^2}\right)\sqrt{b}}{1 - \left(\frac{n_f^4}{n_c^2 n_s^2}\right)\frac{\sqrt{b(b+a)}}{1-b}} \quad (6.19)$$

Equations 6.14 and 6.19 can be solved numerically to determine the effective index,  $n_{\text{eff}}$ , of the guided mode. Once the effective index is known the power distribution in the waveguide structure is given by

$$P = \int_{-\infty}^{\infty} \frac{1}{2} (E_y H_x^* - E_x H_y^*) dy = \begin{cases} \frac{\beta}{2\omega\epsilon_0} \int_{-\infty}^{\infty} |E_y|^2 dy & \text{TE polarization} \\ \frac{\beta}{2\omega\epsilon_0} \int_{-\infty}^{\infty} \frac{1}{n^2} |H_y|^2 dy & \text{TM polarization} \end{cases} \quad (6.20)$$

The power confinement factor,  $\Gamma$ , in the core can be calculated through the expression

$$\Gamma = \frac{P_{core}}{P_{overcladding} + P_{core} + P_{undercladding}} \quad (6.21)$$

which for TE polarizations is

$$\Gamma = \frac{\int_{-d}^0 [\cos(k_y y + \phi)]^2 dy}{\int_0^{\infty} [\cos(\phi) e^{-\alpha_c y}]^2 dy + \int_{-d}^0 [\cos(k_y y + \phi)]^2 dy + \int_{-\infty}^{-d} [\cos(-k_y d + \phi) e^{\alpha_s(y+d)}]^2 dy} \quad (6.22)$$

and TM polarizations is

$$\Gamma = \frac{\int_{-d}^0 \left[ \frac{1}{\epsilon_f} \cos(k_y y + \phi) \right]^2 dy}{\int_0^{\infty} \left[ \frac{1}{\epsilon_c} \cos(\phi) e^{-\alpha_c y} \right]^2 dy + \int_{-d}^0 \left[ \frac{1}{\epsilon_f} \cos(k_y y + \phi) \right]^2 dy + \int_{-\infty}^{-d} \left[ \frac{1}{\epsilon_s} \cos(-k_y d + \phi) e^{\alpha_s(y+d)} \right]^2 dy} \quad (6.23)$$

Figure 6.2 shows the electric field profile for an Er-doped SRO slab waveguide structure considered in the measurement of optical gain discussed in the next section.

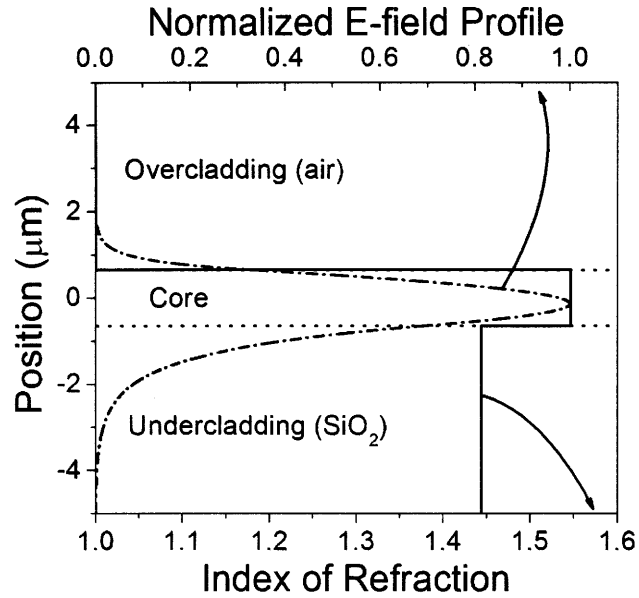


Figure 6.2 Refractive index and E-field profile for an Er-doped SRO slab waveguide with an index of refraction of 1.5465 and thickness of 1.3 $\mu\text{m}$ . The power confinement factor was calculated to be 0.8474.

The effective index, electric field profile, and power confinement factor were determined using a Matlab program presented in Appendix A.

## 6.2. Optical Amplification – The Variable Stripe Length Technique

### 6.2.1. Description of the Technique and Apparatus

A schematic of the variable stripe length [158] setup assembled for this experiment is shown in Figure 6.3.

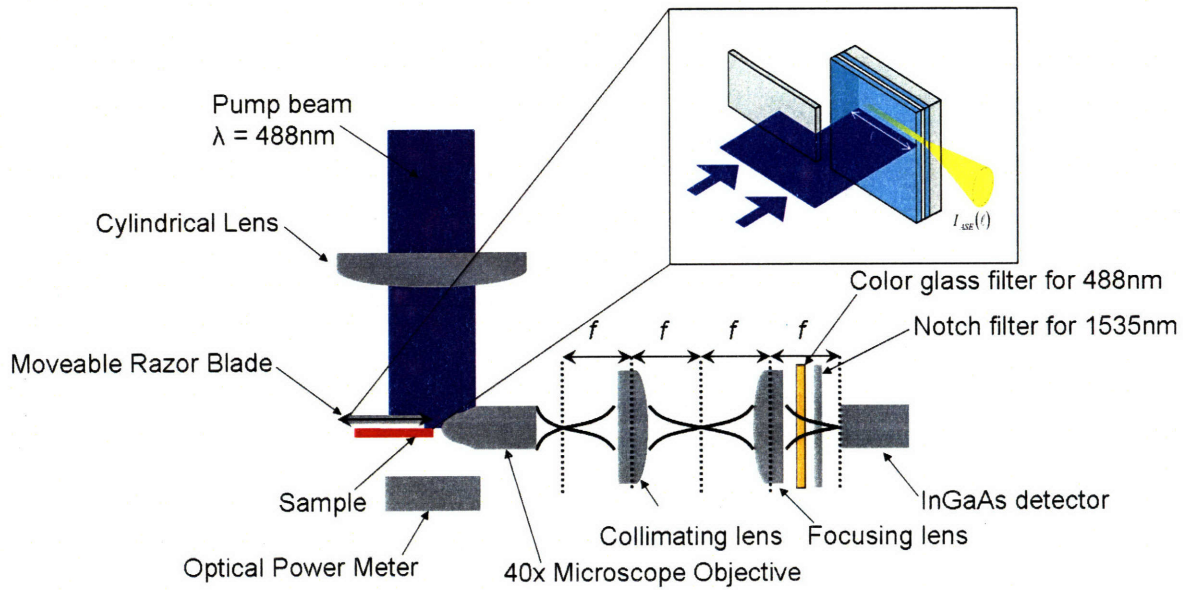


Figure 6.3 Side view schematic of the variable stripe length optical gain measurement setup.

Despite the apparent simplicity of the system there are several potential pitfalls leading to false observation of gain which have been documented in the literature [159,160]. We have assembled the current system with these issues in mind. The sample is pumped with an Ar-ion laser at 488 nm from overhead in a thin stripe by using a cylindrical lens. The length of the stripe is varied using a razor blade mounted on a moveable stage and the emitted light is collected from the sample edge using a 40x microscope objective. The light is collimated and focused onto an InGaAs detector using identical lenses taking care to match the focal positions of the lenses such that a 1-to-1 image of the sample edge is observed at the detector and the collected intensity is not effected by confocal effects in the collection system. Care was taken to locate the sample edge at the focal plane of the microscope objective such that the edge emitted signal was collected. The razor blade was lowered very close to the sample surface in order to minimize diffraction effects of the pump beam on the sample surface. Two filters were placed in front of the detector to remove the scattered pump signal and SRO light emission signal from the collected beam to ensure that only the Er emission is considered in the measurement. We measured the pump beam profile in the longitudinal direction by scanning the sample edge through the beam and taking the derivative of the transmitted signal (integrated intensity) collected with an optical power meter. Figure 6.4 shows the pump beam profile.



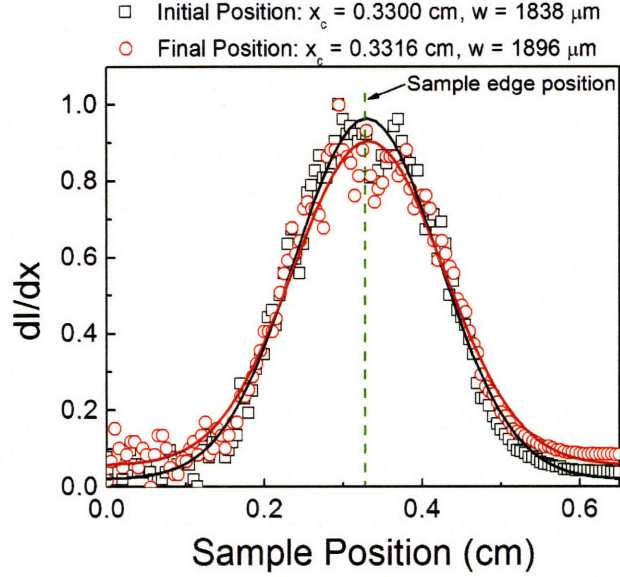


Figure 6.4 Pump beam profile measured in the longitudinal direction at the beginning of the gain measurement (squares) and at the end of the gain measurement (circles). The solid lines are Gaussian fits of the data with a center position and width of 0.3300 cm and 1.838mm measured for the beam at the beginning of the measurement and a center position and width of 0.3316 cm and 1.896 mm measured for the beam at the end of the measurement. The dash line indicates the position of the sample edge relative to the beam profile during the gain measurements.

The beam profile was Gaussian with a beam width of  $\sim 1.85$ mm. The sample edge was placed at half the beam width as indicated in Figure 6.4.

During the VSL measurement spontaneous emitted light at the end of the excitation stripe is amplified proportional to the product of the modal gain of the slab waveguide and the excitation stripe length leading to a buildup of the emitting intensity as the excitation stripe length is increased. This buildup of intensity with increasing excitation stripe length can be analyzed using a one-dimensional amplifier model [161]. In the one-dimensional amplifier model the emitted intensity is given by the differential equation

$$\frac{dI}{dz} = gI + \frac{A_{sp} N h \nu \Omega}{4\pi} \quad (6.24)$$

where  $g$  is the gain coefficient,  $A_{sp}$  is the spontaneous emission rate,  $N$  is the excited-state population of the emitter,  $h\nu$  is the energy of the emitted photon and  $\Omega$  is the emission solid

angle subtended by the exit amplifier face. The solution to equation 6.24 is an exponentially increasing function

$$I(z) = \frac{J}{g_{\text{mod}}} (e^{g_{\text{mod}}z} - 1) \quad (6.25)$$

where  $J = \frac{A_{\text{sp}} N h \nu \Omega}{4\pi}$  is a factor which does not depend on  $z$  and where we have generalized the gain coefficient to be the modal gain,  $g_{\text{mod}}$

$$g_{\text{mod}} = \Gamma g - \alpha \quad (6.26)$$

The expression for the modal gain takes into account the waveguide properties through the confinement factor  $\Gamma$  and the pump independent propagation loss  $\alpha$ . We note that in the case that  $\alpha$  is greater than  $\Gamma g$  the net gain would be negative. However, under these conditions, the signal enhancement observed for increasing pump-power densities can still be analyzed to reveal several relevant parameters related to the gain such as the emission cross section as will be discussed in the following sections.

## 6.2.2. Measurement of Er:SRO Samples Annealed at 600°C

We have performed measurements on Er:SRO samples annealed at 600°C to determine the magnitude of the signal enhancement. Figure 6.5 shows the results of emitted intensity versus stripe length for three different pump powers.

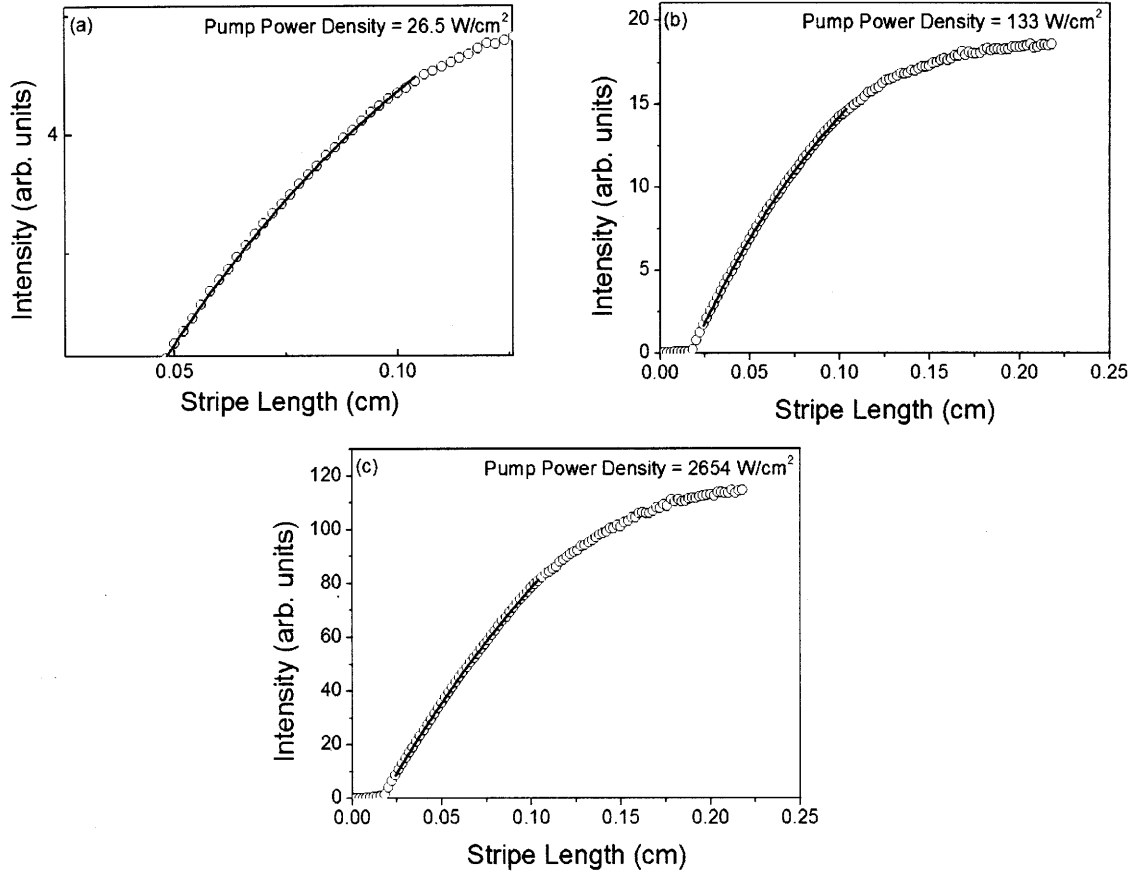


Figure 6.5 Measured intensity versus excitation stripe length for an Er-doped SRO sample with 36.5at% Si and  $1.2 \times 10^{20}$  Er ions/cm<sup>3</sup> annealed at 600°C for 1 hour (circles) collected at pump-power densities of (a) 26.5 W/cm<sup>2</sup>, (b) 133 W/cm<sup>2</sup> and (c) 2654 W/cm<sup>2</sup>. The solid lines are fits to the data using the one-dimensional amplifier model equation 7.25 yielding modal gain values of (a)  $-11.6 \text{ cm}^{-1}$  (b)  $-8.74 \text{ cm}^{-1}$  and (c)  $-5.3 \text{ cm}^{-1}$ .

We observe that the VSL data, obtained over a range of pump-power densities, are well fit using the one-dimensional amplifier approach within an 800  $\mu\text{m}$  length which is within the half-width of the longitudinal pump beam profile. We have intentionally excluded the first 60 nm of the VSL data since this region is the most susceptible to pump diffraction effects. The modal gain obtained by fitting the VSL data with the one-dimensional amplifier model (as in Figure 6.5) at various pump-power densities is plotted in Figure 6.6.

We see from Figure 6.6 that the modal gain values are negative for all pump-power densities indicating that net gain is not achieved due to the high losses within this slab waveguide sample.

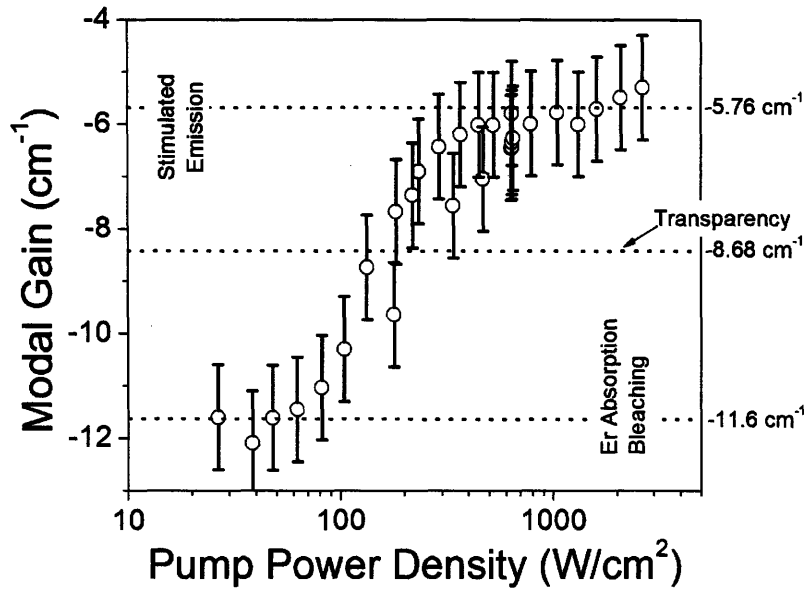


Figure 6.6 Modal gain versus pump-power density determined from fits of emission intensity versus excitation stripe length data for various pump-power densities for an Er-doped SRO sample with 36.5 at% Si and  $1.2 \times 10^{20}$  Er ions/cm<sup>3</sup> annealed at 600°C for 1 hour. The horizontal dotted lines are guides to the eyes to indicate the saturation regions at low and high pump-power densities as well as the transparency threshold at  $-8.68 \text{ cm}^{-1}$  which separates the absorption bleaching and stimulated emission regimes.

However, the signal enhancement that is observed with increasing pump-power densities shows a saturation at  $-11.6 \text{ cm}^{-1}$  for low pump-power densities and  $-5.76 \text{ cm}^{-1}$  for high pump-power densities which is evidence that population inversion and stimulated emission has been achieved. The total gain is half the difference in modal gain at high and low pump-power densities and is equal to  $2.92 \text{ cm}^{-1}$ . For an Er concentration of  $1.2 \times 10^{20} \text{ cm}^{-3}$  and a confinement factor of 0.9 we calculate an emission cross section for the Er of  $2.7 \pm 1 \times 10^{-20} \text{ cm}^2$  since  $\sigma_{emis} = \frac{g}{\Gamma N_{tot}}$ . We note that this value of the emission cross section is  $\sim 4$ x stronger than Er in several glass hosts [100] but significantly smaller than values reported in the literature [57,59,60]. We will discuss this enhanced cross section in reference to direct measurements of the absorption cross section of the same sample presented in Section 6.4

### 6.3. Rate Equation Modeling of the Er – SRO System

Rate equation models are frequently used in the design and analysis of semiconductor lasers to determine how carrier and photon concentrations respond due to perturbations effecting the gain and loss of the system. The advantage of the rate equation treatment is its simplicity; it provides an effective mathematical description that allows the user to extract numerical parameters that are useful to describe the response of complex optical systems in simple numerical terms. Instead of using complex microscopic physical models, transitions between energy levels are related through phenomenological coefficients. In the spirit of the simplicity of the rate equation treatment Dal Negro proposed modeling the SRO sensitizer – Er interaction as coupled two level systems as shown in Figure 6.7 [162].

The model, shown schematically in Figure 6.7, is a simplification of the model developed by Pacifici *et al.* [94] and later applied by Lee *et al.* [163] which considers the second excited-state of the SRO sensitizer as well as the third through fifth excited-states for the Er ion. Due to the relatively short lifetime of these states and energy levels their effect on the light emission kinetics of the system is small. We notice several parameters in the model that have been measured directly through experiments. These include  $\sigma_{ab}$  the excitation cross section of the SRO sensitizer,  $\tau_{ba}$  the emission lifetime of the SRO sensitizer,  $C_A$  the inter-site upconversion coefficient for the SRO sensitizer,  $\sigma$  the Er excitation cross section and  $\tau$  the Er emission lifetime.

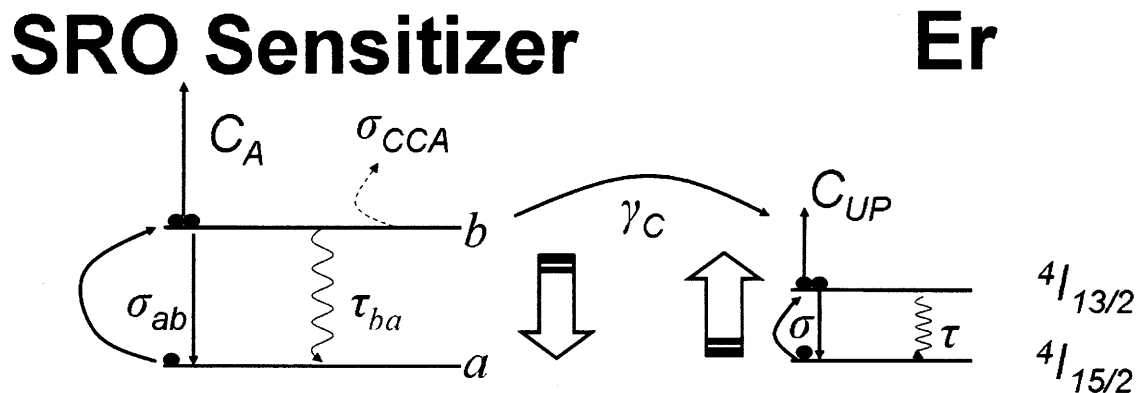


Figure 6.7 Schematic of a coupled two level system for the SRO sensitizer – Er interaction with phenomenological parameters describing the transitions between levels as described in the text.

We also define three new parameters  $\gamma_c$  the coupling coefficient between the SRO sensitizer and Er,  $n_{\text{tot}}$  the total concentration of SRO sensitizers and  $\sigma_{\text{emis}}$  the emission cross section of the material. The possible values of these last three unknowns and the upconversion coefficient for Er,  $C_{UP}$ , are constrained through the requirement of fitting experimental results obtained through different experimental techniques performed on the same samples using a single set of values. The rate equations which determine the excited and ground-state populations of the SRO sensitizer and Er ion as a function of time are given by:

$$\frac{\partial n_b}{\partial t} = \sigma_{ab} \phi_p n_a - \frac{n_b}{\tau_{ba}} - \gamma_c n_b N_1 - 2C_A n_b^2 \quad (6.27)$$

$$\frac{\partial N_2}{\partial t} = \sigma_p \phi_p N_1 - \frac{N_2}{\tau} + \gamma_c n_b N_1 - 2C_{UP} N_2^2 \quad (6.28)$$

In the following figures we will demonstrate that each of these parameters has a unique contribution to the VSL data which can be addressed independently of the others in a self-consistent manner.

For the gain, from the simulations we note that the sensitizer density has the strongest influence on the threshold of the amplifier, the emission cross section is directly linked to the total gain (for a fixed Er concentration) and the coupling coefficient between the sensitizer and Er influences the shape of the curve at threshold. For the Er excited-state population (proportional to the emitted intensity) variation of these parameters only induces a small perturbation with the shape of the curve strongly dependent on the upconversion coefficient in agreement with the analysis of the steady-state intensity in Section 5.4.3. We also note that the value of the upconversion coefficient will influence the threshold for gain.

We have repeated the measurements of the Er excitation cross section ( $1.6 \times 10^{-17} \text{ cm}^2$ ), lifetime (4.2 ms) and steady-state emission for the gain sample in order to accurately model the dynamics of the system. Keeping our observations of the influence of the fitting parameters in mind we

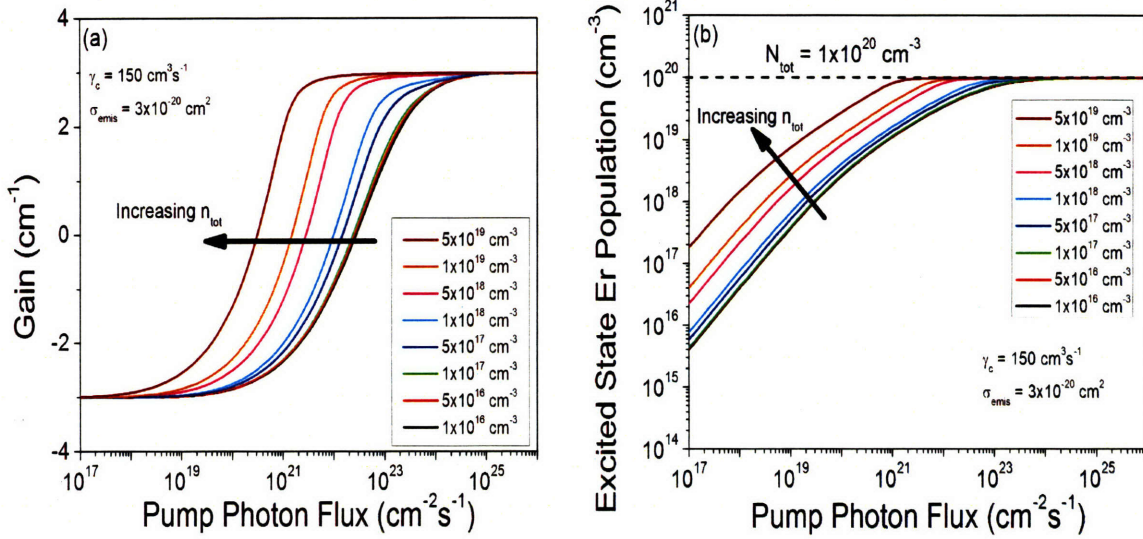


Figure 6.8 Simulations of (a) gain and (b) Er excited-state population using the rate equations in equation 6.27 and 6.28 to demonstrate the effect of changing sensitizer density,  $n_{tot}$ . The other simulation parameters were held constant at values of  $N_{tot} = 1.1 \times 10^{20} \text{ cm}^{-3}$ ,  $\gamma_{ac} = 150 \times 10^{-15} \text{ cm}^3 \text{ s}^{-1}$ ,  $\sigma = 1 \times 10^{-19} \text{ cm}^2$ ,  $\tau = 3 \times 10^{-3} \text{ s}$ ,  $\sigma_{ab} = 9 \times 10^{-17} \text{ cm}^2$ ,  $\tau_{ba} = 1 \times 10^{-6} \text{ s}$ ,  $C_A = 1 \times 10^{-13} \text{ cm}^3 \text{ s}^{-1}$ ,  $C_{up} = 2.5 \times 10^{-17} \text{ cm}^3 \text{ s}^{-1}$  and  $\sigma_{emis} = 3 \times 10^{-20} \text{ cm}^2$ .

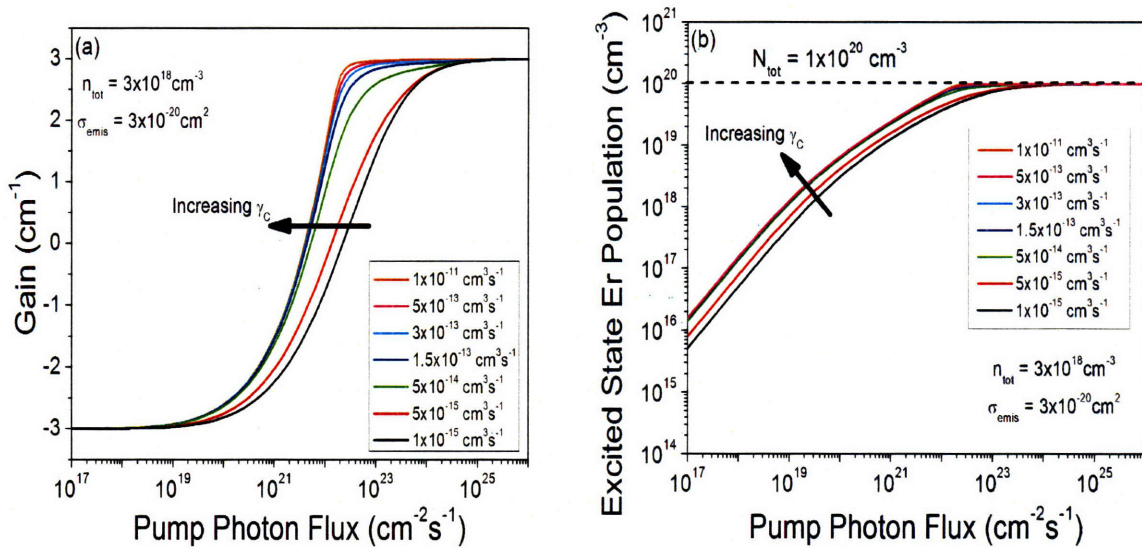


Figure 6.9 Simulations of (a) gain and (b) Er excited-state population using the rate equations in equation 6.27 and 6.28 to demonstrate the effect of changing the coupling coefficient between the sensitizer and Er,  $\gamma_{ac}$ . The other simulation parameters were held constant at values of  $N_{tot} = 1.1 \times 10^{20} \text{ cm}^{-3}$ ,  $n_{tot} = 3 \times 10^{18} \text{ cm}^{-3}$ ,  $\sigma = 1 \times 10^{-19} \text{ cm}^2$ ,  $\tau = 3 \times 10^{-3} \text{ s}$ ,  $\sigma_{ab} = 9 \times 10^{-17} \text{ cm}^2$ ,  $\tau_{ba} = 1 \times 10^{-6} \text{ s}$ ,  $C_A = 1 \times 10^{-13} \text{ cm}^3 \text{ s}^{-1}$ ,  $C_{up} = 2.5 \times 10^{-17} \text{ cm}^3 \text{ s}^{-1}$  and  $\sigma_{emis} = 3 \times 10^{-20} \text{ cm}^2$ .



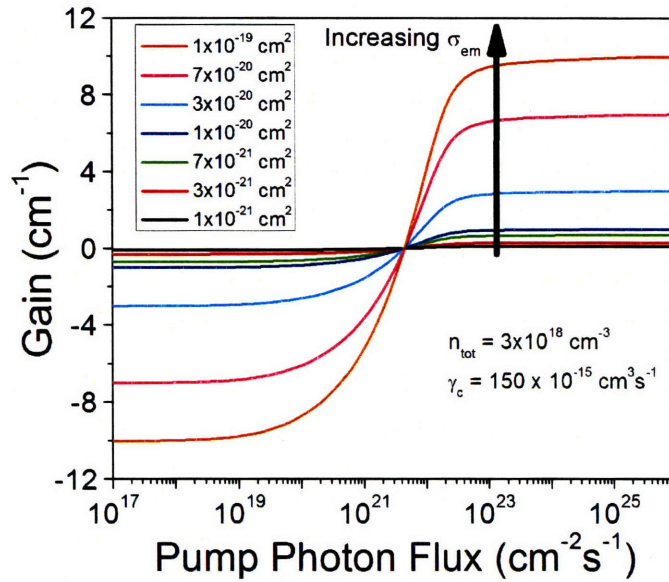


Figure 6.10 Simulations of gain using the rate equations in equation 6.27 and 6.28 to demonstrate the effect of changing the emission cross section of Er. The other simulation parameters were held constant at values of  $N_{\text{tot}} = 1.1 \times 10^{20} \text{ cm}^{-3}$ ,  $n_{\text{tot}} = 3 \times 10^{18} \text{ cm}^{-3}$ ,  $\gamma_{\text{ac}} = 3 \times 10^{-15} \text{ cm}^3 \text{ s}^{-1}$ ,  $\sigma = 1 \times 10^{-19} \text{ cm}^2$ ,  $\tau = 3 \times 10^{-3} \text{ s}$ ,  $\sigma_{\text{ab}} = 9 \times 10^{-17} \text{ cm}^2$ ,  $\tau_{\text{ba}} = 1 \times 10^{-6} \text{ s}$ ,  $C_{\text{A}} = 1 \times 10^{-13} \text{ cm}^3 \text{ s}^{-1}$  and  $C_{\text{up}} = 2.5 \times 10^{-17} \text{ cm}^3 \text{ s}^{-1}$ .

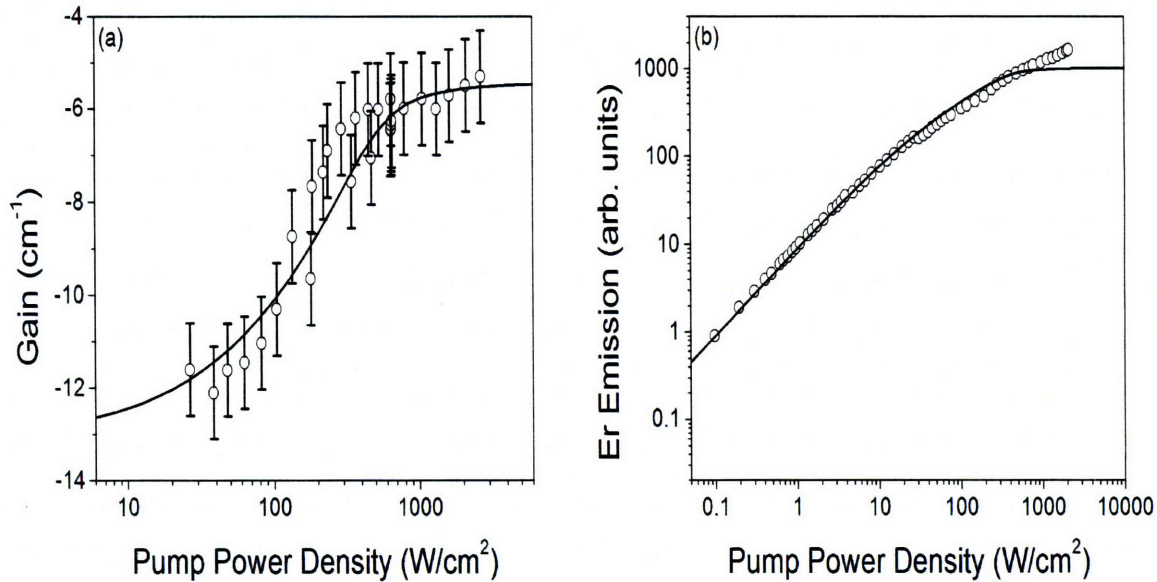


Figure 6.11 (a) Measured optical gain versus pump-power density for the Er-doped SRO gain sample with 36.5 at% Si and  $1.2 \times 10^{20} \text{ Er ions/cm}^3$  annealed at  $600^\circ\text{C}$  for 1 hour (open circles). (b) Measured steady-state Er emission at 1535nm for the same gain sample (open circles). The solid lines is a linear fit using the rate equation model for the Er – SRO interaction with the following parameters  $n_{\text{tot}} = 6 \times 10^{18} \text{ sensitizers/cm}^3$ ,  $\gamma_{\text{C}} = 150 \times 10^{-15} \text{ cm}^3 \text{ s}^{-1}$ ,  $\sigma = 1 \times 10^{-19} \text{ cm}^2$ ,  $\tau = 4.2 \text{ ms}$ ,  $\sigma_{\text{ab}} = 1.6 \times 10^{-17} \text{ cm}^2$ ,  $\tau = 1 \text{ } \mu\text{s}$ ,  $C_{\text{A1}} = 1 \times 10^{-13} \text{ cm}^3 \text{ s}^{-1}$ ,  $C_{\text{UP}} = 3 \times 10^{-18} \text{ cm}^3 \text{ s}^{-1}$ ,  $\sigma_{\text{emis}} = 3.5 \times 10^{-20} \text{ cm}^2$  and  $\alpha = 9.2 \text{ cm}^{-1}$ .



performed simulations of the VSL results obtained in section 6.2.2. to determine the parameters of  $\gamma_C$ ,  $\sigma_{emis}$  and  $n_{tot}$ . The comparison is shown in Figure 6.11.

The best agreement is for the parameters of  $\gamma_C = 150 \times 10^{-15} \text{ cm}^3 \text{ s}^{-1}$ ,  $n_{tot} = 6 \times 10^{18} \text{ cm}^{-3}$  and  $\sigma_{emis} = 3.5 \times 10^{-20} \text{ cm}^2$ . The upconversion coefficient of  $3 \times 10^{-18}$  is comparable to values measured for Er-doped glasses [143]. We notice that the density of sensitizers is 100x greater than what was observed for Si nanocrystal samples annealed at high temperatures. Additionally the coupling coefficient is 50x larger than what has been published in the literature for samples annealed at high temperatures [94]. This conclusion is consistent with the temperature-resolved photoluminescence study discussed in Section 5.5 which revealed two emission sensitizers for samples annealed at low and high temperatures. Our simultaneous measurement of the enhanced coupling coefficient confirms the fact that the emission sensitizer present in the low temperature annealed samples has a higher transfer efficiency compared to Si nanocrystals. Finally we note that the gain data could only be fit assuming negligible carrier induced losses. This is consistent with the fact that our sample with 36.5 at% Si is below the threshold Si content for carrier induced losses.

## **6.4. Transmission Loss through Prism Coupling Measurements**

### **6.4.1. Description of the Technique and Apparatus**

Figure 6.12 shows a schematic of the setup used to measure propagation losses in our slab waveguide samples. The sample is placed on a stage mounted to a goniometer which can be rotated with respect to the input laser beam to excite the guided mode in the film. Prisms are held against the sample surface using Teflon tipped screws. A two-axis stage is used to scan the input prism and sample across the laser beam to optimize the coupling into the guided mode. An output prism is used to couple the light out of the sample after it has propagated a length L. The

light output from the sample is collected with a collimating lens and focused onto a wide area InGaAs detector. An IR camera was used to monitor the position of the laser spot on the detector face to ensure that all of the light coupled out of the film was collected. Propagation losses were determined from an exponential fit of the power output from the sample versus prism separation  $L$ . To minimize input coupling variations the input prism was never removed from the sample until measurements were performed for all wavelengths. Since the optimum angle for coupling changes with wavelength the goniometer rotation, sample  $x$  and  $y$  position, collimating lens position and focusing lens position all needed to be adjusted for each change in wavelength and prism spacing. The possible sources for error in this measurement are output prism coupling variations and a misalignment of sample and collecting optics. To quantify this error we have performed several measurements on the same sample at the same wavelength over the course of several days. Our analysis allows us to estimate an error of 0.04 dB/cm.

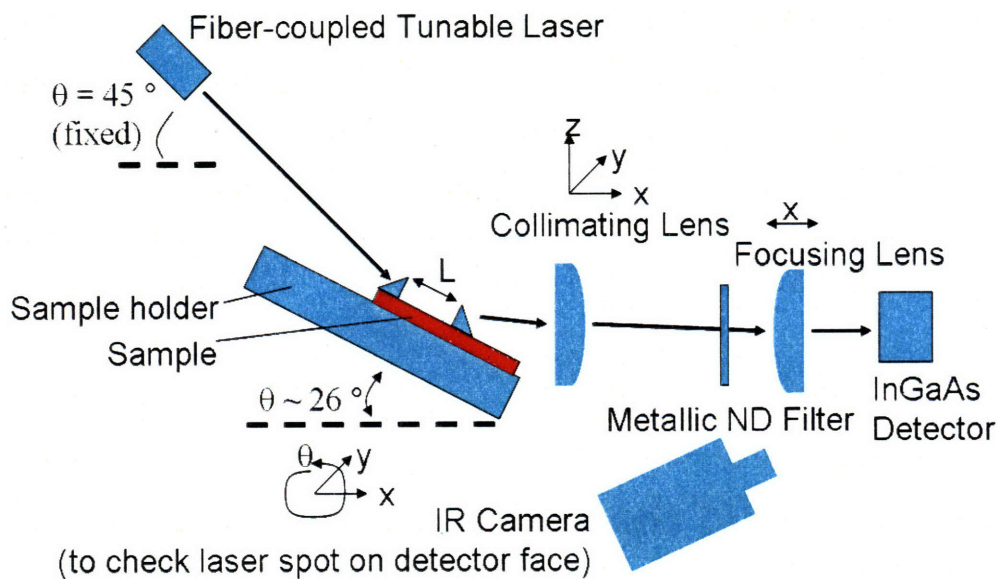


Figure 6.12 Schematic of the prism coupling loss setup for measuring propagation losses in slab waveguides.

## 6.4.2. Measurement of Er:SRO and Er,Ge SiO<sub>2</sub> Absorption Spectra

To obtain a comparison of the losses in Er-doped SRO and more traditional Er-doped glasses we performed loss measurements for the same SRO sample considered in the gain measurements (Section 6.3) and fabricated an Er,Ge-doped SiO<sub>2</sub> sample with identical confinement factor so all results could be compared directly between the two samples without the need to perform any corrections for sample differences. For the Er,Ge-doped SiO<sub>2</sub> sample the Ge was introduced to increase the index of refraction of the core layer so optical confinement could be achieved. The detailed sample characteristics are listed in Table 6.1.

For this study we have examined the losses for Er,Ge-doped SiO<sub>2</sub> annealed at 600°C and 1000°C and for Er-doped SRO annealed at 600°C, 800°C and 1000°C. Experimental data of output power versus prism spacing along with the exponential fit of the data for several different wavelengths is shown in Figure 6.13 for Er,Ge-doped SiO<sub>2</sub> samples and Figure 6.14 for Er-doped SRO samples.

We see for all data sets a nearly perfect exponential decay with increasing prism spacing. The data recorded for the Er,Ge-doped SiO<sub>2</sub> samples at 1620nm (away from the Er absorption contribution) show a minimal loss of 0.1 dB/cm which is roughly the resolution limit of this technique. The loss spectra for the samples are shown in Figure 6.15.

Table 6.1 Sample characteristics for the Er,Ge-doped SiO<sub>2</sub> and Er-doped SRO slab waveguides considered in this study.

Sample	n	Thickness (μm)	Er Concentration (atoms/cm <sup>3</sup> )	Confinement Factor
Er51 (Er,Ge-doped SiO <sub>2</sub> )	1.4705	3.00	1.1x10 <sup>20</sup>	0.88
Er44 (Er-doped SRO)	1.5465	1.30	1.1x10 <sup>20</sup>	0.85

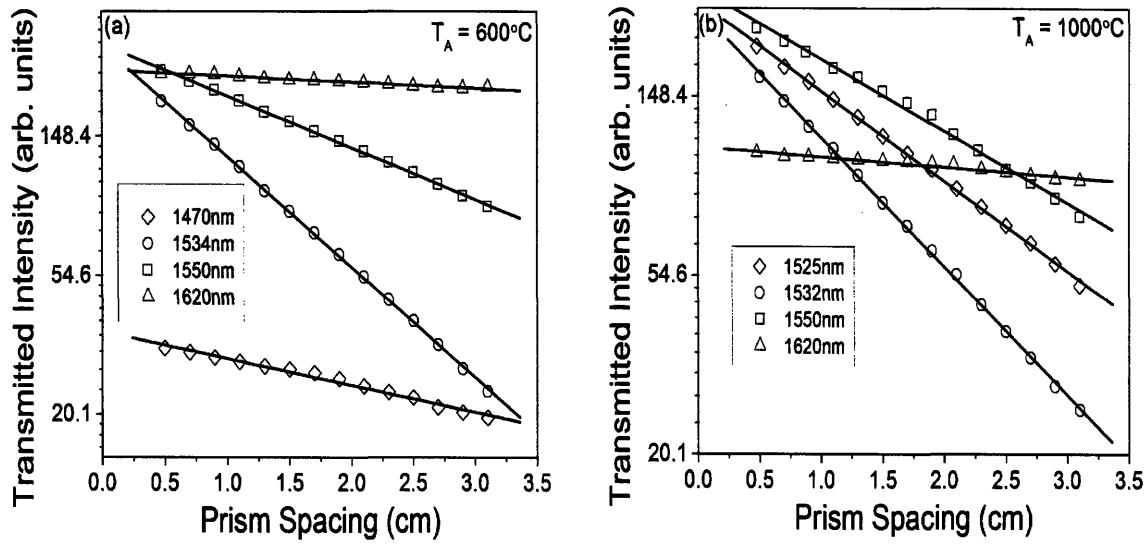


Figure 6.13 Experimental data of transmitted intensity versus prism spacing for Er,Ge-doped  $\text{SiO}_2$  samples (a) annealed at  $600^\circ\text{C}$  at 1470nm (diamonds)  $\alpha = -0.193 \text{ cm}^{-1}$ , 1534nm (circles)  $\alpha = -0.794 \text{ cm}^{-1}$ , 1550nm (squares)  $\alpha = -0.371 \text{ cm}^{-1}$  and 1620nm (triangles)  $\alpha = -0.043 \text{ cm}^{-1}$  and (b)  $1000^\circ\text{C}$  at 1525nm (diamonds)  $\alpha = -0.503 \text{ cm}^{-1}$ , 1532nm (circles)  $\alpha = -0.720 \text{ cm}^{-1}$ , 1550nm (squares)  $\alpha = -0.401 \text{ cm}^{-1}$  and 1620nm (triangles)  $\alpha = -0.056 \text{ cm}^{-1}$ . The solid lines are linear fits of the experimental data yielding the loss coefficients stated above.

From Figure 6.15 we see the characteristic Er absorption profile with a peak which varies between samples within the range of 1530 – 1540 nm. This variation in peak absorption wavelength is due to the effect of the embedding matrix on the Er ions and is consistent with observations for Er in different glass hosts. For the Er,Ge-doped sample the background loss due to the matrix is very low (given by the loss at 1620 nm  $\sim 0.1 \text{ dB/cm}$ ) and is not strongly dependent on the annealing temperature. For Er-doped SRO the background loss is much higher,  $\sim 3 \text{ dB/cm}$ , and is strongly dependent on the annealing temperature due to the influence of structural modifications in the SRO matrix on the loss for samples annealed at high temperatures. For the sample annealed at  $1000^\circ\text{C}$  the background loss becomes so significant that it completely masks the Er absorption peak. We also note that the matrix loss of  $0.8 \text{ cm}^{-1}$  measured at 1620 nm for the sample annealed at  $600^\circ\text{C}$  is a factor of 10 smaller than the loss derived from the VSL gain measurement analysis. We attribute this difference in matrix losses to differences in the output coupling losses for the two measurement techniques suggesting that, for the VSL

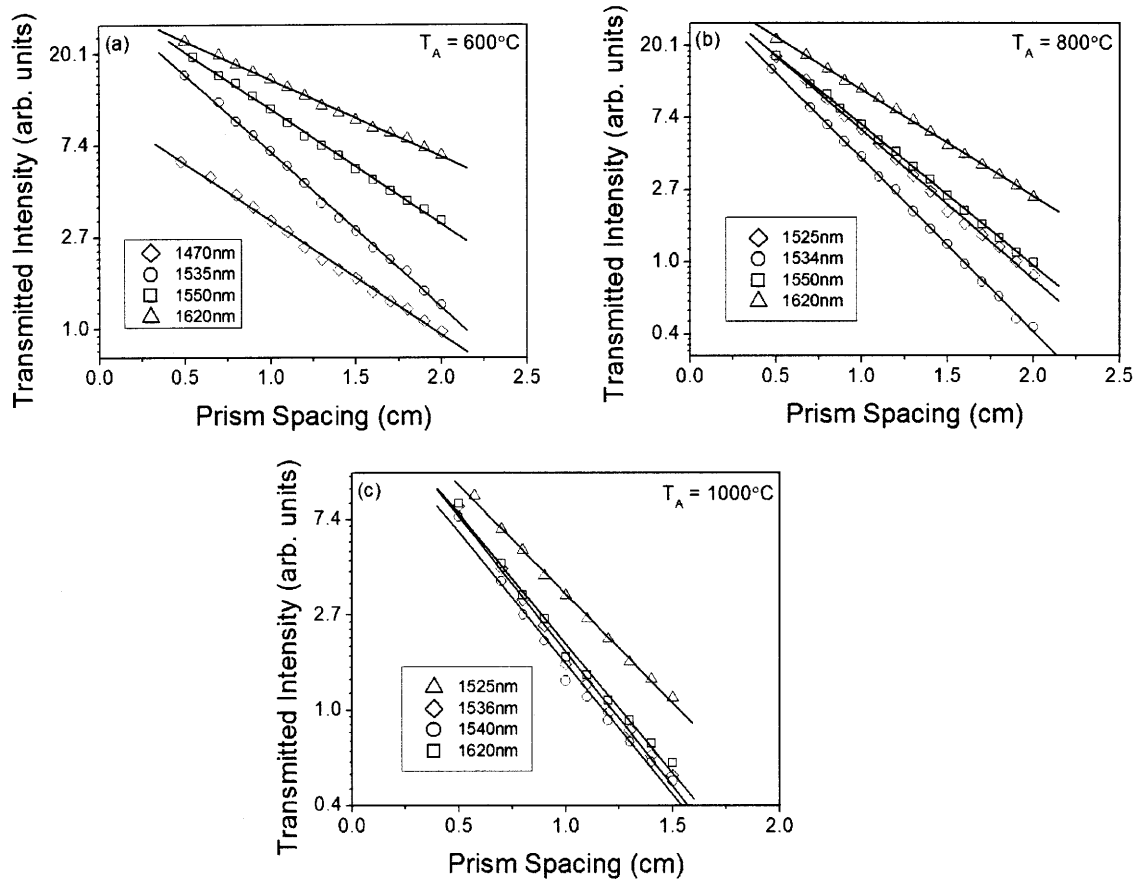


Figure 6.14 Experimental data of transmitted intensity versus prism spacing for Er,Ge-doped  $\text{SiO}_2$  samples (a) annealed at  $600^\circ\text{C}$  at  $1470\text{nm}$  (diamonds)  $\alpha = -0.124\text{ cm}^{-1}$ ,  $1535\text{nm}$  (circles)  $\alpha = -1.686\text{ cm}^{-1}$ ,  $1550\text{nm}$  (squares)  $\alpha = -1.250\text{ cm}^{-1}$  and  $1620\text{nm}$  (triangles)  $\alpha = -0.840\text{ cm}^{-1}$  (b)  $800^\circ\text{C}$  at  $1525\text{nm}$  (diamonds)  $\alpha = -2.066\text{ cm}^{-1}$ ,  $1534\text{nm}$  (circles)  $\alpha = -2.399\text{ cm}^{-1}$ ,  $1550\text{nm}$  (squares)  $\alpha = -1.948\text{ cm}^{-1}$  and  $1620\text{nm}$  (triangles)  $\alpha = -1.477\text{ cm}^{-1}$  and (c)  $1000^\circ\text{C}$  at  $1525\text{nm}$  (diamonds)  $\alpha = -2.830\text{ cm}^{-1}$ ,  $1536\text{nm}$  (circles)  $\alpha = -2.757\text{ cm}^{-1}$ ,  $1540\text{nm}$  (squares)  $\alpha = -2.719\text{ cm}^{-1}$  and  $1620\text{nm}$  (triangles)  $\alpha = -2.288\text{ cm}^{-1}$ . The solid lines are linear fits of the experimental data yielding the loss coefficients stated above.

measurement, scattering losses at the end facet of the sample are the dominant contribution to the loss.

In the next two sections we will separate the two sources of loss, Er absorption and the SRO matrix, and discuss their implications for device performance.

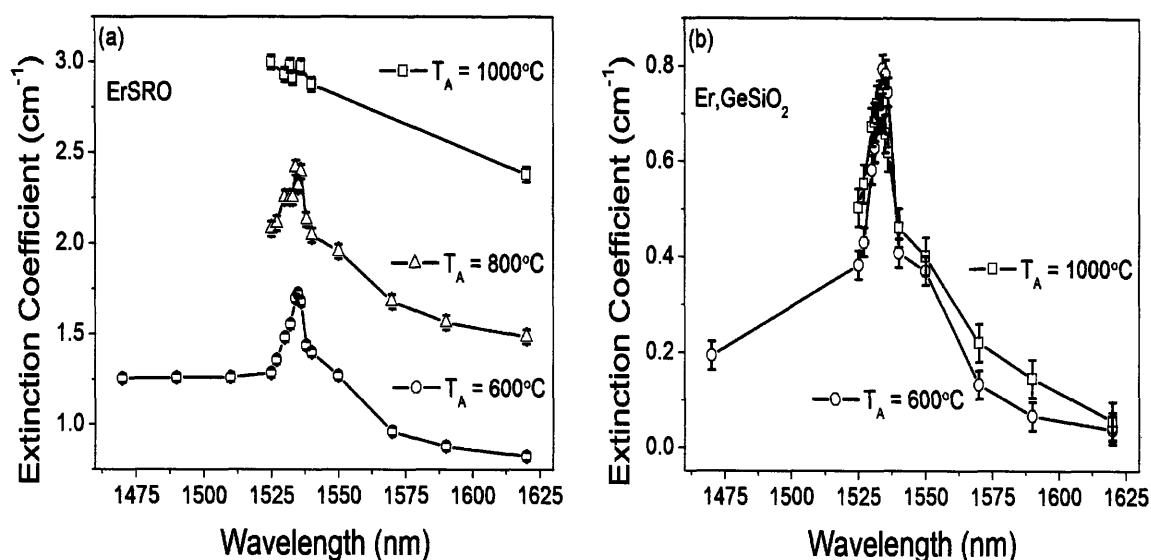


Figure 6.15 Transmission loss spectra for (a) Er-doped SRO and (b) Er,Ge-doped SiO<sub>2</sub>.

### 6.4.3. Measurement of the Er Absorption Cross Section for Er:SRO and Er,Ge:SiO<sub>2</sub>

By eliminating the background losses from the transmission loss spectrum of the Er:SRO and Er,Ge:SiO<sub>2</sub> samples we can obtain a measurement of the absorption cross section of Er in both matrixes. We expect that the dominant background loss mechanism is scattering due to Si nanoclusters within the SRO matrix with a linear wavelength dependence on a log-log plot [101]. We also know that the Er related absorption goes to zero at 1470nm and 1630nm. We removed the background by subtracting a straight line between 1470nm and 1630nm from the data when plotted on a log-log plot. Figure 6.16 (a) shows this background subtraction.

Figure 6.16 (b) shows the resulting Er absorption spectrum after background subtraction. By dividing the peak absorption by the Er concentration we obtain an Er absorption cross section for both samples of  $7.1 \times 10^{-21} \text{ cm}^2$  which is consistent with the values measured for Er in several

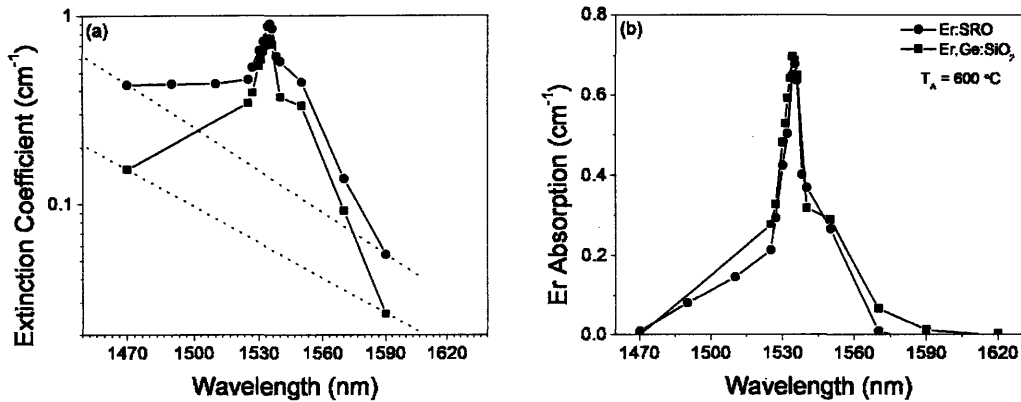


Figure 6.16 (a) Log-log plot of the extinction coefficient for Er,Ge-doped SiO<sub>2</sub> annealed at 600°C for 1 hour (solid squares) and Er-doped SRO annealed at 600°C for 1 hour (solid circles). The dotted lines represent the linear subtraction that was performed to remove the background losses. (b) Plot of the Er absorption spectrum obtained after the background subtraction in panel (a) for an Er,Ge-doped SiO<sub>2</sub> sample annealed at 600°C for 1 hour (solid squares) and an Er-doped SRO sample annealed at 600°C for 1 hour (solid circles).

glass hosts [100]. This confirms the measurements of an unchanged absorption cross section conducted by Mertens *et al.* [99] and Daldosso *et al.* [58]. The fact that two different values for the emission and absorption cross sections of the same sample have been obtained is unexpected since the transition cross sections at a single frequency should be identical for non-degenerate states. The difference in the measured values could be due to the role of the surrounding matrix for the two different experimental conditions. For the absorption measurement the SRO matrix is inactive with the Er absorption occurring directly. For the emission experiment the SRO matrix plays an active role by absorbing and transferring energy to the Er ions. As a result we suggest that the local electronic environment of the Er is influenced by the presence of excited sensitizers. It is also possible that the electronic structure of the Er ions could be distorted during the energy-transfer process. Further experiments are necessary to determine the role of these mechanisms and local field corrections [164] in the gain enhancement.

## 6.4.4. SRO Matrix Transmission Loss

### Scattering from Si Nanoclusters

We have applied Mie Theory to calculate the propagation loss coefficient from Si nanoclusters imbedded in SiO<sub>2</sub>. In this theory each nanocluster independently scatters the incoming field. The size and density of the nanoclusters is low enough that within the matrix the field scattered by neighboring nanoclusters is small with respect to the external field. The total scattered field can be calculated by adding the individual contribution of each nanocluster. Calculation of the transmission loss requires determining the scattering cross section of each nanocluster from the scattering coefficients and multiplying this scattering cross section by the density of nanoclusters in the matrix. Details of the derivation of the scattering coefficients for a sphere can be found in Bohren and Huffman [101]. Briefly, to determine the scattering efficiency of a sphere of index  $n_1$  embedded in a matrix of index  $n$  you start by expanding the input plane wave in vector spherical harmonics and solving the wave equation in spherical polar coordinates subject to the appropriate boundary conditions. The linearly independent solutions to the wave equation in spherical polar coordinates are spherical Bessel functions. The scattering coefficients,  $a_n$  and  $b_n$ , which represent the amplitude of the field outside of the sphere, are given by

$$a_i = \frac{m \psi_i(mx) \psi_i'(x) - \psi_i(x) \psi_i'(mx)}{m \psi_i(mx) \xi_i'(x) - \xi_i(x) \psi_i'(mx)} \quad (6.29)$$

$$b_i = \frac{\psi_i(mx) \psi_i'(x) - m \psi_i(x) \psi_i'(mx)}{\psi_i(mx) \xi_i'(x) - m \xi_i(x) \psi_i'(mx)} \quad (6.30)$$

where  $\psi_i$  and  $\xi_i$  are Riccati-Bessel functions,  $m$  is the relative refractive index  $m = n_1/n$  and  $x$  is a size parameter  $x = ka$  where  $a$  is the size of the sphere. The scattering cross section which is the ratio of the rate at which energy is scattering at the sphere surface to the incident power is given by



$$C_{scattering} = \frac{2\pi}{k^2} \sum_{i=1}^{\infty} (2n+1) (|a_i|^2 + |b_i|^2) \quad (6.31)$$

The attenuation coefficient due to scattering is given by

$$\alpha_{scattering} = n_{tot} C_{scattering} \quad (6.32)$$

where  $n_{tot}$  is the total density of nanoclusters. In Appendix C we present a Matlab program we used to calculate the scattering cross sections and the attenuation coefficient. In the calculation we assume that the spheres are pure Si and the matrix is stoichiometric SiO<sub>2</sub>. To calculate the scattering loss versus wavelength we calculated the wavelength dependent refractive index for silica using the Sellmeier equation

$$n_{SiO_2}^2 - 1 = \sum_{i=1}^2 \frac{A_i \lambda^2}{\lambda^2 - l_i^2} \quad (6.33)$$

with the coefficients  $A_i$  and  $l_i$  from Ref. 165. For silicon we calculated the wavelength dependent refractive index using the equation from Ref. [166]

$$n_{Si} = A + BL + CL^2 + D\lambda^2 + E\lambda^4 \quad (6.34)$$

with the coefficients A, B, C, D, E and L from the same reference. Figure 6.17 shows the results of the calculation compared to the transmission loss spectrum of the Er-doped SRO sample annealed at 1000°C which showed the presence of Si nanocrystals with 1.5 nm radius under TEM.

We see from Figure 6.17 that the Mie scattering theory accurately predicts the wavelength dependence of the transmission loss but the magnitude of the scattering loss is > 10,000 smaller than what was measured experimentally.

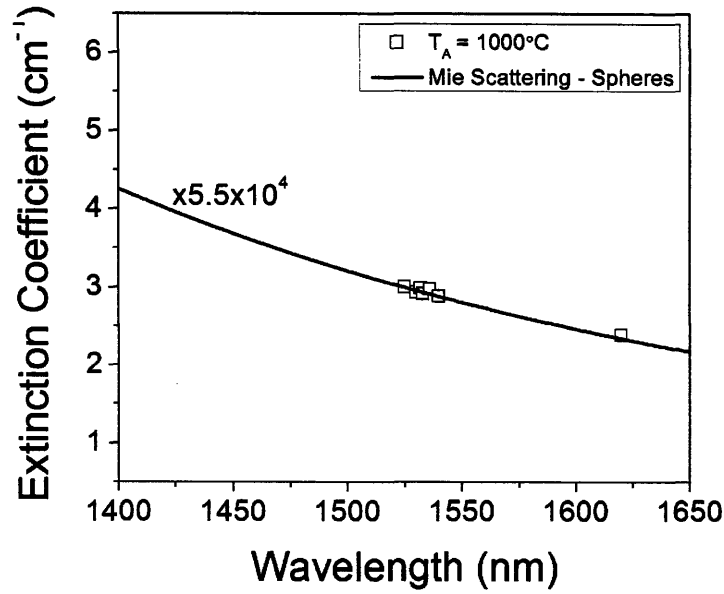


Figure 6.17 Transmission loss spectrum for an Er-doped SRO sample with 36.5 at% Si and an Er concentration of  $1.22 \times 10^{20} \text{ cm}^{-3}$  annealed at  $1000^\circ\text{C}$  (open squares). The solid line is a calculation of the attenuation coefficient assuming  $1.2 \times 10^{17}$  nanocrystals/ $\text{cm}^3$  with a 1.5 nm radius.

## Scattering from the Columnar SRO Medium

The columnar SRO matrix is another potential source of scattering losses which can be calculated through Mie Theory. In this case the column is idealized as a cylinder which is embedded in a uniform matrix. The scattering coefficient  $a_i$  is derived through a approach that is similar to that of spheres embedded in a medium except that in the case of cylinders the solutions to the wave equation in spherical polar coordinates are Bessel's function of the first and second kind. The scattering coefficient for an input field polarized normal to the cylinder axis (TE polarization) is

$$a_i = \frac{mJ'_n(x)J_n(mx) - J_n(x)J'_n(mx)}{mJ_n(mx)H_n^{(1)}(x) - J'_n(mx)H_n^{(1)}(x)} \quad (6.35)$$

The scattering coefficient is given by

$$C_{scattering} = \frac{4at}{x} \left[ |a_0|^2 + 2 \sum_{i=1}^{\infty} |a_i|^2 \right] \quad (6.36)$$

where  $t$  is the film thickness. In Appendix D we present a Matlab program we used to calculate the scattering cross sections and the attenuation coefficient. To calculate the scattering loss due to the columnar film morphology we performed a Cauchy fit of the index of refraction versus wavelength measured by prism coupling for the Er-doped Si-rich SiO<sub>2</sub> slab waveguide sample annealed at 600°C. The index of refraction for the TE and TM polarizations was given by the formula

$$n = A_0 + A_1 \lambda^{-2} + A_2 \lambda^{-4} \quad (6.37)$$

For the TE polarization the coefficients were  $A_0 = 1.5441$ ,  $A_1 = 1.2860 \times 10^4$  and  $A_2 = -6.8099 \times 10^8$ . For the TM polarization the coefficients were  $A_0 = 1.5499$ ,  $A_1 = 9.4680 \times 10^3$  and  $A_2 = 2.8412 \times 10^8$ . The refractive index of the column and boundary region were calculated by solving the system of equations 4.11 and 4.12 with  $f_{column} = 0.83$  and  $f_{boundary} = 1 - f_{column}$ . Figure 6.18 shows the results of the calculation compared to the transmission loss spectrum of the Er-doped SRO sample

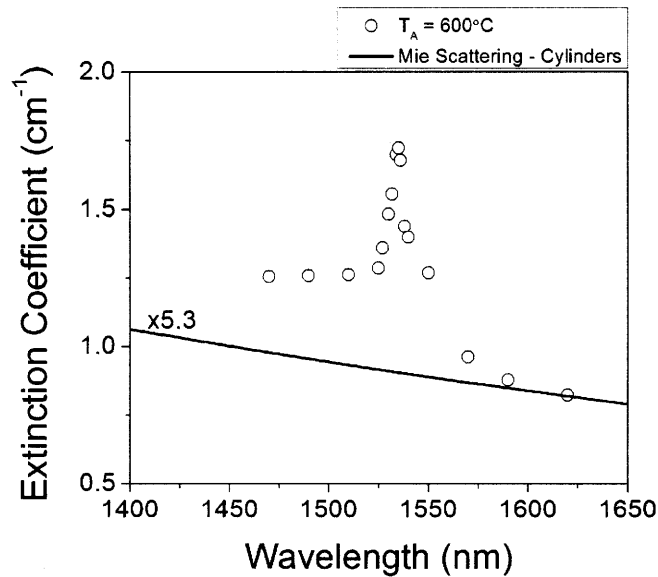


Figure 6.18 Transmission loss spectrum for an Er-doped SRO sample with 36.5 at% Si and an Er concentration of  $1.22 \times 10^{20} \text{ cm}^{-3}$  annealed at 600°C (open squares). The solid line is a calculation of the attenuation coefficient assuming columns of 170 nm radius and a volume fraction of 0.83.

annealed at 600°C.

Unlike the result of the calculation for scattering from spheres, the Mie scattering theory for cylinders does not accurately predict the wavelength dependence of the transmission loss. However, the magnitude of the scattering loss is closer to the values we measured experimentally.

## Effect of Multiple Scattering

The single scattering condition assumed by the calculations of the previous two sections is most appropriate for small scatterers separated by large distances. For a high density of scatterers (such as is the case for the columnar matrix) the propagation of light through the matrix is better described by multiple scattering [167]. In this case the propagation of light is described as a diffusive transport process through a randomly disordered matrix characterized by a mean free path. For the case of scatterers embedded in a matrix of different material the mean free path is given by

$$l = \frac{B'_d \sqrt{\epsilon_2 / \epsilon_{comp}}}{\pi k_{comp} (k_{comp} R)^d} \left[ \int_b^a D(p') O^2(p') dp' \right]^{-1} \quad (6.38)$$

with

$$O(p') = \frac{(\epsilon_{comp} - \epsilon_2)(\epsilon_1 + (d-1)\epsilon_2) + p'(\epsilon_{comp} + (d-1)\epsilon_2)(\epsilon_2 - \epsilon_1)}{(\sqrt{\epsilon_2 \epsilon_{comp}} + (d-1))(\epsilon_1 + (d-1)\epsilon_2) + (d-1)p'(\sqrt{\epsilon_2 \epsilon_{comp}})(\epsilon_1 - \epsilon_2)} \quad (6.39)$$

where  $\epsilon_1$  is the dielectric of the scatterer,  $\epsilon_2$  is the dielectric constant of the matrix,  $\epsilon_{comp}$  is the dielectric constant of the composite material ( $\epsilon = \sqrt{n}$ ),  $k_{comp} = 2\pi n_{comp} / \lambda$ ,  $d$  is the dimension of the system ( $d = 2$  for cylinders,  $3$  for spheres) and  $R$  is the scatterer radius. The coefficient  $B'_d =$

$\frac{2}{\pi}$  and 1 for  $d = 2$  and 3, respectively. The function  $D(p')$  represents the distribution of the local volume fraction of scatterers. If we assume that the local volume fraction of scatterers is a delta function around an average volume fraction  $p$  ( $D(p') = \delta(p' - p)$ ) since the delta function obeys the sifting property

$$\int f(x)\delta(x-x_0)dx = f(x_0) \quad (6.40)$$

equation 6.38 becomes

$$l = \frac{B'_d \sqrt{\epsilon_2/\epsilon_{comp}}}{\pi k_{comp} (k_{comp} R)^d} \left[ \frac{(\epsilon_{comp} - \epsilon_2)(\epsilon_1 + (d-1)\epsilon_2) + p(\epsilon_{comp} + (d-1)\epsilon_2)(\epsilon_2 - \epsilon_1)}{(\sqrt{\epsilon_2 \epsilon_{comp}} + (d-1))(\epsilon_1 + (d-1)\epsilon_2) + (d-1)p(\sqrt{\epsilon_2 \epsilon_{comp}})(\epsilon_1 - \epsilon_2)} \right]^{-2} \quad (6.41)$$

Using the same values for the column and boundary index of refraction versus wavelength from the previous section we calculated the mean free path versus wavelength with the attenuation

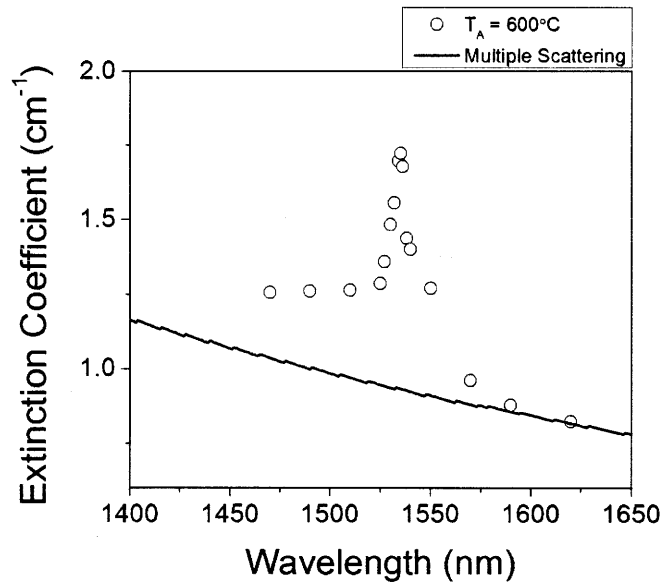


Figure 6.19 Transmission loss spectrum for an Er-doped SRO sample with 36.5 at% Si and an Er concentration of  $1.22 \times 10^{20} \text{ cm}^{-3}$  annealed at  $600^\circ\text{C}$  (open squares). The solid line is a calculation of the attenuation coefficient according to multiple scattering theory with a volume fraction of 0.82 and a scatterer radius of 150 nm.

coefficient is given by the inverse of the mean free path. Figure 6.19 shows a comparison of the calculation with the transmission loss spectrum of the Er-doped SRO sample annealed at 600°C.

As in the Mie Theory calculation of scattering from cylinders, the multiple scattering calculation does not accurately predict the wavelength dependence of the transmission loss. However, there is excellent agreement between the magnitude of the calculated and measured transmission loss when considering scatterers at a volume fraction of 0.82 and a radius of 150 nm. These optimum calculation parameters are very similar to the observed column size (170 nm) and volume fraction (0.83) for as-deposited SRO thin films. Finally, we note that the theory of multiple scattering described above is relevant for the case of disorder small compared to the wavelength of light or  $k_{comp}R \rightarrow 0$ . In this sense the theory of multiple scattering is not as general as the Mie theory. Also since the size of the columns used to calculate the extinction coefficient based on multiple scattering are ~ 10x smaller than the wavelength of light it is not clear how accurate the multiple scattering theory is in describing the transmission loss through the columnar film structure.

## Absorption in the SRO Matrix

The above calculations assume that the index of refraction of the matrix and scatterer are purely real such that there is no contribution to the loss from absorption. Figure 6.20 shows a measurement of the real and imaginary index of refraction measured using a SOPRA spectroscopic ellipsometer for an Er-doped SRO sample after annealing at 600°C for 1 hour. We see from the inset of Figure 6.20 (b) that the imaginary portion of the index of refraction is only equal to 0 for wavelengths > 1.5 μm most likely due to the resolution limit of the instrument. We can calculate the absorption loss coefficient from the imaginary portion of the index of refraction using the equation

$$\alpha = \frac{4\pi k}{\lambda} \tag{6.42}$$

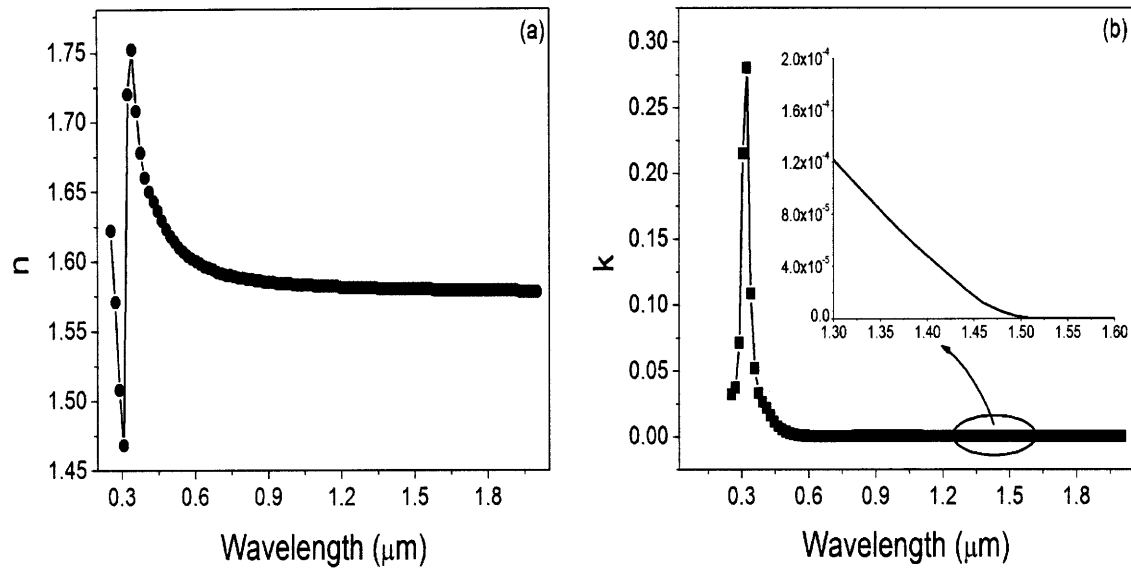


Figure 6.20 Measurement of the (a) real and (b) imaginary index of refraction of an Er-doped SRO sample with a thickness of 1.885  $\mu\text{m}$ , 38 at% Si and an Er concentration of  $8.2 \times 10^{19} \text{ cm}^{-3}$ .

If we consider a  $k$  value of  $6 \times 10^{-6}$  at 1.477  $\mu\text{m}$  we obtain an absorption coefficient of  $0.51 \text{ cm}^{-1}$ .

Since the imaginary portion of the index of refraction is equal to zero in the range of 1 – 2  $\mu\text{m}$  for both Si and  $\text{SiO}_2$  we attribute the non-zero imaginary refractive index to impurities or dangling bonds within the SRO matrix.

We have also observed evidence of Fe incorporation during the process of sputter target conditioning which was performed on new targets to stabilize the sputtering rate. During target conditioning the target was sputtered with the shutter closed at a power of 400 W for 2 hours at a pressure of 3 mTorr of pure Ar. We performed the target conditioning with a  $\text{SiO}_2$  wafer in the chamber and then performed an SRO deposition immediately after the target conditioning. During energy-filtered STEM analysis of the SRO thin film after annealing we observed several large clusters located near the film/substrate interface that did not correspond with the Si or  $\text{SiO}_2$  energy-loss peaks. Figure 6.21 is a bright-field STEM image which where the clusters appear light gray; some of the more prominent clusters are identified with arrows.

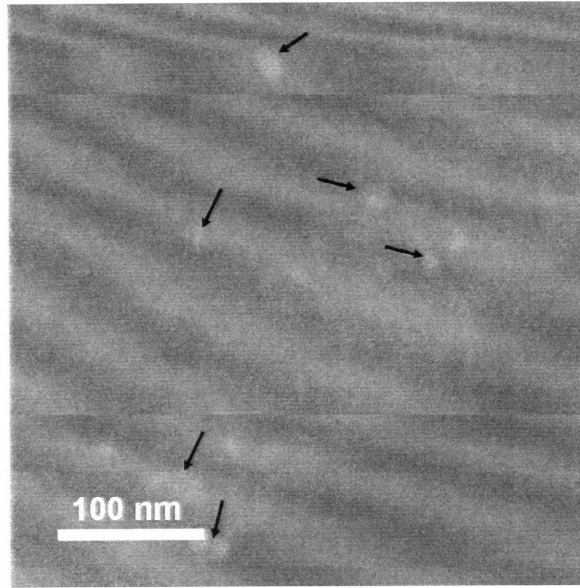


Figure 6.21 Cross section STEM image of an SRO sample with 50 at% Si after annealing at 1100°C for 1 hour.

We performed energy dispersive x-ray analysis of the film in the STEM to determine the composition of the clusters (Figure 6.22).

The spectrum of Figure 6.22 (a) clearly indicates that the clusters are Fe silicate. In comparison the spectra for the SRO film (Figure 6.22 (b)) and SiO<sub>2</sub> substrate (Figure 6.22 (c)) show negligible concentrations of Fe. Since our depositions was performed using a 99.999% pure Si target and the Fe silicate clusters were located near the film/substrate interface we attribute the Fe incorporation to evolution of Fe from the stainless steel shutter or other cathode assembly components during the target conditioning process. This observation indicates the care that is required to minimize impurity incorporation and loss during the target conditioning process.



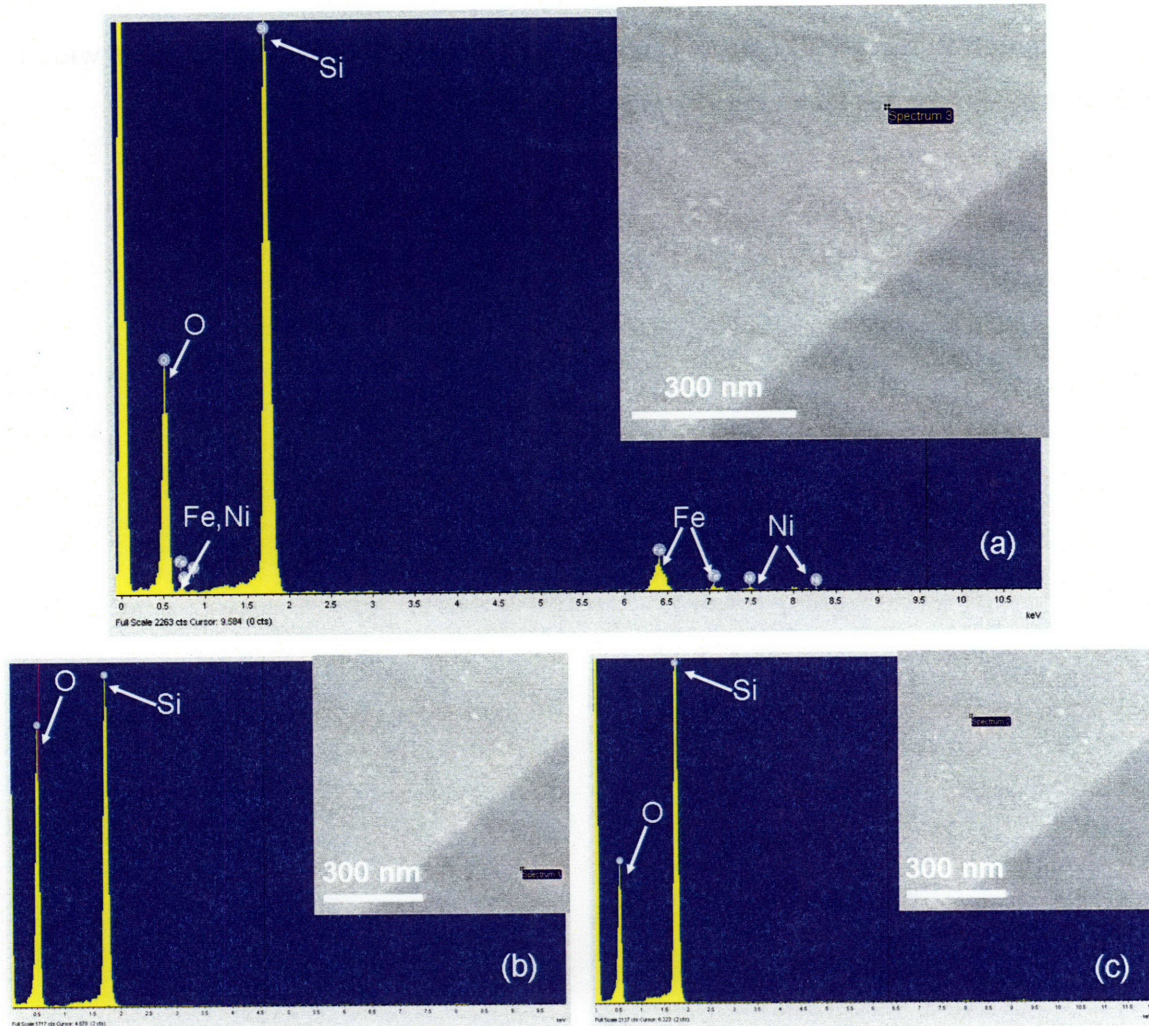


Figure 6.22 (a) Energy dispersive x-ray spectra of (a) the embedded cluster, (b) the SiO<sub>2</sub> substrate and (c) the SRO film. The inset in each spectrum indicates the region of the sample where the x-ray signal was collected.

## Discussion of the Scattering Calculation Results

On the basis of the calculations performed in the previous sections we interpret the origin of the SRO matrix losses as multiple scattering from the columnar matrix with embedded Si nanoclusters with a possible contribution from SRO absorption. An exact calculation of the annealing temperature dependence of the SRO matrix loss using multiple scattering theory would require a calculation of the mean free path with two different local volume fraction distributions of scatterers corresponding to the columns and Si nanoclusters which is not considered here. However, within our interpretation we attribute the increase scattering losses for samples

annealed at high temperatures with this increase in the size of the embedded nanoclusters within the SRO matrix which increases their contribution to the overall scattering loss.

# Chapter 7 | Er-doped SRO Ridge Waveguide Devices

In Chapter 6 we discussed an analysis of the performance of slab waveguides where light is confined in one dimension. Two dimensional confinement can be achieved through patterning of the waveguide layer through photolithography and reactive ion etching techniques. The two dimensional confinement is required to develop complex optical systems for integration through the fabrication of bends [6], splitters [6] and directional couplers [7] for the on-chip routing of light and resonant structures [8,9] necessary to provide optical feedback and lasing. In this Chapter we discuss the design, fabrication and performance of etched ridge waveguides in Er-doped SRO.

## 7.1. Design and Fabrication of SRO Ridge Waveguides

Figure 7.1 shows a schematic of a ridge waveguide.

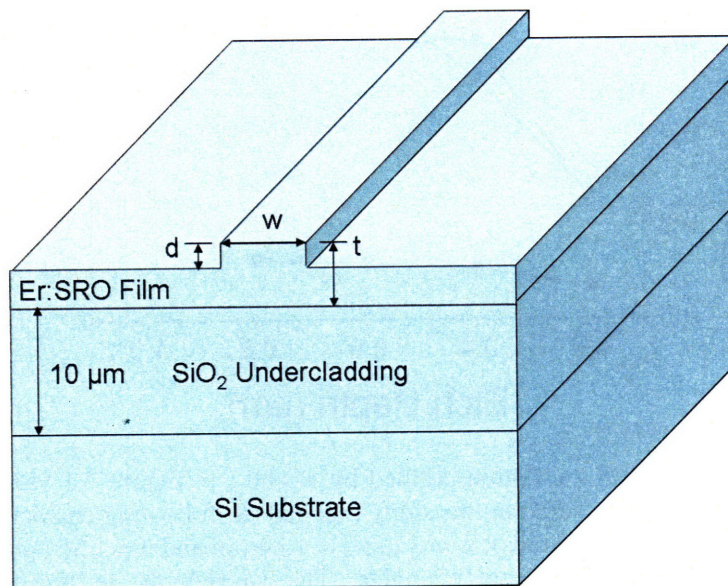


Figure 7.1. Schematic of a ridge waveguide.



The design of these structures requires specifying the parameters  $d$ ,  $w$  and  $t$  to obtain the optimum confinement of light. Figure 7.2 shows the results of simulations using APSS software package from Apollo Photonics where we calculated the power confined in the region defined by  $w$  and  $t$  in Figure 7.1 for three waveguide structures considered in this study.

For the 3  $\mu\text{m}$  wide waveguide structures with indexes of refraction of 1.56 and 1.62 we used etch depths of 0.6  $\mu\text{m}$  and 0.5  $\mu\text{m}$ , respectively to achieve a power confinement factor of  $\sim 80\%$ . For the 9  $\mu\text{m}$  wide waveguide structure with an index of refraction of 1.49 we used an etch depth of 0.4  $\mu\text{m}$  to achieve a power confinement factor of  $\sim 56\%$ .

The fabrication process for forming the Er-doped SRO ridge waveguides is shown in Figure 7.3. We start with a Si wafer with 10 $\mu\text{m}$  thermal  $\text{SiO}_2$  (Figure 7.3 a) and deposit the Er-doped SRO film (Figure 7.3 b). To selectively etch the Er-doped SRO layer we deposit photoresist through a spin on process (Figure 7.3 c) and pattern the photoresist by exposing it through a mask.

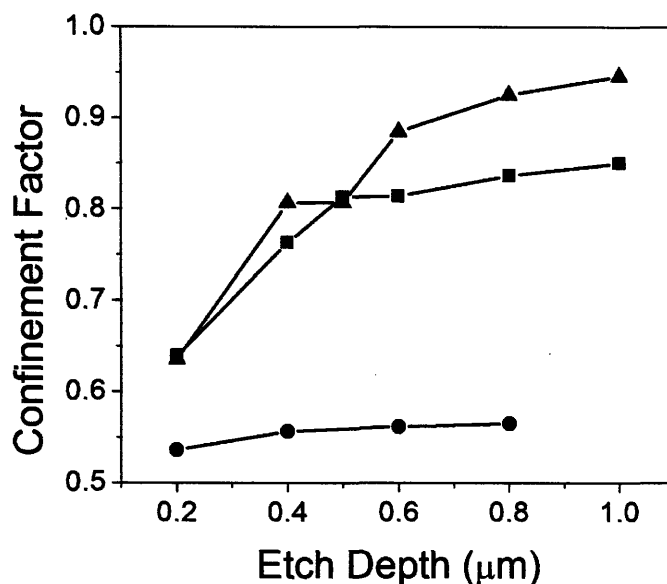


Figure 7.2 Power confined in the region defined by  $w$  and  $t$  in Figure 7.1 versus etch depth for three waveguide samples considered in this study that had the following characteristics:  $w = 9 \mu\text{m}$ ,  $t = 1.38 \mu\text{m}$  and  $n = 1.49$  (solid circles),  $w = 3 \mu\text{m}$ ,  $t = 1.34 \mu\text{m}$  and  $n = 1.56$  (solid squares) and  $w = 3 \mu\text{m}$ ,  $t = 1.81 \mu\text{m}$  and  $n = 1.62$  (solid triangles). The wavelength used for the calculation was 1.551  $\mu\text{m}$  with  $n = 1.444$  for the 10  $\mu\text{m}$  thick  $\text{SiO}_2$  undercladding and  $n = 3.48$  for the Si wafer. The waveguide overcladding is air.

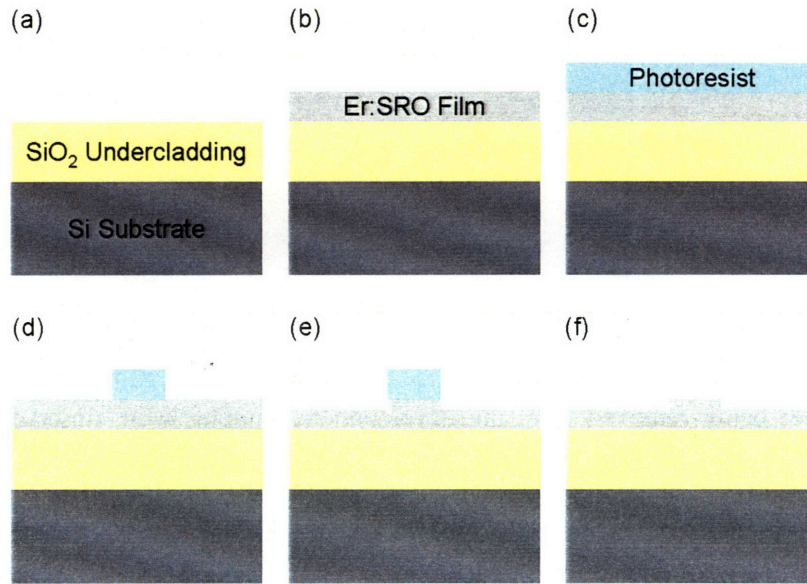


Figure 7.3 Fabrication process for forming ridge waveguides. A description of each step is given in the text.

The exposed areas are then removed with developer (Figure 7.3 d). The photoresist was then hard-baked and used as the etch mask. The exposed Er-doped SRO layer was etched (Figure 7.3 e) using a Plasmatherm 300 Series reactive ion etcher. The process parameters that gave us the smoothest etch surface were a pressure of 20 mTorr with 40 sccm of  $\text{CHF}_3$  as the etch gas at a power of 300 W. Since there was no etch stop layer the etch depth was controlled by limiting the time of the etch. The etch rate under these conditions was  $\sim 16 - 19$  nm/minute. After the reactive ion etch step the photoresist was removed (Figure 7.3 f) using a piranha solution (3:1 ratio of sulfuric acid to hydrogen peroxide).

After the processing of our first devices we noticed a roughening of the wafer surface after the etch. As a simple test we immersed a SRO thin film sample in the developer to observe if there was an interaction between the columnar film and the developer when removing the exposed photoresist (Figure 7.3 d). We considered two different development times along with one control sample that was not exposed to the developer. Before being placed into the RIE all the samples were rinsed in DI water for 1 minute. The film surface after etching for the three samples is shown in Figure 7.4. We can see that the etch surface is significantly roughened for development times  $\leq 1$  minute. This correlation between surface roughness after etching and



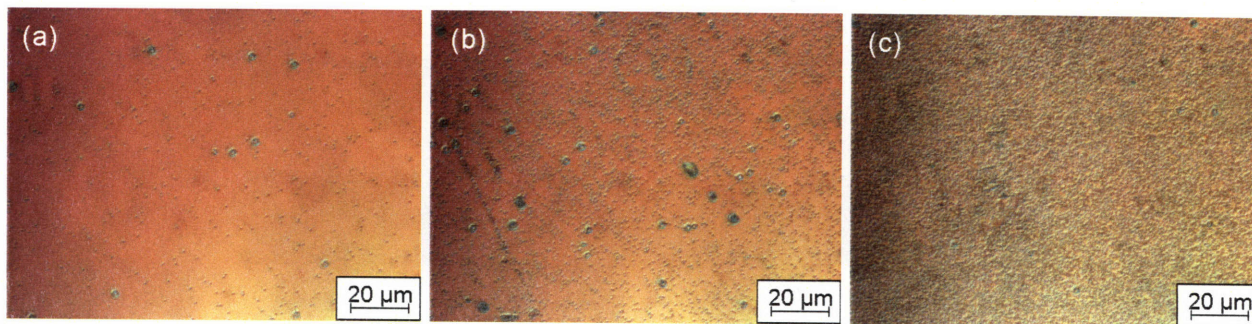


Figure 7.4 Etch surface of SRO films after being exposed to the AZ422 developer for 0, 1 and 5 minutes. After being removed from the developer the samples were rinsed in DI water for 1 minute. The etch parameters used for all samples were 20 sccm  $\text{CHF}_3$  at 300 W RF power and a pressure of 20 mTorr for 22 minutes. All images were taken at 100x using circularly polarized differential interference contrast.

development time suggests that minimizing the time in the developer would yield a better etched surface. As a result we optimized the exposure parameters of our process to limit the maximum development time to  $\sim 1$  minute. The problem of surface roughening was also reduced by lowering the pressure during the etch. Figure 7.5 (a) shows an optical microscope image of Er-doped Si-rich  $\text{SiO}_2$  ridge waveguides fabricated using the techniques described above.

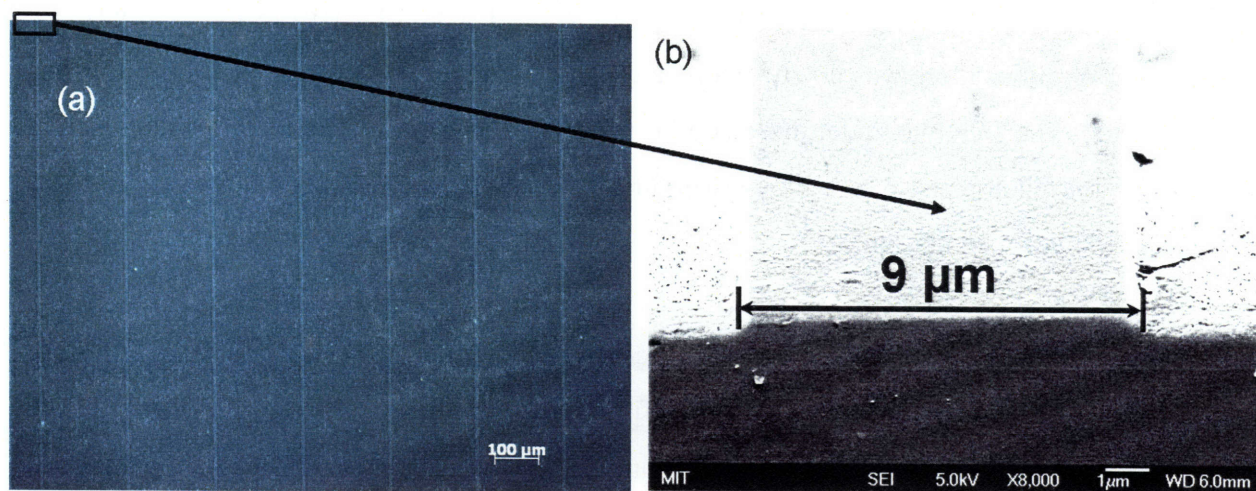


Figure 7.5 (a) Er-SRO ridge waveguides on a silica substrate. The etch parameters used were 20 sccm  $\text{CHF}_3$  at 300 W RF power and a pressure of 20 mTorr for 23.25 minutes. The etch depth was  $\sim 0.4 \mu\text{m}$ . The image was taken at 10x using circularly polarized differential interference contrast. (b) Scanning electron microscope image of the  $\sim 9 \mu\text{m}$  wide waveguide at the input facet indicated by the black box in panel (a).

## 7.2. Transmission Loss – The Cutback Loss Technique

### 7.2.1. Description of the technique and apparatus

To measure losses in straight waveguides we performed the cutback loss technique. In this measurement technique the waveguide is trimmed between measurements to obtain measurements of insertion loss (combination of the loss due to propagation through the waveguide and input/output coupling losses) versus propagation length. In our case we cleaved the output end of the waveguide in 2 mm increments which left a consistent smooth edge for out coupling. The measurements were performed using a Newport Auto-Align station and a JDS Uniphase Swept Wavelength System using Nanonics lens-tipped fibers with a mode field diameter of 1.7  $\mu\text{m}$  for input and output coupling to the waveguide. To perform the measurement, a coarse alignment of the input fiber to the waveguide is performed by observing the output laser spot using a microscope objective and IR camera. Fine alignment was performed using the computer controlled Auto-Align system which maximizes the output power by moving the input and output fibers in the lateral, vertical and focusing directions. The Swept Wavelength system,

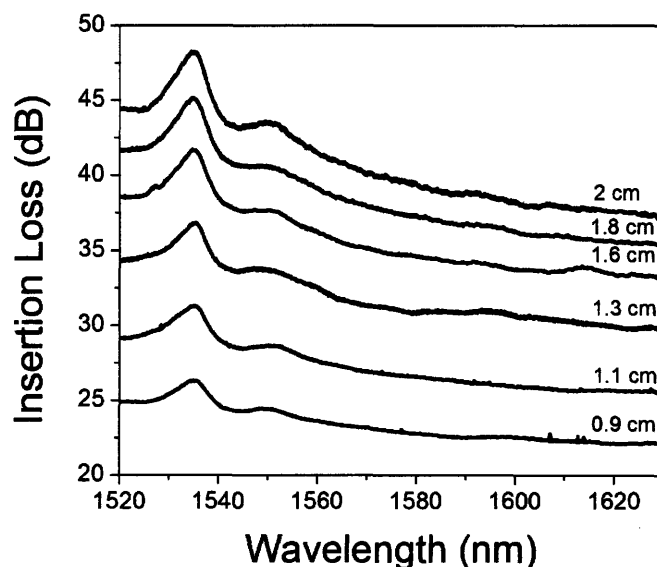


Figure 7.6 Insertion loss versus waveguide length for a 3 $\mu\text{m}$  wide Er-doped SRO waveguide with 0.5 $\mu\text{m}$  etch depth, 38 at% Si, an Er concentration of  $1 \times 10^{20} \text{ cm}^{-3}$  annealed at 600°C for 1 hour.

which consists of a tunable laser, polarization controller and optical detectors, was then used to measure the polarization dependent insertion loss of the waveguide. Figure 7.6 shows measurements of insertion loss for various waveguide lengths. Since the coupling loss contribution is independent of sample length we fit the insertion loss data for various lengths with an exponential decay at each wavelength. This allowed us to determine the wavelength dependent propagation loss coefficient.

## 7.2.2. Er-doped SRO Ridge Waveguide Losses and Comparison to Prism Coupling

The cutback loss technique allowed for the measurement of the transmission loss spectrum of our ridge waveguide devices. The spectra obtained for samples annealed at 600°C and 1100°C are shown in Figure 7.7 along with the loss measured through the prism coupling technique for the slab waveguide device in Chapter 6.

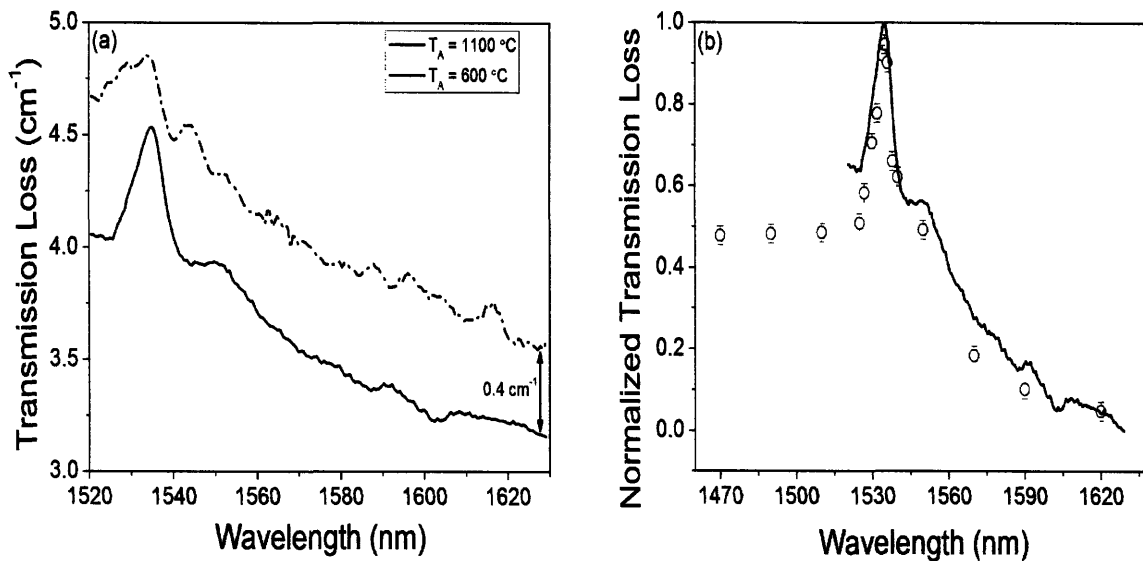


Figure 7.7 (a) Comparison of the transmission loss for Er:SRO ridge waveguides with 3 $\mu\text{m}$  width and 0.5  $\mu\text{m}$  etch depth, an Er concentration of  $1 \times 10^{20} \text{ cm}^{-3}$  and 38 at% Si annealed for 1 hour at 600°C (solid line) and 1100°C (dash-dot line). (b) Normalized transmission loss for the Er:SRO ridge waveguide from panel (a) (solid line) and the Er:SRO slab waveguide analyzed in Chapter 6 (open circles). Both waveguides were annealed at 600°C for 1 hour.



For the cutback loss measurements waveguides annealed at 600°C and 1100°C (Figure 7.7 (a)) the spectra show the typical Er absorption peak near 1535 nm. We also notice the background loss measured at 1630 nm is larger in the sample annealed at 1100°C, in agreement with the prism coupling measurements of Chapter 6. Additionally we notice that the background loss of the ridge waveguides is very high, greater than 12 dB/cm. We attribute the additional loss to losses introduced during the waveguide fabrication process. Figure 7.7 (b) shows the comparison of the cutback loss measurements to those obtained through prism coupling. Although the background losses measured for the two cases were different the shape of the spectra are in excellent agreement confirming the accuracy of the two techniques for measuring the transmission loss spectra of our samples.

## **7.3. Optical amplification – The Pump and Probe Technique**

### **7.3.1. Description of the technique and apparatus**

Figure 7.8 shows a schematic of the pump and probe optical gain setup developed for this study. Light from an amplitude modulated, tunable infrared laser was input into the ridge waveguide using a lens tipped fiber with a 1.7  $\mu\text{m}$  mode field diameter. The lens tipped fiber was mounted on a piezoelectric stage so the vertical and horizontal position of the fiber tip with respect to the waveguide end facet could be precisely controlled to optimize the coupling of light into the waveguide. The light output from the waveguide was collected by a 20x microscope objective and detected by an InGaAs detector. The signal from the detector was input into a lock-in amplifier referenced to the modulation frequency of the tunable laser. The modulation frequency was set at 10 kHz to remove the spontaneous emission (photoluminescence) from the detected signal. The last 1 mm of the sample was pumped from overhead at 488 nm through a cylindrical lens which focused the pump beam to a line  $\sim 40$   $\mu\text{m}$  wide on top of the waveguide. The cylindrical lens was attached to a three-axis stage on a goniometer to minimize the angle  $\alpha$  between the waveguide and the pump stripe and optimize the overlap between the pump stripe

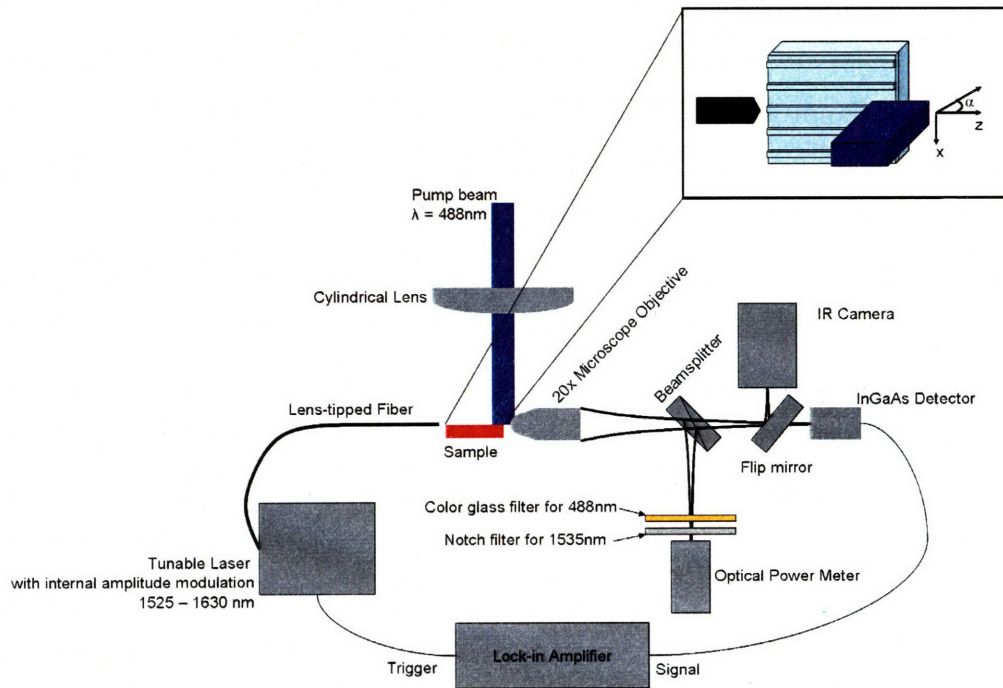


Figure 7.8 Schematic of the pump and probe measurement setup.

and the waveguide in the  $x$  direction. A camera (not shown in the schematic) was mounted along the side of the sample at a  $45^\circ$  angle with respect to the sample surface to ensure perfect overlap between the pump beam and the waveguide. We used the following alignment procedure:

1. With the pump beam blocked the fiber was coupled to the waveguide of interest and the intensity the transmitted beam was roughly optimized by viewing the output spot on an infrared camera
2. The position of the detector and optical power meter was adjusted to maximize the measured signal; a fine alignment of the input fiber to the end of the waveguide was performed using the piezoelectric-controlled stage.
3. The probe beam was turned off and the pump beam was shined on the sample surface. The photoluminescence signal was optimized by varying the angle,  $\alpha$ , the  $x$  position and  $z$  position of the beam. The maximum signal was observed for a  $z$  position such that half of the beam was illuminating the sample.

Once the alignment procedure was complete the probe signal was measured using a lock-in amplifier referenced to the modulation frequency of the laser with and without pumping.

## 7.3.2. Measurement of Er:SRO Samples

### Thermal Effects in Waveguides Deposited on Clad Silicon Wafers

Figure 7.9 shows the results of the pump and probe experiment performed on a ridge waveguide deposited on a clad Si wafer similar to the device shown schematically in Figure 7.3. We observed that the detected probe signal decreased during pumping for all pump-power densities suggesting that the effect of the pump is only to induce losses within the waveguide. To understand the origin of this induced loss we performed a time-resolved pump and probe measurement. The probe signal wavelength was changed to 1310 nm which is not resonant with any Er absorption/emission band. The pump beam was mechanically chopped at a frequency of 10 Hz with the measured probe signal triggered to the pump frequency. Figure 7.10 shows the results of measurements performed at low and high pump-power densities. When the pump is on

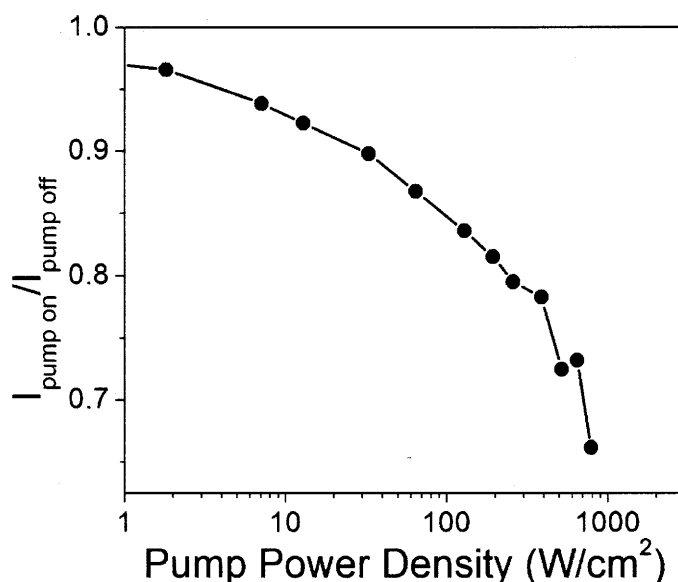


Figure 7.9 Ratio of the probe signal with the pump on to the probe signal with the pump off versus pump-power density for an Er-doped SRO ridge waveguide sample with 36.5 at% Si annealed at 600°C for 1 hour. The waveguide width was 3  $\mu\text{m}$ , the probe wavelength was 1.535  $\mu\text{m}$ , the probe power was 200  $\mu\text{W}$  and the probe frequency was 10 kHz.

we notice that the decay of the probe signal (Figure 7.10 (a) and (b)) has an initial fast component with a characteristic time of 0.5 – 1 ms followed by a slow recovery. When the pump is off the signal recovers as a single exponential with a recovery time greater than 1 ms. This recovery time when the pump is off is longer than the typical exciton lifetime in SRO (1 - 100  $\mu$ s). We calculate an effective absorption length of the pump in the waveguide layer of  $\sim 200$   $\mu$ m from the excitation cross section ( $1 \times 10^{-17}$   $\text{cm}^2$  and sensitizer density  $6 \times 10^{18}$   $\text{cm}^{-3}$ ). Since a thin waveguide layer ( $< 2$   $\mu$ m) is used to achieve signal mode propagation a significant amount of the pump light will be absorbed in the Si substrate and induce local heating. The measured recovery times in the milliseconds is consistent with the influence of thermal gradients on the propagation. The observed recovery while the pump is on is also consistent with thermal effects since the magnitude of the effect is proportional to the thermal gradient. We expect the largest gradient immediately after the pump is introduced followed by a gradual reduction as the system enters a

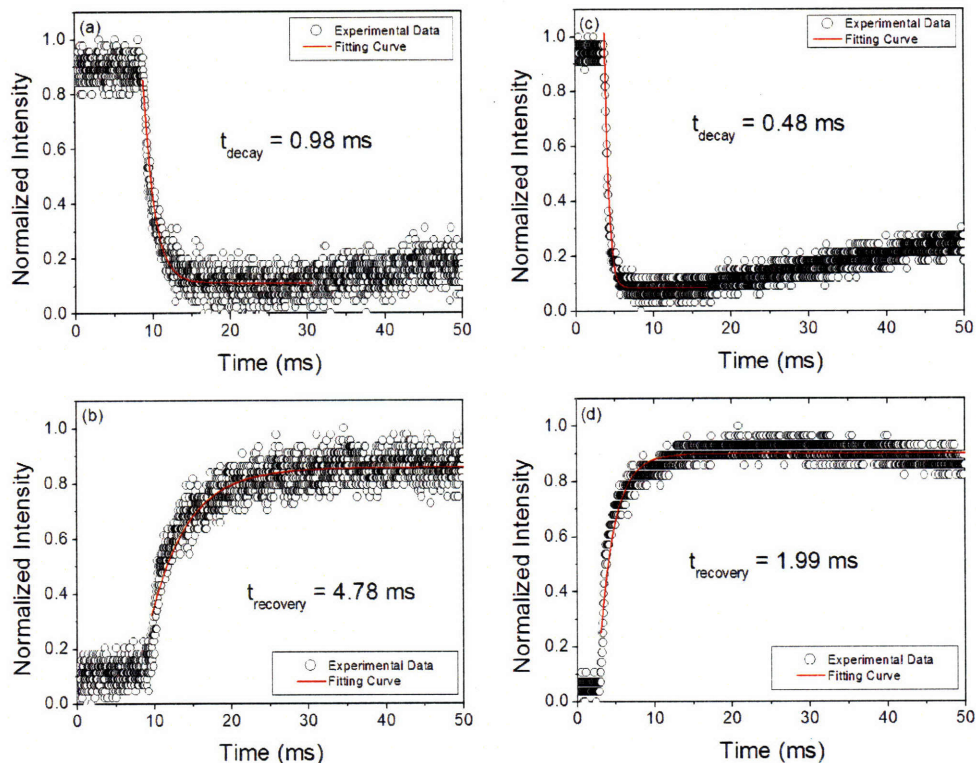


Figure 7.10 (a) Decay and (b) recovery of the probe intensity at a pump-power density of 55 W/cm<sup>2</sup> for an Er:SRO ridge waveguide sample with 36.5 at% Si and  $1 \times 10^{20}$  ions/cm<sup>3</sup> annealed at 600°C for 1 hour. (c) Decay and (d) recovery of the probe intensity at a pump-power density of 788 W/cm<sup>2</sup> for the same waveguide. The probe wavelength was 1310 nm. The measurement was triggered to the 488 nm pump chopping frequency of 10 Hz. The solid lines are exponential decay and rise fits to the data with decay and recovery times as indicated on the figure.

steady-state.

## Signal Enhancement in Waveguides Deposited on Fused Silica Wafers

In the previous section a large induced loss that we interpret as thermal effects due to the absorption of the pump light in the Si substrate prevented the observation of signal enhancement. To avoid any potential substrate heating effects we fabricated ridge waveguides on an SiO<sub>2</sub> substrate (see Figure 7.5). Additionally, when performing the experiment we placed the pumped region of the sample off the sample holder such that the residual pump signal would pass through the sample to the table surface below. Figure 7.11 shows the results of the pump and probe experiment performed on a sample with 35.75 at% Si annealed at 600°C for 1 hour. For pump-power densities greater than 100 W/cm<sup>2</sup> we observed signal enhancement with a maximum enhancement of 3% for the highest pump-power density considered in this measurement.

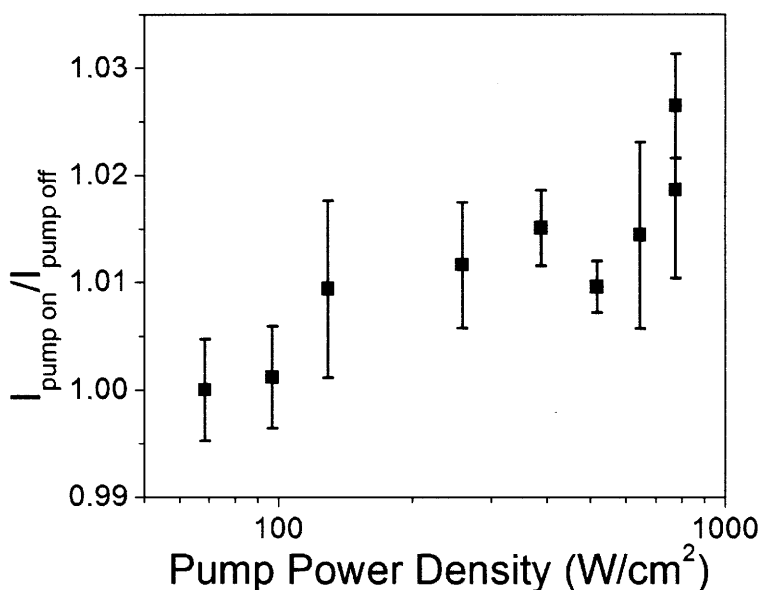


Figure 7.11 Ratio of the probe signal with the pump on to the probe signal with the pump off versus pump-power density for an Er-doped SRO ridge waveguide sample with 35.75 at% Si and an Er concentration of  $8.3 \times 10^{19}$  ions/cm<sup>3</sup> annealed at 600°C for 1 hour. The waveguide width was 9  $\mu$ m, the probe wavelength was 1.535  $\mu$ m, the probe power was 100  $\mu$ W and the probe frequency was 10 kHz.



We calculated a signal enhancement coefficient using

$$s = \frac{1}{\Gamma L} \ln \left( \frac{I_{pump\ on}}{I_{pump\ off}} \right) \quad (7.1)$$

where  $\Gamma$  is the waveguide confinement factor and  $L$  is the pumping length. Figure 7.12 shows the dependence of the calculated signal enhancement coefficient on the pump-power density. From Figure 7.12 we see that the maximum signal enhancement coefficient is  $\sim 2.2$  dB/cm. If the entire Er population was inverted we would expect to observe a total signal enhancement of at least 6 dB/cm. Since the measured value is smaller than half the expected saturation signal enhancement we conclude that population inversion has not occurred and the observed signal enhancement is due to bleaching of the Er absorption. We can estimate the fraction of the Er ions in the excited-state from signal enhancement coefficient according to the equation

$$\theta_{Er,excited} = \frac{s}{2\sigma_{emis} N_{tot}} \quad (7.2)$$

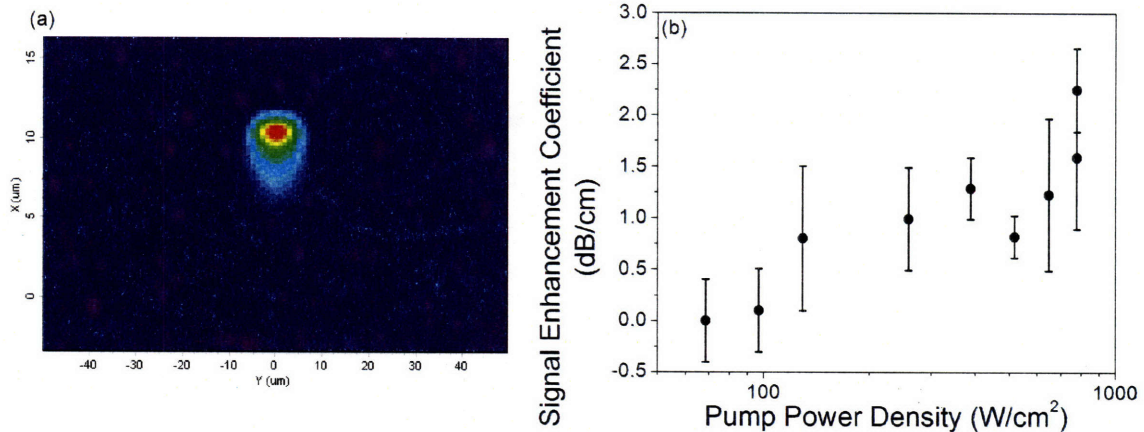


Figure 7.12 (a) Optical mode profile for the Er-doped SRO waveguide on a SiO<sub>2</sub> substrate considered in this experiment. The mode profile was calculated using the Apollo Photonics, Inc. APSS software. (b) Calculate signal enhancement coefficient from the signal enhancement data reported in Figure 7.10 using equation 7.1. For the calculation we used a waveguide confinement factor of 0.55 and a pumping length of 0.09 cm.

Table 7.1 Guided photoluminescence intensity and signal enhancement coefficient for the Er-doped SRO waveguide with 35.75 at% Si and an Er concentration of  $8.3 \times 10^{19}$  ions/cm<sup>3</sup> annealed at 600°C for 1 hour at a pump-photon flux of  $2.3 \times 10^{20}$  photons/cm<sup>2</sup>s for both pumping wavelengths.

Pump Wavelength (nm)	Guided PL Intensity (nW)	Signal Enhancement Coefficient (dB/cm)
457 nm (Non-resonant)	$44 \pm 1$	$0.44 \pm 0.35$
488nm (Resonant)	$46 \pm 1$	$0.72 \pm 0.35$

Assuming  $\sigma_{emis} = 7 \times 10^{-21}$  cm<sup>2</sup>, and that all of the Er in the medium is optically active, we calculate an excited-state fraction of 0.36. If we chose to perform the calculation using the enhanced emission cross section derived from the VSL measurements of  $\sigma_{emis} = 3.5 \times 10^{-20}$  cm<sup>2</sup> the calculated excited-state fraction would be reduced to 0.07.

In addition to the experiment describe above we measured the guided photoluminescence and signal enhancement coefficient under resonant (488 nm) and non-resonant conditions (457 nm); the results are shown in Table 7.1. Since the guided photoluminescence intensity and signal enhancement coefficient are equivalent within the error of the measurement for both pumping conditions we conclude that the observed signal enhancement due to stimulate emission is achieved through sensitized excitation of the Er ions through energy-transfer from the SRO matrix.

# Chapter 8 | Conclusions and Future Work

We have performed a systematic study of the effect of nanostructure on the optical properties Si-rich SiO<sub>2</sub>. We have identified three different size scales to the nanostructure that have application to the fabrication of high-performance optical devices. These are shown schematically in Figure 8.1.

The most widely investigated size scale is the Si nanocrystal which shows Er emission sensitization and the strongest light emission from SRO. The challenge was to develop a more CMOS compatible processing technology by investigating Er emission sensitization for low annealing temperatures. Through our study we have demonstrated Er excitation and non-resonant excitation through SRO can be achieved for annealing temperatures as low as 600°C through the optimization of nanostructure occurring at size scales smaller than Si nanocrystals achieved through high temperature annealing. Through a comparison of the excitation cross section for Er-doped SRO samples with and without observable nanocrystals along with rate equation modeling of the SRO – Er system we have demonstrated that the stronger Er emission sensitization is due to a combination of a more efficient energy-transfer process and a higher density of sensitizing

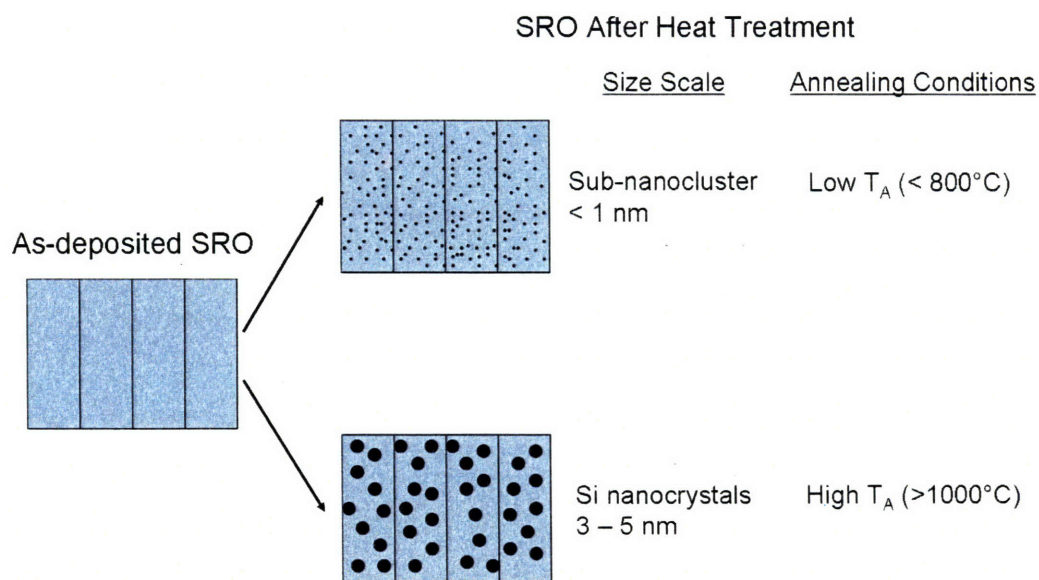


Figure 8.1 Schematic of the size scale of the nanostructure considered in this thesis.



centers. Our temperature-resolved photoluminescence study confirmed that the Er emission sensitization for samples annealed at high temperatures occurs through Si nanocrystals while demonstrating the existence of a completely different emission sensitizer for samples annealed at low temperatures which is characterized by a weak room temperature light emission and a temperature dependence that follows a typical defect ionization trend consistent with localized defects within the SRO matrix.

The literature discussing Si nanocrystal properties, including our results, has defined the optimum processing parameters as those that reduce the nanocrystal size and improve the crystalline quality to achieve strong quantum confinement and enhance the probability of radiative recombination. For low annealing temperatures the conditions required to optimize the energy-transfer are not clearly understood due to a lack of understanding of the detailed mechanism of the energy-transfer process and the lack of a microscopic structural model of the sensitizing center. We suggest that a study of the defects in SRO through spin resonance techniques and high-resolution energy filtered transmission electron microscopy along with a thorough study of the annealing time and temperature dependence of the Er emission sensitization process should be performed to identify the emission sensitizer and the nature of the sensitization process.

Our study of the performance of Er-doped SRO slab waveguides has demonstrated stimulated emission and large optical gain of  $3.5\text{cm}^{-1}$ , reduced passive losses and no carrier induced loss in samples annealed at low temperatures. This suggests a possible route for the fabrication of compact, high-gain planar light sources and amplifiers with a low thermal budget for integration with standard Si CMOS processes. The current limitation of this technology are the high transmission losses of the sputtered SRO material. The lower losses demonstrated for samples annealed at low temperatures is an added benefit to the low temperature process. Further studies are required to identify the specific mechanism leading to lower transmission losses at low temperatures and to minimize this loss in SRO. We suggest a study of the influence of the sputter deposition parameters of deposition pressure, substrate temperature and including bias sputtering to determine their effect on the film structure and the loss. Also routes to directly incorporate Er into films deposited by chemical vapor deposition techniques should also be considered since the

lowest transmission losses ( $<2$  dB/cm) for SRO have been demonstrated in PECVD deposited SRO. A comparison of sputtering and CVD techniques would also help to determine if the principles leading to strong Er emission enhancement for low annealing temperatures are general to SRO or a unique feature of the sputtered material. A related unresolved problem is the enhancement of the Er emission cross section in SRO under pumping. Further experiments must be performed to identify the detailed mechanism leading to a cross section enhancement. A careful analysis of pump and probe experiments performed on optimized Er-doped SRO ridge waveguides would help to confirm the magnitude of the gain enhancement. Identifying the energy-transfer mechanism and development of a structural model for the sensitizer center would also help in identifying the mechanism of the gain enhancement.

All of these processes are occurring within a matrix that also has nano-scale structure. We have demonstrated optical anisotropy with a sign and symmetry that can be explained according to an effective-medium model for the columnar film morphology which is formed through the sputter deposition process. The large birefringence, more than 3%, generated in these films enables the fabrication of polarization dependent devices, normally reserved for anisotropic crystals, using Si and SiO<sub>2</sub> which are optically isotropic. Since the large birefringence is achieved after annealing these films are also more robust than traditional birefringent sculptured thin films which have a high porosity and are susceptible to environmental conditions. Our analysis of the origin of the birefringence enhancement suggests that a sintering process involving flow of SiO molecules creating high-index regions previously occupied by the porous boundary is responsible for the enhancement. Further analysis is required to confirm this mechanism of the birefringence enhancement. If confirmed, the high Si concentration at the boundary region could be used to achieve spatial control of nanocrystal nucleation through a self-assembled process. This process could be further refined to fabricate nanocrystal chains for enhanced electrical injection and the fabrication of optoelectronic devices. Additionally, modifying the sputtering process by depositing at a glancing angle to achieve the formation of a columnar morphology oriented at 45° would allow for the fabrication of half-wave and quarter-wave plates to modify the polarization state of light on chip.

The columnar film structure is a potential source of the high transmission losses of our films compared to those prepared by chemical vapor deposition techniques. Comparison to studies of columnar structure formed through ion-assisted processes suggests a fourth critical length scale in these films: the film thickness. In the ion-assisted process the size scale of the columnar structure could be controlled through the film thickness with the finer structure formed for the thinnest films. A study should be conducted to determine if the size scale for the columnar structure could be controlled through the film thickness as a means to minimize the transmission loss and optimize the birefringence.

# **Appendix A | Computing the Effective Index, Confinement Factor and E-field Profile for Optical Modes in a Slab Waveguide**

In this appendix we present a Matlab program to calculate the effective index, power confinement factor and E-field or H-field profile for an arbitrary slab waveguide for TE or TM polarizations. After the user specifies the index of refraction for the core and cladding layers, the core thickness, wavelength and polarization the program calls the function `slabtransTE.m` or `slabtransTM.m` to solve the transcendental equation for the effective index of the first mode in the waveguide (equation 6.14 for the TE polarization and equation 6.19 for the TM polarization). Once the effective index is known the power confinement factor is calculated from equation 6.22 for the TE polarization and from equation 6.23 for the TM polarization. The E-field profile is generated from equation 6.3 for the TE polarization and the H-field profile is generated from equation 6.15 for the TM polarization. The program also allows the user to plot the E-field or H-field profile as well as save the profile to a data file.

## effslab.m

```
global lamda d n0 n1 n2 %Define variables as global so they can be
                        %Accessed by the function slabtrans.m

%Define sample parameters
lamda=1551e-9; %wavelength of light
n1=input('Enter core index: ');
n1=1.5465; %core
n0=1; %top cladding
n2=1.444; %bottom cladding (substrate) index
%thickness=input('Enter core thickness in microns: ');
thickness=1.3;
d=thickness*1e-6; %core layer thickness
k=2*pi/lamda;

%Calculate single mode cutoff thicknesses
if(n0==n2) %single mode cutoff thickness for symmetric case
    message='symmetric'
    tg=pi/(sqrt(n1^2-n2^2)*k);
    tg*1e9
else %single mode cutoff thickness for asymmetric case
    message='asymmetric'
    tg1=(atan(sqrt(n2^2-n0^2)/sqrt(n1^2-n2^2)))/(sqrt(n1^2-n2^2)*k);
    disp('The single mode cutoff is: ')
    tg1*1e9
end

%polarization = input('Which polarization should be calculated (TE or TM): ',
's');
%polarization = 'TE';
polarization = 'TM';

polTE=strcmp(polarization,'TE');
polTM=strcmp(polarization,'TM');

%Determine the normalized propagation parameter b from the root of the
%transcendental equation from the slab waveguide and solve for the
%effective index, neff, of the waveguide

if(polTE==1)
    disp('The polarization is TE.')
    %neffguess=input('Enter guess for the effective index: ');
    neffguess=1.5; %guess for effective index of the guided mode
    bguess=(neffguess^2-n2^2)/(n1^2-n2^2); %guess for b parameter
    options=optimset('Display','iter'); % Turn off Display
    %Given the guessed b parameter call the function slabtrans which
    %solves the transcendental equation for a slab waveguide and returns the
    %value for b
    [b,Fval,exitflag]=fsolve(@slabtransTE,bguess,options); % Call optimizer
    neff=(b*(n1^2-n2^2)+n2^2)^(1/2) %calculate the effective index
                                    %using the b parameter from the
                                    %solver
    %Calculate the power confinement factor in the core
    beta=k*neff; %calculate propagation constant
    %Define layer characteristics
```

```

kx=sqrt(k^2*n1^2-beta^2);    %core
alphac=sqrt(beta^2-k^2*n0^2);    %top cladding
alphas=sqrt(beta^2-k^2*n2^2);    %bottom cladding (substrate)
phi=kx*d-atan(alphas/kx);
%Calculate the power fraction in each layer from the integral of the
%E-field in each layer
syms x;
%Power fraction in the top cladding layer
Pclad=int(((cos(phi)*exp(-alphac*(x)))^2),0,inf);
Pclad=double(Pclad);
%Power fraction in the bottom cladding (substrate) layer
Psubs=int(((cos(-kx*d+phi)*exp(alphas*(x+d)))^2),-inf,-d);
Psubs=double(Psubs);
%Power fraction in the core layer
Pcore=int(((cos(kx*x+phi))^2),-d,0);
Pcore=double(Pcore);
%Power confinement factor in the core layer
Pconf=Pcore/(Pcore+Pclad+Psubs)
%Calculate the E-field profile in the waveguide along with the
%index profile of the waveguide
%Define the structure thickness from top to bottom
simwin=10;
dimension=simwin*20000+1;
%Initialize matrices
E=zeros(1,dimension);
n=zeros(1,dimension);
pos=zeros(1,dimension);
%Define the E-field in each layer
for(i=1:1:dimension)
    y=(i-dimension/2)/20;
    dbottom = -d*10^(9);
    dtop = 0;
    %E-field and index profile in top cladding layer
    if(y>=dtop)
        E(1,i)=(cos(phi)*exp(-alphac*(y*10^(-9))));
        n(1,i)=n0;
    %E-field and index profile in the bottom cladding (substrate) layer
    elseif(y<=dbottom)
        E(1,i)=(cos(-kx*d+phi)*exp(alphas*(y*10^(-9)+d)));
        n(1,i)=n2;
    %E-field and index profile in the core layer
    elseif((y<dtop) & (y>dbottom));
        E(1,i)=(cos(kx*y*10^(-9)+phi));
        n(1,i)=n1;
    end
    pos(i)=y/1000;
end

%Plot E-field and index profiles in the waveguide
[AX,H1,H2] = plotyy(pos,E,pos,n,'plot');
%Label the axes
set(get(AX(1),'Ylabel'),'String','Normalized E-field');
set(get(AX(2),'Ylabel'),'String','Index of Refraction');
xlabel('Position (nm)');
%Add plot title
title('E-field and Index Profiles of the Slab Waveguide');

```

```

%Create matrix to output the E-field profile in the waveguide
dataprof=[pos',E'];
dataindex=[pos',n'];

%Write E-field data to file
csvwrite('profile.dat',dataprof);
csvwrite('indexprof.dat',dataindex);

elseif(polTM==1)
disp('The polarization is TM.')
%neffguess=input('Enter guess for the effective index: ');
neffguess=1.5; %guess for effective index of the guided mode
bguess=(neffguess^2-n2^2)/(n1^2-n2^2); %guess for b parameter
options=optimset('Display','iter'); % Turn off Display
%Given the guessed b parameter call the function slabtrans which
%solves the transcendental equation for a slab waveguide and returns the
%value for b
[b,Fval,exitflag]=fsolve(@slabtransTM,bguess,options); % Call optimizer
neff=(b*(n1^2-n2^2)+n2^2)^(1/2) %calculate the effective index
%using the b parameter from the
%solver

%Calculate the power confinement factor in the core
beta=k*neff; %calculate propagation constant
%Define layer characteristics
kx=sqrt(k^2*n1^2-beta^2); %core
alphac=sqrt(beta^2-k^2*n0^2); %top cladding
alphas=sqrt(beta^2-k^2*n2^2); %bottom cladding (substrate)
phi=kx*d-atan(n1^2*alphas/(n2^2*kx));
%Calculate the power fraction in each layer from the integral of the
%E-field in each layer
syms x;
%Power fraction in the top cladding layer
Pclad=int(((1/(n0^2))*(cos(phi)*exp(-alphac*(x))))^2),0,inf);
Pclad=double(Pclad);
%Power fraction in the bottom cladding (substrate) layer
Psubs=int(((1/(n2^2))*(cos(-kx*d+phi)*exp(alphas*(x+d))))^2),-inf,-d);
Psubs=double(Psubs);
%Power fraction in the core layer
Pcore=int(((1/n1^2)*(cos(kx*x+phi))^2),-d,0);
Pcore=double(Pcore);
%Power confinement factor in the core layer
Pconf=Pcore/(Pcore+Pclad+Psubs)
%Calculate the E-field profile in the waveguide along with the
%index profile of the waveguide
%Define the structure thickness from top to bottom
simwin=10;
dimension=simwin*20000+1;
%Initialize matrices
H=zeros(1,dimension);
n=zeros(1,dimension);
pos=zeros(1,dimension);
%Define the H-field in each layer
for(i=1:1:dimension)
y=(i-dimension/2)/20;
dbottom = -d*10^(9);
dtop = 0;
%H-field and index profile in top cladding layer

```

```

if(y>=dtop)
    H(1,i)=(cos(phi)*exp(-alphac*(y*10^(-9)))));
    n(1,i)=n0;
    %H-field and index profile in the bottom cladding (substrate) layer
elseif(y<=dbottom)
    H(1,i)=(cos(-kx*d+phi)*exp(alphas*(y*10^(-9)+d)));
    n(1,i)=n2;
    %H-field and index profile in the core layer
elseif((y<dtop) & (y>dbottom));
    H(1,i)=(cos(kx*y*10^(-9)+phi));
    n(1,i)=n1;
end
pos(i)=y/1000;
end

%Plot H-field and index profiles in the waveguide
[AX,H1,H2] = plotyy(pos,H,pos,n,'plot');
%Label the axes
set(get(AX(1),'Ylabel'),'String','Normalized H-field');
set(get(AX(2),'Ylabel'),'String','Index of Refraction');
xlabel('Position (nm)');
%Add plot title
title('H-field and Index Profiles of the Slab Waveguide');

%Create matrix to output the E-field profile in the waveguide
dataprof=[pos',H'];
dataindex=[pos',n'];

%Write H-field data to file
csvwrite('profile.dat',dataprof);
csvwrite('indexprof.dat',dataindex);

else
    disp('You must enter a polarization!!!')
end

```



## slabtransTE.m

```
function F = slabtransTE(b) %function declaration
global lamda d n0 n1 n2 %receive global variables defined in effslab.m
k=2*pi/lamda;
V=sqrt(k^2*d^2*(n1^2-n2^2)); %define normalized frequency parameter
gamma=(n2^2-n0^2)/(n1^2-n2^2); %define asymmetry parameter
m=0; %perform calculation for the fundamental mode
%Transcendental equation for a general slab waveguide
F=sqrt(b/(1-b))+sqrt((b+gamma)/(1-b))...
-(tan(V*sqrt(1-b))*(1-(sqrt(b*(b+gamma)))/(1-b)));
```

## slabtransTM.m

```
function F = slabtransTM(b) %function declaration
global lamda d n0 n1 n2 %receive global variables defined in effslab.m
k=2*pi/lamda;
V=sqrt(k^2*d^2*(n1^2-n2^2)); %define normalized frequency parameter
gamma=(n2^2-n0^2)/(n1^2-n2^2); %define asymmetry parameter
m=0; %perform calculation for the fundamental mode
%Transcendental equation for a general slab waveguide
F=(n1^2/n2^2)*sqrt(b/(1-b))+(n1^2/n0^2)*(sqrt((b+gamma)/(1-b)))...
-(tan(V*sqrt(1-b))*(1-(n1^4/(n0^2*n2^2))*((sqrt(b*(b+gamma)))/(1-b))));
```

# Appendix B | Program for Rate Equation Modeling of the Er-Sensitizer Coupling

In this appendix we present a Matlab program, *Ergain.m*, that was used to analyze the emission and gain results presented in Chapter 6. First the coefficients representing the various processes in the sensitizer – Er system are defined. Then the differential equations 6.27 and 6.28 representing the time dependent excited-state populations of the SRO sensitizer and Er ion are defined in the function *rateeqns.m* and solved using the Matlab ordinary differential equation solver *ode15s*. The solver starts with the initial condition of zero excited-state population for both the sensitizer and Er ion at time equal to zero and evaluates the differential equation for various pump-photon fluxes at a long time ( $t = 100$  s) such that the calculated value represents the steady-state population. The sensitizer and Er emission is proportional to the excited-state populations. The gain is calculated using the excited-state Er population from equation 6.26 with

$$g = \sigma_{em}(2N_2 - N_{tot}) \quad (\text{B1})$$

The gain results can also take into consideration the confined carrier absorption of the sensitizer through the confined carrier absorption coefficient,  $\alpha_{CCA}$ ,

$$\alpha_{CCA} = \sigma_{CCA}n_b \quad (\text{B2})$$

where  $\sigma_{CCA}$  is the confined carrier absorption cross section. The program also allows the user to plot the sensitizer emission, Er emission and gain versus pump-power density as well as save the results to a data file.

## **%Ergain.m**

%This program runs together with rateeqns.m to solve the rate equations  
%defining the time dependent excited-state populations of Si-nc and Er in the  
%steady-state. Once the excited-state populations are known, additional  
%calculations of the gain, energy-transfer time, energy-transfer efficiency  
%and the number of Er ions excited per Si-nc are calculated as a function of  
%pump power.

```
global Ntot ntot gammac sigma tau sigmaaab tauba Cal Cup;
```

```
%Define Variables
```

```
Ntot = 1.2*10^(20); %total Er concentration  
ntot=6*10^(18); %total Si-nc concentration  
gammac=150*10^(-15); %Si-nc -> Er coupling coefficient  
sigma = 1*10^(-19); %Er excitation cross section  
tau = 4.2*10^(-3); %Er emission lifetime  
sigmaaab=1.6*10^(-17); %Si-nc mediated excitation cross section  
tauba=1*10^(-6); %Si-nc emission lifetime  
Cal=1*10^(-13); %Coefficient for Auger recombination in Si-nc (assume 2  
%exciton process)  
Cup=3e-18; %Coefficient for cooperative upconversion in Er  
sigmaEr=3.5*10^(-20); %Er emission cross section  
alpha=9.2; %propagation losses (used for simulating gain data)  
sigmacca = 1*10^(-20); %confined carrier absorption of the Er emission  
conffact=0.9; %slab  
waveguide confinement factor
```

```
%Initialize matrices
```

```
Y = zeros(100,2);  
y = zeros(2,100);  
dy = zeros(2,100);  
gaindata=zeros(1,100);  
pump=zeros(1,100);  
nb=zeros(1,100);  
N2=zeros(1,100);
```

```
for(i=1:1:100);
```

```
    global phi; %define phi as a global variable so it can be accessed by  
        %rateeqns  
    phi = 1e16*10^(i/10); %define pump-photon flux  
    options = odeset('RelTol',1e-3,'AbsTol',[1e-3 1e-3]); %sets the options  
        %for ODE solver  
    [T,Y] = ode15s(@rateeqnsnew,[0 100],[0 0]); %solve the system of  
        %differential equations found in rateeqns  
  
    Er=Y(:,2);  
    Nano=Y(:,1);  
    valEr=length(Er);  
    valnano=length(Nano);  
    nb(i)=Nano(valnano); %Si-nc excited-state population evaluated at long  
        %times  
    N2(i)=Er(valEr); %Er excited-state population evaluated at long times
```

```
end
```

```
%Define the pump-power density for plotting and calculations  
x=1:1:100;
```

```

p=1e16*10.^(x/10);
pump=p*4.07058905951e-19;

%Calculate the Er gain
alphacca = sigmacca.*nb;%confined carrier absorption contribution
gaindata = conffact*sigmaEr*(2*N2-Ntot)-alpha;%calculate gain without
%the confined carrier loss term
gaindataacca = conffact*(sigmaEr*(2*N2-Ntot)-alphacca)-alpha;%calculate the
%gain with the confined carrier loss term
erbiumention=N2/1.1e17;%scale the excited state Er population to compare to
%the steady state emission results

%Plot results
subplot(2,1,1);
loglog(exppump_PL,Eremisdata, 'o', pump,erbiumention);
title('Er Emission');
xlabel('Pump-photon Flux (cm-2 s-1)');
ylabel('Er Excited-state Population');
subplot(2,1,2);
semilogx(exppump_gain, expgain, 'o', pump,gaindata);
title('Gain');
xlabel('Pump-photon Flux (cm-2 s-1)');
ylabel('Gain(cm-1)');
%figure;
%semilogx(p,nb);
%title('Si-nc Emission');
%xlabel('Pump-photon Flux (cm-2 s-1)');
%ylabel('Si-nc Excited-state Population');
%semilogx(p,gaindata,p,alphacca,p,gaindataacca);
%title('Gain');
%xlabel('Pump-photon Flux (cm-2 s-1)');
%ylabel('Gain(cm-1)');

%Create matrices for output
%Sincemis=[pump',nb'];
gain=[pump',gaindata'];
Eremis=[pump',erbiumention'];
%datagaincca=[pump',gaindataacca'];
%dataalphacca=[pump', alphacca'];

%Write data to file
%gainfilename = input('Enter filename for gain data: ', 's');
%Eremisfilename = input('Enter filename for Er emission data: ', 's');
csvwrite('Eremis.dat',Eremis);
csvwrite('gain.dat',gain);
%csvwrite('Sincemis.dat',Sincemis);
%csvwrite('alphacca.dat',dataalphacca);
%csvwrite('gaincca.dat',datagaincca);

```

## **%rateeqns.m**

%This program defines a set of differential equations which are the rate equations defining the excited-state populations of Er and Si-nc. Together with the program Ergain these rate equations are solved at long times (steady-state) to determine the excited-state population of Er and Si-nc as a function of pump power.

```
function [dy] = rateeqns (t,y)
```

```
global phi Ntot ntot gammac sigma tau sigmaab tauba Cal Cup;
```

```
%Rate Equations. Note that y(1)->nb and y(2)->N2
```

```
%Rate equation for time dependent SRO excited-state population
```

```
dy(1) = phi*sigmaab*(ntot-y(1))-y(1)/tauba-gammac*y(1)*(Ntot-y(2))-  
2*Cal*(y(1)^2);
```

```
%Rate equation for time dependent Er excited-state population
```

```
dy(2) = phi*sigma*(Ntot-y(2))-y(2)/tau+gammac*y(1)*(Ntot-y(2))-  
2*Cup*(y(2)^2);
```

```
dy = dy'; % This makes yprime into a column vector
```

# Appendix C | Program for Calculating the Scattering Cross Section, Scattering Efficiency and Loss Coefficient for Spherical Scatterers

In this appendix we present the Matlab program, `particlescattering.m`, used to calculate the loss coefficient for scattering from spherical particles. We have followed exactly the approach of Bohren and Huffman [101]; below is a summary of the approach outlined in detail in [101] for calculating the scattering values.

The scattering coefficients  $a_n$  and  $b_n$  are calculated by introducing the logarithmic derivative

$$D_n(\rho) = \frac{d}{d\rho} \ln(\psi_n(\rho)) \quad (C1)$$

where  $\psi_n(\rho)$  is a Riccati-Bessel function.

The scattering coefficients then become

$$a_n = \frac{\left[ \frac{D_n(mx)}{m} + \frac{n}{x} \right] \psi_n(x) - \psi_{n-1}(x)}{\left[ \frac{D_n(mx)}{m} + \frac{n}{x} \right] \xi_n(x) - \xi_{n-1}(x)} \quad (C2)$$

$$b_n = \frac{\left[ mD_n(mx) + \frac{n}{x} \right] \psi_n(x) - \psi_{n-1}(x)}{\left[ mD_n(mx) + \frac{n}{x} \right] \xi_n(x) - \xi_{n-1}(x)}$$

where  $m = N_{\text{scatterer}} / N_{\text{medium}}$  is the normalized index of refraction and  $x = \frac{2\pi N_{\text{medium}} a}{\lambda}$  is the size parameter with  $a$  as the scatterer radius. In equation C2 we have substituted the derivatives of the Bessel and Hankel functions by their recurrence relations

$$\begin{aligned}\psi'_n(x) &= \psi_{n-1}(x) - \frac{n\psi_n(x)}{x} \\ \xi'_n(x) &= \xi_{n-1}(x) - \frac{n\xi_n(x)}{x}\end{aligned}\tag{C3}$$

The higher order Bessel and Hankel functions are generated through upward recurrence from the lowest order functions using the relations

$$\begin{aligned}\psi_{n+1}(x) &= \frac{2n+1}{x}\psi_n(x) - \psi_{n-1}(x) \\ \chi_{n+1}(x) &= \frac{2n+1}{x}\chi_n(x) - \chi_{n-1}(x)\end{aligned}\tag{C4}$$

with  $\xi_n(x) = \psi_n(x) - i\chi_n(x)$  and the lowest order functions of

$$\begin{aligned}\psi_{-1}(x) &= \cos(x) \\ \psi_0(x) &= \sin(x) \\ \chi_{-1}(x) &= -\sin(x) \\ \chi_0(x) &= \cos(x)\end{aligned}\tag{C5}$$

where only  $x + 4x^{1/3} + 2$  terms are included.

The program `particlescattering.m` calls the function `logderivativeD.m` which calculates the logarithmic derivative through downward recurrence using the relation

$$D_{n-1} = \frac{n}{\rho} - \frac{1}{D_n + \frac{n}{\rho}}\tag{C6}$$



starting from  $D_{\max} = 0 + i0$  at an order much larger than the maximum number of terms calculated for the Bessel and Hankel functions. Bohren and Huffman [101] have determined that an appropriate starting point for the calculation of the logarithmic derivative is  $\max\left(x + 4x^{1/3} + 2, |mx|\right) + 15$ .

To calculate the scattering loss versus wavelength we calculated the wavelength dependent refractive index for silica using the Sellmeier equation

$$n_{\text{SiO}_2}^2 - 1 = \sum_{i=1}^2 \frac{A_i \lambda^2}{\lambda^2 - l_i^2} \quad (\text{C7})$$

with the coefficients  $A_i$  and  $l_i$  from Ref.165. For silicon we calculated the wavelength dependent refractive index using the equation from Ref. 166

$$n_{\text{Si}} = A + BL + CL^2 + D\lambda^2 + E\lambda^4 \quad (\text{C8})$$

with the coefficients A, B, C, D, E and L from the same reference.

The program also allows the user to plot the scattering loss coefficient versus wavelength as well as save the results to a data file.

We compared our numerical results with those reported in Bohren and Huffman for the extinction efficiency of water spheres in air considering the real and imaginary contributions to the refractive index of water for various wavelengths [168]. The perfect agreement is shown in Figure C1.

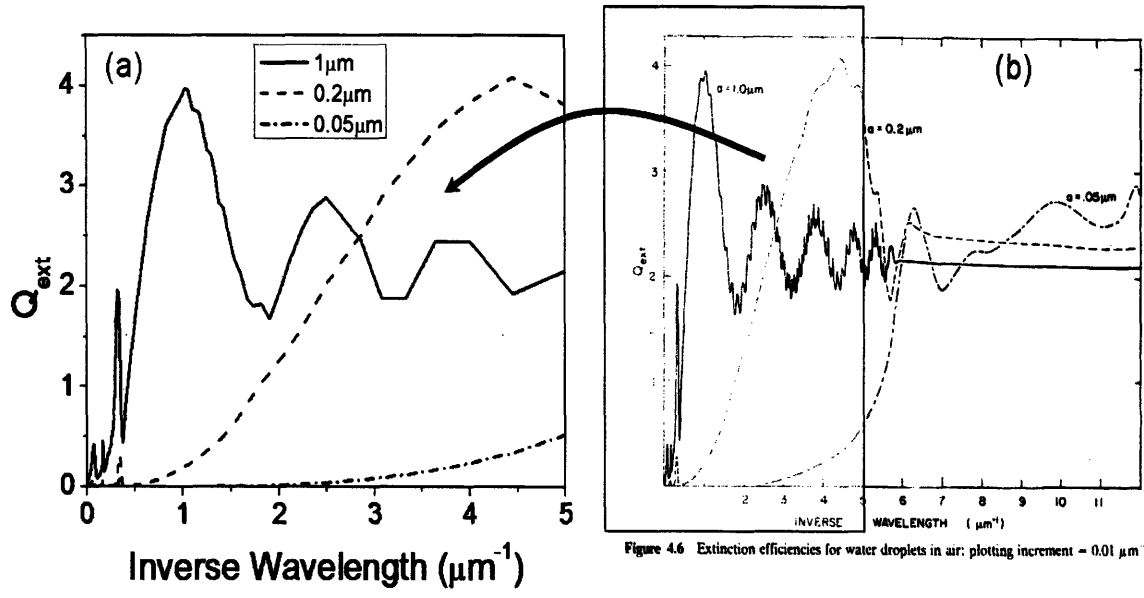


Figure 4.6 Extinction efficiencies for water droplets in air: plotting increment =  $0.01 \mu m^{-1}$ .

Figure C1 (a) Calculated extinction efficiency of water spheres in air using our computer program. (b) Calculated extinction efficiency of water spheres in air from Bohren and Huffman [101].

## **%particlescattering.m**

```
%Input wavelengths for the calculation from a file
lamda=csvread('lamdascattering.dat');

%To calculate the scattering efficiency of water in air input the real and
imaginary
%index of refraction for water
%Nreal=csvread('nwater.dat');
%Nimag=csvread('kwater.dat');
%N=complex(Nreal,Nimag);
%N1=1;

%Define Sellmeier constants for SiO2 index calculation (from J. W. Fleming
%and J. W. Shiever, J.Am.Ceram.Soc., 62, pp. 526 (1979).

A1=0.69681;
A2=0.40817;
A3=0.89493;
l1=0.06853;
l2=0.11612;
l3=9.9140;

%Calculate the SiO2 index from the Sellmeier equation (index of the matrix)
N1=sqrt(1+(A1.*lamda.^2./(lamda.^2-l1^2))+(A2.*lamda.^2./(lamda.^2-l2^2))...
      +(A3.*lamda.^2./(lamda.^2-l3^2)));

%Define the coefficients for the dispersion of Si (from H.H. Li,
%J.Phys.Chem.Ref.Data,9 (3), pp. 561 (1980)
A=3.41696;
B=0.138497;
C=0.013924;
D=-0.0000209;
E=0.000000148;
L=1./(lamda.^2-.168^2);
N=A+B.*L+C.*L.^2+D.*lamda.^2+E.*lamda.^4; %index of the scatterer (Si
nanocrystal)

%Define the particle radius in microns
particlesize=1.5e-3;

calculationsize=size(lamda);
%Initialize the matrix for the scattering efficiencies
Cscatot=zeros(calculationsize);

for(j=1:1:calculationsize)
    m=N(j)/N1(j); %define the relative refractive index
    x=(2*pi*N1(j)*particlesize)/lamda(j); %define the size parameter
    STOP=round(x+4*x^(1/3)+2); %calculate the total number of terms to..
    %consider in the sum
    D=zeros(1,STOP+1); %initialize the matrix for the...
    %logarithmic derivative
    D=logderivativeD(m,x,m*x); %use recursion to calculate the...
    %logarithmic derivative
    %Cexttot=0;
    Cscatot=0;
```

```

    psi0=cos(x);    %define the 0th spherical Bessel function
    psi1=sin(x);    %define the 1st spherical Bessel function
    chi0=-sin(x);   %define the 0th spherical Bessel function of the second
kind
    chil=cos(x);    %define the 1st spherical Bessel function of the second
kind
    eta0=complex(psi0,-chi0); %calculate the 0th spherical Hankel function
    etal=complex(psi1,-chil); %calculate the 1st spherical Hankel function
    for(i=1:1:STOP)
        %Calculate the next spherical Bessel functions from recursion
        psi=((2*i-1)*psi1)/(x)-psi0;
        chi=((2*i-1)*chil)/x)-chi0;
        eta=complex(psi,-chi);
        %Calculate the scattering coefficients for this iteration
        a=((D(i)/m)+(i/x))*psi-psi1)/(((D(i)/m)+(i/x))*eta-etah);
        b=((D(i)*m)+(i/x))*psi-psi1)/(((D(i)*m)+(i/x))*eta-etah);
        %Cextcurrent=(2*i+1)*real(a+b);
        %Calculate the scattering cross section for this iteration
        Cscacurrent=(2*i+1)*(abs(a)*abs(a)+abs(b)*abs(b));
        %TotalCext=Cexttot+Cextcurrent;
        %Add the current scattering cross section to the total
        TotalCsca=Cscatot+Cscacurrent;
        psi0=psi1;
        chil=chil;
        psi1=psi;
        chil=chi;
        etah=eta;
        Cscatot=TotalCsca;
        %Cexttot=TotalCext;
    end
    Cscatotout(j)=Cscatot;
    %Cexttotout(j)=Cexttot;
end

xcalc=((2.*pi.*N1.*particlesize)./lamda);
Qscattering=(2./(xcalc.^2)).*Cscatotout; %calculate the scattering
efficiency
%Qext=(2./(xcalc.^2)).*Cexttotout; %calculate the extinction efficiency
density=1e19; %define the density of scatterers
alpha=density*pi*(particlesize*1e-4)^2*Qscattering; %define the loss
coefficient for scattering
plot(lamda,alpha); %plot the results
title('Loss Coefficient Due to Scattering from Spherical Particles');
xlabel('Wavelength (microns)');
ylabel('Loss Coefficient (cm^-1)');
dataext=[lamda,Qscattering]; %prepare the results for file export
csvwrite('extinctionefficiency.dat',dataext); %export the results to a file

```

## **%logderivativeD.m**

```
function [D]=logderivative(m,x,rho)

mx=round(abs(rho));
STOP=round(x+4*x^(1/3)+2);
NMX=max(STOP,mx)+15; %calculate the number of terms to include in the
                    %calculation
D=zeros(1,NMX); %initialize the matrix

%Determine the logarithmic derivative through downward recurrence
for(i=1:1:NMX-1)
    D(NMX-i)=((NMX-i+1)/rho)-(1/(D(NMX-i+1)+(NMX-i+1)/rho));
end
```

# Appendix D | Program for Calculating the Scattering Cross Section, Scattering Efficiency and Loss Coefficient for Cylindrical Scatterers

In this appendix we present the Matlab program `cylinderscattering.m` which calculates the loss coefficient due to scattering from cylinders at a single wavelength where we have also followed the approach of Bohren and Huffman [101]. Similar to the calculation for spherical scatterers we introduce the logarithmic derivative

$$G_n(\rho) = \frac{J'_n(\rho)}{J_n \rho} \quad (D1)$$

where  $J_n$  is a Bessel function of the first kind.

The scattering coefficients are

$$a_n = \frac{\left[ \frac{G_{n+1}(mx)}{m} + \frac{n}{x} \right] J_n(x) - J_{n-1}(x)}{\left[ \frac{G_{n+1}(mx)}{m} + \frac{n}{x} \right] H_n^{(1)}(x) - H_{n-1}^{(1)}(x)} \quad (D2)$$

$$b_n = \frac{\left[ mG_{n+1}(mx) + \frac{n}{x} \right] J_n(x) - J_{n-1}(x)}{\left[ mG_{n+1}(mx) + \frac{n}{x} \right] H_n^{(1)}(x) - H_{n-1}^{(1)}(x)}$$

where  $H_n^{(1)}$  are Hankel functions.

The function logderivativeg.m is called in the program to calculate the logarithmic derivative through downward recurrence through the relation

$$G_{n-1}(\rho) = \frac{n-2}{\rho} - \frac{1}{\frac{n-1}{\rho} + G_n(\rho)} \quad (\text{D3})$$

Instead of using recursion to calculate the higher order Bessel and Hankel functions we take advantage of the built-in Matlab functions `besselj(n,x)` which calculates the  $n^{\text{th}}$  order Bessel function of the first kind ( $J_n$ ) and `bessely(n,x)` which calculates the  $n^{\text{th}}$  order of the Bessel function of the second kind ( $Y_n$ ) where

$$H_n^{(1)}(x) = J_n(x) + iY_n(x) \quad (\text{D4})$$

For the special case of the  $0^{\text{th}}$  order scattering coefficients we use the expressions

$$a_0 = \frac{\frac{G_1(mx)J_0(x)}{m} + J_1(x)}{\frac{G_1(mx)H_0^{(1)}(x)}{m} + H_0^{(1)}(x)} \quad (\text{D5})$$

$$b_0 = \frac{mG_1(mx)J_0(x) + J_1(x)}{mG_1(mx)H_0^{(1)}(x) + H_0^{(1)}(x)}$$

We calculated the density of cylinder scatterers (columns in the columnar film) from the approximate column size,  $a$ , and volume fraction,  $f$  using the expression

$$\text{Density} = \frac{f}{a^2} \quad (\text{D6})$$

To calculate the scattering loss due to the columnar film morphology we performed a Cauchy fit of the index of refraction versus wavelength measured by prism coupling for the Er-doped Si-rich

SiO<sub>2</sub> slab waveguide sample annealed at 600°C. The index of refraction for the TE and TM polarizations was given by the formula

$$n = A_0 + A_1\lambda^{-2} + A_2\lambda^{-4} \quad (D7)$$

For the TE polarization the coefficients were  $A_0 = 1.5441$ ,  $A_1 = 1.2860 \times 10^4$  and  $A_2 = -6.8099 \times 10^8$ . For the TM polarization the coefficients were  $A_0 = 1.5499$ ,  $A_1 = 9.4680 \times 10^3$  and  $A_2 = 2.8412 \times 10^8$ . The refractive index of the column and boundary region were calculated by solving the system of equations 4.11 and 4.12 with  $f_{\text{column}} = 0.83$  and  $f_{\text{boundary}} = 1 - f_{\text{column}}$ . These results are input into the program from comma delimited data files `matrixindex.dat` and `columnindex.dat` for the matrix (boundary) and column index of refraction, respectively, with the corresponding wavelength input from the file `lamdascattering.dat`.

The program also allows the user to plot the scattering loss coefficient versus wavelength as well as save the results to a data file.

We have compared our calculation to the values quoted in Bohren and Huffman for the scattering efficiency of a single cylinder with a size of 0.525  $\mu\text{m}$  and refractive index of 1.55 in air at a wavelength of 0.6328  $\mu\text{m}$ . We calculated scattering efficiencies of 1.94587 and 1.48165 for light polarized perpendicular and parallel to the cylinder, respectively. These values are comparable to those reported in Bohren and Huffman (2.09716 and 1.92782 for the perpendicular and parallel case, respectively) with the difference most likely due to the different approaches for calculating the higher order Bessel and Hankel functions.



## **%cylinderscattering.m**

```
%Read the wavelength and index of refraction for the column and boundary
%regions from a file
lamda=csvread('lamdascattering.dat');
N1=csvread('matrixindex.dat');
N=csvread('columnindex.dat');

%lamda=1.551;
%N1=1.4652;
%N=1.5923;
%neff=1.5493;
%km=(2*pi*neff/lamda)

%lamda=0.6328;
%N1=1.55;
%N=1;

%Define the column radius in microns
particlesize=170e-3;
%Define the filling fraction of the columns
f=.83;
%Define the effective radius of the coated column
RC=particlesize*1e-4/f^(1/2);
%Calculate the density of columns
density=1/RC^2

%particlesize=0.525;

%Intitialize matrices
calculationsize=size(lamda);
Cscatotoutperp=zeros(calculationsize);
Cscatotoutpar=zeros(calculationsize);
Cextout=zeros(calculationsize);
Extinctiondata=zeros(calculationsize,2);

for(j=1:1:calculationsize)
    m=N(j)/N1(j);%define the relative refractive index
    x=(2*pi*N1(j)*particlesize)/lamda(j);%define the size parameter
    STOP=round(x+4*x^(1/3)+2);%calculate the total amount of terms to include
        %in the sum
    G=zeros(1,STOP+1);%initialize the matrix for the logarithmic derivative
    G=logderivativeG(m,x,m*x);%use recursion to calculate the logarithmic
        %derivative

    Cscatotpar=0;
    Cscatotperp=0;
    Cexttot=0;
    for(i=1:1:STOP)
        %Compute the Bessel's and Hankel's functions using built-in Matlab
        %routines
        J0=besselj(i-1,x);
        J1=besselj(i,x);
        Y0=bessely(i-1,x);
        Y1=bessely(i,x);
        H0=complex(J0,Y0);
        H1=complex(J1,Y1);
```

```

%Calculate the scattering coefficients for this iteration
a=((G(i+1)/m)+(i/x))*J1-J0/(((G(i+1)/m)+(i/x))*H1-H0);
b=((G(i+1)*m)+(i/x))*J1-J0/(((G(i+1)*m)+(i/x))*H1-H0);
%Calculate the scattering cross section for this iteration (TE case)
Cscacurrentperp=2*(abs(a)*abs(a));
%Calculate the extinction cross section for this iteration (TE case)
Cextcurrent=2*a;
%Add the current extinction cross section to the total
TotalCext=Cexttot+Cextcurrent;
Cexttot=TotalCext;
%Add the current scattering cross section to the total
TotalCscaperp=Cscatotperp+Cscacurrentperp;
Cscatotperp=TotalCscaperp;
%Calculate the scattering cross section for this iteration (TM case)
Cscacurrentpar=2*(abs(b)*abs(b));
%Add the current scattering cross section to the total
TotalCscapar=Cscatotpar+Cscacurrentpar;
Cscatotpar=TotalCscapar;
end
%Calculate the scattering coefficients for the zeroth order term in the
%sum and add it to the total scattering cross section
J00=besselj(0,x);
J01=besselj(1,x);
Y00=bessely(0,x);
Y01=bessely(1,x);
H00=complex(J00,Y00);
H01=complex(J01,Y01);
a0=(((G(1)*J00/m)+J01))/((G(1)/m)*H00+H01);
b0=(((G(1)*J00*m)+J01))/((G(1)*m)+(i/x))*H00+H01);
Cextout(j)=a0+Cexttot;
Cscatpreoutperp=abs(a0)*abs(a0);
Cscatotoutperp(j)=Cscatotperp+Cscatpreoutperp;
Cscatpreoutpar=abs(b0)*abs(b0);
Cscatotoutpar(j)=Cscatotpar+Cscatpreoutpar;
end

xcalc=((2.*pi.*N1.*particlesize)./lamda);
Qscatteringperp=(2./(xcalc)).*Cscatotoutperp; %calculate the scattering
%efficiency (TE Case)
Cscatteringperp=(2.*1.5.*particlesize.*Qscatteringperp);
Qscatteringpar=(2./(xcalc)).*Cscatotoutpar; %calculate the scattering
%efficiency (TM case)
Cscatteringpar=(2.*particlesize.*1.5.*Qscatteringpar);
diameter=2.*particlesize;
%plot(diameter,Cscatteringperp,diameter,Cscatteringpar);
size(lamda);
%Calculate the loss coefficient from scattering
alphaperp=density.*2.*particlesize.*1.5.*Qscatteringperp.*1e-8
alphapar=density.*2.*particlesize.*1.5.*Qscatteringpar.*1e-8;
%Plot the results
plot(lamda,alphaperp);
%Prepare the results for file export
extinctiondata(:,1)=lamda;
extinctiondata(:,2)=alphaperp;
%Export the results to a file
csvwrite('cylinderextinction.dat',extinctiondata);

```

## **%logderivativeg.m**

```
function [G]=logderivative(m,x,z)
```

```
mx=round(abs(z));
```

```
STOP=round(x+4*x^(1/3)+2);
```

```
NMX=max(STOP,mx)+15; %calculate the number of terms to include in the  
%calculation
```

```
G=zeros(1,NMX); %initialize the matrix
```

```
%Determine the logarithmic derivative through downward recurrence
```

```
for(i=1:1:NMX-1)
```

```
    G(NMX-i)=((NMX-i-1)/z)-(1/(G(NMX-i+1)+(NMX-i)/z));
```

```
end
```

# References

---

- [1] D. K. Sparacin, S. J. Spector and L. C. Kimerling, *IEEE Journal of Lightwave Technology*, **23** (8), pp. 2455 (2005).
- [2] S.J. Spector, M.W. Geis, D.M. Lennon, R.C. Williamson and T.M. Lyszczarz, *Proceedings of the Integrated Photonics Research Conference, Paper IThE5* (2004).
- [3] M.J. Shaw, J. Guo, G.A. Vawter, S. Habermehl and C.T. Sullivan, *Proceedings of the SPIE – Photonics West*, **5720** (15), (2005).
- [4] S. Akiyama, Ph.D. Thesis, Massachusetts Institute of Technology (2004).
- [5] J. Lee, K. Cheng, J. Lyding and H.W.M. Salemink, *Materials Research Society Symposium Proceedings*, **609**, pp. 26.8.1 (2000).
- [6] C. Manolatu, S. G. Johnson, S. Fan, P. R. Villeneuve, H. A. Haus and J. D. Joannopoulos, *IEEE Journal of Lightwave Technology*, **17** (9), pp. 1682 (1999).
- [7] L. H. Slooff, P. G. Kik, A. Tip, and A. Polman, *IEEE Journal of Lightwave Technology*, **19** (11), pp. 1740 (2001).
- [8] D. R. Lim, B. E. Little, K. K. Lee, M. Morse, H. H. Fujimoto, H. A. Haus and L. C. Kimerling, *Proceedings of SPIE*, **3847**, pp. 65 (1999).
- [9] L. Yang, D. K. Armani and K. J. Vahala, *Applied Physics Letters*, **83** (5), pp. 825 (2003).
- [10] P.D. Trinh, S. Yegnanarayanan, F. Coppinger and B. Jalali, *IEEE Photonics Technology Letters*, **9**, pp. 940 (1997).
- [11] J.H. den Besten, *IEEE Photonics Technology Letters*, **14**, pp. 62 (2002).
- [12] A. Liu, R. Jones, L. Liao, D. Samara-Rubio, D. Rubin, O. Cohen, R. Nicolaescu and M. Paniccia, *Nature*, **427**, pp. 615 (2004).
- [13] V. R. Almeida, C. A. Barrios, R. R. Panepucci and M. Lipson, *Nature*, **431**, pp. 1081 (2004).
- [14] G.F. Dionne, G.A. Allen, P.R. Haddad, C.A. Ross and B. Lax, *Lincoln Laboratory Journal*, **15** (2), pp. 323 (2004).
- [15] J. Liu, J. Michel, W. Giziewicz, D. Pan, D.D. Cannon, D.T. Danielson, S. Jongthammanurak, K. Wada, L.C. Kimerling, J. Chen, F.Ö. Ilday, F.X. Kärtner and J. Yasaitis, *Applied Physics Letters*, **87**, pp. 103501 (2005).
- [16] G. Dehlinger, S.J. Koester, J.D. Schaub, J.O. Chu, Q.C. Ouyang and A. Grill, *IEEE Photonics Technology Letters*, **16** (11), pp. 2547 (2004).
- [17] W.P. Dumke, *Physical Review*, **127** (5), pp. 1559 (1962).
- [18] O. Boyraz and B. Jalali, *Optics Express*, **12**, pp. 5269 (2004).
- [19] H. Rong, A. Liu, R. Jones, O. Cohen, D. Hak, R. Nicolaescu, A. Fang and M. Paniccia, *Nature*, **433**, pp. 292 (2005).
- [20] M.A. Green, J. Zhao, A. Wang, P. Reece, and M. Gal, *Nature*, **412**, pp. 805 (2001).
- [21] T. Trupke, J. Zhao, A. Wang, R. Corkish, and M.A. Green, *Applied Physics Letters*, **82** (18), pp. 2996 (2003).
- [22] L. Pavesi, S. Gaponenko and L. Dal Negro, eds., *Towards the first silicon laser*, NATO Advanced Studies Institute, Series 11, Kluwer Academic, Dordrecht, **93** (2003).
- [23] L. Pavesi and D. J. Lockwood eds., *Silicon Photonics*, Springer-Verlag, Berlin (2004).
- [24] J. C. Vial, A. Bsiesy, F. Gaspard, R. Hèrino, M. Ligeon, F. Muller, R. Romestain and R. M. Macfarlane, *Physical Review B*, **45** (24), pp. 14171 (1992).
- [25] B. Gelloz, T. Nakagawa and N. Koshida, *Applied Physics Letters*, **73** (14), pp. 2021 (1998).
- [26] S.G. Cloutier, P.A. Kossyrev and J. Xu, *Nature Materials*, **4**, pp. 887 (2005).
- [27] K. Shuto, K. Hattori, T. Kitagawa, Y. Ohmori and M. Horiguchi, *Electronics Letters*, **29** (2), pp. 139 (1993).

- 
- [28] Y. C. Yan, A. J. Faber, H. de Waal, P. G. Kik and A. Polman, *Applied Physics Letters*, **71** (20), pp. 2922 (1997).
- [29] G. N. van den Hoven, R. J. I. M. Koper, A. Polman, C. van Dam, J. W. M. van Uffelen, and M. K. Smit, *Applied Physics Letters*, **68** (14), pp. 1886 (1996).
- [30] J. Michel, J.L. Benton, R.F. Ferrante, D.C. Jacobson, D.J. Eaglesham, E.A. Fitzgerald, Y.H. Xie, J.M. Poate and L.C. Kimerling, *Journal of Applied Physics*, **70**, pp. 2672 (1991).
- [31] B. Zheng, J. Michel, F.Y.G. Ren, L.C. Kimerling, D.C. Jacobson and J.M. Poate, *Applied Physics Letters*, **64**, pp. 2842, (1994).
- [32] J. Palm, F. Gan, B. Zheng, J. Michel and L.C. Kimerling, *Physical Review B*, **54**, pp. 17603 (1996).
- [33] G. Franzò, F. Priolo, S. Coffa, A. Polman and A. Carnera, *Applied Physics Letters*, **64**, pp. 2235 (1994).
- [34] F. Priolo, G. Franzò, S. Coffa and A. Carnera, *Physical Review B*, **57**, pp. 4443 (1998).
- [35] S. Coffa, G. Franzò and F. Priolo, *Applied Physics Letters*, **69**, pp. 2077 (1996).
- [36] A. J. Kenyon, P. F. Trwoga, M. Federighi and C. W. Pitt, *Journal of Physics Condensed Matter*, **6**, pp. L319 (1994).
- [37] M. Fujii, M. Yoshida, Y. Kanzawa, S. Hayashi and K. Yamamoto, *Applied Physics Letters*, **71** (9), pp. 1198 (1997).
- [38] G. Franzò, F. Iacona, V. Vinciguerra and F. Priolo, *Materials Science and Engineering B*, **69/70**, pp. 338 (1999).
- [39] P. G. Kik, M. L. Brongersma, and A. Polman, *Applied Physics Letters*, **76** (17), pp. 2325 (2000).
- [40] F. Priolo, G. Franzò, F. Iacona, D. Pacifici and V. Vinciguerra, *Materials Science and Engineering B*, **81** (1-3), pp. 9 (2001).
- [41] J. H. Shin, M.-J. Kim, S.-Y. Seo, and C. Lee, *Applied Physics Letters*, **72** (9), pp. 1092 (1998).
- [42] K. D. Hirschman, L. Tsybeskov, S. P. Duttagupta, and P. M. Fauchet, *Nature*, **384**, pp. 338 (1996).
- [43] L. Pavesi, L. Dal Negro, C. Mazzoleni, G. Franzò and F. Priolo, *Nature*, **408**, pp. 440 (2000).
- [44] L. Khriachtchev, M. Rasanen, S. Novikov and J. Sinkkonen, *Applied Physics Letters*, **79** (9), pp. 1249 (2001).
- [45] L. Dal Negro, M. Cazzanelli, L. Pavesi, S. Ossicini, D. Pacifici, G. Franzò, F. Priolo and F. Iacona, *Applied Physics Letters*, **82** (26), pp. 4636 (2003).
- [46] J. Ruan, P. M. Fauchet, L. Dal Negro, M. Cazzanelli and L. Pavesi, *Applied Physics Letters*, **83** (26), pp. 5479 (2003).
- [47] L. Dal Negro, M. Cazzanelli, B. Danese, L. Pavesi, F. Iacona, G. Franzò and F. Priolo, *Journal of Applied Physics*, **96** (10), pp. 5747 (2004).
- [48] M. Cazzanelli, D. Kovalev, L. Dal Negro, Z. Gaurro and L. Pavesi, *Physical Review Letters*, **93** (20), pp. 207402 (2004).
- [49] J.H. Shin, S.-Y. Seo, S. Kim and S.G. Bishop, *Applied Physics Letters*, **76** (15), pp. 1999 (2000).
- [50] J. Lee, J. H. Shin and N. Park, *IEEE Journal of Lightwave Technology*, **23** (1), pp. 19 (2005).
- [51] F. Priolo, G. Franzò, D. Pacifici, V. Vinciguerra, F. Iacona, and A. Irrera, *Journal of Applied Physics*, **89**, pp. 264 (2001).
- [52] G. Franzò, A. Irrera, E. C. Moreira, M. Miritello, F. Iacona, D. Sanfilippo, G. Di Stefano, P. G. Fallica, and F. Priolo, *Applied Physics A – Materials Science and Processing*, **74** (1), pp. 1 (2002).
- [53] J. H. Shin, K.-S. Cho, J.-H. Jhe, G. Y. Sung, B.-H. Kim and S. J. Park, *Proceedings of SPIE*, **5359**, pp. 31 (2004).
- [54] F. Iacona, C. Bongiorno, C. Spinella, S. Boninelli and F. Priolo, *Journal of Applied Physics*, **95** (7), pp. 3723 (2004).
- [55] G. Franzò, S. Boninelli, D. Pacifici, F. Priolo, F. Iacona and C. Bongiorno, *Applied Physics Letters*, **82** (2), pp. 3871 (2003).
- [56] G.Z. Ran, Y. Chen, F.C. Yuan, Y.P. Qiao, J.S. Fu, Z.C. Ma, W.H. Zong and G.G. Quin, *Solid State Communications*, **118** pp. 599 (2001).
- [57] P.G. Kik and A. Polman, *Journal of Applied Physics*, **91** (1) pp. 534 (2002).

- 
- [58] N. Daldosso, D. Navarro-Urrios, M. Melchiorri, L. Pavesi, F. Gourbilleau, M. Carrada, R. Rizk, C. García, P. Pellegrino, B. Garrido and L. Cognolato, *Applied Physics Letters*, **86**, pp. 261103 (2005).
- [59] H.-S. Han, S.-Y. Seo and J.H. Shin, *Applied Physics Letters*, **79** (27), pp. 4568 (2001).
- [60] H.-S. Han, S.-Y. Seo, J.H. Shin and N. Park, *Applied Physics Letters*, **81** (20), pp. 3720 (2002).
- [61] P. Pellegrino, B. Garrido, C. Garcia, J. Arbiol, J. R. Morante, M. Melchiorri, N. Daldosso, L. Pavesi, E. Scheid and G. Sarabayrouse, *Journal of Applied Physics*, **97**, pp. 074312 (2005).
- [62] L. A. Nesbit, *Applied Physics Letters*, **46** (1), pp. 38 (1985).
- [63] T. Shimizu-Iwayama, K. Fujita, S. Nakao, K. Saitoh, T. Fujita and N. Itoh, *Journal of Applied Physics*, **75** (12), pp. 7779 (1993).
- [64] K. S. Min, K. V. Shcheglov, C. M. Yang, H. A. Atwater, M. L. Brongersma and A. Polman, *Applied Physics Letters*, **69** (14), pp. 2033 (1996).
- [65] F. Iacona, G. Franzò and C. Spinella, *Journal of Applied Physics*, **87** (3), pp. 1295 (2000).
- [66] S. Hayashi, T. Nagareda, Y. Kzawa and K. Yamamoto, *Japanese Journal of Applied Physics*, **32**, pp. 3840 (1993).
- [67] U. Kahler and H. Hoffmeister, *Optical Materials*, **17** (1-2), pp. 83 (2001).
- [68] S. Hayashi, T. Nagareda, Y. Kzawa and K. Yamamoto, *Japanese Journal of Applied Physics*, **32**, pp. 3840 (1993).
- [69] Y.Q. Wang, G.L. Kong, W.D. Chen, H.W. Diao, C.Y. Chen, S.B. Zhang and X.B. Lao, *Applied Physics Letters*, **81** (22), pp. 4174 (2002).
- [70] D.J. Olego and H. Baumgart, *Journal of Applied Physics*, **63**, (8), pp. 2669 (1988).
- [71] L.T. Canham, *Applied Physics Letters*, **57** (10), pp. 1046 (1990).
- [72] J. Valenta, P. Janda, K. Dohnalová, D. Nižňanský, F. Vácha and J. Linnros, *Optical Materials*, **27** (5), pp. 1046 (2005).
- [73] G. Ledoux, J. Gong, F. Huisken, O. Guillois and C. Reynaud, *Applied Physics Letters*, **80** (25), pp. 4834 (2002).
- [74] S. Botti, R. Coppola, F. Gourbilleau and R. Rizk, *Journal of Applied Physics*, **88** (6), pp. 3396 (2000).
- [75] J.P. Wilcoxon, G.A. Samara, and P.N. Provencio, *Physical Review B*, **60** (4), pp. 2704 (1999).
- [76] L. Tsybeskov, K. D. Hirschman, S. P. Duttagupta, M. Zacharias, P. M. Fauchet J. P. McCaffrey and D. J. Lockwood, *Applied Physics Letters*, **72** (1), pp. 43 (1998).
- [77] M. Zacharias, J. Heitmann, R. Scholz, U. Kahler, M. Schmidt and J. Bläsing, *Applied Physics Letters*, **80** (4), pp. 661 (2002).
- [78] D. Kovalev and J. Diener, in *Towards the first silicon laser*, NATO Advanced Studies Institute, Series 11, Kluwer Academic, Dordrecht, **93**, pp. 123 (2003).
- [79] F. Riboli, D. Navarro-Urrios, A. Chiasera, N. Daldosso, L. Pavesi, C. J. Oton, J. Heitmann, L. X. Yi, R. Scholz, and M. Zacharias, *Applied Physics Letters*, **85** (7), pp. 1268 (2004).
- [80] G. Beydaghyan, K. Kaminska, T. Brown and K. Robbie, *Applied Optics*, **43** (28), pp. 5343 (2004).
- [81] G. Ledoux, O. Guillois, D. Porterat, C. Reynaud, F. Huisken, B. Kohn and V. Paillard, *Physical Review B*, **62** (23), pp. 15942 (2000).
- [82] G. Franzò, F. Iacona, C. Spinella, S. Cammarata and M. Grazia Giamaldi, *Materials Science and Engineering B*, **69-70**, pp. 454 (2000).
- [83] J. Linnros, N. Lalic, A. Galeckas, and V. Grivickas, *Journal of Applied Physics*, **86** (11), pp. 6128 (1999).
- [84] I. Sychugov, R. Juhasz, A. Galeckas, J. Valenta and J. Linnros, *Optical Materials*, **27** (5), pp. 973 (2005).
- [85] D. Kovalev, H. Heckler, G. Polisski and F. Koch, *Physica Status Solidi*, **215**, pp. 871 (1999).
- [86] M. V. Wolkin, J. Jorne, P. M. Fauchet, G. Allan and C. Delerue, *Physical Review Letters*, **82** (1), pp. 197 (1999).
- [87] A. Puzder, A. J. Williamson, J. C. Grossman and G. Galli, *Journal of Chemical Physics*, **117** (14), pp. 6721 (2002).
- [88] P.G. Kik and A. Polman, *Journal of Applied Physics*, **88** (4), pp. 1992 (2000).

- 
- [89] K. Watanabe, S. Takeoka, M. Fujii, S. Hayashi and K. Yamamoto, *Journal of Luminescence*, **87-89**, pp. 426 (2000).
- [90] G. Franzo, V. Vinciguerra and F. Priolo, *Applied Physics A - Materials Science and Processing*, **69**, pp. 3 (1999).
- [91] M. Falconieri, E. Borsella, L. De Dominicis, F. Enrichi, G. Franzò, F. Priolo, F. Iacona, F. Gourbilleau and R. Rizk, *Applied Physics Letters*, **87**, pp. 061109 (2005).
- [92] K. Watanabe, M. Fujii and S. Hayashi, *Journal of Applied Physics*, **90** (9), pp. 4761 (2001).
- [93] D. Pacifici, E.C. Moreira, G. Franzo, V. Martorino, F. Priolo and F. Iacona, *Physical Review B*, **65**, pp. 144109 (2002).
- [94] D. Pacifici, G. Franzo, F. Priolo, F. Iacona and L. Dal Negro, *Physical Review B*, **67**, pp. 245301 (2003).
- [95] M. Fujii, K. Imakita, K. Watanabe and S. Hayashi, *Journal of Applied Physics*, **95** (1), pp. 272 (2004).
- [96] F. Priolo, G. Franzò, S. Coffa, A. Polman, S. Libertino, R. Barklie and D. Carey, *Journal of Applied Physics*, **78**, pp. 2874 (1995).
- [97] I.N. Yassievich and L.C. Kimerling, *Semiconductor Science and Technology*, **8**, pp. 718 (1993).
- [98] P.G. Kik and A. Polman, in *Towards the first silicon laser*, NATO Advanced Studies Institute, Series 11, Kluwer Academic, Dordrecht, **93**, pp. 383 (2003).
- [99] H. Mertens, A. Polman, I. M. P. Aarts, W. M. M. Kessels, and M. C. M. van de Sanden, *Applied Physics Letters*, **86**, pp. 241109 (2005).
- [100] P.C. Becker, N.A. Olsson and J.R. Simpson, *Erbium-Doped Fiber Amplifiers Fundamentals and Technology*, Academic Press, San Diego (1999).
- [101] C.F. Bohren and D.R. Huffman, *Absorption and Scattering of Light by Small Particles*, Wiley-VCH Verlag GmbH & Co. KGaA, Weinheim (2004).
- [102] S. Berg and T. Nyberg, *Thin Solid Films*, **476**, pp. 215 (2005).
- [103] J. Sandland, Ph.D. Thesis, Massachusetts Institute of Technology (2005).
- [104] L.R. Doolittle, *Nuclear Instruments and Methods in Physics Research*, **B9**, pp. 334 (1985).
- [105] L.R. Doolittle, *Nuclear Instruments and Methods in Physics Research*, **B15**, pp. 227 (1986).
- [106] G. Konac, S. Kalbitzer, Ch. Klatt, D. Nieman and R. Stoll, *Nuclear Instruments and Methods in Physics Research*, **B 136 – 138**, pp. 159 (1998).
- [107] G. Boudreault, R.G. Elliman, R. Grötzschel, S.C. Gujrathi, C. Jeynes, W.N. Lennard, E. Rauhala, T. Sajavaara, H. Timmers, Y.Q. Wang and T.D.M. Weijers, *Nuclear Instruments and Methods in Physics Research*, **B 222**, pp. 547 (2004).
- [108] Operating manual for the Cryo-torr 8 series cryopump, CTI Cryogenics.
- [109] CTI Cryogenics GUTS support - private communication.
- [110] D. Depla and R. De Gryse, *Surface and Coatings Technology*, **183** (2-3), pp. 190 (2004).
- [111] D. Depla and R. De Gryse, *Surface and Coatings Technology*, **183** (2-3), pp. 184 (2004).
- [112] D. Guttler, B. Abendroth, R. Grotzschel, W. Moller and D. Depla, *Applied Physics Letters*, **85** (25), pp. 6134 (2004).
- [113] D. Guttler, B. Abendroth and W. Moller, "An investigation of target poisoning during reactive magnetron sputtering using ion beam analysis and energy resolved mass spectroscopy," downloaded from the world-wide web from [http://www.uni-leipzig.de/~iom/muehlleithen/2006/guttler\\_muehlleithen\\_06.pdf](http://www.uni-leipzig.de/~iom/muehlleithen/2006/guttler_muehlleithen_06.pdf) on Thursday July 11, 2006 at 10:15pm.
- [114] T.B. Massalski, H. Okamoto, P.R. Subramanian and L. Kacprzak, eds., *Binary Alloy Phase Diagrams*, 2<sup>nd</sup> Edition, ASM International, Materials Park (1990).
- [115] D. A. Porter and K. E. Easterling, *Phase Transformations in Metals and Alloys*, 2<sup>nd</sup> Edition, Chapman and Hall, London (1992).
- [116] J. W. Christian, *The Theory of Transformations in Metals and Alloys Parts I and II*, 3<sup>rd</sup> Edition, Elsevier Science Ltd., Oxford (2002).

- 
- [117] R.W. Balluffi, S.M. Allen and W.C. Carter, *Kinetics of Materials*, 1<sup>st</sup> Edition, Wiley-Interscience (2005).
- [118] D. Tsoukalas, C. Tsamis, and P. Normand, *Journal of Applied Physics*, **89** (12), pp. 7809 (2001).
- [119] O. Jaoul F. Bédjina, F. Élie and F. Abel, *Physical Review Letters*, **74** (11), pp. 2038 (1995).
- [120] F.R.N. Nabarro, *Proceedings of the Royal Society*, **A175**, pp. 519 (1940).
- [121] P. Mishra and K. P. Jain, *Physical Review B*, **64** (7), pp. 073304 (2001).
- [122] I. H. Campbell and P. M. Fauchet, *Solid State Communications*, **58** (10), pp. 739 (1986).
- [123] Y. Kanemitsu, H. Uto, Y. Masumoto, T. Matsumoto, T. Futagi and H. Mimura, *Physical Review B*, **48** (4), pp. 2827 (1993).
- [124] Details on the specifications and operation of the 2010 prism coupler can be found at the Metricon Corporation website: [www.metricon.com](http://www.metricon.com).
- [125] R. Ulrich and R. Torge, *Applied Optics*, **12**, 2901 (1973).
- [126] A. C. Adams, D. P. Schinke, and C. D. Capio, *Journal of the Electrochemical Society*, **126**, 1539 (1979).
- [127] H.J. Lee, C.H. Henry, K.J. Orlowsky, R.F. Kazarinov and T.Y. Kometani, *Applied Optics*, **27** (19), pp. 4104 (1988).
- [128] L.P. Kuznetsova, A.I. Efimova, L.A. Osminkina, L.A. Golovan, V. Yu. Timoshenko and P.K. Kashkarov, *Physics of the Solid State*, **44** (5), pp. 811 (2002).
- [129] F. Riboli, D. Navarro-Urrios, A. Chiasera, N. Daldosso, L. Pavesi, C.J. Oton, J. Heitmann, L.X. Yi, R. Scholz and M. Zacharias, *Applied Physics Letters*, **85** (7), pp. 1268 (2004).
- [130] X. D. Pi, O. H. Y. Zalloum, J. Wojcik, A. P. Knights, P. Mascher, A. D. W. Todd and P. J. Simpson, *Journal of Applied Physics*, **97**, pp. 096108 (2005).
- [131] A. Yariv and P. Yeh, *Optical Waves in Crystals*, John Wiley & Sons, Inc. (1984).
- [132] G.W. Sherer, *Applied Optics*, **19** (12), pp. 2000 (1980).
- [133] G.G. Stoney, *Proceedings of the Royal Society*, **A82**, pp.172 (1909).
- [134] J. Thornton, *Journal of Vacuum Science and Technology*, **11** (4), pp. 666 (1974).
- [135] R. Messier, A.P. Giri and R.A. Roy, *Journal of Vacuum Science and Technology A*, **2** (2), pp. 500 (1984).
- [136] F. Burmeister, C. Kohn, R. Kuebler, G. Kleer, B. Bläsi and A. Gombert, *Surface and Coatings Technology*, **200**, pp. 1555 (2005).
- [137] S.V. Krishnaswamy, R. Messier, Y.S. Ng and T.T. Tsong, *Journal of Non-Crystalline Solids*, **35/36** (1), pp. 531 (1980).
- [138] D.E. Aspnes, *American Journal of Physics*, **50** (8), pp. 704 (1982).
- [139] A. Kirchner, K. Busch and C.M. Soukoulis, *Physical Review B*, **57** (1), pp. 277 (1998).
- [140] R.H. Doremus, *Journal of Applied Physics*, **92** (12), pp. 7619 (2002).
- [141] B.A.E. Saleh and M.C. Teich, *Fundamentals of Photonics*, John Wiley and Sons, Inc., New York (1991).
- [142] X. D. Pi, O. H. Y. Zalloum, J. Wojcik, A. P. Knights, P. Mascher, A. D. W. Todd and P. J. Simpson, "Formation and oxidation of Si nanoclusters in Er-doped Si-rich SiO<sub>x</sub>," *Journal of Applied Physics*, **97**, pp. 096108 (2005).
- [143] A. Polman, *Journal of Applied Physics*, **82**, pp. 1 (1997).
- [144] A.J. Kenyon, P.F. Trwoga, C.W. Pitt and G. Rehm, *Journal of Applied Physics*, **79** (12), pp. 9291 (1996).
- [145] M. Watanabe, S. Juodkazis, H.-B. Sun, S. Matsuo and H. Misawa, *Physical Review B*, **60** (14), pp. 9959 (1999).
- [146] C. Barthou, P.H. Duong, A. Oliver, J.C. Cheang-Wong, L. Rodríguez-Fernández, A. Crespo-Sosa, T. Itoh and P. Lavallard, *Journal of Applied Physics*, **93** (12), pp. 10110 (2003).
- [147] P.D.J. Calcott, K.J. Nash, L.T. Canham, M.J. Kane, and D. Brumhead, *Journal of Physics Condensed Matter*, **5** (7), pp. L91 (1993).
- [148] A.G. Cullis, L.T. Canham, and P.D.J. Calcott, *Journal of Applied Physics*, **82** (3), pp. 909 (1997).



- 
- [149] P.D.J. Calcott, K.J. Nash, L.T. Canham, M.J. Kane, and D. Brumhead, *Journal of Luminescence*, **57** (1-6), pp. 257 (1993).
- [150] M.L. Brongersma, P.G. Kik, A. Polman, K.S. Min and H.A. Atwater, *Applied Physics Letters*, **76** (3), pp. 351 (2000).
- [151] T.S. Rose, D. Gunn, and G.C. Valley, *IEEE Journal of Lightwave Technology*, **19** (12), pp. 1918 (2001).
- [152] H. Imai, K. Arai, J. Isoya, H. Hosono, Y. Abe and H. Imagawa, *Physical Review B*, **48** (5), pp. 3116 (1993).
- [153] Y. Sakurai, K. Nagasawa, H. Nishikawa and Y. Ohki, *Journal of Applied Physics*, **75** (3), pp. 1372 (1993).
- [154] H.A. Haus, *Waves and Fields in Optoelectronics*, Prentice-Hall, Inc., Engelwood Cliffs (1984).
- [155] S.L. Chuang, *Physics of Optoelectronic Devices*, John Wiley and Sons, New York (1995)
- [156] K. Okamoto, *Fundamentals of Optical Waveguides*, 2<sup>nd</sup> Edition, Academic Press, Burlington (2006)
- [157] R.G. Hunsperger, *Integrated Optics Theory and Technology*, 5<sup>th</sup> Edition, Springer-Verlag, Berlin (2002)
- [158] K.L. Shaklee, R.E. Nahaori and L.F. Leheny, *Journal of Luminescence*, **7**, pp. 284 (1973).
- [159] L. Dal Negro, P. Bettotti, M. Cazzanelli, D. Pacifici and L. Pavesi, *Optics Communications*, **229**, pp. 337 (2004).
- [160] J. Valenta, K. Luterova, R. Tomasiunas, K. Dohnalova, B. Honerlage and I. Pelant, in *Towards the first silicon laser*, NATO Advanced Studies Institute, Series 11, Kluwer Academic, Dordrecht, **93**, pp. 223 (2003).
- [161] P.W. Milonni and J.H. Eberly, *Lasers*, John Wiley & Sons, New York (1988).
- [162] L. Dal Negro, "Rate equation modeling of energy coupling processes in Si nanocrystal – erbium systems," (unpublished)
- [163] H. Lee, J.H. Shin and N. Park, *Optics Express*, **13** (24), pp. 9881 (2005).
- [164] P. W. Milonni, *Journal of Modern Optics*, **42** (10), pp. 1991 (1995).
- [165] J. W. Fleming and J. W. Shiever, *Journal of the American Ceramic Society*, **62**, pp. 526 (1979).
- [166] H.H. Li, *Journal of Physical and Chemical Reference Data*, **9** (3), pp. 561 (1980).
- [167] P. Sheng, *Introduction to Wave Scattering, Localization, and Mesoscopic Phenomena*, Academic Press, San Diego (1995).
- [168] G.M. Hale and M.R. Querry, *Applied Optics*, **12** (3), pp. 555 (1973).